



Virginia Commonwealth University
VCU Scholars Compass

Theses and Dissertations

Graduate School

2010

Density Functional Studies of the Stability of Clusters

Penee Clayborne
Virginia Commonwealth University

Follow this and additional works at: <https://scholarscompass.vcu.edu/etd>

 Part of the [Chemistry Commons](#)

© The Author

Downloaded from

<https://scholarscompass.vcu.edu/etd/2194>

This Dissertation is brought to you for free and open access by the Graduate School at VCU Scholars Compass. It has been accepted for inclusion in Theses and Dissertations by an authorized administrator of VCU Scholars Compass. For more information, please contact libcompass@vcu.edu.

Virginia Commonwealth University

This is to certify that the thesis prepared by P. A. Clayborne entitled DENSITY FUNCTIONAL STUDIES OF THE STABILITY OF CLUSTERS has been approved by her committee as satisfactory completion of the dissertation requirement for the degree of Doctor of Philosophy.

Shiv N. Khanna, Ph.D., Department of Physics

Alison Baski, Ph.D., Department of Physics

Everett Carpenter, Ph.D., Department of Chemistry

P.N. Raychowdhury, Ph.D., Department of Mathematics and Applied Mathematics

M. Samy El-Shall, Ph.D., Department of Chemistry

Scott Gronert, Ph.D., Chair, Department of Chemistry

Fred M. Hawkridge, Ph.D., Interim Dean, College of Humanities & Sciences

F. Douglas Boudinot, Ph.D., Dean of the Graduate School

November 24, 2009

© Peneé A. Clayborne 2009
All Rights Reserved

Density Functional Studies of the Stability of Clusters

A dissertation submitted in partial fulfillment of the requirements for the degree of Doctor of Philosophy in Chemistry at Virginia Commonwealth University.

by

P. A. CLAYBORNE

B.S. Radford University, 2002
M.S. Virginia Commonwealth University, 2006

Director: Dr. Shiv N. Khanna, Ph.D.
Professor, Department of Physics

Virginia Commonwealth University
Richmond, Virginia
December 2009

Acknowledgments

I would like to thank my mentor and educator Professor Shiv. N. Khanna for his support and guidance throughout my time as a graduate student at VCU. Also, the wonderful theoretical group he has assembled together deserves a great deal of credit for assisting me to grow as a researcher. For the experimental work, I would like to thank the collaborators in Professor Castleman's group at The Pennsylvania State University. My gratitude goes to my wife, Ayana, who gave her continued support and devotion through this entire educational process. Lastly, thank you to everyone who has given their financial support over the past four years. However, I would like to express my ever gracious gratitude to the members at Saint Paul's Baptist Church, who in 2004 provided me with the financial backing to reenter school show that I could pursue my dream of obtaining a Ph.D. in the field of science.

Table of Contents

	Page
Acknowledgements	ii
List of Figures	vi
List of Tables	xv
Abstract	xviii
CHAPTER	
1 Introduction	1
1.1 Motivation	1
1.2 The Nearly Free Electron Gas: Jellium Model	4
1.3 All-Metal Aromaticity	11
1.4 Zintl Analogue Clusters.....	14
1.5 Metal-Carbides and Metallocarbohedrenes	17
1.6 Chapter 1 Summary	18
2 Experimental Method	19
3 Numerical Methods	20
3.1 Quantum Mechanics	20
3.2 Hartree-Fock Method.....	23
3.3 Density Functional Theory	25
3.3.1 Thomas-Fermi-Dirac Approximation	25
3.3.2 Hohenberg and Kohn Theorems	27
3.3.3 The Kohn-Sham Approach	28
3.3.4 Functionals for exchange-correlation	30
3.3.5 Basis Sets	34

3.4 Implementation of Density Functional Theory.....	38
3.4.1 deMon2k	38
3.4.2 Amsterdam Density Functional Package	40
3.4.3 Gaussian03	41
3.4.4 Naval Research Laboratory Molecular Orbital Library code	42
3.4.5 Vienna Ab-initio Simulation Package	42
3.4.6 Methodology	43
4 Stability using the Jellium Model	47
4.1 Al_nX clusters ($X = As, Sb, Bi; n = 1 - 6$)	47
4.2 $Ag_nMn^{+/0/-}$ ($n = 1 - 6$) Clusters: Designing Magnetic Superatoms	63
4.3 Chapter 4 Summary	79
5 Stability using All-metal Aromaticity	80
5.1 All-metal Aromaticity in Al_3X ($X = As, Sb, Bi$)	80
5.2 All-metal Aromaticity and the Ellipsoidal Jellium Model	87
5.3 Chapter 5 Summary	100
6 Stability Analogous to Zintl Polyanions: Zintl Analogue Clusters	101
6.1 Sn_nBi^- System ($n = 1 - 9$)	100
6.2 $Sn_xBi_y^-$ System ($x + y = 9$): Deltahedral Gas Phase Zintl Analogues	113
6.3 Stable Zintl Analogues using Counteranions.....	119
6.4 Chapter 6 Summary	125
7 Forming Metallo-carbides: Trinobium-carbide Clusters	126
8 Cluster Assemblies I: All-metal Aromatic Assemblies	144
9 Cluster Assemblies II: Assemblies using Magnetic Superatoms	152

10 Cluster Assemblies III: Using Zintl Analogues	155
10.1 $(\text{KSn}_6\text{Bi}_3)_n$ ($n = 2 - 6$)	155
10.2 Organo-Zintl Cluster Assemblies	163
10.3 Chapter 10 Summary	172
11 Conclusions	173
12 Future Prospects	174
References	176
Appendix A Publications relevant to this work	197
Appendix B Point Group Character Tables	199
Vita	200

List of Figures

Figure 1.2.1 Comparison of the atomic levels in the chlorine anion to the spherical jellium levels in the Al_{13} anion	7
Figure 1.2.2 Example of the ellipsoidal jellium model. Lower figure shows the splitting of p-energy levels for the oblate (left), spherical (middle) and prolate (right) jellium case. An example of the change in shape of the electron gas can be seen above each of the energy level columns.....	8
Figure 1.2.3 Comparison of the spherical and two-dimensional jellium model. Panel A shows the electronic shells for a 3-D jellium model and the electronic shells for the 2-D jellium models for the triangle and square geometries based on a square well potential can be seen in Panel B. The numbers in red represent the total number of electrons in the system. The values to the right represent the jellium shells.....	10
Figure 1.3.1 Schematic of aromatic orbitals in all-metal systems	13
Figure 1.4.1 Example of Wade-Mingos rules for clusters.	15
Figure 1.4.2 Electronic structure and geometries of the Sn_9^{2-} and Sn_9^{4-} Zintl clusters	16
Figure 2.1 Schematic of experimental apparatus used to generate and mass select gas phase clusters	19
Figure 4.1.1 Optimized geometries of the anionic, neutral, and cationic Al_nAs clusters ($n = 1 - 6$). The superscripts indicate the spin multiplicities. Bond lengths are given in Angstroms. The pink and green balls are the Al and As atoms, respectively.....	49

Figure 4.1.2 Optimized geometries of the anionic, neutral, and cationic Al_nSb clusters ($n = 1 - 6$). The superscripts indicate the spin multiplicities. Bond lengths are given in Angstroms. Pink and red balls represent Al and Sb atoms respectively.....50

Figure 4.1.3 Optimized geometries of the anionic, neutral, and cationic Al_nBi clusters ($n = 1 - 6$). Superscripts indicate the spin multiplicities. Bond lengths are given in Angstroms.....51

Figure 4.1.4 Experimental photoelectron spectra at 308 nm for each of the Al_nX^- clusters ($n = 1-5$; X = As, Sb, and Bi). Arrows mark the adiabatic detachment energies .54

Figure 4.1.5 Theoretical energy gain (Panel A) and second energy difference (Panel B) for Al_nX ($n = 1 - 5$) clusters. For definitions of the energy gain and second energy difference, refer to the text.61

Figure 4.1.6 One electron energy levels, isosurfaces (isovalue = 0.01 au), and symmetries of the molecular orbitals for the neutral Al_5As , Al_5Sb and Al_5Bi clusters. The superscripts indicate the spin multiplicities. The continuous lines are occupied states, the dashed lines represent unoccupied levels. The levels are singly degenerate unless otherwise noted. The arrows indicate majority and minority, spin up and spin down states, respectively62

Figure 4.2.1 Ground state geometries of Ag_nMn^- , Ag_nMn , and Ag_nMn^+ ($n = 1 - 6$) clusters. The superscripts indicate spin multiplicity. Green and gray circles represent manganese and silver atoms, respectively.66

Figure 4.2.2 Variation of the energy gain for the neutral, cation, and anion Ag_nMn clusters ($n = 2 - 6$)69

Figure 4.2.3 Variation of the second energy difference (S.E.D) for the neutral, cation, and anion Ag_nMn clusters ($n = 2 - 5$).70

Figure 4.2.4 One electron energy levels for MnAg_4 and molecular orbital charge density (isosurfaces 0.03 a.u.). The continuous lines are occupied levels, the dotted lines correspond to unfilled states. The degeneracy of each level is assumed to be one unless otherwise noted. The symbols α and β indicate the majority (up) and minority (down) spin states, respectively. Upper-case letters stand for delocalized *IS* and *IP* shells, and lower-case letters for localized *3d* atomic shells.74

Figure 4.2.5 One electron energy levels for MnAg_5^+ and molecular orbital charge density (isosurfaces 0.03 a.u.). The continuous lines are occupied levels, the dotted lines correspond to unfilled states. The degeneracy of each level is assumed to be one unless otherwise noted. The symbols α and β indicate the majority (up) and minority (down) spin states, respectively. Upper-case letters stand for delocalized *IS* and *IP* shells, and lower-case letters for localized *3d* atomic shells.75

Figure 4.2.6 One electron energy levels for MnAg_5^- and molecular orbital charge density (isosurfaces 0.03 a.u.). The continuous lines are occupied levels, the dotted lines correspond to unfilled states. The degeneracy of each level is assumed to be one unless otherwise noted. The symbols α and β indicate the majority (up) and minority (down) spin states, respectively. Upper-case letters stand for delocalized *IS* and *IP* shells, and lower-case letters for localized *3d* atomic shells.77

Figure 4.2.7 Lowest energy structure of the $\text{MnAg}_{24}(\text{SH})_{18}$ cluster78

Figure 5.1.1 Optimized geometries of the neutral and anionic Al ₃ As, Al ₃ Sb, and Al ₃ Bi clusters (Bond lengths are given in Angstroms) and collected photodetachment spectra for the anion species. The red lines represent the calculated vertical electron detachment energies from the anion	81
Figure 5.1.2 The isosurfaces (isovalue = 0.01 au) and symmetries of Al ₃ As (Panel a), Al ₃ Sb (Panel b) and Al ₃ Bi (Panel c) of the molecular orbitals for the neutral ground state geometries.....	83
Figure 5.1.3 Nucleus-Independent Chemical Shift (NICS) values of cationic, neutral and anionic Al ₃ As and Al ₃ Sb in ppm. Previous results for Al ₃ Bi are shown for comparison. The NICS values are calculated at the position of a ghost atom placed at the ring center in the molecular plane, and 0.5, 1.0, and 1.5 Å above the plane, respectively	85
Figure 5.2.1 Schematic of the C _{2v} , D _{3h} , and C _{3v} geometries.....	88
Figure 5.2.2 One-electron levels and molecular orbital isosurfaces with symmetry assignments for the Al ₃ P cluster. The molecular orbital isosurfaces (isovalue = 0.01 a.u.) and levels for the D _{3h} (Panel A) and C _{2v} geometry (Panel B) structures are given. The solid and dashed lines represent the occupied and unoccupied levels, respectively. The superscripts indicate spin multiplicity. The degeneracy is assumed to be 2, unless otherwise noted.....	91

Figure 5.2.3 One-electron levels, molecular orbital isosurfaces (isovalue = 0.01 au) and geometries for the Al_3N cluster with C_{3v} (Panels A and C) and D_{3h} (Panels B and D) geometry. Each orbital is labeled with its representation. The Cartesian axis is given as a reference for the molecular orbitals. The pink and blue balls represent the Al and N atoms, respectively. For further information refer to Figure 5.2.2.....93

Figure 5.2.4 One-electron levels, molecular orbital isosurfaces (isovalue = 0.01 au) and geometries for the Al_3Sb cluster. The geometries and isosurfaces for the C_{3v} and C_{2v} geometries are given in Panel A and Panel B respectively. The red and pink balls represent the Sb and Al atoms respectively. For further information, please refer to Figure 5.2.394

Figure 5.2.5 One-electron levels, molecular orbital isosurfaces (isovalue = 0.01 au) for the lowest energy Al_3As cluster. The green and pink balls represent the Sb and Al atoms respectively. For further information, please refer to Figure 5.2.497

Figure 6.1.1 Lowest energy structures for Sn_nBi^- clusters ($n = 2 - 9$). The gray and purple balls represent the Sn and Bi atoms respectively.....103

Figure 6.1.2 Collected mass spectra of Sn_nBi^- ($n = 3 - 9$) clusters. The insert is a magnified portion of the tin-bismuth anionic clusters104

Figure 6.1.3 Plot of the energy gain (E.G.) and HOMO-LUMO gap (Gap) for the Sn_nBi^- clusters ($n = 2 - 9$).107

Figure 6.1.4 Isosurfaces of the molecular orbitals for Sn_4Bi^- and Sn_5^{2-} . The white balls represent Sn atoms and the blue balls represent the Bi atom.....108

Figure 6.1.5 One-electron levels of Sn_4Bi^- (Column A) and Sn_5Bi^- (Column B). Molecular orbital NICS values are given for the group of molecular orbitals (in ppm) .111

Figure 6.2.1 Comparison of the D_{3h} and C_{4v} structures for the Sn_9^{q-} ($q = 1 - 4$) and $Sn_xBi_y^-$ ($x + y = 9$) deltahedral clusters. The difference in relative energies is given in electron volts. The bond lengths are in Angstroms. The pink and gray balls represent the Bi and Sn atoms respectively115

Figure 6.2.2 One electron levels and isosurfaces of the molecular orbitals of interest of the Sn_9^{2-} , Sn_9^{4-} and $Sn_6Bi_3^-$ clusters. The dashed lines represent the unoccupied states, while the solid lines represent doubly occupied states117

Figure 6.3.1 Optimized geometries of KSn_6Bi_3 (Panels A and D), $Sn_6Bi_3-CH_3$ (Panels B and E) and $Sn_6Bi_3-C_2H_3$ (Panels C and F) clusters120

Figure 6.3.2 Lowest energy structures for the $Sn_7Bi_2-C_2H_3$ and $Sn_8Bi-C_2H_3$ clusters. The bond length between the $-C_2H_3$ and the parent clusters are given in Angstroms.....123

Figure 7.1 Mass spectrum of $Nb_mC_n^-$ clusters formed. The $Nb_3C_n^-$ clusters ($n = 5 - 10$) examined in the present study are labeled.128

Figure 7.2 Anion photoelectron spectra of $Nb_3C_n^-$ ($n = 5-10$) clusters.....131

Figure 7.3 The ground state and relevant isomer structures for $Nb_3C_5^-$ (A), $Nb_3C_6^-$ (B-E), and $Nb_3C_7^-$ (F-H) with the theoretical vertical detachment energies (VDE) and relative energies (ΔE_{rel}). Vertical Detachment and Relative energies are in eV and do not include zero-point energies. The blue and yellow balls represent the Nb and C atoms, respectively.....132

Figure 7.4 The ground state and relevant isomer structures for Nb_3C_8^- (A-D), Nb_3C_9^- (E-G), and $\text{Nb}_3\text{C}_{10}^-$ (H-J) with the theoretical vertical detachment energies (VDE) and relative energies (ΔE_{rel}). The reported VDEs and relative energies do not include the zero-point energies and are in eV. The blue and yellow balls represent the Nb and C atoms, respectively.....133

Figure 7.5 Comparison of experimental electron detachment energy with calculated vertical detachment energies for Nb_3C_n^- ($n = 5 - 10$). Red squares represent the “capping” motifs for each of the clusters. Experimental values are open squares with error of +/- 0.02 eV140

Figure 7.6 Comparison of experimental electron detachment energy with calculated vertical detachment energies for Nb_3C_n^- ($n = 6 - 9$). Red circles represent the D-bridging motifs. Blue triangles represent the single C_2 bridging chain structures. Experimental values are open squares with error of +/- 0.02 eV.....142

Figure 8.1 Lowest Energy structures for the optimized Al_3Sb dimer assemblies. The fused Al_6Sb_2 structure (Panel A) and the unfused structure (Panel B) are given with relative energies in electron volts. The pink and orange balls represent the Al and Sb atoms, respectively.....145

Figure 8.2 Initial and optimized configurations of the homodecked all-metal assemblies. The starting $(\text{Al}_3\text{Sb})_2\text{M}$ geometry is located in Panel A. The final configurations of the $\text{Al}_6\text{Sb}_2\text{V}$ (Panel B) is given as a representation of the lowest energy structure for the optimized homodecked assemblies. The red, light pink, and dark pink balls represent the Sb, Al and V atoms respectively147

Figure 8.3 Initial and optimized configurations of the heterodecked assemblies. The starting $(Al_3Sb)VBz$ structure is located in Panel A. The lowest energy structure (Panel B) and lowest lying isomer (Panel C) are given with spin multiplicities (M) and relative energies (E_{rel}) in electron volts. The red, light pink, green, white and blue balls represent the Sb, Al, C, H, and V atoms respectively150

Figure 9.1 Lowest energy structures with relative energies (E_{rel} (eV)) for the fused $Ag_{12}Mn_2$ cluster. The gray and green balls represent the Ag and Mn atoms respectively153

Figure 10.1.1 Lowest Energy structures for the $[KSn_6Bi_3]_2$ system. Lowest energy configuration (Panel A), lowest isomer (Panel B) and second lowest isomer (Panel C). The blue, gray and pink balls represent the K, Sn, and Bi atoms respectively. The distance between parent clusters are given in Angstroms and are represented with the blue line.....157

Figure 10.1.2 Lowest energy geometries for $[KSn_6Bi_3]_3$ (Panel A), $[KSn_6Bi_3]_4$ (Panel B), $[KSn_6Bi_3]_5$ (Panel C) and $[KSn_6Bi_3]_6$ (Panel D) are given with the pink, gray, and blue balls representing the Bi, Sn, and K atoms, respectively. The distance between the parent clusters are given in Angstroms and are marked with the solid blue line159

Figure 10.1.3 Removal Energy and HOMO-LUMO gap for $(KSn_6Bi_3)_n$ ($n = 1 - 6$) assemblies160

Figure 10.1.4 One-electron levels for $(KSn_6Bi_3)_n$ assemblies. The gray lines are the unoccupied states, while the solid lines with arrows are the occupied states162

Figure 10.2.1 Lowest Energy structures for the $\text{Sn}_7\text{Bi}_2^{x-}$, $(\text{C}_2\text{H}_3)\text{Sn}_7\text{Bi}_2^{y-}$, and $(\text{C}_2\text{H}_3)_2\text{Sn}_7\text{Bi}_2$ clusters ($x = 1-2$; $y = 0-1$). The HOMO-LUMO gap (E_{gap}) values are given below the structures in electron volts. The gray, pink, green, and white balls represent the Sn, Bi, C, and H atoms respectively.....165

Figure 10.2.2 Lowest Energy structures for the $(\text{C}_2\text{H}_2)_k(\text{C}_2\text{H}_3)_2(\text{Sn}_7\text{Bi}_2)_j$ cluster assemblies ($j = 2 - 4$; $k = j - 1$). The HOMO-LUMO gap (E_{gap}) values are given in electron volts. The gray, pink, green, and white balls represent the tin, bismuth, carbon, and hydrogen atoms respectively.....169

Figure 10.2.3 Electron levels for the organo-Zintl cluster assemblies. The gray lines are the unoccupied states, while the solid lines with arrows are the occupied states170

List of Tables

- Table 3.1** The functionals and basis sets in software packages for the atoms used in the systems studied. Also listed is if any relativistic effects were taken into account, as well as if any auxiliary functions were used in the calculations. The \$ is used to denote a basis used with diffuse functions for the atom.46
- Table 4.1** Experimental adiabatic detachment energies (ADE) and vertical detachment energies (VDE) of Al_nAs^- ($n = 1-5$) clusters. Calculated ADEs and VDEs of Al_nAs^- ($n = 1-6$) clusters. For theoretical VDEs, transitions to both the lower and higher spin states are listed where appropriate. Calculated adiabatic ionization potentials (IP) and HOMO-LUMO gap (HL gap) values for the ground state Al_nAs ($n = 1-6$) clusters..All values are in units of eV. Experimental VDEs have an uncertainty of ± 0.05 eV56
- Table 4.2** Experimental adiabatic detachment energies (ADE) and vertical detachment energies (VDE) of Al_nSb^- ($n = 1-5$) clusters. Calculated ADEs and VDEs of Al_nSb^- ($n = 1-6$) clusters. For theoretical VDEs, transitions to both the lower and higher spin states are listed where appropriate. Calculated adiabatic ionization potentials (IP) and HOMO-LUMO gap (HL gap) values for the ground state Al_nSb ($n = 1-6$) clusters..All values are in units of eV. Experimental VDEs have an uncertainty of ± 0.05 eV57
- Table 4.3** Experimental adiabatic detachment energies (ADE) and vertical detachment energies (VDE) of Al_nBi^- ($n = 1-5$) clusters. Calculated ADEs and VDEs of Al_nBi^- ($n = 1-6$) clusters. For theoretical VDEs, transitions to both the lower and higher spin states are listed where appropriate. Calculated adiabatic ionization potentials (IP) and HOMO-LUMO gap (HL gap) values for the ground state Al_nBi ($n = 1-6$) clusters. All values are in units of eV. Experimental VDEs have an uncertainty of ± 0.05 eV58

Table 4.2.1 The comparison of the bond length (r), dissociation energy (D_e), frequency (ω), and ionization potential (IP) of the silver dimer. The units for each measure are in parenthesis	65
Table 4.2.2 HOMO-LUMO gap for the neutral, cationic and anionic Ag_nMn clusters ($n = 1 - 6$) and their ionization potential (I.P.) and electron affinity (E.A.).....	71
Table 4.2.3 Electronic properties of the $Ag_nMn^{0/+/-}$ clusters ($n = 1 - 6$). Magnetic moments (μ), Ag gain in energies (ΔE_{Ag}), and HOMO-LUMO Gaps (E_{gap}) as well as the magnetic moment of the higher in energy isomer with a different magnetic moment, and the energy difference with respect to the ground state ΔE	72
Table 5.1.1 C Calculated and experimental Adiabatic Detachment Energies (ADE), calculated Adiabatic Ionization Potentials (IP), HOMO-LUMO gap values and removal energies for the ground state Al_nAs , Al_nSb , Al_nBi ($n = 2 - 4$) clusters (in eV)....	82
Table 5.2.1 Relative Energies for the Al_3M ($M = N, P, As, Sb, \text{ and } Bi$) clusters in the C_{2v} , D_{3h} and C_{3v} geometries	89
Table 5.2.2 The symmetry, separation energies of the p-states (E_p), d-states (E_d) and average (Avg.), with the HOMO-LUMO gaps (E_{gap}) for the ground state Al_3M ($M = N, P, As, Sb, \text{ and } Bi$) clusters (in eV)	98
Table 6.1 Theoretical and experimental adiabatic and vertical electron detachment energies, as well as the calculated HOMO-LUMO gaps for the Sn_nBi^- clusters. Experimental error is ± 0.1 eV for ADE and VDE; experimental error is ± 0.2 for VDE2 and VDE3. All energies are in eV.	105
Table 6.1.2 NICS (0) values for Sn_nBi^- , Sn_{n+1}^{2-} and Ge_{n+1}^{2-} where $n = 4 - 9$. All NICS values are in ppm	109

Table 6.2.1 The experimental and theoretical values for the vertical electron detachment energies (VDE and VDE2), adiabatic electron detachment energies (ADE) and calculated HOMO-LUMO gap (Gap) and removal energies (R.E.) for the deltahedral tin-bismuth clusters Sn_xBi_y^- ($x + y = 9$) (in eV). The values in parenthesis represent the experimental error116

Table 6.3.1 The calculated HOMO-LUMO Gap, Binding Energies (B.E.), electron affinities (E.A.) and parent cluster symmetries for Sn_6Bi_3^- , $\text{ASn}_6\text{Bi}_3^-$ (A = Na, K, and Cs), and $\text{Sn}_6\text{Bi}_3\text{-R}$ (R = CH_3 and C_2H_3).....121

Table 7.1 Experimental (Exp.) adiabatic (AEDE) and vertical electron detachment energies (VEDE) for Nb_3C_n^- observed features shown in Figure 7.2. The experimental uncertainty for each measurement is 0.2 eV129

Table 10.2.1 The HOMO-LUMO gap (E_{gap}), fragmentation energy (F.E.) and removal energy (R.E.) for the organo- $(\text{Sn}_7\text{Bi}_2)_n$ assemblies (in eV)167

Abstract

DENSITY FUNCTIONAL STUDIES OF THE STABILITY OF CLUSTERS

By P. A. Clayborne, M.S.

A dissertation submitted in partial fulfillment of the requirements for the degree of Doctor of Philosophy in Chemistry at Virginia Commonwealth University.

Virginia Commonwealth University, 2009

Director: Shiv N. Khanna, Ph.D.
Professor, Department of Physics

Theoretical studies using the Kohn-Sham density functional formalism have been carried out to identify and investigate the stability of a variety of atomic clusters for their use in cluster assembled materials. The stable behavior found in a cluster system provides a way to classify inorganic clusters. The clusters in this study can be categorized in one of the following, jellium, all-metal aromatic, Zintl analogue or as a covalent metal-carbide. By understanding the electronic structure and ultimately the stable nature of a cluster first, it is proposed one can construct assemblies based on the stable cluster. The methodology presented is a viable way to design future nanomaterials with a variety of architectures and precise control over properties based on stable cluster motifs.

Chapter 1 Introduction

1.1 Motivation

Over the past few decades many of the significant scientific and technological developments have been inspired by developments in material science. The motivation is rooted in the need for the design and synthesis of nanoscale materials with precise desired properties. One of the most promising prospects to meet this challenge is using stable atomic clusters as building blocks in a “bottom-up” approach leading to nanoscale cluster assemblies.

Atomic clusters are aggregates of atoms with a variation in size from a few to a few thousands of atoms. It is well known that the thermodynamic, electronic, magnetic and optical properties of clusters can differ extensively from their macroscopic bulk phase counterparts. In fact the properties of atomic clusters have been shown to vary as a function of size, composition, and geometrical shape. The most interesting systems of clusters are those in which the properties vary dramatically with the number of atoms and composition, instead of linearly with size. In order to understand how properties evolve, it is important to know how a specific desired property behaves, like magnetism, geometry or ionization potential, as the number of atoms increase one by one. A few examples include Au, Rh, and Fe clusters. In the bulk, Au is a noble metal, however small clusters of Au are highly effective catalysts for the conversion of CO to CO₂ [1]. While bulk Rh is non-magnetic, small Rh clusters are magnetic with magnetic moments per atom comparable to other itinerant ferromagnetic solids [2]. Another example is found using aluminum clusters and its bulk counterpart. In the bulk, aluminum is readily oxidized forming a variety of reactive aluminum-oxides [3 - 5]. However, aluminum clusters are very different.

Aluminum cluster anions containing 13, 23, and 37 atoms, for example, are unreactive towards oxygen [6].

The differences between atomic clusters and the bulk counterpart is grounded in the small volume of the potential well that confines the electrons in clusters, which result in the emergence of discrete one-electron energy levels instead of bands seen in bulk [7]. This realization leads to the question; How does this difference between clusters and bulk change the properties in a cluster assembled material? In order to answer that question one must compare the various properties in a solid versus those expected of a cluster assembled material. In a solid the energy bands are the results from the overlap of atomic energy levels. However, in a cluster assembled material, the energy bands would result from the overlap of the discrete cluster energy levels. The nature of bonding in a solid between atoms is well understood and characterized, but in a CAM the bonding within the individual cluster may be covalent, but between clusters it may be different, such as van der Waals in character. The vibrations in CAMs can combine the intra- and inter-cluster modes. If one were able to design a magnetic solid, the combination of weak inter-cluster couplings with the strong intra-cluster interactions could lead to novel characteristics [8].

The task of designing and synthesizing cluster assemblies appears on the surface to be a simple task; however this is far from true. The problem: Many clusters are metastable! Thus, once a cluster is introduced to other clusters, the group of clusters tend to conglomerate and lose all reference to the original cluster used in the attempt at synthesizing the material. However over the recent two decades there are discoveries that show promise such as the fullerene C₆₀. Molecular beam experiments conducted by Kroto and co-workers showed an intense magic peak for clusters containing sixty carbon atoms in the mid eighties [9]. This discovery led to the

identification of a “soccer ball” like structure containing sixty carbon atoms with remarkably different properties than that of graphite or diamond. C_{60} proved to be not only stable in the gas phase, but even stable when exposed to the environment. This has since led to the development of using other fullerenes as novel ways to aid in various fields including cancer identification and treatment [10 – 11]. Fullerites, the crystal form of fullerenes, are formed and governed by Van der Waals forces that weakly bond the clusters together. Fullerites have been known to form fcc structures, as well as other stable structures with the hope of various device applications [12 – 13]. There are other more recent examples possible clusters that may and have been used in cluster assemblies, such as *Superatoms*, and the unique cluster $Te_2As_2^{2-}$ [14 – 15].

The success of these small cluster assembled materials leads us to the nature of a cluster’s unique stable behavior. In the case of fullerenes, superatoms and even $Te_2As_2^{2-}$, they were found to be extremely stable using experimental and theoretical techniques and consequently the source of their stable behavior was identified as well [15]. These results have placed heavy implications on understanding the mechanism of stability within a cluster. In becoming knowledgeable of the precise stability mechanism, a designer can better create cluster assemblies with the optical, magnetic and catalytic properties of choice. Even more advantageous, is the possibility to better predict cluster-cluster interaction, opening the door to a series of cluster assembled architectures that potentially would be resistant to oxygen etching.

At the core of cluster assemblies is the cluster’s ability to maintain its inherent geometry and electronic character when interacting with other atoms and clusters. This idea originated with two pioneers in cluster science, Khanna and Jena [16]. These authors eloquently pointed out that the clusters needed to achieve this goal must be required to exhibit an enhanced stability. Thus, the mechanism of stability within a cluster system is met with great importance. In order

to take advantage of a cluster's stability, one must first become aware of the different stability classifications. In the remainder of this chapter, I will introduce three common mechanisms of stability, which is the framework of this thesis.

1.2 The Jellium model

When the idea of stable clusters as building blocks was introduced, it was proposed by Khanna and Jena it was indeed possible to design stable clusters [16]. These unique clusters would interact weakly instead of coalescing, when introduced to each other. At the time there was one cluster class that showed extreme promise in this endeavor; jellium “magic” metallic clusters.

Magic metallic clusters were first observed by Knight and co-workers [17]. Knight and co-workers noticed when the number of sodium atoms in a cluster were 2, 8, 18, 20, etc., these particular clusters were more abundant. These “magic” numbers were interpreted as reflecting an electronic shell structure, much like in atoms or nuclei in nucleons as predicted by Ekardt [18 – 19]. Knight, Clemenger and co-workers developed an empirical jellium model based on quantum mechanics from the boundary conditions imposed by a potential [20]. The empirical jellium model is based on single particle potentials and solving the one-electron Schrodinger equation for a particle inside a sphere.^A The jellium wavefunctions or orbitals (i.e.- the solutions to the Schrodinger equation) can be separated into radial (R) and angular (Y) parts, due to the spherical nature of the potential via,

$$\Psi_{nlm}(r, \theta, \varphi) = R_{nl}(r)Y_{lm}(\theta, \varphi)$$

^A For more information on the Schrodinger equation please refer to Chapter 3 of this text.

where n , l , and m are the principal, angular momentum and magnetic quantum numbers, respectively. Notice these are analogous to the atomic quantum numbers and the jellium orbitals are labeled as such. The allowed values for the jellium quantum numbers are,

$$n = 1, 2, 3 \dots$$

$$l = 0, 1, 2, 3, \dots$$

$$m = 0, \dots \pm l$$

with no restriction on l , which is different from the atomic case. Thus, the first few orbitals in the jellium case would correspond to:

$$1s: n = 1 \quad l = m = 0$$

$$1p: n = 1 \quad l = 1 \quad m = 0, \pm 1$$

$$1d: n = 1 \quad l = 2 \quad m = 0, \pm 1, \pm 2$$

in which the number of orbitals resemble the number of orbitals found in atomic shells. From this model, magic numbers arise once a jellium level is completely filled by electrons ($1s$, $1p$, $1d$, $2s$, $1f$, etc.). It should be noted in the spherical jellium model the energies of the jellium orbitals increase with increasing principal quantum number (n) and angular momentum quantum number, while orbitals with the same m value are degenerate, similar to the atomic case. However, the ordering of the jellium levels are dependent on the radial form of the assumed effective jellium potential [21].

There are three types of radial jellium potentials, the 3-D harmonic potential, the 3-D square well potential, and the Woods-Saxon potential. The Woods-Saxon potential is the most widely used and most successful radial potential for the empirical jellium model. The Woods-Saxon potential is a finite, almost square well with rounded sides, which is an intermediate between the harmonic and square well potentials, with the form

$$U(R) = \frac{-U_0}{\exp[(R - R_0)/\sigma] + 1}$$

where σ is a constant scaling factor with the approximate value of 7.94×10^{-11} m, R_0 is the effective radius of the cluster sphere, with U_0 dependent upon the Fermi energy and the work-function of the bulk metal via,

$$U_0 = E_F - W.$$

When comparing the three commonly used potentials for the jellium model, one realizes there is a slight difference in the order of the jellium levels. As for the square well potential, shell closings occur when the number of electrons correspond to 2, 8, 18, 20, 34, 40, 58, etc, while for the 3-D harmonic potential magic numbers are predicted for 2, 8, 20, 40, and 70. The difference between the square well and Woods-Saxon potential occurs above the $2d$ orbital or more than 68 electrons [22].

The *Spherical Jellium Model* (SJM) has been used in understanding the stability for many metal clusters, including the alkali and noble metal clusters. However, it has played a significant role in one of the most significant discoveries in the realm of cluster science, the *Superatom*. The superatom concept was born out of the initial idea of a “unified atom” from experiments performed on aluminum cluster anions by the Castleman group in the eighties [6]. From experimental observations, cluster anions containing 13, 23, and 37 atoms were found to be unreactive when oxygen (O_2 gas) was introduced in the chamber. It was deduced that since the Al atom contains three valence electrons ($[Ne] 3s^2 3p^1$), the number of electrons in the observed stable cluster systems corresponded to the magic numbers 40, 70, and 112 within the jellium model. This was followed by the introduction of the “superelement” concept from a group of papers beginning in 1992 from Khanna and Jena [16]. In their work, they proposed it was possible to design stable clusters by combing the geometric and electronic stability. In fact, upon

further theoretical investigations it was discovered that the electron affinity of the Al_{13} cluster was close to that of the Cl atom (3.7 eV), which for the first time suggested the Al_{13} cluster was analogous to a halogen atom or a “superhalogen” (Figure 1.2.1). This was followed by a multitude of theoretical and experimental studies in the cluster science field with the term superatom evolving from the synergistic efforts by the groups of Castleman and Khanna [23].^B However, it should be noted that the current definition of a superatom cannot solely be limited to a cluster mimicking one selected property of an atom, but must demonstrate 1) energetic stability; 2) chemical stability; and 3) new chemical features beyond the analogue atoms [23]. For example, Bergeon and co-workers not only showed that the Al_{13} behaved like a chlorine atom filling the electronic shells within the SJM and with the addition of one electron, the Al_{13}^- cluster was stable, but that one could produce polyhalides [24].

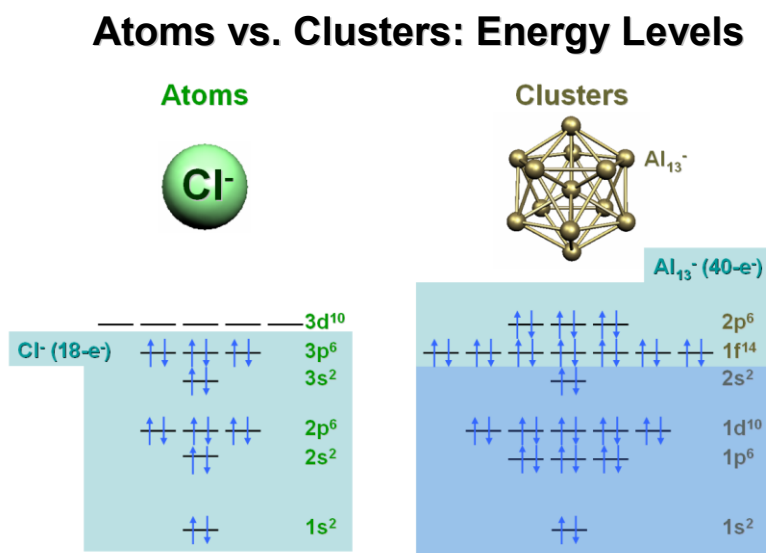


Figure 1.2.1 Comparison of the atomic levels in the chlorine anion to the spherical jellium levels in the Al_{13} anion.

^B For a comprehensive review of these studies refer to Reference 23 and the references therein.

The novel discovery of superatoms utilizing the SJM has since lead to the expansion of the periodic table to three-dimensions [25]. There are several superatoms which include multivalent, magnetic, and even gold and silver thiolated complexes as superatoms [26 – 28]. The most recent addition to the third dimension of the periodic chart are magnetic superatoms which adhere to the SJM and fills a localized magnetic sub-shell [27].

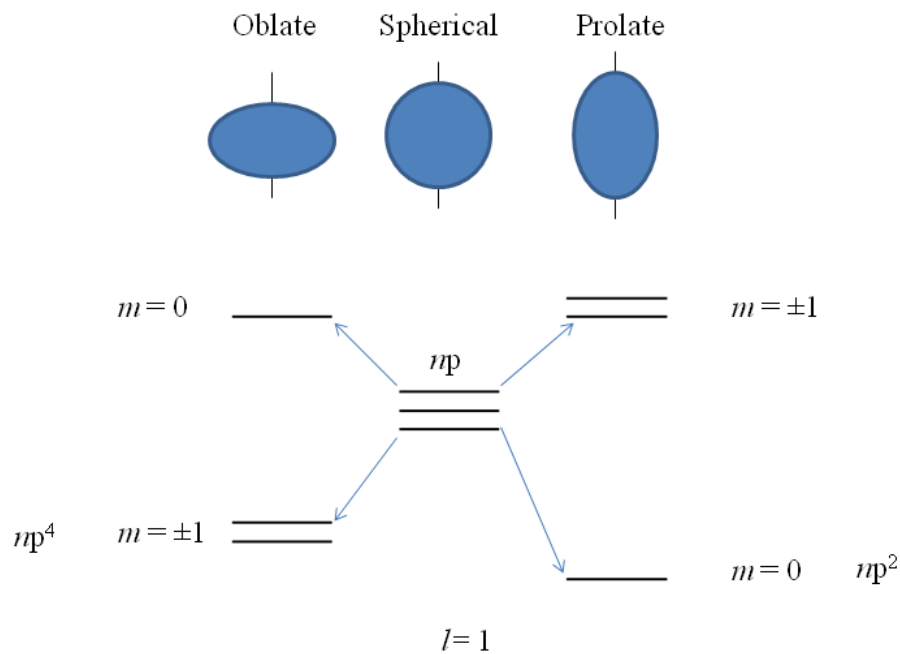


Figure 1.2.2 Example of the ellipsoidal jellium model. Lower figure shows the splitting of p-energy levels for the oblate (left), spherical (middle) and prolate (right) jellium case. An example of the change in shape of the electron gas can be seen above each of the energy level columns.

The spherical jellium model though useful in explaining the more dominant peaks in the original sodium gas phase experiments and the concept of superatoms, could not explain the smaller peaks that appeared in the sodium gas phase experiment. However, in 1985 Clemenger used a theory developed by Nilsson to explain these smaller abundant peaks in the experiment

[29]. Clemenger utilized an ellipsoidal scaling factor within the Hamiltonian and derived what is termed as the ellipsoidal jellium model or Clemenger-Nilsson model for clusters. In the ellipsoidal shell model, distortions are allowed for partially filled jellium orbital shells, with a perturbed 3-D harmonic oscillator potential. The spherical symmetry is lowered, which results in the loss of the $(2l+1)$ degeneracy of each jellium nl shell, however axial symmetry is retained meaning the $\pm m$ orbitals split into $l(\pm m)$ pairs and the $m = 0$ orbital is on its own. This model predicts stable clusters with distorted geometries, oblate and prolate (Figure 1.2.2), will show signs of stability with closed shells, but at different values than in the spherical jellium model. Since the derivation of the ellipsoidal jellium model a variety of systems have utilized the model to explain a variety of systems such as, quantum dots, fullerene studies, and other clusters [30 – 34]. The ellipsoidal jellium model is very illustrative on how the shape of a cluster can indeed change the shell structure. This point is further brought out in the two-dimensional jellium shell model.

The two-dimensional shell model has been used to explain the stability seen in a variety of gold cluster systems [35]. E. Janssens and co-workers showed using Schrodinger's electron in a box problem for an infinitely square potential well for a two-dimensional equilateral triangle, circle and square geometries that the number of electrons corresponding to a stable species is slightly different from those found in the spherical jellium model [36]. Since, this model has been used to explain the stability in a variety of planar clusters. Hakkinen used the two-dimensional model to explain the stability in a multitude of gold clusters [35]. Studies on cluster systems such as Cu_7Sc , Au_3Al and Au_5Al , and Ag_n , have shown the strong presence and applicability of the jellium model in two-dimensions to explain the stable behavior for a variety

of electron counts. It should be noted, that no matter the geometry in the 2-D jellium model (Figure 1.2.3) there are magic numbers at 2, 6, 12, 16 and 20 [37 – 39].

The spherical, ellipsoidal, and two-dimensional jellium model can explain a cluster's stable behavior as the electronic shells become filled by electrons. Therefore, one should be able to take advantage of the unique shell filling to build cluster assemblies. There have been attempts using superatoms as building blocks for new materials with some success [40]. Thus, it should be possible to design cluster assemblies using of the stable clusters defined through the ellipsoidal and two-dimensional jellium models as well.

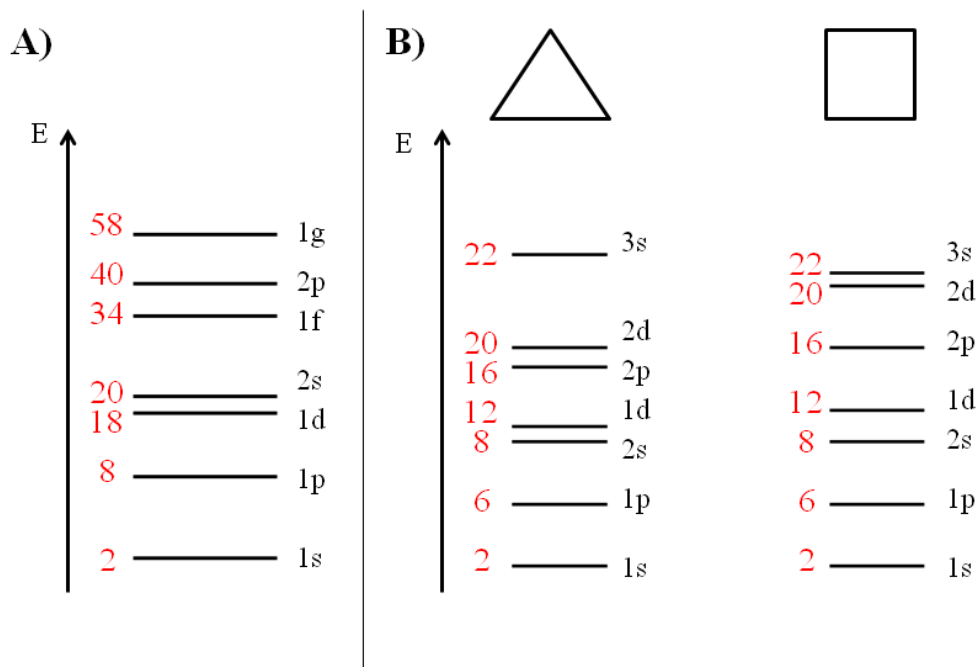


Figure 1.2.3 Comparison of the spherical and two-dimensional jellium model. Panel A shows the electronic shells for a 3-D jellium model and the electronic shells for the 2-D jellium models for the triangle and square geometries based on a square well potential can be seen in Panel B. The numbers in red represent the total number of electrons in the system. The values to the right represent the jellium shells. The axis is the energy (E).

1.3 All-Metal Aromaticity

The jellium model has been very effective in identifying stable clusters towards the ideal of cluster-assemblies, however it cannot explain all stable clusters such as that of boron and polyanions. Boron is a trivalent element with $1s^2 2s^2 2p^1$ electronic configuration. However it has a tendency to form directional bonds and a short covalent radius. When looking at B_n^+ clusters, clusters containing 5, 11 and 13 atoms appear to magic in laser ablation experiments [41]. The number of electrons in these experiments would correspond to 14, 32, and 38 electrons respectively, which do not correspond to the “magic” numbers seen in the spherical jellium model. In order to explain the stability, several theoretical calculations have been attempted and the resulting explanation relied on an organic chemistry construct, *aromaticity*.

The concept of “pure” aromaticity originates in a delocalization of the molecular orbitals that ultimately is responsible for the stabilization of a cluster system. The most well known aromatic system is the Benzene molecule or cluster (C_6H_6). The p -orbitals overlap, which result in the formation of π -bonds. The stabilization is rooted in the delocalized pi-electrons being spread equally around the ring. The concept of “pure” aromaticity is reserved for the organic compounds that must fulfill both the following criteria,

1. It must have an uninterrupted cloud of delocalized π electrons circling above and below the plane of the molecule.
2. The π cloud must contain an odd number of pairs of π electrons.

Notice that criteria number one implies that the compound must be cyclic and planar. It is also important that the aromatic compound follows Hückel's Rule. The rule states that for a compound to be aromatic, it must have $4n + 2$ π electrons, where n is any whole number. Thus,

Hückel's Rule requires an aromatic system have 2, 6, 10, 14, 18, etc. π electrons, where $n = 0, 1, 2, 3, 4$, etc. respectively [42].

Even though aromaticity is an organic construct, in 2001 Li and co-workers used this concept to explain stability found in an inorganic metallic system [43]. The authors illustrated through examination of bonding and structure, that Al_4^{2-} exhibited characteristics of aromaticity, by meeting the two minimum criteria above. In fact, they proposed the Al_4^{2-} cluster had achieved the status of *all-metal aromaticity*. Since this 2001 study, various systems have been identified as all-metal aromatic systems, including the aforementioned boron clusters, arsenic clusters (As_5^-), clusters composed of gold such as Au_3 , transition-metal systems, heteroatomic systems ($Te_2As_2^{2-}$) and some studies have opened yet another door to include three-dimensional all-metal aromatic systems [44 – 45]. The mounds of research in the field of all-metal aromaticity has led to various types of aromaticity including sigma (σ), pi (π), and delta (δ) aromaticity (Figure 1.3.1) along with the advent of Hirsch's $2(N + 1)^2$ electron counting rule for spherical aromaticity [46 – 48].

In order to identify an aromatic or all-metal aromatic system, one may evaluate not only the orbital shapes, but employ the Nucleus-Independent Chemical Shift calculation. The Nucleus-Independent Chemical Shift value, often abbreviated NICS, was introduced by Schleyer [49]. This value is based on the idea of a magnetic field inducing a current on a ring. Schleyer and co-workers proposed the diamagnetic susceptibility is uniquely associated with aromaticity by evaluating a variety of known organic compounds and a few inorganic clusters [50]. Using this idea, one can determine both aromatic and antiaromatic character in a cluster system. By definition aromaticity is a as a negative NICS value and antiaromaticity a positive value. Since its initial applications, the NICS value has been used successfully in the identification of

aromatic and antiaromatic clusters and molecules [51]. However, it should be pointed out that even with the success of this method, there is controversy over the applicability of this criterion; this will not be addressed here, but the reader is encouraged to read reviews on the subject such as the review by Gomes and Mallion [52]. There is a more typical way to evaluate conventional aromaticity in organic and inorganic clusters. The aromatic stabilization energy (ASE) and resonance energy can be used as a method to determine the aromatic character of an all-metal aromatic cluster. Both of these energetic values require reference systems in order to complete their evaluations [53].

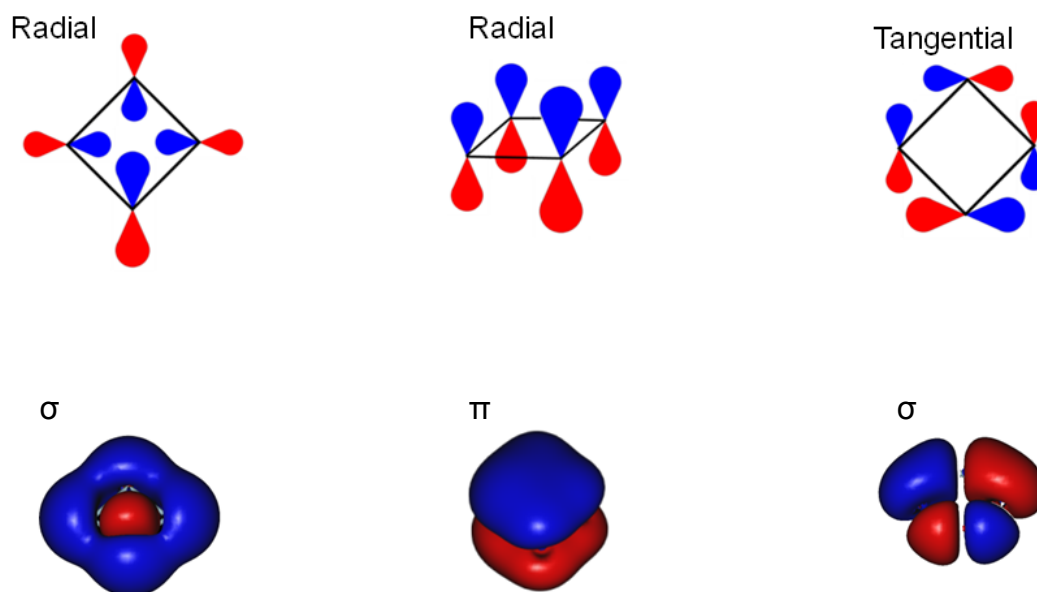


Figure 1.3.1 Schematic of aromatic orbitals in all-metal systems.

The concept of all-metal aromatic clusters as a stable classification is due to the unique character of delocalization is reminiscent of those seen in organic chemistry. From the first identification of the all-metal aromatic cluster, it was believed by some researchers these all-metal aromatic cluster would be incapable of forming viable assemblies [54]. This idea has

recently been discarded in direct response to the recently reported cluster assembly using the all-metal aromatic species $\text{Te}_2\text{As}_2^{2-}$ by Reber and co-workers [15]. Therefore if one can identify more of these stable all-metal aromatic systems it may be possible design new cluster assemblies.

1.4 Zintl Analogues

There are groups of polyanions that are stable but whose stability cannot be fully explained through either the jellium model or the all-metal aromaticity concept. These stable clusters are referred to as Zintl polyanions and are commonly seen in Zintl phases. Zintl cluster compounds were first reported by Joannis in 1891 [55]. However, this diverse class of clusters received its name from E. Zintl, who in the early 1930s investigated the polyatomic anions of the post-transition metals and semimetals in liquid ammonia [56]. Following his lead, research on Zintl ions focused on improving the synthesis and on analyzing their geometric structures. As a result there have been several Zintl ions observed and characterized in both chemistry and physics, such as E_9^{3-} , E_9^{4-} , and E_5^{2-} ($\text{E} = \text{Ge}, \text{Sn}, \text{Pb}$), Sb_7^{3-} , Sb_7^{3-} , Sb_4^{2-} and Bi_4^{2-} [57 - 66].

The geometry and bonding in Zintl clusters is achieved through the delocalization of electrons and lone pairs. The foundation of which is rooted in polyhedral skeletal electron pair theory born out of studies on borane ($\text{B}_n\text{H}_n^{2-}$) clusters by Williams, Wade and Mingos. Initially, Williams recognized from structural observation that boranes generated closo, nido and arachno structures by the loss of vertices in various ions, even proposing “...there is a rational alternative to considering carborane-borane structures as icosahedral fragments...which predicts a new and different set of structures...” [67]. The study by Williams was followed by Wade, who recognized the structural relationship in boranes could be associated with the number of valence electrons [68 – 69]. Wade realized particular borane and carboranes adopted the same number of

skeletal electron pairs providing an explanation, from an electronic standpoint, for Williams observations. Then Mingos incorporated the ideas of Williams and Wade into a simple method in order to understand the structure in many clusters [70]. Mingos' "polyhedral skeletal electron pair approach" and the contributions from Wade in understanding the number of electrons seen in polyhedral clusters, have resulted in what is termed the "Wade-Mingos Rules" for electron counting (Figure 1.4.1) [71].

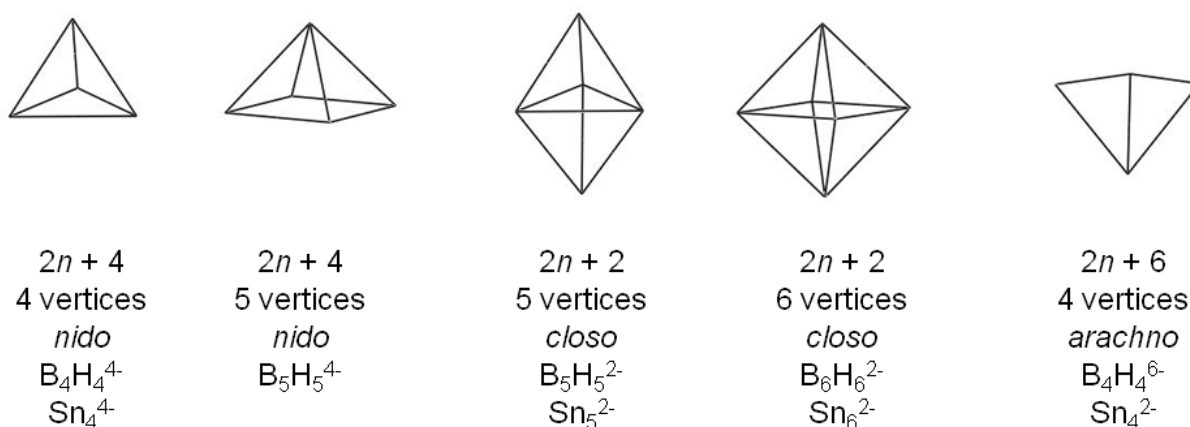


Figure 1.4.1 Example of Wade-Mingos rules for clusters. The number of electrons is represented by the equation in the top row (where n = number of vertices).

Zintl clusters are structurally and electronically analogous to the aforementioned borane clusters. This correlation realized by Corbett allows for the classification of various Zintl ions to fall into many of the same geometric designations for boranes using Wade-Mingos rules [72]. For example, in the *closo*- $B_5H_5^{2-}$ has $2n+2 = 12$ bonding electrons (each vertex provides two electrons), much like E_5^{2-} species ($E = Si, Ge, Sn, Pb$). The E_9^{4-} species are *nido*-clusters with $2n + 4 = 22$ cluster-bonding electrons, which in turn correspond to the *nido*- $B_9H_9^{4-}$. The geometry

of a cluster has proven to be extremely important, especially in the Zintl cluster realm. This is not more evident than in the case of the 22-electron system Sn_9^{4-} .

The deltahedral Sn_9^{4-} illustrates high fluxional behavior for its C_{4v} and D_{3h} structures. In contrast Sn_9^{2-} cluster adhere strongly to maintaining a closo (D_{3h}) lowest energy structure. These observations have allowed Group 14 deltahedral Zintl clusters (i.e.- E_9^{4-} , E_9^{3-} and E_9^{2-}) to be considered as a special class of Zintl clusters. As it turns out the specific geometry and electronic structure of nine-atom clusters are well suited for handling different charges, with very little distortion in the geometry of the cluster (Figure 1.4.2). The geometry of the deltahedral Zintl clusters can be thought of a tricapped trigonal prism in which the edges can be elongated to some extent. For these Zintl clusters, there is very little energy cost for the lengthening and shortening of these edges, however the electronic structure is affected greatly. The result is a charge flexibility that is believed to be responsible for the diverse chemistry of Zintl clusters [73].

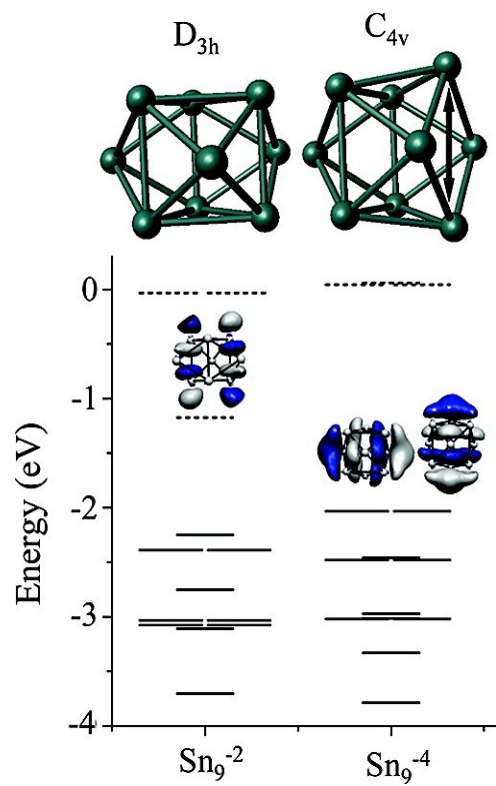


Figure 1.4.2 Electronic structure and geometries of the Sn_9^{2-} and Sn_9^{4-} Zintl clusters.

Over the years, there have been a multitude of studies on the Zintl ions in solution as well as their crystal structures (Zintl phases). However, using identified gas phase Zintl analogue clusters (GPZC) for cluster assembled materials is not as abundant. For example, recent studies on a variety of hetero-atomic cluster systems have revealed their stability mechanisms may be traced to the Zintl mechanism such as, $\text{Sn}_x\text{Bi}_y^{q-}$ ($x + y = 9$; $q = 1-3$), Bi_3Ga_2^- , and Al_2Bi_3^- ; but none of these have been shown to be successful in the formation of cluster assemblies [74 – 76]. One recent study by Reber and co-workers showed the Zintl cluster As_{11}^{3-} with potassium as a cation, shown to be stable in the gas phase, could be used to form a variety of Zintl cluster assemblies, which shows hope in using GPZC clusters for cluster assemblies [77].

1.5 Metal-Carbides and Metallocarbohedrenes

Metal-Carbide clusters have been proposed for various applications in nanotechnology with their unique, tailored properties as cluster assembled materials [78 – 80]. This fascinating cluster class has been explored both theoretically and experimentally by many researchers [81 – 83]. By studying metal-carbide clusters, it can provide insight into the formation and electronic characteristics of metal-carbon junctions. One rich category of metal-carbide clusters, Metallocarbohedrenes or commonly referred to as Met-Cars, has a stoichiometry M_8C_{12} with M being one or more of several early transition metals and are of particular interest in cluster-assemblies due to their enhanced stability [84 – 85]. Previously Met-Cars have been shown to exhibit low ionization energies, delayed ionization, unique relaxation dynamics, and have been proposed as effective catalysts [86 – 88]. Metallofullerenes and metal carbide nanocrystals have also been shown as important potential precursors to future nanomaterials [89 – 90]. Despite their importance, many structures of metal-carbide clusters are unknown. It is critical to identify the structures of metal-carbides. In particular, the electronic structure of metal carbide clusters

must be characterized in order to understand their unique properties that differ from both their atomic and bulk counterparts.

The vast landscape of metal-carbides such as niobium-carbides and met-cars has grown considerably. Yet in order for these clusters to be used as viable mass produced cluster assembled materials much work needs to be completed. At the beginning of this endeavor is to gain understanding of the electronic properties at finite dimensions, utilizing both theoretical and experimental techniques.

1.6 Chapter 1 Summary

One of the greatest possibilities in cluster science is the idea of designing nanomaterials with tunable properties from a bottom-up approach. In order to complete this daunting task it is necessary to not only identify stable cluster motifs as possible building blocks, but to understand the source of stability. Theoretical calculation based on the density functional formalism can aid in this endeavor by exploring both the electronic structure and energetics in the identification process. Once a stable cluster has been identified, a cluster's stability mechanism can be ascertained from theoretical results. This allows for the stable motif to be placed into a specific category based on the source of stability. A few categories used to define a cluster's stability mechanism include jellium, all-metal aromatic, Zintl analogues and metal-carbide clusters. Each category contains a variety of clusters that range in size and composition, many of which contain specialized sub-categories. The following chapters are devoted to the concept of using the step-wise process of first identifying and then classifying stable cluster motifs for the development of nanomaterials with precise tunable properties.

Chapter 2 Experimental Method

Whenever possible, the identification of stable cluster motifs can be verified along with the theoretical methods used, using experimental data. The experimental method for many of the clusters identified in the following pages of this document was synthesized gas phase via laser ablation. A schematic of the actual setup can be seen in Figure 2.1. The experiments were carried out using a mass spectrometer based on a design first conceived by Wiley and McLaren in conjunction with a magnetic bottle time-of-flight photodetachment electron spectra apparatus, which has been described in a previous publication [91]. The clusters were generated with a pulsed laser vaporization (LaVa) supersonic cluster beam source. The clusters of interest are then mass selected prior to photodetachment. Following mass selection the electrons are detached with a 308 nm (3.02 eV) excimer laser and a spectrum of the cluster is collected. If the reader would like more details on the precise experimental set up and method, the reader is encouraged to view the publications in Appendix A.

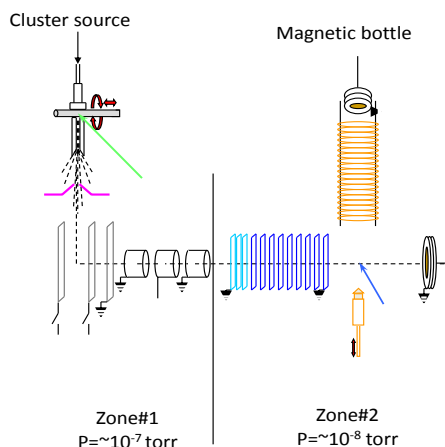


Figure 2.1 Schematic of experimental apparatus used to generate clusters.

Chapter 3 Numerical Methods

Over the past decades computational chemists and physicists have strived to describe the many-body effects for a many-electron system. The foundation of these methods lies in quantum and statistical mechanics. One method that explains many-particle interactions is the Hartree-Fock method. The second method, and the theoretical method of choice in this work, is the Kohn-Sham density functional theory. This chapter is devoted to the explanation of theoretical methods and will proceed as follows: Section 3.1 is about quantum mechanics followed by the Hartree-Fock method (Section 3.2). Section 3.3 is on the intricacies of density functional theory, Section 3.3 is on the exchange-correlation functionals, section 3.4 will briefly introduce basis sets and the final section will explain the methods used in this work.

3.1 Quantum Mechanics

Essential to the discussion of the electronic structure of matter is based upon the theoretical tenets of quantum mechanics. The time dependent Schrodinger equation given to us by E. Schrodinger governs this conversation. However, when one is concerned with atoms and molecules, the time-independent Schrodinger equation is utilized and is defined as,

$$\hat{H}\Psi = E\Psi$$

where, E is the energy, Ψ is an arbitrary wave function, and \hat{H} is the Hamiltonian operator. The Hamiltonian is one of the most important pieces in quantum mechanics and it should come as no surprise to the reader this must be defined for a system of electrons and nuclei. The Hamiltonian for the system of electrons and nuclei is represented by,

$$\hat{H} = -\frac{\hbar^2}{2m_e} \sum_i \nabla_i^2 - \sum_{i,I} \frac{Z_I e^2}{|\vec{r}_i - \vec{R}_I|} + \frac{1}{2} \sum_{i \neq j} \frac{e^2}{|\vec{r}_i - \vec{r}_j|} - \sum_I \frac{\hbar^2}{2M_I} \nabla_I^2 + \frac{1}{2} \sum_{I \neq J} \frac{Z_I Z_J e^2}{|\vec{R}_I - \vec{R}_J|}$$

where electrons are denoted by lowercase subscripts and nuclei, with charge Z_I and mass M_I , denoted by uppercase subscripts. In this general Hamiltonian the inverse mass of the nuclei ($1/M_I$) can be regarded as “small”. Since the mass of the electrons is much smaller than nuclei, the electrons will rapidly relax to the ground state configurations. This is the Born-Oppenheimer or Adiabatic approximation which allows one to decouple the nuclear and electronic motions. Thus, one can assume that the nuclei are stationary and solve for the electronic ground state. The calculation of the energy in different nuclear configurations can then allow studies of nuclear motions [92]. By ignoring the nuclear kinetic energy, the Hamiltonian for electronic structure becomes,

$$\hat{H} = \hat{T} + \hat{V}_{ext} + \hat{V}_{int} + E_{II}$$

The kinetic energy operator for electrons is described as,

$$\hat{T} = \sum_i -\frac{1}{2} \nabla_i^2$$

The potential acting on the electrons due to the nuclei is,

$$\hat{V}_{ext} = \sum_{i,I} V_I(|\vec{r}_i - \vec{R}_I|)$$

The electron-electron interaction term,

$$\hat{V}_{int} = \frac{1}{2} \sum_{i \neq j} \frac{1}{|\vec{r}_i - \vec{r}_j|}$$

The final term is the classical interaction of nuclei with one another, E_{II} , and any other terms that contribute to the total energy of the system. This Hamiltonian for electrons is central to the theory of electronic structure [92].

Now we turn to solving for the ground state energy of the Schrodinger equation using the principle of variation. Let us begin by stating we have a system in the state Ψ . The energy formula is given by,

$$E[\Psi] = \frac{\langle \Psi | \hat{H} | \Psi \rangle}{\langle \Psi | \Psi \rangle}$$

where $\langle \Psi | \hat{H} | \Psi \rangle = \int \Psi^* H \Psi d\mathbf{x}$. We can see that each measurement of the energy will result in the eigenvalues of the Hamiltonian operator, which is the energy computed from the guessed state Ψ to the true ground state energy or,

$$E[\Psi] \geq E_0$$

If the functional $E[\Psi]$ is fully minimized with respect to N-electron wave function one would obtain the true ground state Ψ_0 and energy E_0 . The formal proof of the minimum-energy principle requires the expansion of Ψ in the terms of the normalized eigenstates of the Hamiltonian and Ψ_k or

$$\Psi = \sum_k C_k \Psi_k$$

Therefore, the energy becomes

$$E[\Psi] = \frac{\sum_k |C_k|^2 E_k}{\sum_k |C_k|^2}$$

where E_k is the energy for the k^{th} eigenstates of the hamiltonian operator. Every eigenstates is an extremum of the energy functional, thus one may replace the Schrodinger equation with the variational principle

$$\delta E[\Psi] = 0.$$

It is beneficial to restate the above equation such that Ψ can be normalized. This can be accomplished using the method of Lagrange undetermined multipliers. The end result yields,

$$\delta[\langle\Psi|\hat{H}|\Psi\rangle - E\langle\Psi|\Psi\rangle] = 0$$

In this equation, one must solve for Ψ as a function of E and adjust E until normalization is achieved and the ground state energy is found.

3.2 Hartree-Fock Method

One standard method of many-particle theory is the Hartree-Fock method and is mentioned here for completeness. In this method, the electrons obey Fermi-Dirac statistics which allows the wave function to be antisymmetric. The result is that one can write an antisymmetrized determinant for a fixed number of electrons (N), in the Hartree-Fock approach, from which the single determinant that minimizes the total energy for the full interacting hamiltonian is found. If there is no spin-orbit interaction, the determinant wavefunction Φ can be written as a Slater determinant

$$\Phi = \frac{1}{\sqrt{N!}} \begin{vmatrix} \phi_1(r_1, \sigma_1) & \phi_1(r_2, \sigma_2) & \phi_1(r_3, \sigma_3) & \dots \\ \phi_2(r_1, \sigma_1) & \phi_2(r_2, \sigma_2) & \phi_2(r_3, \sigma_3) & \dots \\ \phi_3(r_1, \sigma_1) & \phi_3(r_2, \sigma_2) & \phi_3(r_3, \sigma_3) & \dots \\ \vdots & \vdots & \vdots & \ddots \end{vmatrix}$$

where $\phi_i(r_j, \sigma_j)$ are single particle “spin-orbitals” each of which is a product of a function of the position and a function of the spin variable. The spin-orbitals must be linearly independent. If the Hamiltonian is independent of the spin, the expectation value of the Hamiltonian in Hartree atomic units with the wavefunction is,

$$\begin{aligned} \langle\Phi|\hat{H}|\Phi\rangle &= \sum_{i,\sigma} \int d\vec{r} \psi_i^{\sigma*}(r) \left[-\frac{1}{2} \nabla^2 + V_{ext}(r) \right] \psi_i^\sigma(r) + E_{II} \\ &+ \frac{1}{2} \sum_{i,j,\sigma_i,\sigma_j} \int dr dr' \psi_i^{\sigma*}(r) \psi_j^{\sigma*}(r') \frac{1}{|r-r'|} \psi_i^\sigma(r) \psi_j^\sigma(r') \\ &- \frac{1}{2} \sum_{i,j,\sigma} \int dr dr' \psi_i^{\sigma*}(r) \psi_j^{\sigma*}(r') \frac{1}{|r-r'|} \psi_j^\sigma(r) \psi_i^\sigma(r') \end{aligned}$$

The first term involves a sum over orbitals and groups the single-body expectation values together. The third and fourth terms are the direct and exchange interactions among electrons. Here the “self-interaction” is included but cancels in the sum of direct and exchange terms [92].

The Hartree-Fock approach minimizes the total energy with respect to all degrees of freedom in the wavefunction. When the variational principle is applied will lead to the Hartree-Fock equations,

$$\left[-\frac{1}{2}\nabla^2 + V_{\text{ext}}(\mathbf{r}) + \sum_{j,\sigma_j} \int d\mathbf{r}' \psi_j^{\sigma_j*}(\mathbf{r}') \psi_j^{\sigma_j}(\mathbf{r}') \frac{1}{|\mathbf{r}-\mathbf{r}'|} \right] \psi_i^\sigma(\mathbf{r}) - \sum_j \int d\mathbf{r}' \psi_j^\sigma(\mathbf{r}') \psi_i^\sigma(\mathbf{r}') \frac{1}{|\mathbf{r}-\mathbf{r}'|} \psi_j^\sigma(\mathbf{r}) = \varepsilon_i^\sigma \psi_i^\sigma(\mathbf{r}).$$

Within the Hartree-Fock approximation, the exchange term is summed over all orbitals of the same spin, which includes the self-term $i = j$ that cancels the unphysical self-term included in the direct term. It should be noted that the Hartree-Fock approximation is a self-consistent approach and the Hartree-Fock equations can be solved directly only in special cases and will not be discussed further [93]. There are disadvantages to using the Hartree-Fock approximation (HFA). For example, the HFA requires four center integrals that require a great deal of computational time and the energy gaps are overestimated, thus this approach can only be used for simple system like molecules.

One method to reduce the limitations of the Hartree-Fock method is to go to post-Hartree-Fock methods some of which are based on the variational principle. The configuration interaction method (commonly referred to as CI) can be used for solving the many body Hamiltonian. This variational method is used in conjunction with the orbitals from the Hartree-

Fock determinants. Even though the CI method is an improvement over the Hartree-Fock method, it also has an extensive computational cost.

3.3 Density Functional Theory

Density Functional Theory (DFT) is a theory of correlated many-body systems. The history of density functional theory spans back to 1927, however its usefulness was established in 1964 and 1965 [94 – 95]. We begin by discussing the original formulation of density functional theory of quantum systems which was proposed by Thomas and Fermi in 1927.

3.3.1 Thomas-Fermi-Dirac Approximation

The original assumptions on the ideal of using density rose out of the paper by Thomas in 1927 where he stated, “Electrons are distributed uniformly in the six-dimensional phase space for the motion of an electron at the rate of two for each h^3 of volume,” He went on to state that the effective potential field “is itself determined by the nuclear charge and this distribution of electrons.” Thus, in the original Thomas-Fermi approximation (TF) the kinetic energy of the system of electrons can be approximated as an explicit functional of the density. The electrons are idealized as a non-interacting system in a homogeneous gas with a density that is equal to the local density at any given point, such that

$$E_{TF}[\rho] = C_1 \int d\mathbf{r} \rho(\mathbf{r})^{5/3}$$

Here, $C_1 = \frac{3}{10} (3\pi^2)^{2/3} = 2.871$ in atomic units. Equation --- is known as the Thomas-Fermi kinetic energy. The importance of the Thomas-Fermi kinetic energy rests in that this approximation defines the electronic kinetic energy in terms of the density. It should be noted that in their original formulation, both Thomas and Fermi neglected exchange and correlation

among the electrons. However, in 1930 Dirac extended the original formulation and added a local approximation for the exchange, via,

$$E_D[\rho] = C_2 \int d\mathbf{r} \rho(\mathbf{r})^{4/3}$$

where $C_2 = -\frac{3}{4} \left(\frac{3}{\pi}\right)^{1/3}$. By placing the Thomas-Fermi kinetic energy and Dirac's exchange energy into the energy functional, we get the Thomas-Fermi-Dirac approximation (TFD)

$$E_{TFD}[\rho] = E_{TF}[\rho] + E_D[\rho] + \int d\mathbf{r} V_{ext}(\mathbf{r})\rho(\mathbf{r}) + \frac{1}{2} \int d\mathbf{r} d\mathbf{r}' \frac{\rho(\mathbf{r})\rho(\mathbf{r}')}{|\mathbf{r} - \mathbf{r}'|}$$

for electrons in an external potential $V_{ext}(\mathbf{r})$, where the last term is the classical electrostatic Hartree energy [96]. The ground state density and energy can be found by minimizing the functional in the TFD approximation given a constraint on the total number of electrons (N). However using the method of Lagrange multipliers the solution can be found by an unconstrained minimization of the functional,

$$\Omega_{TFD}[\rho] = E_{TFD}[\rho] - \mu \left\{ \int d\mathbf{r} \rho(\mathbf{r}) - N \right\}$$

where the Lagrange multiplier μ is defined as,

$$\mu = \frac{\delta E[\rho(\mathbf{r})]}{\delta \rho(\mathbf{r})}$$

or the Fermi energy. This form then result in the Euler-Lagrange equation,

$$\frac{5}{3} C_F \rho^{2/3}(\mathbf{r}) - \phi(\mathbf{r}) = \mu$$

where $\phi(\mathbf{r})$ is the electrostatic potential at point \mathbf{r} due to the nucleus and the entire electron distribution.

The approach taken by Thomas, Fermi and Dirac is quite attractive compared to the full many-body Schrodinger equation that involves $3N$ degrees of freedom for N electrons, since

there is only one equation that needs to be solved. However, this original approach has several flaws in its implementation and was not useful in the description of electrons in matter. Thus, this approximation was put on the shelf by most scientists. Then in the mid 1960's modern day density functional theory gained renewed interest due to two essential theorems by Hohenberg and Kohn and is the foundation upon which the density functional formalism is built.

3.3.2 Hohenberg and Kohn Theorems

The central foundation of the density functional formalism is built upon the Hohenberg-Kohn theorems presented in 1964. The relations established by Hohenberg and Kohn are important for any practitioner of density functional theory to understand. The first theorem states,

For any system of interacting particles in an external potential $V_{ext}(\vec{r})$, the potential is determined uniquely, except for a constant, by the ground state particle density $\rho_0(\vec{r})$.

This theorem implies that all properties of the system are completely determined if one knows the ground state density, since the hamiltonian is fully determined, except for a constant shift of the energy. This is followed by the second theorem, which states,

A universal functional for the energy $E[\rho]$ in terms of the density $\rho(\mathbf{r})$ can be defined, valid for any external potential $V_{ext}(\mathbf{r})$. For any particular potential, the exact ground state energy of the system is the global minimum value of this functional, and the density that minimizes the functional is the exact ground state density $\rho_0(\mathbf{r})$.

Essentially theorem two asserts that the functional itself is sufficient to determine the precise ground state density and energy. The original proof for the second theorem is restricted to ground state densities of the electron Hamiltonian with some external potential V_{ext} , or “V-representable” densities. This defines a space of possible densities within which one can

construct functionals of the density. From theorem II, the exact ground state energy can be obtained by,

$$E[\rho] = \min \left(F[\rho] + \int d\vec{r} \rho(\vec{r}) v_{ext}(\vec{r}) \right)$$

where the exact ground-state density is the density that minimizes the expression for the energy. The functional $F[\rho]$ contains the kinetic energy of electrons and electron-electron interaction energy.

The Hohenberg-Kohn theorems do establish that the energy functional exists, however there is no information on how to construct it [97]. One of the main difficulties resides in determining the kinetic energy directly from the density. In order to address this challenge, we are now led to the Kohn-Sham DFT approach, which includes the kinetic energy of non-interacting electrons in terms of independent-particle wavefunctions, in addition to the interaction terms being explicitly modeled as functionals of the density.

3.3.3 The Kohn-Sham Approach

So far the idea of obtaining the ground-state energy of a many-electron system by minimizing the energy functional is indeed appealing. However, one must construct the functionals in order to make the approach work. In what resulted as a successful attempt to do just that, Kohn and Sham invented an approach to the kinetic-energy functional now called the Kohn-Sham method. Their novel 1965 paper turned density functional theory into a useful tool for calculations.

The Kohn-Sham approach relies on two points:

1. The ground state density can be represented by the ground density of an auxiliary system of non-interacting particles termed “non-interacting V -representability”.
2. The auxiliary hamiltonian is chosen to have the usual kinetic operator and an effective local potential V_{eff}^σ acting on a electron of spin σ at point \vec{r} .

Essentially, the Kohn-Sham approach replaced the many-body interacting system that obeys the Hamiltonian with a different auxiliary system. This means that the actual calculations are performed on the auxiliary independent-particle system. The density of this auxiliary or model system is written in terms of the molecular orbitals of the non-interacting system as,

$$\rho(\vec{r}) = \sum_i \varphi_i(\vec{r}) \varphi_i(\vec{r})$$

with the total energy of the system being obtained by,

$$E_{KS}[\rho] = T_S[\rho] + U[\rho] + E_{xc}[\rho] + \int d\vec{r} \rho(\vec{r}) v_{ext}(\vec{r})$$

The kinetic energy T_S is given for the non-interacting system as,

$$T_S[\rho] = -\frac{1}{2} \sum_i \langle \varphi_i | \nabla^2 | \varphi_i \rangle$$

The classical Coulomb energy $U[\rho]$ is defined as,

$$U[\rho] = \frac{1}{2} \int d\vec{r}_1 d\vec{r}_2 \frac{\rho(\vec{r}_1)\rho(\vec{r}_2)}{|\vec{r}_1 - \vec{r}_2|}.$$

By solving the Kohn-Sham equations,

$$\left(-\frac{1}{2} \nabla^2 + v_{ext}(\vec{r}) + J(\vec{r}; \rho) + v_{xc}(\vec{r}; \rho) \right) \varphi_i = \varepsilon_i \varphi_i$$

where,

$$J(r; \rho) = \frac{\delta U[\rho]}{\delta \rho(\vec{r})}$$

and

$$v_{xc} = \frac{\delta E_{xc}[\rho]}{\delta \rho(\vec{r})}$$

one can obtain the molecular orbitals that are used to build the density and kinetic energy. These equations are self-consistent. First an initial trial density is chosen and the potentials J and v_{xc} are constructed. After which, the molecular orbitals are solved for and the total energy is obtained. If the density from the molecular orbitals is deemed not to be self-consistent, the procedure is repeated. However, once self-consistency is achieved, depending on the exchange-correlation functional, $E_{xc}[\rho]$, the density and energy is understood to be the exact ground state.

The genius of the Kohn-Sham approach lies in the explicit separation of the independent-particle kinetic energy and the long-range Hartree terms, which result in the exchange-correlation functional E_{xc} being approximated. The down side of the exact exchange-correlation functional is it requires one to solve the Schrödinger equation and obtain the wavefunction. However, the functional can be reasonably approximated as local or nearly local functional of the density. The functional for exchange-correlation is so important the next section is devoted to the various functionals for exchange-correlation.

3.3.4 Functionals for exchange-correlation

The local density approximation (LDA) or more generally the local spin density approximation (LSDA) is a functional in which the exchange-correlation energy is an integral over all space with the exchange-correlation energy density at each point is assumed to be the same as in a homogeneous electron gas with that density. This is represented by,

$$E_{xc}^{LSDA}[\rho^\uparrow, \rho^\downarrow] = \int dr \epsilon_{xc}^{hom}(\rho_\uparrow(\vec{r}), \rho_\downarrow(\vec{r}))$$

where the exchange energy density, which can be calculated directly, for the homogeneous electron gas is,

$$\epsilon_{xc}^{hom} = -\frac{3}{4} \left(\frac{6}{\pi}\right)^{1/3} (\rho_{\uparrow}^{4/3}, \rho_{\downarrow}^{4/3}).$$

The LSDA is the most general local approximation, while for the unpolarized system the LDA is found by setting $\rho_{\uparrow}(\vec{r}) = \rho_{\downarrow}(\vec{r}) = \rho(\vec{r})/2$. The LSDA functional's correlation energy has been calculated to great accuracy with Monte Carlo methods. It should be noted this functional works very well for solids close to a homogeneous gas but much worst for systems that are inhomogeneous, like atoms. Other downfalls of this functional include underestimated bond lengths, poor total energies, and the functional is unable to describe reaction barriers. As one can imagine these shortcomings show the need for improved functionals.

In an effort to improve the exchange-correlation functional, one may think to expand the interactions using a gradient of the density as well as the value at each point. This gradient expansion approximation (GEA) was suggested and attempted. However, the GEA does not lead to improvements over the LSDA and violates the sum rules as well as a divergent exchange-correlation potential in finite systems. Even though the GEA does not lead to improvements, the idea of using a local gradient of the density has resulted in the emergence of the generalized-gradient approximations (commonly referred to as GGA).

Generalized-gradient expansion (GGA) is a term that refers to a variety of ways for functions that modify the behavior at large gradients in such a way to preserve the desired properties. In a typical GGA, the LSDA energy density (homogeneous electron gas) is multiplied by a dimensionless factor (F_{xc}) which results in the expression,

$$E_{xc}^{GGA} = E_{xc}^{LSDA} F_{xc} .$$

There are many popular GGA functional for exchange and correlation. Some examples include B88 exchange functional, LYP correlation functional, and the PW91 functional for exchange and correlation. One of the most widely used functional for exchange and correlation is the functional described by Perdew, Burke, and Enzerhof (PBE). The PBE functional for exchange and correlation is defined as,

$$E_{XC}^{PBE}[\rho_{\uparrow}, \rho_{\downarrow}] = \int d^3r \rho(\mathbf{r}) \epsilon_{XC}^{PBE}(r_s(\mathbf{r}), \zeta(\mathbf{r}), s(\mathbf{r}))$$

where, ϵ_{XC}^{PBE} is the exchange energy per particle of a uniform electron gas and depends on ρ, s , and ζ . In this project, most cases involve using the original PBE functional shown here. The benefit of using such GGA functionals for the exchange-correlation, like PBE, is shown by achieving better results such as, total energies, atomization energies, and correcting of the underestimation of bond lengths. However, there continues to be room for improvement.

For completeness, I would like to mention that there are other functionals such as meta-GGAs which incorporate the Laplacian and/or the kinetic energy of the density,

$$\tau(\vec{r}) = \frac{\hbar^2}{2m} \sum_i |\nabla \varphi_i(\vec{r})|^2.$$

Meta-GGAs do show improvements over GGAs, but still suffer from at times over correcting the bond lengths. There are also non-local functionals, which include the average density approximations (ADA) and the weighted density approximation (WDA). These functionals not only take into account the density at the point r and its derivatives, but also the behavior of the density at different points. In practice these non-local functionals are computationally expensive and are rarely used.

So far, we have discussed non-local functionals and semilocal functionals (LSDA, GGA, and meta-GGAs). Of these two categories, semilocal functionals appear to be simple and efficient. However, many of these semilocal functionals fail for describing van der Waals

interactions. If one would like to achieve more accuracy, one could take a mixture of semilocal and nonlocal methods. This has been accomplished using hybrid functionals. Hybrid functionals incorporate both the semilocal and nonlocal Hartree-Fock type exchange. The actual hybrid “global” formulation can be written as,

$$E_{xc} = E_{xc}^{DFA} + c(E_x^{HF} - E_x^{DFA})$$

where c is some constant, E_x^{HF} is the exact Hartree-Fock type exchange, and E_{xc}^{DFA} is the exchange energy form a semilocal density functional approximation. For example Perdew, Ernzerhof, and Burke proposed the a mixing in $1/4$ Hartree-Fock exchange energy which has the form,

$$E_{xc} = E_{xc}^{LDA} + \frac{1}{4}(E_x^{HF} - E_x^{DFA}).$$

There are many examples of hybrid functionals. The most popular which uses 20% exact exchange is the B3LYP functional. In general, these functionals describe the thermochemistry and reaction barriers very well, but like the GGA and LSDA functionals nonlinear optical properties are still poor. The question now becomes, what is the main cause for the problems in the functionals of DFT? The answer can be traced to on major issue: *Self-Interaction Error*.

The self interaction error (SIE) arises from the fact that DFT functionals allow an electron to interact with itself. This is not the case in the Hartree-Fock approximation. In the Hartree-Fock approximation the unphysical self-term is exactly cancelled by the non-local exchange interaction. Since this term is present using the DFT functionals, one must ascertain how it can affect the results. In many-electron systems, the presence of the SIE causes artificial stabilization of delocalized electronic states. Thus, the delocalization can lead to underestimation of reaction barriers, errors in polarizabilities and descriptions of the charge transfer processes. However, semilocal functionals can mimic important nondynamical

correlation effects that would otherwise require expensive correlated calculations. It should be noted that the remaining spurious self-interaction terms are negligible in the homogeneous gas, but can be large in confined systems. There is also a self interaction correction method that can be employed that can correct the self interaction issue and does allow for improvements in the theory.

3.3.5 Basis Sets

Essential to computations in the KS-DFT approach are the atomic orbitals. Practically all applications of KS-DFT make use of the linear combination of atomic orbitals expansion (LCAO) of the KS molecular orbitals. In the LCAO approach, the orbitals are linearly expanded as,

$$\varphi_i = \sum_{\mu=1}^L c_{\mu i} \eta_{\mu}$$

where L is a set of predefined basis functions $\{\eta_{\mu}\}$ and $c_{\mu i}$ represents expansion coefficients. *Basis functions* are used to express the orbitals for atoms in the KS scheme, while a *basis set* is a combination of the mathematical functions (basis functions) used to represent the atomic orbitals. The basis functions describe the radial and angular distributions of the electron density. There are two types of basis functions used in the computational approach of KS-DFT, they are *Slater-type-orbitals* and *Gaussian-type-orbitals* [98].

Slater-type-orbitals (STO) were proposed by Slater in 1930 for the description of the radial part of the atomic orbitals [99]. These functions were initially defined by Slater's rules, thus they were not determined variationally. However, Roothaan and Bagus wrote an SCF code for atoms using the LCAO approximation discussed above [100]. They introduced the form used in practice for the typical STO, i.e--

$$\eta^{STO} = Nr^{n-1} \exp[-\zeta r] Y_{lm}(\Theta, \phi).$$

here, N is the normalization factor, n corresponds to the principal quantum number, the orbital exponent is termed ζ , and Y_{lm} are the usual spherical harmonics. The parameter ζ were optimized variationally with respect to each total atomic energy. The STO functions have benefits and their downfalls. One huge benefit is STO basis sets reproduce the regions near the nucleus correctly and they decay properly a long r distances, in a similar way that atomic orbitals do. However, one huge downfall is computational time. It is well known that STO functions are difficult to handle because they cannot be calculated analytically.

Gaussian-type-orbitals (GTO) are alternatives to the STOs mentioned above and are more commonly used. These consist of the form,

$$\eta^{GTO} = Nx^l y^m z^n \exp[-\alpha r^2] .$$

Here N is a normalization factor, α represents the orbital exponent which determines how compact (large) or diffuse (small) the resulting function will be. While $L = l + m + n$ is used to classify the GTO as either s - ($L=0$), p - ($L=1$), d - ($L=2$), etc. The largest advantage of GTO is they are easy to handle since they can be calculated analytically. However, unlike Slater-type-orbitals, the Gaussian-type-orbitals give a poor description close to the nucleus of the atom and fall off too rapidly at $r \rightarrow \infty$. These problems can be overcome by using a linear combination of GTO. Thus, GTO are typically the choice in many programs.

There is another basis employed in other DFT schemes, however it does not comply with the LCAO approach and that is *plane waves*. Plane waves are solutions of the Schrodinger equation of a free particle and are simple exponential functions of the general form $\eta^{PW} = \exp[i\vec{k}\vec{r}]$ where the vector \vec{k} is related to the momentum of the wave via, $\vec{p} = \hbar\vec{k}$. Plane waves are not centered at the nuclei, but they extend throughout the complete space.

Regardless of which type of function is chosen for the representation of the atomic orbital, there are ways to categorize the quality of the chosen basis set. For example, the simplest and least accurate uses only one basis function and termed minimal. One example is the STO-3G basis set, which is three primitive GTO functions are combined into one CGF. The next level of basis sets are termed *split basis sets*. The split basis has a set of two (or more) functions of different sizes or radial distributions. The “split” is due to the doubled set of functions being applied to on the valence electrons, while the core electrons are still treated in a minimal set. In this category, one finds the *double-zeta* basis where one finds there are two functions for each orbital, which is represented as DVZ. There are various basis sets with various numbers of functions, such as triple, quadruple, and even quintuple zeta basis sets and each are represented with the typical VXZ notation (where X represents the number of functions). In most applications the basis set is augmented by polarization functions. Polarization functions are functions of higher angular momentum than those occupied in the atom. Thus, polarized X-zeta basis sets are used very readily in calculations and are typically denoted as either XVZP or -pVXZ. Often higher representatives of these basis sets are noted as cc-pVXZ, where cc-pV stands for *correlation-consistent polarized valence*; these are built to recover amounts of correlation energy in an atomic calculation. One also finds various augmented (aug-) correlation consistent polarized valence functions and those with added diffuse functions as well. Many of the aug-cc-pVXZ basis sets consist of some type of orbital contraction. In most cases, any of the above basis sets are good when considering many of the atoms on the periodic chart, however if the atom is heavier than Krypton, one must begin to think about relativistic effects.

There are two main ways to take relativistic effects into account one such way is to use a relativistic effective core potential (RECP). Effective core potentials (ECP) model the

energetically deep-lying inert core electrons, or treat them as if they are “frozen”; thereby only treating the valence electrons explicitly. These ECPs are only termed relativistic or quasi-relativistic if they have been fitted to atomic calculations that explicitly incorporate relativistic effects. The other way is to deal with the relativistic effects using “regular approximations” introduced by Lenthe and co-workers [101]. Both methods are used in computations for atoms larger than Krypton and transition metals. It should be noted that there are also auxiliary basis functions that can be incorporated into the theory, but these will not be discussed here. For more information on auxiliary basis functions please refer to the book by Trindle and Shillady [102].

There are some problems with using basis sets, such as the basis set superposition error (BSSE). This arises from the use of a finite sized basis set which is adopted to compute the interaction energy as the difference between the total energy of the complex and the sum of the total energies of the non-interacting fragments. The interacting of the complex will expand its respective wave function using virtual orbitals of the other. A result of this is the lowering of the total energy of the complex with respect to its fragments and as such, an artificial overestimation of the complex energy. One way to estimate the BSSE is using the counterpoise correction.

The counterpoise correction (CP) was introduced by Boys and Bernardi in 1970 [103]. I will give a brief example of the original Boys and Bernardi (BB) CP correction for the potential energy surface. Let’s say there are two atoms, atom A and B. The BSSE content of the interaction energy is defined as

$$\delta^{BSSE} = E_A(AB) - E_A(A) + E_B(AB) - E_B(B)$$

where $E_A(A)$ and $E_B(B)$ are the energies of the monomers calculated in the respective monomer basis sets; $E_A(AB)$ and $E_B(AB)$ are energies of the two atoms calculated in the complex of interest. The BBCP-correction for the potential energy surface for a dimer is defined as,

$$E^{BB} = E_{AB}(AB) - \delta^{BSSE}$$

where $E_{AB}(AB)$ is the total energy of the complex. If one looks at the previous equation, one has to calculate five different total energies at every geometrical arrangement of the system of interest to determine a CP-corrected potential energy surface. Simon *et al.* showed that various derivatives of the BBCP-correction can be calculated easily and set up UNIX scripts and small FORTRAN programs to do so [104]. Since the initial BB CP-approach was published in 1970, it has been used in many calculations with various sizes of basis sets.^C However, it should be noted that this correction, though useful tends to overestimate the BSSE in some cases.

3.4 Implementation of Density Functional Theory

In this project, the actual implementation of DFT will be accomplished by employing various software programs. The mainstay of geometry optimization and energetic will come from deMon2k, established by Andreas and co-workers [105]. Other codes used include, Naval Research Laboratory Molecular Orbital Library code (NRLMOL) by Pederson and co-workers, as well as Amsterdam Density Functional package (ADF) and Guassian03 [106 -108]. Throughout this text there may be comparisons made between the various programs, when applicable. However, this author will not explicitly state advantages or disadvantages between any of the packages used for this project. The following sections are devoted to the codes used for this project and the precise method for obtaining the lowest energy structures for the cluster and cluster assemblies in the following chapters.

3.4.1 deMon2k

The deMon2k (density of Montreal) code was developed by Köster and co-workers. It is a software package designed for the implantation of density functional theory calculations. The

^C The original paper by Boys and Benardi (Reference 103) has been cited over 7,000 times.

code uses a linear combination of Gaussian-type orbital (LCGTO) approach in order to solve the self-consistent KS-DFT equations. In order to calculate the four-center electron repulsion integrals, the code uses a variational fitting of the Coulomb potential. Another feature of the deMon2k code is the use of an auxiliary density. The approximated density is expanded in primitive Hermite Gaussians which are centered at the atoms. The auxiliary density $\tilde{\rho}(\mathbf{r})$ is defined as,

$$\tilde{\rho}(\mathbf{r}) = \sum_k x_k \bar{k}(\mathbf{r})$$

where $\bar{k}(\mathbf{r})$ is the Hermite Gaussians. The auxiliary density is expanded in primitive Hermite Gaussian functions, either the GEN-A2 or GEN-A2* function sets. The GEN-A2 function set contains s, p, and d functions for the atom chosen. The GEN-A2* function set has a similar structure as the GEN-A2, but includes the f and g functions for the atom of choice. When calculating the exchange-correlation potential, this is done along with the orbital density. The integration of both the exchange-correlation energy and potential is carried out on an adaptive grid. In the cases where an ECP is chosen as the basis for a particular atom, a half-numeric integrator is employed for the ECP integrals [109].

One big advantage is that deMon2k can be employed for any atom on the periodic table of elements. The code can also take into relativistic effects by using either relativistic or quasi-relativistic ECPs, RECP and QECP respectively. However, one downfall with the program is its inability to use hybrid functionals for exchange-correlation. In light of this, deMon2k is the primary code employed in this document for optimization of the atomic clusters studied here. For the clusters studied here, various initial geometries were attempted and allowed to optimize without constraints so as to not get trapped in a potential well [110]. Within the deMon2k code

there are various functionals that can be applied for the exchange and correlation. However, it does not support hybrid functionals.

3.4.2 Amsterdam Density Functional Package (ADF)

The Amsterdam Density Functional Package (ADF) is a molecular DFT program available through Scientific Computing & Modeling [111]. One large feature of the ADF package is it uses Slater-type functions or STOs versus GTOs for the basis sets. The numerical integration for the matrix elements of the exchange-correlation potential, as well as other integrals that cannot be done analytically, is carried out using a Gaussian-type quadrature method which is based on the partitioning of space in atomic cells. The integration is completed on an adaptive grid. The analytical calculation of the Coulomb matrix is carried out using a numerical integration scheme. ADF also uses a set of auxiliary “fit functions” for the density which are also STO-type functions, but differ from the basis functions [112]. The geometry optimization is carried out using the Broyden Fletcher Goldfarb Shanno (BFGS) method, which contains a bias to keep the Hessian positive-definite [113].

Another feature of ADF is its ability to compute all atoms on the periodic table, much like deMon2k. However, instead of using either ECPs or pseudopotentials, it can treat the all-electron basis sets by simply using a frozen core approximation. By employing the frozen core approximation, one can obtain the total charge density and potential in the valence and in the core region, ignoring the slight change in the deep-core orbitals upon the formation of a chemical bond. As mentioned above when treating atoms with atomic numbers larger than 36, it is important to take into account the relativistic effects for an atom. ADF does this by incorporating the quasi-relativistic method based on the Pauli Hamiltonian or using the Zeroth Order Relativistic Approximation (ZORA). In this study the relativistic effects are accounted for

in ADF using only the ZORA scheme. The ZORA method can be obtained by rewriting the energy expression and expanding the parameter,

$$\frac{E}{(2mc^2 - V)}$$

This value remains small even close to the nucleus. If one only retains the Zeroth order term, the resulting ZORA Hamiltonian becomes,

$$H_{ZORA} = \sum_i p_i \frac{c^2}{2mc^2 - V} p_i + \frac{mc^2}{(2mc^2 - V)^2} \sigma \cdot (\nabla V \times \mathbf{p}) + V.$$

The more intricate details on the ZORA approximation please refer to the articles by Lenthe and coworkers [114 – 116].

An added useful feature in ADF is the ability of the program to calculate the shielding tensor of nuclear magnetic resonance (NMR) spectroscopy [117]. The NMR shielding tensor is the second derivative of the energy with respect to the magnetic field B_k in each direction $k = x, y, z$ and the magnetic moment of the nucleus μ_t in each direction $t = x, y, z$, and is defined as,

$$\sigma_{kt} = \frac{\partial^2 E}{\partial B_k \partial \mu_t}$$

The method to calculate the tensor has been formulated in the gauge including atomic orbitals (GIAO) framework [118]. The importance of this feature is due to the possibility to run nucleus independent chemical shift (NICS) calculations and well as molecular orbital NICS (MO-NICS) calculations for various clusters. One can also run a variety of other calculations for the identification of other important cluster properties, including Electron Spin Resonance (ESR), Time-dependent DFT, excitation energies, and polarizabilities.^D

3.4.3 Gaussian03

^D For more details refer to Reference 20.

The Gaussian03 package is a program used by various theoretical chemists for cluster studies and other applications. In this project, the program has been employed only for various NMR or NICS calculations. The method to do this in the program may be computed with the Continuous Set of Gauge Transformations (CSGT) method and the GIAO method [119 – 121]. For more details on the Gaussian software package please visit their website.^E

3.4.4 Naval Research Laboratory Molecular Orbital Library code

The Naval Research Laboratory Molecular Orbital Library (NRLMOL) code was developed by M. R. Pederson et al [106]. NRLMOL uses Gaussian functions as the basis sets and are centered at the atomic sites. The atomic sites are incorporated and used on a mesh that integrates the charge density. The electron spin densities for the atoms are integrated over to yield the local magnetic moment at each atomic site. The actual code creates a mesh of points that are numerically integrated over to obtain the Hamiltonian matrix elements. In all cases, the NRLMOL code was used by implementing the PBE functional for exchange and correlation. In each calculation the structures attempted were allowed to optimize fully, without constraints. Though this code readily available, it should be noted that NRLMOL code cannot be used for atoms whose atomic number is larger than 50, and does not take into account relativistic effects for atoms.

3.4.5 Vienna Ab-initio Simulation Package

The Vienna Ab-initio Simulation Package or VASP is a package that utilizes pseudopotentials and plane wave basis sets for performing ab-initio quantum mechanical calculations. The package supports three different types of potentials, norm-conserving, ultra-soft, and projector augmented wave potentials. The approach used is based on a finite-

^E <http://www.gaussian.com>

temperature local-density approximation. Some of the properties for the larger cluster assemblies were computed using the VASP package and more precise details on the calculations will be given in the following sections.

3.4.6 Methodology

In order to establish the correct functional and basis set, various values (e.g. ionization potentials and electron affinities) for the atom and dimer of choice are calculated. These values, along with the atomization energies and bond lengths are then compared to previously reported (when available) experimental and theoretical values. If these values are within reasonable error then the cluster calculations can proceed. The systems studied incorporate at least one or more of the atom found Table 3.2.

For the cluster calculations, the initial geometry optimizations were performed using the deMon2k package, with subsequent verification using other packages such as NRLMOL or ADF. The lowest energy clusters were deemed to be the ground state structure for the clusters of interest. Whenever possible, a frequency analysis was performed on the lowest energy structure to ascertain the structure was not trapped in a local minimum.

In order to verify the stability of a cluster in a series, various calculations on the energetics were performed. These included the ionization potentials, electron affinities, removal energy, and when applicable the second energy difference. The ionization potential (abbreviated IP or I.P.) and electron affinity (sometimes referred to as electron detachment energy i.e.- EA or DE) may be determined for two cases, vertical and adiabatic. The vertical ionization potential (VIP) is defined as the difference in energy between the lowest energy structure of the neutral and the cation with the geometry of the neutral, while the vertical detachment energy (VDE) is the difference in energy between the lowest energy of the anion and the neutral with the anions

geometry. This differs in that the adiabatic case is simply the difference in energy between the lowest energy structures for both the neutral and cation or neutral and anion for the AIP and ADE, respectively.^F Each of these quantities can be represented mathematically, via,

$$VIP = E_{geometry\ of\ neutral}^+ - E_{ground\ state}^0$$

$$AIP = E_{ground\ state}^+ - E_{ground\ state}^0$$

$$VDE = E_{geometry\ of\ anion}^0 - E_{ground\ state}^-$$

$$ADE = E_{ground\ state}^0 - E_{ground\ state}^-$$

where E is the energy and the superscripts represent charge of the cluster. There is a high importance in these values. For example, if a cluster has a low electron detachment energy, the neutral cluster prefers not to accept one unit of charge, however a large electron detachment energy is an indication the anion is the more stable species. If a cluster has a large ionization potential, it is indicative of the stable nature of the neutral cluster versus the cation. More important in verification of the stability of a cluster is found in the removal energy or energy gain over a series of clusters. The removal energy (R.E.) or energy gain (E.G.) is defined as the amount of energy it costs to remove an atom from the cluster or the amount of energy gained as an atom is added to the previous cluster, via

$$E(A) + E(A_{n-1}) - E(A_n)$$

where A is the atom and *n* is the number of atoms in the cluster. If this value is larger for a cluster than its nearest neighbors, this is a strong indication this cluster is stable relative to the other clusters. This value can be complemented by the second energy difference (S.E.D.) defined as,

$$E(A_{n-1}) + E(E_{n+1}) - 2E(A_n)$$

^F The adiabatic detachment energy (or electron affinity) and ionization potential are sometimes abbreviated as EA and IP respectively.

where A and n have been described previously. If a large value is obtained for the S.E.D. this implies the cluster shows some stable character.

Once the stable clusters were theoretically determined, many of these clusters were creatively assembled in various configurations. These cluster assemblies were allowed to optimize fully without constraints in the various software packages. Once the cluster assemblies were composed of larger sizes, an infinite cluster assembly was attempted using the VASP program in some cases.

Table 3.1 The functionals and basis sets in software packages for the atoms used in the systems studied. Also listed is if any relativistic effects were taken into account, as well as if any auxiliary functions were used in the calculations.

Atom	Functional ^A	Basis ^B	Relativistic effects ^C	Software Package
Al	PBE	DZVP	N	deMon2k
	PBE	DZVP	N	NRLMOL
	PBE	DZVP	N	Gaussian03
As	PBE	DZVP	N	deMon2k
Bi	PBE96	aug-cc-pVDZ	RECP23	deMon2k
	BP86	QZ4P	ZORA	ADF
	PBE	aug-cc-pVDZ	RECP23	Gaussian03
C	PBE	TZP	ZORA	ADF
	PBE	DZVP	N	deMon2k
	PBE	aug-cc-pVTZ	N	deMon2k
H	PBE	DZVP	N	NRLMOL
	PBE	DZVP	N	deMon2k
	PBE	LANL2DZ	QECP	deMon2k
Ag	PBE	DZVP	N	NRLMOL
	PBE	TZP	Y	ADF
	PBE	aug-cc-pVDZ	RECP23	deMon2k
Sb	PBE	aug-cc-pVDZ	RECP22	deMon2k
	PBE/BP86	QZ4P	Y	ADF
	PBE	DZVP	N	deMon2k
Mn	PBE	DZVP	N	NRLMOL
	PBE	TZP	Y	ADF
	PBE	SD	N	deMon2k
V	PBE	DZVP	N	NRLMOL
	PBE	LANL2DZ	QECP	deMon2k
	PBE	DZVP	N	NRLMOL
Nb	PBE	LANL2DZ	QECP	deMon2k
	PBE	DZVP	N	NRLMOL
	PBE	TZP	Y	ADF
S	PBE	TZP	Y	ADF

^AThe PBE and BP86 functionals can be found in References 122 and 124, respectively.

^BThe references for the DZVP, augmented DZ and TZ, and LANL2DZ basis sets can be found in References 122, 125, 127 and 128.

^CReferences for the relativistics effects can be found in references 123, 129

Chapter 4 Stability using the Jellium Model

Since the ground breaking experiment by Knight, the jellium model has been used to explain stability in a variety of clusters including the superatom.^G This discovery showed that the electronic contributions dominate the stability at small sizes and that clusters with filled shells of electrons show pronounced stability. In this chapter the jellium model is used to understand the observed stability of bimetallic clusters.

4.1 Al_nX clusters (X = As, Sb, Bi; n = 1 - 6)

Pure aluminum clusters have been shown to exhibit superatom character. The most important being the Al₁₃ and Al₁₃⁻ cluster, which have been described as halogen and noble metal-like superatoms, respectively [23]. This type of stability has the prospect to hold true if one can dope the aluminum clusters while maintaining the jellium stable electron count. One possible avenue is to use a group 15 atom as a dopant in pure aluminum clusters. The valence electron configuration of each of the Group 15 atoms (i.e.- N, P, As, Sb, and Bi) has two s-electrons and three p-electrons, while the Al atom, 3s² 3p¹, has been known to behave mono- or tri-valent varying with cluster size. Depending on the size and the nature of valence contributions, the Al₅X clusters could be expected to show stability within the jellium model with an electron count of 8 or 20 electrons.

In order to investigate the possibility of stability, first principle calculations were performed on the neutral, cationic, and anionic Al_nAs, Al_nSb, and Al_nBi clusters (n = 1-6) within

^G Refer to Chapter 1

the density functional formalism. Both the arsenic and aluminum atoms were described using the DZVP basis. The antimony and bismuth atoms were described using the 23 electron scalar relativistic effective core potential proposed by Metz and coworkers in conjunction with the correlation consistent aug-cc-pVDZ valence basis set. The structures were fully optimized without symmetry constraints. All calculations were performed using the deMon2k software explained previously.^H

The ground state structures for $Al_nAs^{-/0/+}$, $Al_nSb^{-/0/+}$, and $Al_nBi^{-/0/+}$ are shown in Figures 4.1.1, 4.1.2, and 4.2.3, respectively. The neutral AlAs, AlSb, and AlBi clusters have bond lengths of 2.33, 2.53 and 2.56 Å, respectively. The bond length increases as the atomic number increases for the dopant in all three cases. The anion dimer clusters are each doublets with $C_{\infty v}$ symmetry and the bonds shorten from their neutral counterparts. For the cation dimers, the ground state structures are quartets with $C_{\infty v}$ symmetry and bond lengths of 2.6, 2.8 and 2.9 Å for the $AlAs^+$, $AlSb^+$ and $AlBi^+$ clusters, respectively.

The lowest energy structures for the Al_2X clusters each have C_{2v} symmetry and are spin doublets. The Al-Al bond length ranges from 2.6 – 2.7 Å, while the M-Al bond ranges from 2.4 – 2.7 Å. In the anion and cation Al_2X clusters, the Al-Al bond is broken, but each cluster still maintains a C_{2v} geometry. The Al_2X anions are singlets and the Al_2X cations are triplets. As we continue to the Al_3X clusters, they can be looked upon as adding one aluminum cluster to form the C_{2v} geometries for both the charged and neutral species. The Al-Al bonds in the charged and neutral species are on average 2.6 Å, with the M-Al bonds varying in length from 2.4 - 2.8 Å. The charged species are doublets, whereas the neutral species are singlets.

^H Refer to Chapter 3

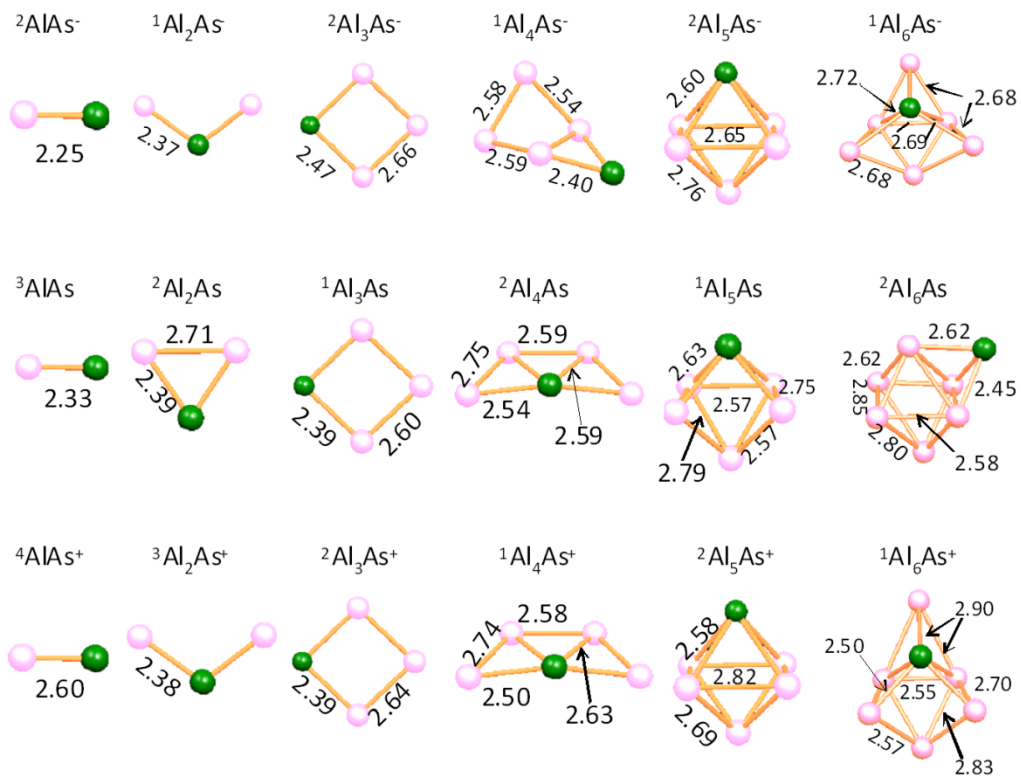


Figure 4.1.1 Optimized geometries of anionic, neutral, and cationic Al_nAs clusters ($n = 1-6$). The superscripts indicate the spin multiplicities. Bond lengths are given in Angstroms.

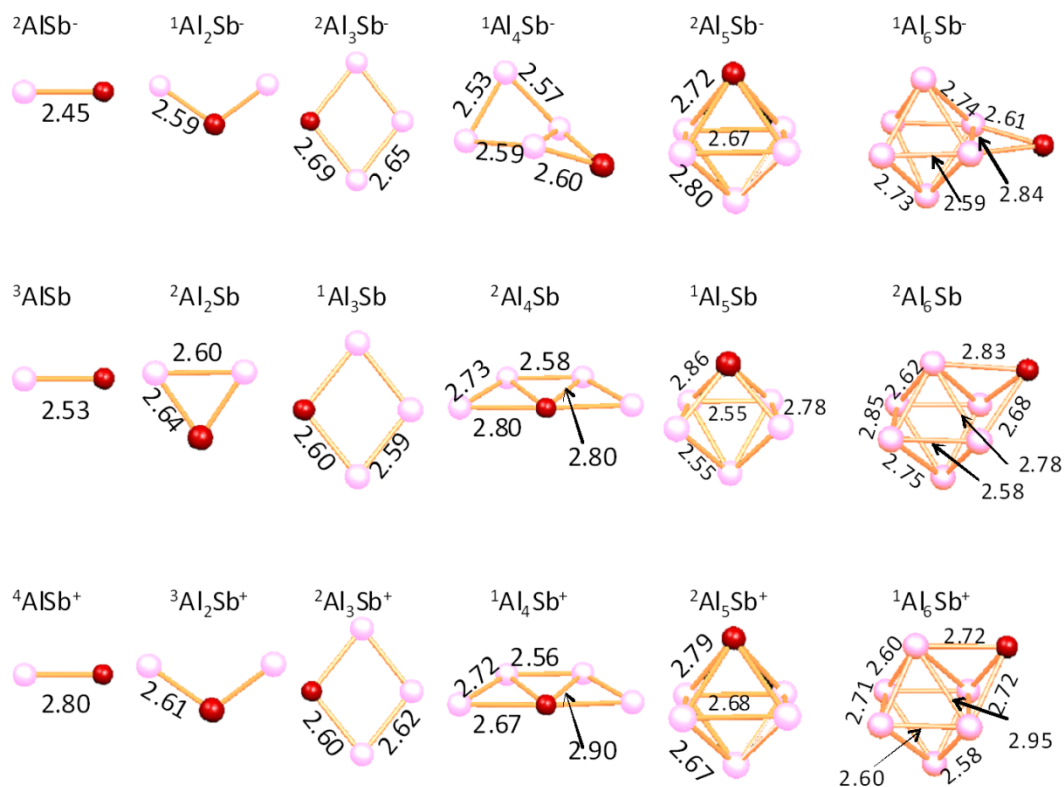


Figure 4.1.2 Optimized geometries of anionic, neutral, and cationic Al_nSb clusters ($n = 1-6$). The superscripts indicate the spin multiplicities. Bond lengths are given in Angstroms.

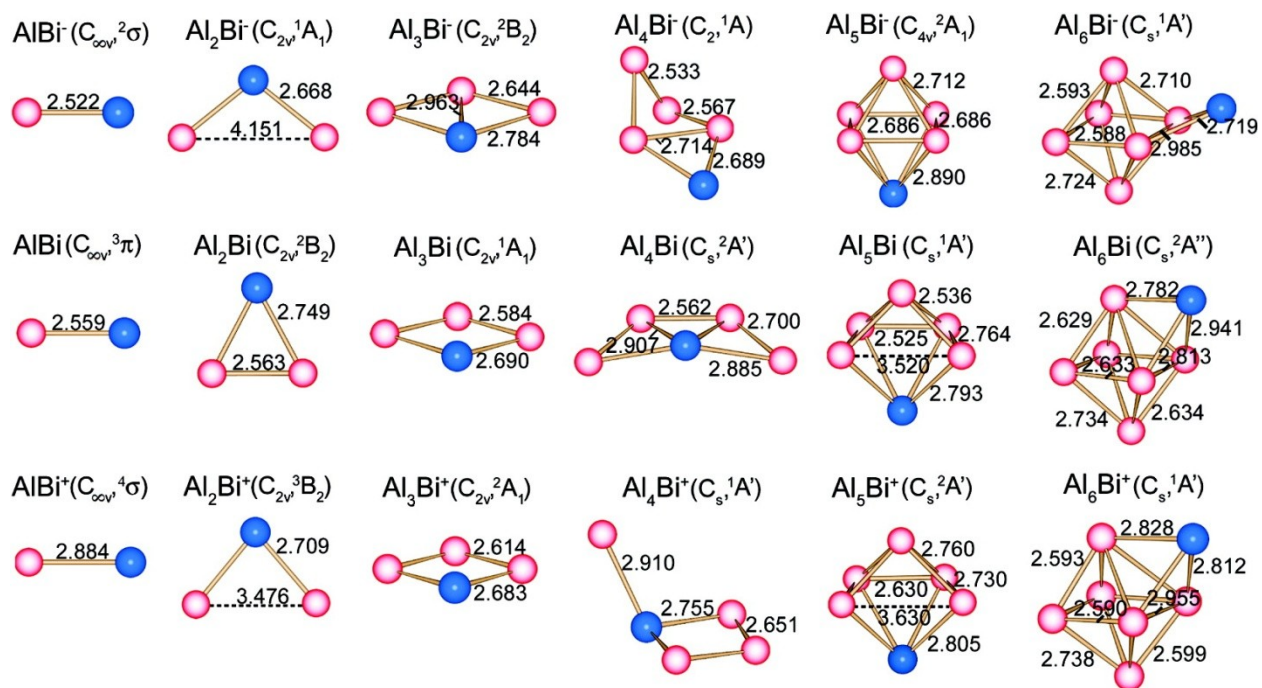


Figure 4.1.3 Optimized geometries of anionic, neutral, and cationic Al_nBi clusters ($n = 1-6$). The superscripts indicate the spin multiplicities. Bond lengths are given in Angstroms.

The Al_4X clusters are the first instance where the clusters exhibit a three-dimensional geometry. Each of the spin singlet anionic clusters have a C_s geometry with three aluminum atoms in the xy -plane, and one Al atom as well as the metal atom above and slightly below the plane, respectively. The neutral clusters are spin doublets, with Al_4Bi and Al_4As having the Bi and As metal clusters slightly out of the plane with respect to the aluminum atoms in the cluster. However, the Al_4Sb cluster is planar much like that of the structure reported for the Al_5 cluster. This planar configuration is the same structure for the Al_4As^+ and Al_4Sb^+ clusters. The Al_4Bi^+ cluster is different from both the Al_4As^+ and Al_4Sb^+ clusters. The Al_4Bi^+ cluster can be looked upon as the Al_3Bi^+ cluster with an extra Al cluster attached to the Bi atom and above the plane.

When $n = 5$, the Al_5X structure becomes truly compact and three-dimensional. The Al_5As^+ , Al_5Sb^+ , Al_5Bi^- , Al_5Sb^- , and Al_5As^- clusters have C_{4v} symmetry. It is interesting to note that the Al_5Bi^+ cluster has C_s symmetry with the Al-Al bond lengths varying in lengths from 2.8 – 2.6 Å. The neutral clusters have C_s symmetry and singlet spin multiplicities. This change in geometry is a direct result of one Al-Al bond breaking going from the anion to the neutral cluster.

The Al_6X neutral clusters are very similar in geometric structure. These clusters can be looked upon as the Al_6 cluster with the addition of the atom to the triangular face of the cluster or as a Bi substituted Al_7 cluster. The Al_6Sb^+ and Al_6Bi^+ clusters both have C_s geometry with the Sb and Bi atoms residing to the exterior of the Al_6 cluster. The Al_6Sb^- and Al_6Bi^- clusters are slightly different in geometry. Both of the clusters have the metal atom residing outside the cage, however they have two bonds to the Al_6 cluster instead of three seen in the anion. It is interesting to note that the Al_6As^- and Al_6As^+ clusters differ in geometry from the other clusters. In these two cases, the structures can simply be view as the Al_5As^- cluster with the addition of

one Al atom to the exterior of the structure. This slight change in geometry may be attributed to either the size of the As atom, as compared to Sb/Bi, or the possible difference in electronegativity.

In order to aid in the determination of the geometries ascertained, photodetachment experiments were carried out on the Al_nAs , Al_nSb , and Al_nBi clusters. Al_nAs or Al_nSb clusters were created in the gas phase by placing a thin coating of arsenic or antimony on a pure aluminum rod. Two methods were successful in creating Al_nBi^- clusters. The first made use of two adjacent rods of pure aluminum and bismuth that met at the laser's focal point. A second method used a thin layer of bismuth coated on an aluminum rod. For further information please refer to Chapter 2 on the apparatus.

The collected photoelectron spectra for all of the clusters in this study can be seen in Figure 4.1.4. Notice many of the features are similar for each of the clusters. The electron binding energies correspond to the electron affinities of the neutral clusters. The determination of the experimental vertical and adiabatic electron detachment energies have been explained previously and are shown for the Al_nAs , Al_nSb and Al_nBi clusters in Tables 4.1.1, 4.1.2, and 4.1.3 respectively. The experimentally obtained vertical electron detachment energies (VDE) and adiabatic electron detachment energies (ADE) correspond to the theoretical values of the same nature. Theoretically the VDE is determined by the difference in energy between the ground state of the anion and the neutral with the geometry of the ground state anion. Whereas, the ADE is defined as, the energy difference between the ground state of the anion and the ground state of the neutral. The theoretical and experimentally obtained values for each of the cluster series show reasonable agreement indicating that we have the correct ground state clusters. The remainder of the text, will focus primarily on the neutral cluster, therefore the

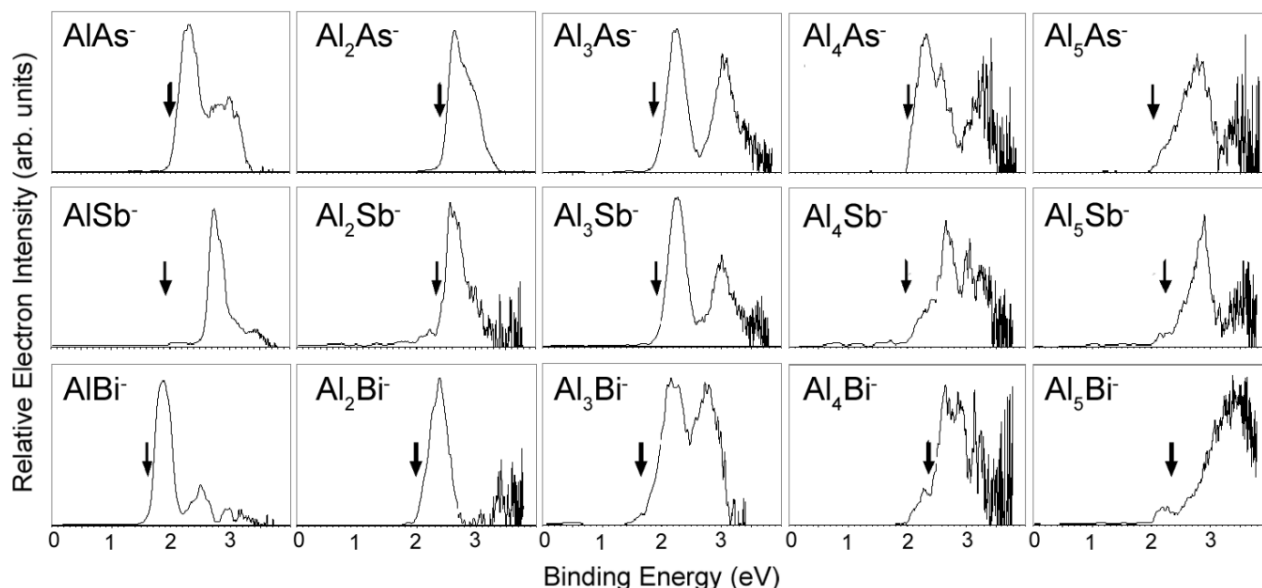


Figure 4.1.4 Photoelectron spectra at 308 nm for Al_nAs^- , Al_nSb^- , and Al_nBi^- clusters ($n = 1-5$).

ionization potentials for the neutral clusters are also listed in each of the respective tables. The ionization potential is defined as the energy difference between the neutral cluster with a ground state geometry and the ground state of the cation, i.e.-

$$IP = E(Al_nX^+) - E(Al_nX)$$

Stability of a cluster can be ascertained in many ways. One of the primary values is the energy gain. The energy gain is the amount of energy gained by adding one aluminum atom to form a cluster,

$$EG = E(Al) + E(Al_{n-1}X) - E(Al_nX)$$

A larger gain in energy in forming the clusters from the preceding size while a smaller gain in energy in going to the higher size indicate preferential formation. Figure 4.1.5 A shows the

energy gains for the neutral clusters. Immediately the Al_5X cluster jumps out with the largest energy gain in each series, an indication this cluster is stable. An additional way to determine a cluster stability is calculating the second energy difference ($\Delta E_{2,n}$), i.e.—

$$(\Delta E_{2,n}) = E(Al_{n-1}X) + E(Al_{n+1}X) - 2 * E(Al_nX)$$

Again, we see the Al_5X cluster with a large value, indicating its stable character. Another measure of stability is the energy difference between the highest occupied molecular orbital (HOMO) and the lowest unoccupied molecular orbital (LUMO), termed the HOMO-LUMO gap. If the gap size is large (> 1 eV) the cluster is considered chemically stable. The HOMO-LUMO gap for each of the clusters can be seen in each of the tables. Notice there are two neutral clusters with gap sizes greater than 1 eV, Al_3X and Al_5X , indicating that these clusters are particularly stable.

Both the Al_3X and Al_5X clusters show stable character based on the energetic criteria. As explained previously, the jellium model shows clusters are stable with electron counts of 2, 8, 18, 20, etc. However, the Al_3X cluster would have the electron count of either 6 or 14 and does not fall into the jellium criteria for stability (this will be addressed in the following chapter); therefore the remainder of this discussion will focus on the Al_5As , Al_5Sb and Al_5Bi clusters.

One key point of the stability is the electron count of a system, while the other is geometry. It has been previously shown that a cluster with compact geometry and even electron counts will show an enhanced stability. The neutral Al_5As , Al_5Sb and Al_5Bi clusters all show a compact three-dimensional geometry as their lowest energy structures. Now the question becomes what is the electron counting scheme of the Al_5X neutral clusters?

Table 4.1 Experimental adiabatic detachment energies (ADE) and vertical detachment energies (VDE) of Al_nAs^- ($n = 1-5$) clusters. Calculated ADEs and VDEs of Al_nAs^- ($n = 1-6$) clusters. For theoretical VDEs, transitions to both the lower and higher spin states are listed where appropriate. Calculated adiabatic ionization potentials (IP) and HOMO-LUMO gap (HL gap) values for the ground state Al_nAs ($n = 1-6$) clusters. All values are in units of eV. Experimental VDEs have an uncertainty of ± 0.05 eV.

#Al atoms	ADE (exp.)	ADE (theo.)	VDE (exp.)	VDE lower (theo.)	VDE higher (theo.)	IP (theo.)	HL gap (theo.)
1	1.96 ± 0.07	1.97	2.32, 2.75	2.70	2.00	7.37	0.23
2	2.39 ± 0.07	2.29	2.66		2.34	7.23	0.70
3	1.85 ± 0.09	1.74	2.19, 2.99	1.98	2.86	7.34	1.86
4	1.98 ± 0.08	1.92	2.29		2.38	6.30	0.56
5	2.03 ± 0.11	2.07	2.74	2.43	2.64	6.65	1.12
6	---	2.25	---		2.46	6.17	0.55

Table 4.2 Experimental adiabatic detachment energies (ADE) and vertical detachment energies (VDE) of Al_nSb^- ($n = 1-5$) clusters. Calculated ADEs and VDEs of Al_nSb^- ($n = 1-6$) clusters. For theoretical VDEs, transitions to both the lower and higher spin states are listed where appropriate. Calculated adiabatic ionization potentials (IP) and HOMO-LUMO gap (HL gap) values for the ground state Al_nSb ($n = 1-6$) clusters. All values are in units of eV. Experimental VDEs have an uncertainty of ± 0.05 eV.

#Al atoms	ADE (exp.)	ADE (theo.)	VDE (exp.)	VDE lower (theo.)	VDE higher (theo.)	IP (theo.)	HL gap (theo.)
1	1.89 ± 0.07	2.02	2.13, 2.75	2.73	2.05	6.99	0.22
2	2.34 ± 0.10	2.16	2.57		2.34	7.09	0.84
3	1.88 ± 0.09	1.76	2.27, 2.99	2.00	2.90	7.18	1.73
4	1.96 ± 0.12	1.94	2.62		2.45	6.29	0.62
5	2.21 ± 0.10	2.17	2.87	2.54	2.64	6.58	1.17
6	---	2.19	---		2.74	6.15	0.52

Table 4.3 Experimental adiabatic detachment energies (ADE) and vertical detachment energies (VDE) of Al_nBi^- ($n = 1-5$) clusters. Calculated ADEs and VDEs of Al_nBi^- ($n = 1-6$) clusters. For theoretical VDEs, transitions to both the lower and higher spin states are listed where appropriate. Calculated adiabatic ionization potentials (IP) and HOMO-LUMO gap (HL gap) values for the ground state Al_nBi ($n = 1-6$) clusters. All values are in units of eV. Experimental VDEs have an uncertainty of ± 0.05 eV.

#Al atoms	ADE (exp.)	ADE (theo.)	VDE (exp.)	VDE lower (theo.)	VDE higher (theo.)	IP (theo.)	HL gap (theo.)
1	1.57 ± 0.07	1.94	1.90, 2.50	1.97	2.70	6.75	0.46
2	1.97 ± 0.05	1.06	2.37		2.32	7.04	0.72
3	1.62 ± 0.07	1.72	2.10, 2.68	1.95	2.78	7.08	1.69
4	2.36 ± 0.10	2.19	2.60		2.42	6.19	0.57
5	2.32 ± 0.10	2.17	2.60	2.59	2.60	6.51	1.15
6	---	2.21	---			6.04	0.51

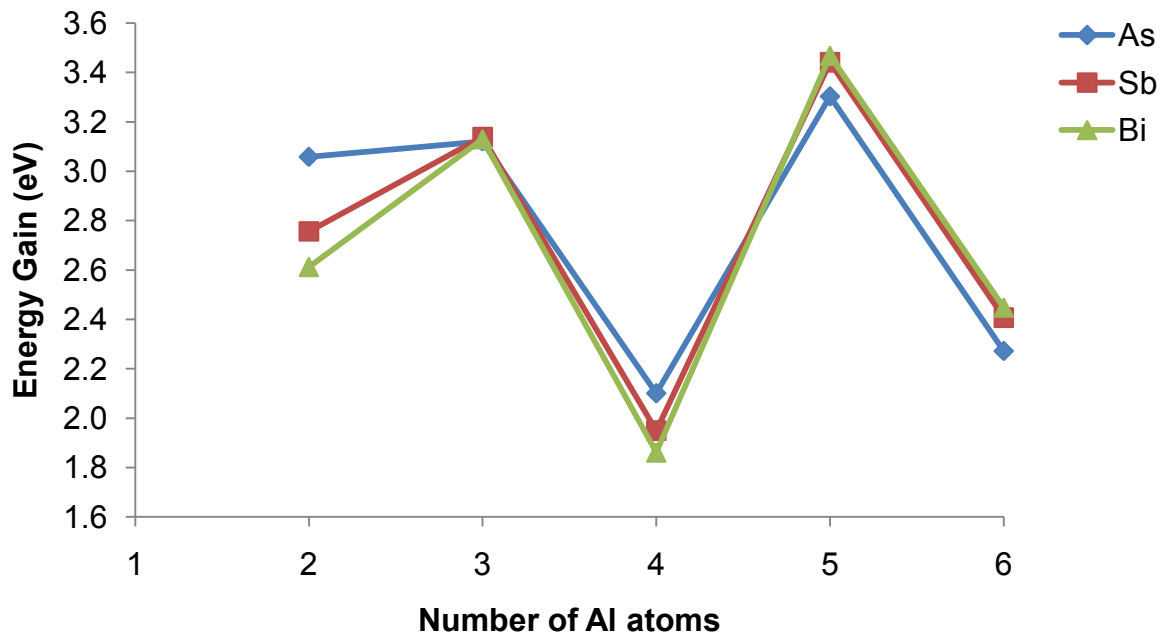
As previously stated, Al has either one or three valence electrons, while the As, Sb, and Bi atoms have a total of three or five valence electrons. The resulting valence electron count for the Al_5X cluster would be either eight or twenty, depending on if Al has one or three valence electrons. The electron counts of 8, 18 and 20 are each *magic* numbers within the jellium scheme, while one more possibility 10 is the lone outlier. In order to determine if this cluster is jellium in the type of stability or that there is another type of stability in accordance with the electron count of 10, the molecular orbitals and one-electron levels were investigated.

Figure 4.1.6 shows the valence one-electron levels and molecular orbitals for the Al_5As , Al_5Sb and Al_5Bi clusters. From the figure, the orbitals are consistent with those expected in a jellium system. In each of the cluster diagrams, the lowest four molecular orbitals represent the $1s^2$ and $1p^6$ states. The HOMO and HOMO-1 levels each represent $1d$ states. For the Al_5Sb and Al_5Bi clusters the HOMO-2 and HOMO-3 states are degenerate and represent the $2s^2$ state as well as an additional $1d^2$ state, with the HOMO-4 residing lower representing a $1d^2$ level. For the Al_5As case the HOMO-2, HOMO-3 and HOMO-4 are degenerate with filling the $2s^2$ and two $1d^2$ levels. The HOMO-5 fills the remaining $1d$ level, for a total of ten electrons in the $1d$ level in each of the clusters. These orbitals present themselves as the electronic configuration $1s^2 1p^6 1d^{10} 2s^2$. Notice that in all three cases, there is mixing of the $2s^2$ and $1d^{10}$ levels. This is an expected result, since upon doping in a metal system the levels in the jellium scheme can shift [130]. The total electron count here is 20, which indeed does correspond to a closed shell stable species within the jellium model for metal clusters.

Using a combination of a theoretical and gas phase experimental approach, three stable jellium clusters have been confirmed. The Al_5As , Al_5Sb and Al_5Bi have large energy gains, second energy differences, and large HOMO-LUMO gaps indicative of stable clusters, such as

superatoms. The compact geometry and total number of electrons (20) reveal the source of stability can be explained using the jellium model. The doped aluminum clusters Al_5As , Al_5Sb and Al_5Bi are not only superatom candidates, but are suitable for cluster assemblies.

A)



B)

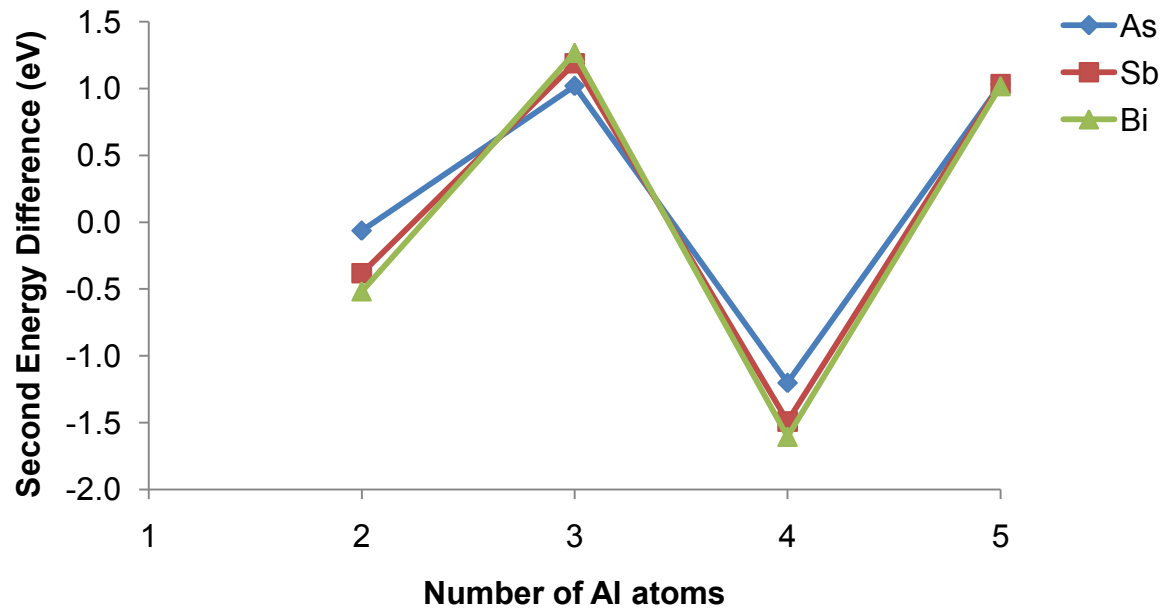


Figure 4.1.5 Theoretical energy gain (Panel A) and second energy difference (Panel B) for Al_nX ($n = 1 - 5$) clusters. For definitions of the energy gain and second energy difference, refer to the text.

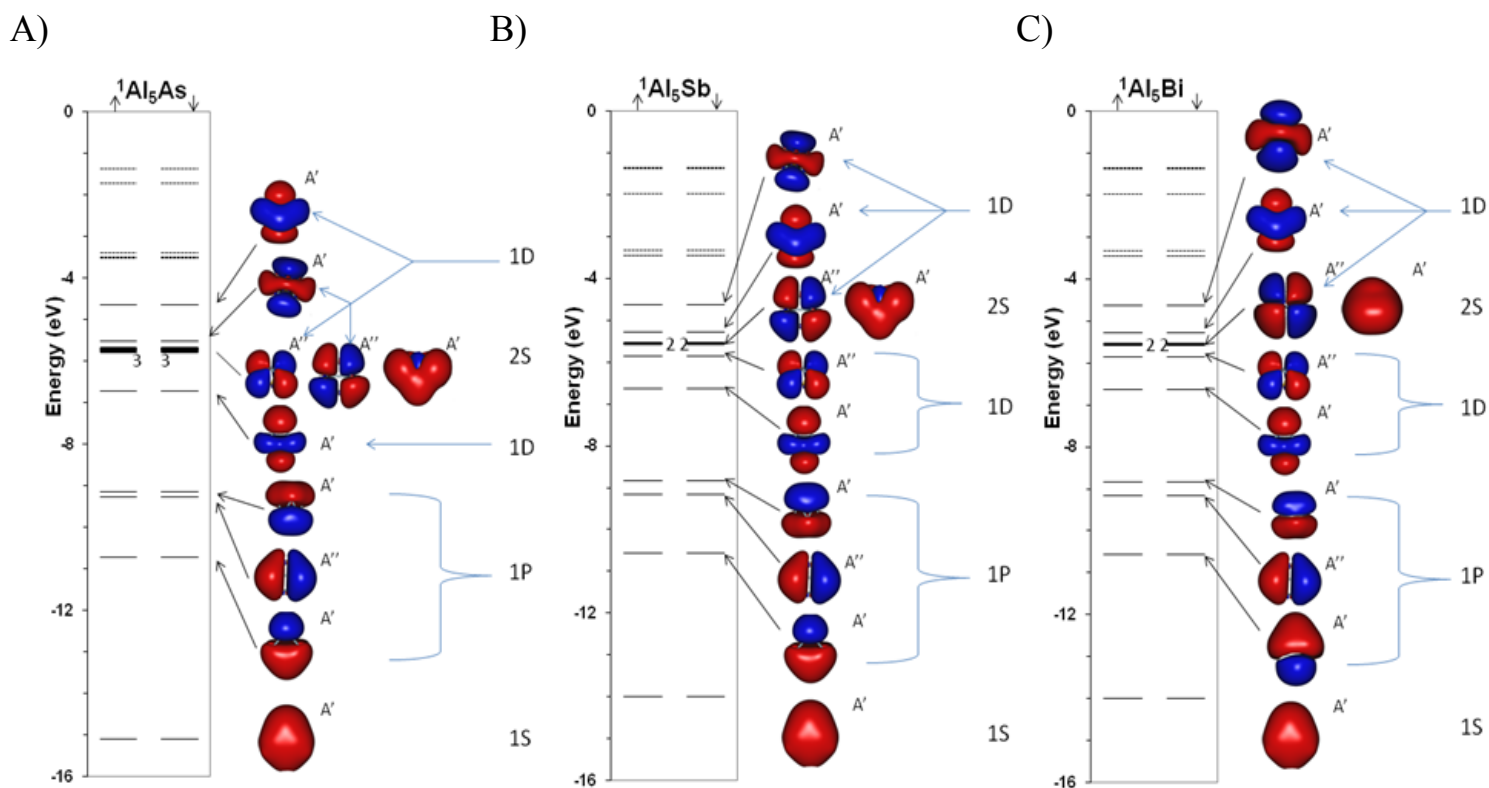


Figure 4.1.6 One electron energy levels, isosurfaces (isovalue = 0.01 au), and symmetries of the molecular orbitals for the neutral Al_5As , Al_5Sb and Al_5Bi clusters. The superscripts indicate the spin multiplicities. The continuous lines are occupied states, the dashed lines represent unoccupied levels. The levels are singly degenerate unless otherwise noted. The arrows indicate majority and minority, spin up and spin down states, respectively.

4.2 $\text{Ag}_n\text{Mn}^{+/0/-}$ ($n = 1-6$) Clusters: Designing Magnetic Superatoms

The concept of the superatom relies on acquiring and maintaining stability through the pairing of electrons which result in closed electronic shells. In the past, this has limited superatoms to only those species which are non-magnetic. A magnetic superatom, on the other hand, would require the electrons to be unpaired and would result in the cluster becoming unstable. One possible way to circumvent this quandary is to design a cluster system where the stability is governed by the jellium model with some atoms that have localized orbitals. Such a system would allow for the magnetic moment, which is localized on atomic sites to remain intact, while the other atomic sites would adhere to the nearly-free electron gas mechanism for stability. Recently, our group, showed this mechanism could indeed work and discovered a class of magnetic superatoms beginning with doped alkalis, for example VCs_8 .

The discovery that one could design a magnetic superatom using atoms that could be stable through the jellium model in conjunction with a magnetic sub-shell, for example the electron configuration of VCs_8 was reported as $1S^2 1P^6 (3d^5)$ [superatom states are designated with uppercase letters, and atomic states with lowercase letters]. This has opened the door for further investigations to design other magnetic superatoms in this manner [131]. Since the alkali clusters, which have been shown to adhere to the jellium model, can be used to design a magnetic superatom, one begins to wonder if other bare clusters that behave like alkali clusters could be used to form such superatoms. Coinage metals (Cu, Ag, and Au) have a filled d shell and one valence *s*-electron in their electronic ground state. The Cu, Ag, and Au atoms delocalize one valence *s*-electron, which in turn allows the coinage metal clusters to be good conductors. Silver clusters have been studied previously due to their importance in industry and biotechnology [132 – 134]. Fournier carried out studies on Ag_n ($n = 2-12$) using density

functional calculations and discovered the ellipsoidal jellium model described the geometries of the silver system very well [135]. Fernandez and co-workers performed theoretical calculations on the Ag_n system and showed neutral clusters where n was even showed an enhanced stability ($n = 2 - 12$) [136]. These authors also pointed out the stability of planar clusters could be understood within the two-dimensional jellium model.

We explored the possibility to design magnetic superatoms using silver clusters with a transition metal as a dopant. It should be noted that experimental studies on the cations of doped silver clusters have been carried out by Janssens and co-workers [137]. Janssens and co-workers also reported on the quenching of the magnetic moment in the $Ag_{10}Co^+$ clusters using experimental and theoretical calculations at the BP86-TZP level [138]. Hou and co-workers performed theoretical studies on the neutral and anionic Ag_5X clusters ($X = Sc, Ti, V, Cr, Mn, Fe, Co, \text{ and } Ni$) using the B3LYP functional with the Stuttgart basis and found each of these clusters maintained a high magnetic moment, with the exception of Ag_5Sc [139]. Other theoretical studies on small bimetallic silver clusters with a transition metal have been carried out by Harb and co-workers [140]. Here, I present a study on the geometries and electron structure of $Ag_nMn^{0/+}$ ($n = 1 - 6$) clusters. To this author's knowledge there has not been a systematic theoretical study on the evolution of size, stability or magnetic character of manganese doped silver clusters.

The theoretical calculations were carried out using a first principles approach within the density functional formalism using the GGA formalism using the PBE functional for exchange and correlation effects. The manganese atom was described using the optimized DZVP-GGA basis. The silver atoms were described using the 19-scalar electron QECP proposed by Andrae

Table 4.2.1. The comparison of the bond length (r), dissociation energy (D_e), frequency (ω), and ionization potential (IP) of the silver dimer. The units for each measure are in parenthesis.

	$r(\text{\AA})$	D_e (eV)	$\omega(\text{cm}^{-1})$	IP (eV)
Expt.	2.5 ^a	1.7 ^b	192.4	7.6
Theor. ^c	2.6	1.7	188.6	
Theor. ^d	2.6			7.8
This Work	2.6	1.8	180.9	7.8

^aReference 141 ^bReference 142 ^cReference 143 ^dReference 144

et al. in combination with the LANL2DZ valence basis.¹ The accuracy of the prescribed theoretical scheme was verified on the silver dimer and compared to previous theoretical and experimental results (Table 4.2.1). Notice the calculated values are within reasonable agreement with previous theoretical and experimental calculations. In order to obtain the lowest energy structures for the $\text{Ag}_n\text{Mn}^{0/+}$ clusters, initial starting geometries were taken from previous studies on neutral and cationic structures and their isomers for Ag_n ($n = 1-7$) clusters. One silver atom was replaced by the Mn atom and multiple spin multiplicities were attempted. A frequency analysis was performed on each of the lowest energy clusters to verify no negative frequencies were attained.

The spin multiplicities and lowest energy structures for the anion, neutral and cation Ag_nMn clusters ($n = 1-6$) are shown in Figure 5.2.1. The AgMn dimer bond lengths are 2.59, 2.74 and 2.58 Å for the neutral, anion, and cation respectively. The anion and cation dimers retain the spin moment of the Mn atom.

¹ Refer to Chapter 3.

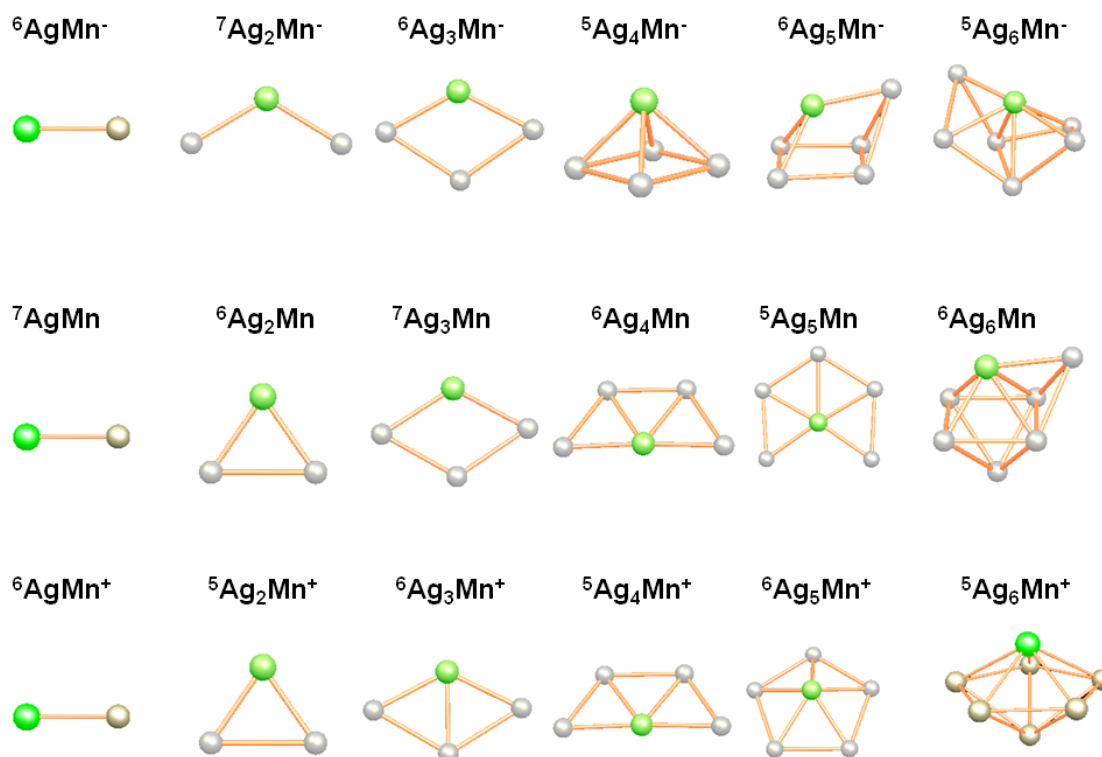


Figure 4.2.1 Ground state geometries of Ag_nMn^- , Ag_nMn , and Ag_nMn^+ ($n = 1 - 6$) clusters. The superscripts indicate spin multiplicity. Green and gray circles represent manganese and silver atoms, respectively.

The Ag_2Mn neutral and cation species have a triangular shape with C_{2v} symmetry and contain two Ag-Mn bonds and form one Ag-Ag bond. The Ag_2Mn^- cluster does not contain any Ag-Ag bonds with C_{2v} symmetry. As we continue to clusters containing three silver atoms, both the anion and cation clusters can be simply viewed as the addition of one silver atom to their previous counterparts. The planar Ag_3Mn cluster is much like the anion cluster has one less Ag-Mn bond than its cation cluster.

The manganese doped silver clusters retain their planar geometry in the case of the neutral and cation Ag_4Mn clusters. Each of these clusters can be viewed as the neutral Ag_5 cluster with the Mn atom substituting the central Ag atom. The neutral cluster retains the spin moment of the Mn atom and the Mn-Ag bond length ranges from 2.62 – 2.76 Å, slightly longer than the Ag-Mn dimer. The two-dimensional picture changes with the Ag_4Mn^- cluster. This is the first instance where the doped clusters exhibit a three-dimensional (C_{2v}) geometry; however a relatively high magnetic moment is still retained.

The Ag_5Mn cluster presents an interesting case. We find both the anion and cation structures are three-dimensional with magnetic moments the same as in a free Mn atom. The lowest energy structure for the cation is the highly symmetric pentagonal pyramid (C_{5v}) structure which is in agreement with the previous reported structure by Janssens and co-workers [137]. The anion, though three-dimensional, is not symmetric as its cation counterpart with C_s symmetry. The lowest energy structure for the neutral cluster is two-dimensional with C_{2v} symmetry. This structure is slightly different from the one previously reported by Hou and co-workers, but in both cases the structure is two dimensional [139].

The neutral, anion, and cation clusters for manganese doped silver clusters are all three-dimensional for clusters containing six silver atoms. The Ag_6Mn^- anion is similar in structure to the Ag_7 neutral cluster, with the Mn atom replacing one silver atom. The geometry of the neutral has little symmetry (C_s) but is more compact than its anion counterpart. The Ag_6Mn^+ cluster can be viewed as the addition of one silver atom below the plane to form the pentagonal bipyramid structure.

For verification of stability we now turn to the energetics. First we investigated the energy gain (E.G.) for each of the clusters in this study. The E.G. is defined as the amount of energy gain upon successively adding Ag atoms, via

$$\text{E.G.} = E(\text{Ag}_{n-1}\text{Mn}) + E(\text{Ag}) - E(\text{Ag}_n\text{Mn}).$$

A similar calculation was performed for the anionic and cationic clusters. Figure 4.2.2 shows the energy gain for the neutral, anionic and cationic clusters. For the neutral clusters, Ag_4Mn shows the largest gain in energy for the series, while Ag_3Mn and Ag_5Mn have large energy gains in the anionic series. The Ag_5Mn^+ cluster shows the largest gain in energy for the cation series. The large gain in energy for these clusters indicates that these cluster have some type of special stability. The second energy difference (S.E.D.), another parameter to ascertain stability is defined as,

$$\text{S.E.D.} = E(\text{Ag}_{n-1}\text{Mn}) + E(\text{Ag}_{n+1}\text{Mn}) - 2 * E(\text{Ag}_n\text{Mn}).$$

A similar calculation was performed for the cation clusters. Figure 4.2.3 shows the S.E.D. for both the neutral and cationic clusters. Notice that for the neutral clusters, the largest peak occurs where $n = 4$. For the cation cluster there is a maxima for $n = 5$. In the anion clusters, many of the values reside at 0 eV.

Two added energetic criteria are the ionization potential and electron affinities for the clusters. The ionization potential (electron affinity) is the difference in energy between the neutral ground state cluster and the ground state of the cation (anion) cluster and can be found in Table 4.2. The Ag_4Mn cluster has the largest ionization potential (6.33 eV) and the lowest electron affinity (1.47 eV). This indicates the cluster prefers to retain its neutrality and is more stable as a neutral cluster. In contrast, Ag_3Mn and Ag_5Mn have the highest electron affinities, 1.62 and 1.70 eV respectively. Thus, both of these clusters prefer to add an electron which is

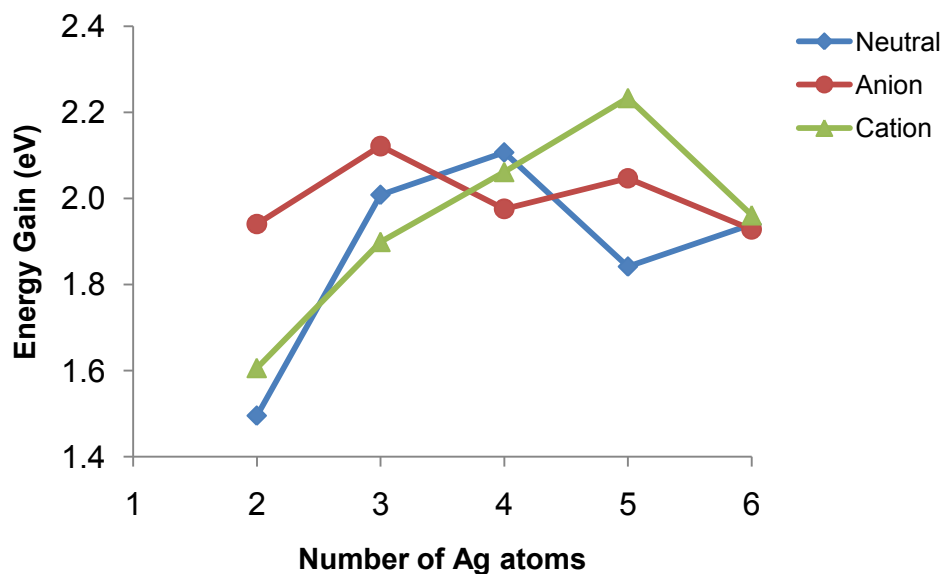


Figure 4.2.2 Variation of the energy gain for the neutral, cation, and anion Ag_nMn clusters ($n = 2 - 6$).

further reiterated through the relatively large energy gain found for both of these anions. It is interesting that the Ag_5Mn cluster has the second lowest ionization potential (6.94 eV) in the series which corresponds to the largest gain in energy for the cation cluster.

We also investigated the energy difference between the highest occupied molecular orbital and the lowest unoccupied molecular orbital, termed the HOMO-LUMO gap (Gap). This quantity is deemed an important criterion for the stability of the cluster. The clusters, Ag_4Mn , Ag_3Mn^- , Ag_5Mn^- , Ag_3Mn^+ , and Ag_5Mn^+ have very large gap sizes (Table 4.2). The largest gap (1.20 eV) can be found for the Ag_5Mn^+ cluster, with only the Ag_4Mn cluster have a gap size greater than 1 eV.

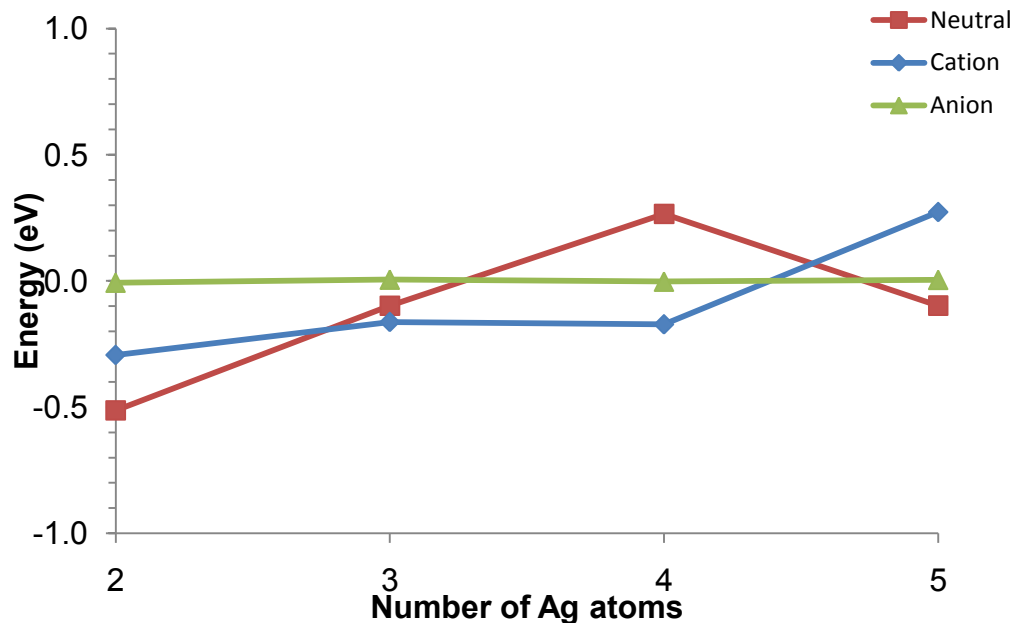


Figure 4.2.3 Variation of the second energy difference (S.E.D) for the neutral, cation, and anion Ag_nMn clusters ($n = 2 - 5$).

On the basis of energetics and gap sizes over 1eV, we can conclude there are two superatom candidates. The neutral cluster, Ag_4Mn has a large ionization potential, low electron affinity, a gap over 1 eV and a large energy gain which is a strong indication of its stability. With the low ionization potential, large HOMO-LUMO gap and large energy gain in the cation series, Ag_5Mn^+ is a strong superatom candidate.

Now we look at the shell effects on the cluster's stability. The magnetic moment on each of the stable cluster species is $5 \mu_B$. Since it is equally as important to verify the cluster's magnetic moment is stable, we examined the energies of various spin states for each cluster size. Table 4.2.3 shows the lowest isomer with a magnetic state closest to the ground state cluster. In each of the stable clusters, the closest magnetic state is at least 0.5 eV higher in energy. This result indicates these clusters are quite stable. Notice the moment on the clusters is the same as the moment found for the Mn atom. The Mn atom has an $3d^5 4s^2$ electronic configuration and

Table 4.2.2 HOMO-LUMO gap for the neutral, cation and anion Ag_nMn clusters ($n = 1 - 6$) and their ionization potential (I.P.) and electron affinity (E.A.).

N	HOMO-LUMO gap (eV)			I.P. (eV)	E.A. (eV)
	Neutral	Cation	Anion		
1	0.10	1.30	0.68	6.29	1.06
2	0.64	0.60	0.26	6.18	1.51
3	0.71	1.05	1.10	6.29	1.62
4	1.06	0.46	0.59	6.33	1.49
5	0.46	1.20	0.84	5.94	1.70
6	0.96	0.42	0.51	5.92	1.68

for each energetically stable cluster one would expect the total valence electron count to be 11 for both Ag_4Mn and Ag_5Mn^+ , none of which correspond to a magic number within the jellium model. Thus, it could be possible that the five d -electrons remain localized on the atom, with only the two s -electrons interacting with the cluster. If this were the case, one could expect three primary results for the clusters in this study, 1) the total number of delocalized electrons in the cluster can be determined by $n_e + 2$ (neutral) and $n_e + 2 - 1$ (cation) (since the Ag atom contributes one electron to the valence shell); 2) the total valence (delocalized) electrons should correspond to a magic number within the jellium model; and 3) the localized electrons would fill the spin-up magnetic subshell (d^5) with a large energy separation between the spin-up and spin-down states. Therefore, the number of delocalized electrons would correspond to six, which is a stable closed shell “magic” number in both the two-dimensional and ellipsoidal jellium model.

Table 4.2.3. Electronic properties of the $\text{Ag}_n\text{Mn}^{0/+/-}$ clusters ($n = 1 - 6$). Magnetic moments (μ), Ag gain in energies (ΔE_{Ag}), and HOMO-LUMO Gaps (E_{gap}) as well as the magnetic moment of the higher in energy isomer with a different magnetic moment, and the energy difference with respect to the ground state ΔE .

Cluster	μ (μ_B)	ΔE_{Ag} (eV)	E_{gap} (eV)	μ (μ_B)	ΔE (eV)
AgMn	6		0.10	4	0.20
Ag ₂ Mn	5	1.50	0.64	7	0.34
Ag ₃ Mn	4	1.67	0.71	6	0.40
Ag ₄ Mn	5	2.45	1.06	3	0.70
Ag ₅ Mn	6	1.60	0.46	4	0.64
Ag ₆ Mn	5	2.18	0.96	3	0.44
AgMn ⁺	5		1.30	7	1.61
Ag ₂ Mn ⁺	4	1.61	0.60	6	0.25
Ag ₃ Mn ⁺	5	1.90	0.71	3	0.53
Ag ₄ Mn ⁺	4	2.06	0.46	6	0.23
Ag ₅ Mn ⁺	5	2.23	1.20	3	0.75
Ag ₆ Mn ⁺	4	1.96	0.42	6	0.11
AgMn ⁻	5		0.68	3	0.97
Ag ₂ Mn ⁻	6	1.94	0.26	4	0.41
Ag ₃ Mn ⁻	5	2.12	1.10	3	0.99
Ag ₄ Mn ⁻	6	1.98	0.59	4	0.03
Ag ₅ Mn ⁻	3	2.05	0.84	3	0.29
Ag ₆ Mn ⁻	2	1.93	0.51	6	0.32

The resulting electronic configuration would become $1S^2 1P^4 (3d^5)$ for the magnetic superatom, which should be seen in the electronic levels and molecular orbital diagram. In order to see if this picture is correct, we investigated the composition and molecular orbital shapes for each of the stable clusters.

Figure 4.2.4 shows the one-electron levels and molecular orbitals for the Ag₄Mn cluster. Immediately, one can see the 1S and 1P states for both the spin up and spin down states in the Ag₄Mn cluster. The HOMO in both the alpha (spin-up) and beta (spin-down) states have one node located in the center, as does the HOMO-1, which is indicative of the 1P orbitals. The 1S state is the HOMO-2 in the beta case while the 1S state is the HOMO-4 for the alpha levels.

This resulting superatomic electron configuration becomes $1S^2 1P^4$ that corresponds to shell closure within the two-dimensional jellium model.

The magnetic states are clearly localized on the Mn atom (Figure 4.2.4) for the Ag_4Mn cluster. Notice in the Ag_4Mn cluster there is approximately 3 eV of separation between the magnetic alpha (spin up) and beta (spin down) states. However there is very little d character residing on the silver atoms. The small amount of d-character is clearly from the silver d-band and resides at approximately the same energy as the localized d-electrons on the Mn atom. The d-band in the pure silver cluster (Ag_4) is located at -7.0 eV, while the d-electrons in the Mn atom are located 1.6 eV lower in energy. Thus, the interaction of the Mn atom with the Ag_4 cluster would result in some d-character on the Ag atoms in the Ag_4Mn cluster.

The Ag_5Mn^+ cluster though not planar exhibits strong stable magnetic character through its shell effects within the ellipsoidal jellium model. According to this model, one would find the magic number to reside at six for oblate clusters. From the molecular orbitals and one-electron levels, this is indeed the case (Figure 4.2.5). Also, the magnetic states are still localized on the Mn atom with minimal d-character residing on the Ag clusters, which was explained previously. Even though the Ag_5Mn^- cluster does not have a HOMO-LUMO gap larger than 1 eV, from the energy gain calculations it shows an enhanced stability over its nearest neighbors. The uniqueness of this cluster is its geometry is a compact three-dimensional structure, which is different from the Ag_4Mn and Ag_5Mn^+ cases and should be addressed. The number of electrons due to the combination of Ag_5^- cluster and the two s-electrons from the Mn atom, would allow the cluster to have a shell closing at eight and a localized atomic magnetic sub-shell.

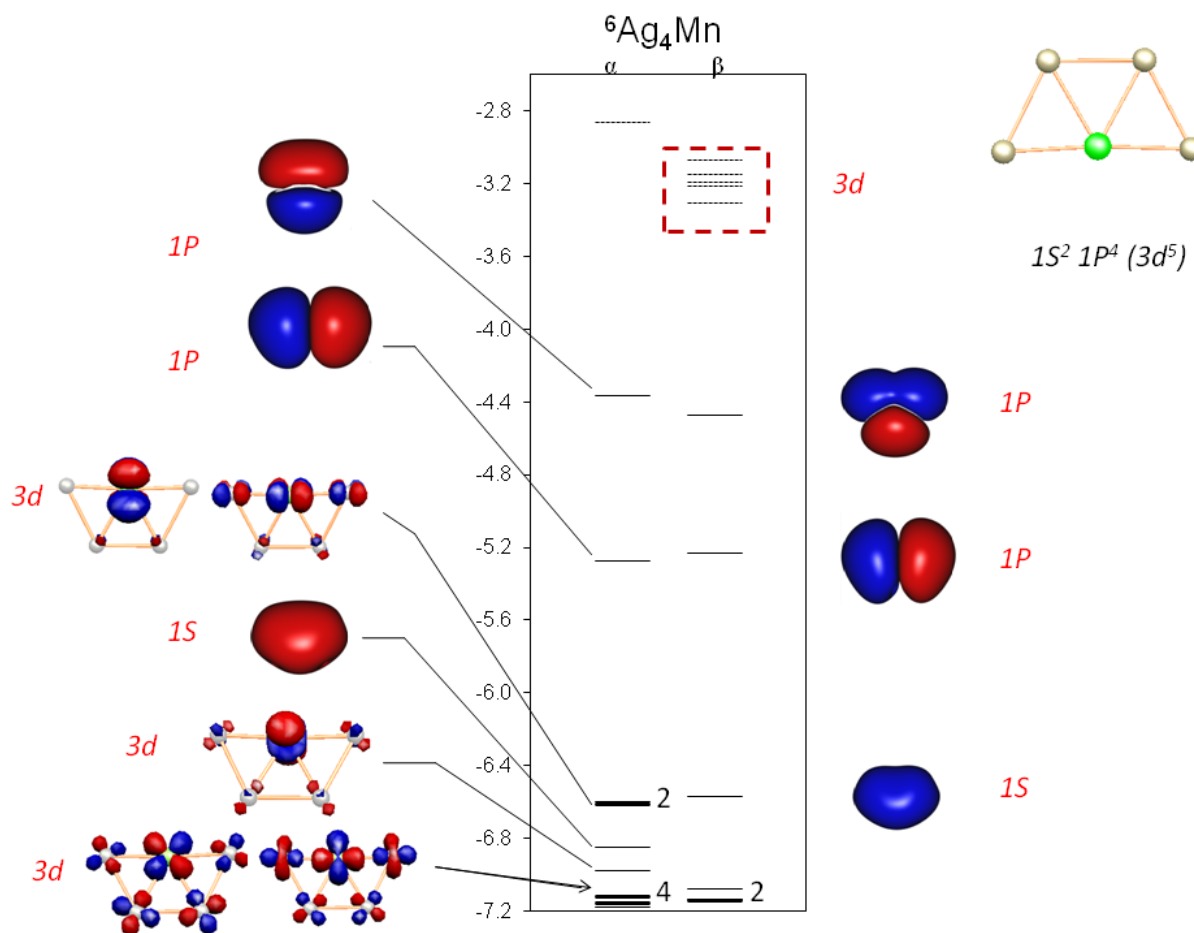


Figure 4.2.4 One electron energy levels for MnAg_4 and molecular orbital charge density (isosurfaces 0.03 a.u.). The continuous lines are occupied levels, the dotted lines correspond to unfilled states. The degeneracy of each level is assumed to be one unless otherwise noted. The symbols α and β indicate the majority (up) and minority (down) spin states, respectively. Upper-case letters stand for delocalized $1S$ and $1P$ shells, and lower-case letters for localized $3d$ atomic shells.

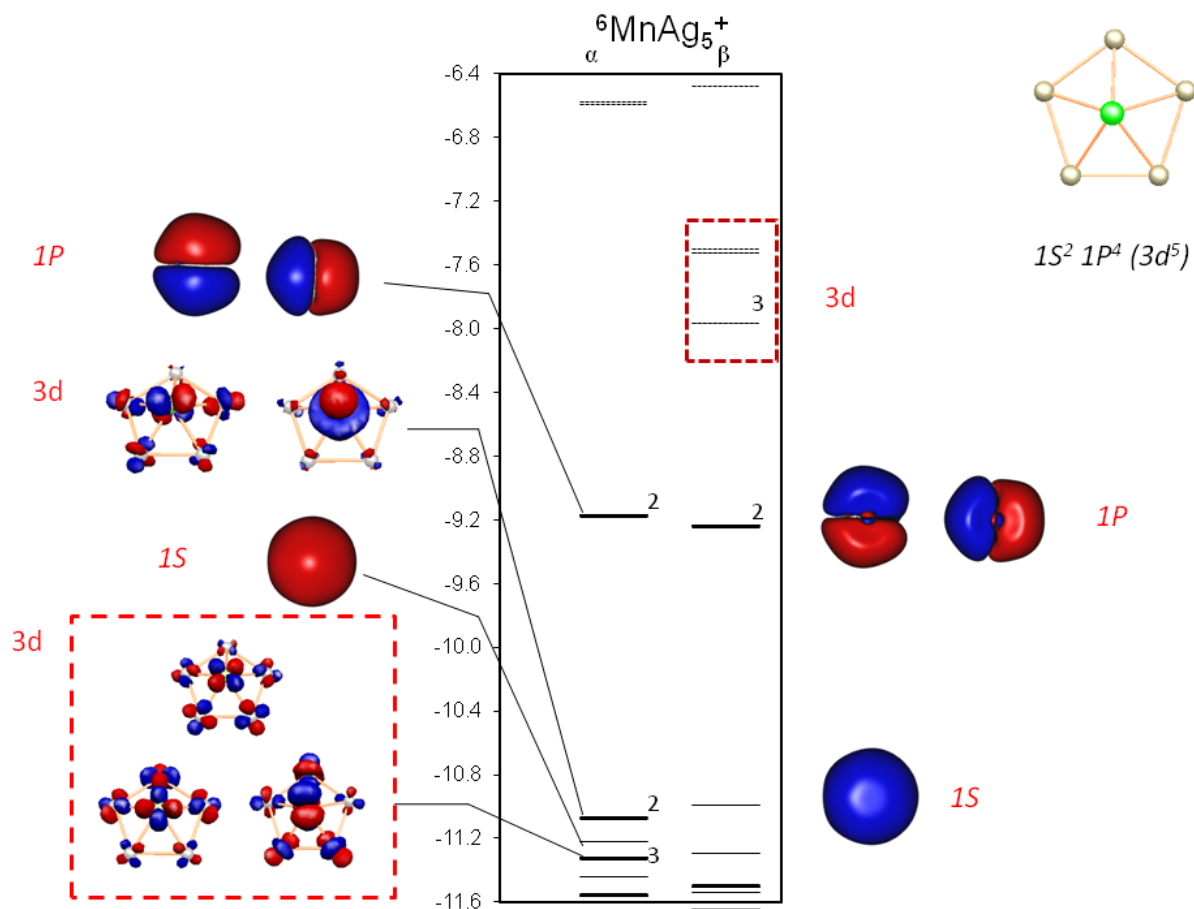


Figure 4.2.5 One electron energy levels for MnAg_5^+ and molecular orbital charge density (isosurfaces 0.03 a.u.). The continuous lines are occupied levels, the dotted lines correspond to unfilled states. The degeneracy of each level is assumed to be one unless otherwise noted. The symbols α and β indicate the majority (up) and minority (down) spin states, respectively. Upper-case letters stand for delocalized $1S$ and $1P$ shells, and lower-case letters for localized $3d$ atomic shells.

This along with its compact three-dimensional geometry is encouraging that it adheres to the three-dimensional jellium shell model. In fact, upon investigation of the electronic structure, this is the case (Figure 4.2.6). The unpaired electron states are clearly localized on the Mn atom, while the orbitals clearly show the electronic configuration needed for a closed shell in the 3D jellium shell model, i.e. $-1S^2 1P^6$. Therefore, the Ag_5Mn^- cluster can be viewed as a magnetic superatom within the constructs of the jellium shell model.

In light of these observations, the magnetic superatom within the jellium model should be extendable to larger silver complexes. Recently, in a theoretical study by Aikens, it was pointed out that the $Ag_{25}(SH)_{18}^-$ cluster exhibited the same geometric configuration found in the $Au_{25}(SH)_{18}^-$ cluster [145]. This was later confirmed through experimental observation by Bakr and co-workers [146]. Their results indicate that the $Ag_{25}(SH)_{18}^-$ cluster can be thought of in the identical superatomic manner as the $Au_{25}(SCH)_{18}^-$. We believe the superatom complex, $Ag_{24}Mn(SH)_{18}$ should exhibit behavior identical to that of the previously reported $Au_{24}Mn(SH)_{18}$ magnetic superatom complex. The starting geometry for the $Ag_{24}Mn(SH)_{18}$ complex was taken by replacing the central Ag atom in the $Ag_{25}(SH)_{18}^-$ structure reported by Aikens and co-workers, with the Mn atom. The atoms were represented by the triple- ζ polarization basis. Relativistic effects were accounted for using the Zeroth order relativistic approximation (ZORA) in the ADF software package. The structure was allowed to optimize without constraints at various spin multiplicities to ensure the correct spin state was achieved. Figure 4.2.7 shows the optimized $Ag_{24}Mn(SH)_{18}$ cluster. The theoretical studies found a ground state with a spin magnetic moment of $5\mu_B$ and its nearest magnetic state, $3\mu_B$, residing 0.52 eV higher in energy. We observed a HOMO-LUMO gap of 0.33 eV similar to the value obtained in the $Au_{24}Mn(SH)_{18}$ case [27].

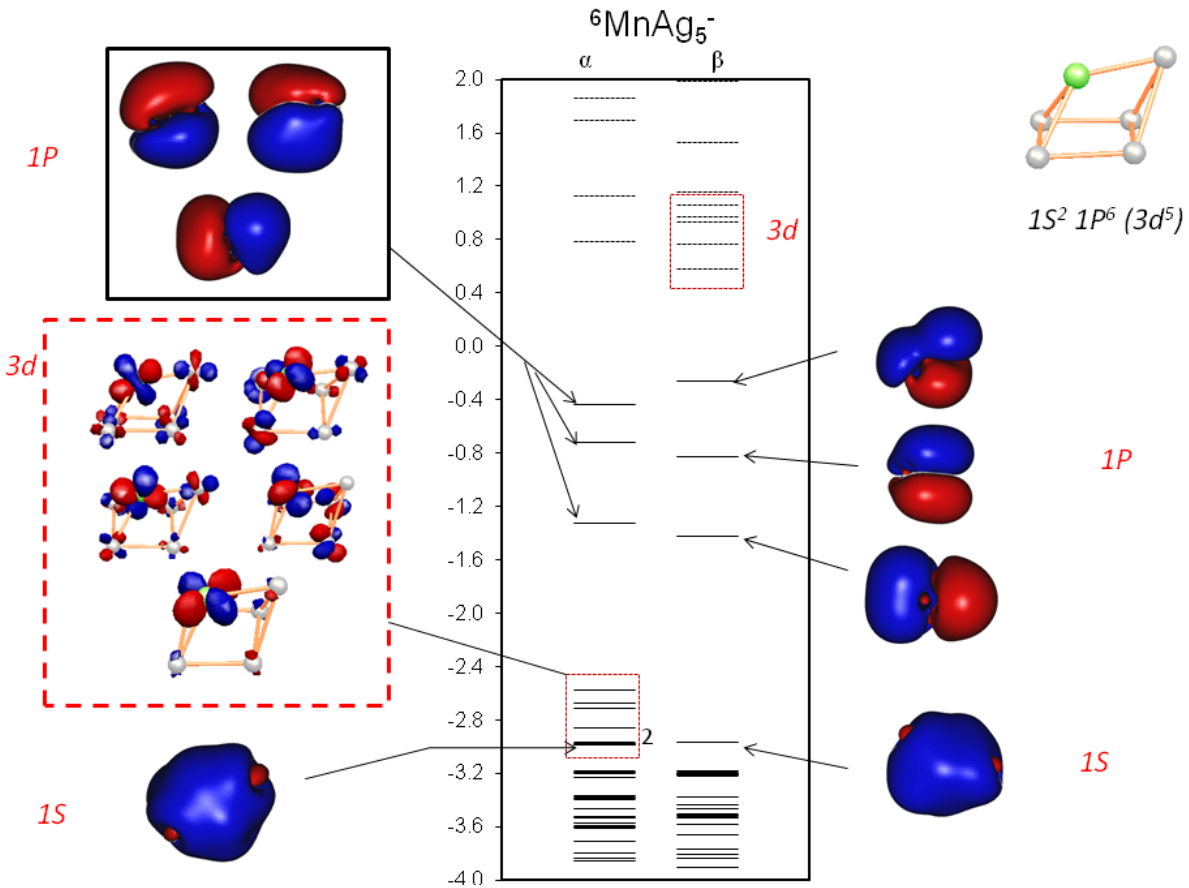


Figure 4.2.6 One electron energy levels for MnAg_5^- and molecular orbital charge density (isosurfaces 0.03 a.u.). The continuous lines are occupied levels, the dotted lines correspond to unfilled states. The degeneracy of each level is assumed to be one unless otherwise noted. The symbols α and β indicate the majority (up) and minority (down) spin states, respectively. Upper-case letters stand for delocalized $1S$ and $1P$ shells, and lower-case letters for localized $3d$ atomic shells.

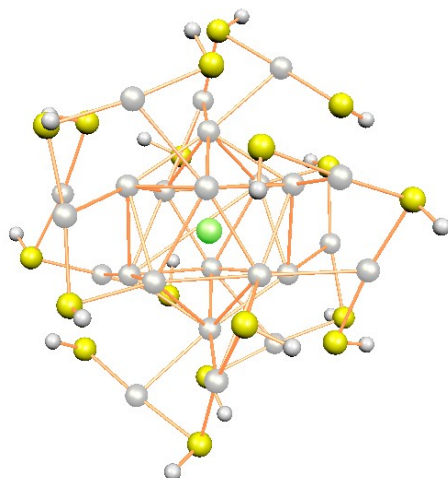


Figure 4.2.7 Lowest energy structure of the $\text{MnAg}_{24}(\text{SH})_{18}$ cluster. The gray, yellow, white and green balls represent the silver, sulfur, hydrogen, and manganese atoms respectively.

Here, I have shown that magnetic superatoms are just confined to the jellium shell model in three dimensions, but can be viewed within a unified jellium construct. The unified view not only uses the jellium model in three-dimensions, but includes the two-dimensional and ellipsoidal jellium models as mechanisms to design stable magnetic superatoms. Also, a magnetic superatom complex, $\text{Ag}_{24}\text{Mn}(\text{SH})_{18}$ shows the possibility of extending the magnetic superatoms from smaller clusters to larger complexes that may be useful in nanomaterials.

4.3 Chapter 4 Summary

Using a combination of theoretical and experimental techniques the bimetallic Al_5As , Al_5Sb and Al_5Bi clusters were identified as stable clusters. The stable nature of these clusters was attributed to the spherical jellium model. The total number of electrons in the aluminum based clusters (20) corresponds to a magic number within the spherical jellium model. From further theoretical investigations, we discovered superatoms within the jellium model were not limited to three-dimensions or non-magnetic species. Using a magnetic dopant atom, such as Mn, with localized d electrons and itinerant s electrons to fill the jellium shells within the two-, three- and ellipsoidal jellium models, we were able to design multiple magnetic superatom candidates using doped silver clusters (i.e-- Ag_4Mn , Ag_5Mn^- , Ag_5Mn^+ , and Ag_6Mn). This concept was further used to design a superatom complex $\text{Ag}_{24}\text{Mn}(\text{SH})_{18}$ much like that of the superatom complex $\text{Au}_{24}\text{Mn}(\text{SH})_{18}$.

Chapter 5 Stability using All-metal Aromaticity

The concept of “pure” aromaticity originates in a delocalization of the molecular orbitals that ultimately is responsible for the stabilization of an organic cluster system. As explained in the introduction this idea has been extended to the inorganic realm. Now we undertake the exploration of all-metal aromaticity through the investigation of various aluminum based heteroatomic systems.

5.1 All-metal Aromaticity in Al_3X ($X = As, Sb, Bi$)

In an effort to add to the field of all-metal aromaticity theoretical and experimental studies were undertaken on the study of various bimetallic III-V cluster systems. The method for the study of these systems has been described previously (See Chapter 4). Here we primarily focus on the planar Al_3X ($X = As, Sb, Bi$) clusters and their anions.

The collected photodetachment electron spectra, along with the matching vertical and adiabatic detachment energies were given in the previous chapter, however for each of the Al_3X ($X = As, Sb, Bi$) species, we give the cluster geometries of the neutral and anion here for completeness (Figure 5.1.1). It is interesting to note that for all the clusters studied the agreement between the theoretical and experimental electron detachment energies is within the margin of error which assures the correctness of the neutral and anionic ground states. Each of the neutral clusters contains C_{2v} symmetry, which is planar for their respective ground states.

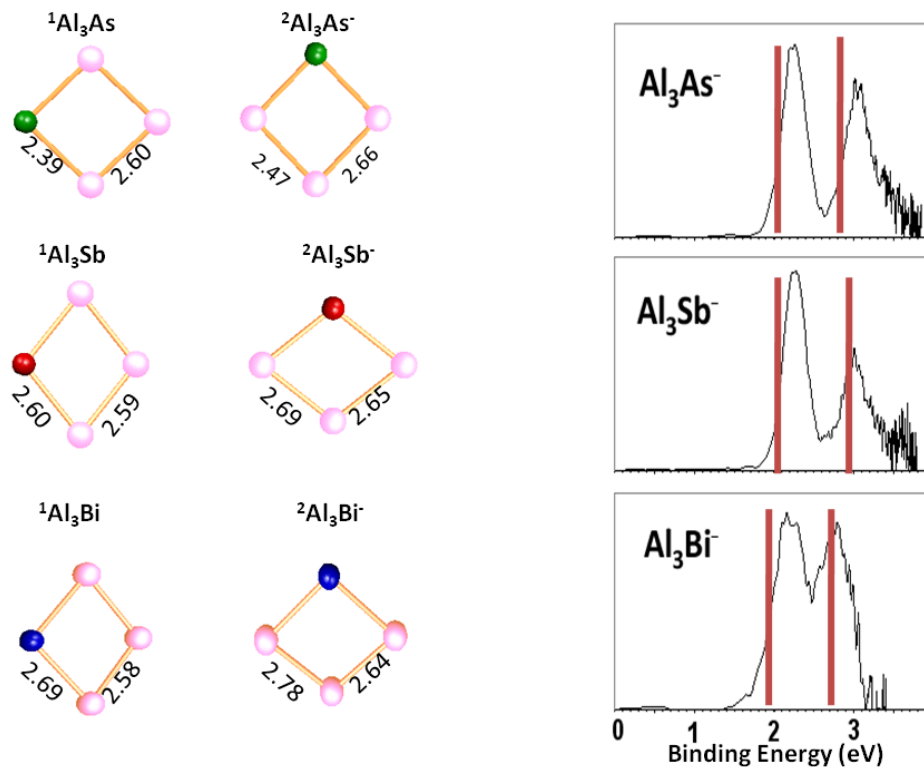


Figure 5.1.1 Optimized geometries of the neutral and anionic Al_3As , Al_3Sb , and Al_3Bi clusters (Bond lengths are given in Angstroms) and collected photodetachment spectra for the anion species. The red lines represent the calculated vertical electron detachment energies from the anion.

It should be noted that there have been previous studies on other Al_3N , Al_3P , and Al_3As clusters. The cluster Al_3As was previously shown to have the same symmetry as we find with this study. The result of the clusters having a planar geometry has given us a hint towards the possibility of the clusters having aromatic character; however the stability of the clusters in question must first be verified.

In order to do so, the various energetics were investigated for the Al_3As , Al_3Sb and Al_3Bi clusters. Table 5.1.1 shows the HOMO-LUMO gap, removal energy, adiabatic detachment energies and ionization potentials for the Al_nAs , Al_nSb and Al_nBi ($n = 2 - 4$) clusters.

Table 5.1.1 Calculated and experimental Adiabatic Detachment Energies (ADE), calculated Adiabatic Ionization Potentials (IP), HOMO-LUMO gap values and removal energies for the ground state Al_nAs , Al_nSb , Al_nBi ($n = 2 - 4$) clusters (in eV).

	n	ADE (exp.)	ADE (theo.)	IP (theo.)	HL gap (theo.)	R.E.
Al_nAs						
	2	2.39 ± 0.07	2.29	7.23	0.70	3.06
	3	1.85 ± 0.09	1.74	7.34	1.86	3.12
	4	1.98 ± 0.08	1.92	6.30	0.56	2.10
Al_nSb						
	2	2.34 ± 0.10	2.16	7.09	0.84	2.76
	3	1.88 ± 0.09	1.76	7.18	1.73	3.14
	4	1.96 ± 0.12	1.94	6.29	0.62	1.95
Al_nBi						
	2	1.97 ± 0.05	2.06	7.04	0.72	2.61
	3	1.62 ± 0.07	1.72	7.08	1.69	3.13
	4	2.36 ± 0.10	2.19	6.19	0.57	1.86

Immediately one can see the HOMO-LUMO gap is the largest for the Al_3X species in all of the clusters studied, which is indicative of cluster stability. Not only is the HOMO-LUMO gap quite large for the Al_3X clusters, but they have a high ionization potential and low electron detachment energies. These two values illustrate that the cluster prefers not to give up or accept an electron very readily, meaning the cluster is stable in a state of neutrality. Another more insightful energetic value is that of removal energy, which was explained previously. The amount of energy it takes to remove an aluminum atom from each of the Al_3X clusters to form the Al_2X cluster is approximately 3.0 eV, but to go from Al_4X to Al_3X only requires 2.0 eV of energy. This shows that the Al_3X neutral cluster is more stable than its nearest neighbor counterparts.

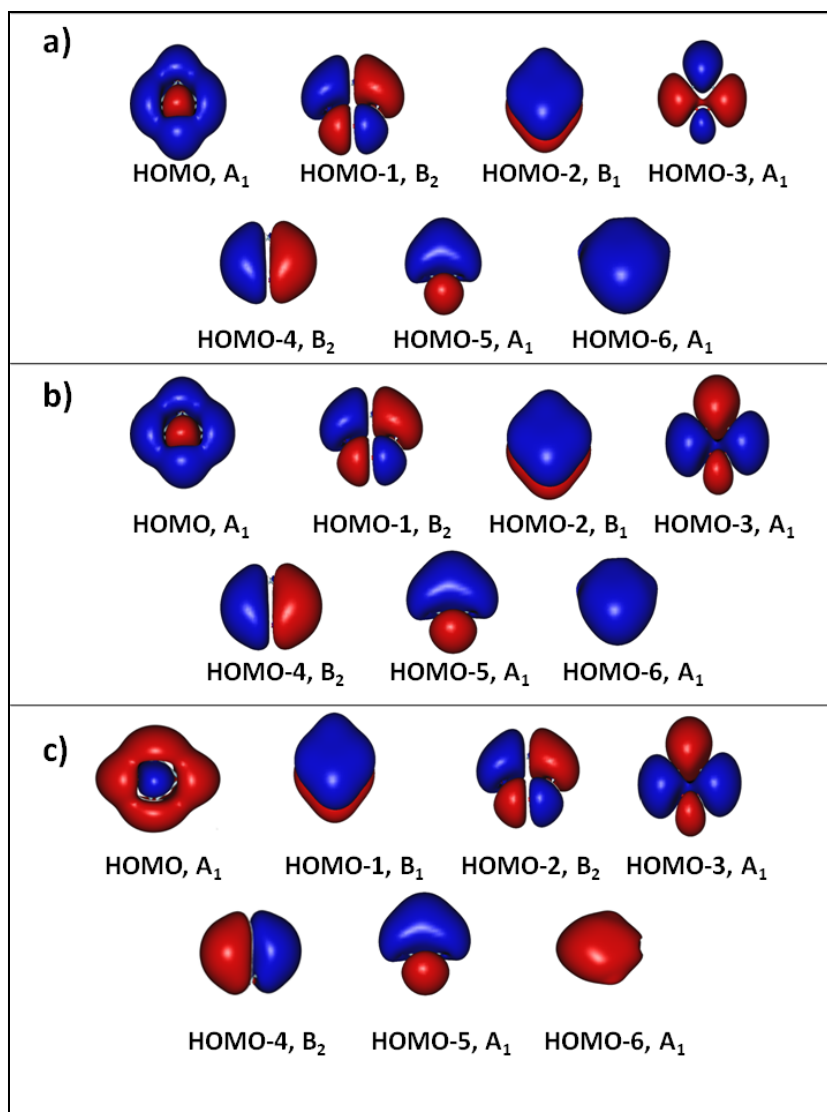


Figure 5.1.2 The isosurfaces (isovalue = 0.01 au) and symmetries of Al₃As (Panel a), Al₃Sb (Panel b) and Al₃Bi (Panel c) of the molecular orbitals for the neutral ground state geometries.

Now, we turn our attention back to the question of do these Al₃X clusters exhibit the characteristics of all-metal aromaticity. It has previously been established that each of the Al₃X clusters have a planar geometry, however the character has not been established due to the criteria put forth above. The main tenet of aromaticity lies in the molecular orbitals as set forth

in the rules of aromatic compounds. Therefore, Figure 5.1.2 gives a plot of the molecular orbitals for Al_3As , Al_3Sb and Al_3Bi . The molecular orbitals for each of the three clusters are seemingly very similar. Each of the clusters the HOMO has A_1 symmetry, however the HOMO-1 and HOMO-2 are slightly different. For both the Al_3As and Al_3Sb the HOMO-2 is delocalized over the entire ring of the cluster, however in the Al_3Bi case the HOMO-1 is the delocalized molecular orbital. Whether or not the delocalized orbital is the HOMO-1 or HOMO-2, it still satisfies both criteria for aromatic character in an all-metal system. Notice also that all three of the clusters do adhere to Hückel's rule too, which is another confirmation on the aromatic behavior of the Al_3X clusters. Even though these clusters meet the minimum requirements for aromatic character, additional confirmation can be arrived at by computing the nucleus independent chemical shift (NICS).

The NICS value can be useful in determining if a cluster is aromatic or antiaromatic. As stated in Chapter 1, a large diatropic (negative) NICS value is an indication that the cluster is aromatic; however, if the NICS value is paratropic (positive) the cluster is considered to be antiaromatic. NICS values were determined using the Gaussian03 program, with the same basis and functional used to determine the ground state geometries of the clusters. For each of the Al_3As , Al_3Sb and Al_3Bi neutral clusters, we find large negative NICS values at the center of their rings (-29.07, -33.08, and -32.98 ppm, respectively). These values increased as we calculated the NICS value above the plane, still remaining highly negative, affirming the aromatic character. We also calculated the NICS values for the charged clusters, Al_3As^+ , Al_3As^- , Al_3Sb^+ , Al_3Sb^- , Al_3Bi^+ , and Al_3Bi^- for comparison. The neutral species Al_3As , Al_3Sb and Al_3Bi had the most negative NICS values compared to their charged counterparts (Figure 5.1.3).

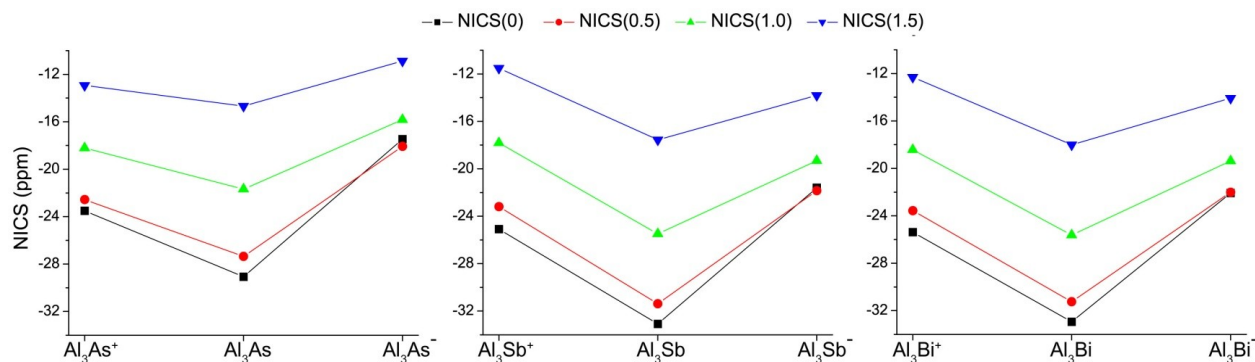


Figure 5.1.3 Nucleus-Independent Chemical Shift (NICS) values of cationic, neutral and anionic Al₃As and Al₃Sb in ppm. Previous results for Al₃Bi are shown for comparison. The NICS values are calculated at the position of a ghost atom placed at the ring center in the molecular plane, and 0.5, 1.0, and 1.5 Å above the plane, respectively.

These results are in agreement with what one would expect for an aromatic species (significantly negative). Although NICS values do not rigorously assign the degree of aromaticity, notice that the Al₃Sb cluster has the most negative value followed closely by the Al₃Bi cluster, with Al₃As being the least aromatic of the species.

It is interesting to note that the rank of aromaticity from most to least, (Al₃Sb > Al₃Bi > Al₃As) seems to follow the trend of differing bond lengths from smallest to largest, with the Al₃Sb cluster having nearly identical values for the entire cluster (Al-Sb = 2.60 Å; Al-Al = 2.59 Å); however, the Al-As bond (2.39 Å) in the Al₃As cluster is significantly shorter than that of the Al-Al bond (2.60 Å) in the cluster (Figure 5.1.1). This correlation between bond lengths and NICS values may be due to the difference in electronegativity. For example, electronegativity difference between aluminum (electronegativity 1.5) and arsenic is the largest at 0.5 [147]. The

difference in electronegativity for Al-Sb and Al-Bi are nearly identical 0.4, which explains the relative closeness of their NICS values. These results imply that as the difference in electronegativity increases, the aromatic character would be lost. In fact, if one looks at the case of Al_3N , which has the largest electronegativity difference (1.5) the lowest energy structure becomes D_{3h} instead of the C_{2v} found here and loses its aromatic character [148].

Thus, by carrying out both theoretical and experimental studies the ground state structure for the Al_3As , Al_3Sb , and Al_3Bi cluster was determined. It follows by investigating the removal energy, adiabatic detachment energies, ionization potentials and HOMO-LUMO gap the Al_3X clusters illustrate enhanced stability over their nearest neighbors. The cause of the inherent stability was determined to be due to the all-metal aromatic construct using a combination of NICS calculations and the delocalization seen in the molecular orbitals [149 -150].

5.2 All-metal Aromaticity and the Ellipsoidal Jellium Model

In Section 5.1, all-metal aromaticity was used to explain the stability in Al_3X ($\text{X} = \text{As}, \text{Sb}, \text{Bi}$) clusters. However, aromaticity may not be the only way to explain the cluster stability in these systems. In order to investigate this possibility, we now extend this study to include nitrogen and phosphorus.

Let us first begin this discussion by looking at the various geometry possibilities for the Al_3M ($\text{M} = \text{N}, \text{P}, \text{As}, \text{Sb}, \text{Bi}$) clusters. There are three primary geometries that have been found for many of the Al_3M clusters in previous studies, C_{2v} , D_{3h} , and C_{3v} (Figure 5.2.1). Studies conducted by Archibong and St-Amant on the neutral and anionic Al_3As cluster, at the B3LYP and CCSD(T) levels using the 6-311+G(2df) basis set found the neutral Al_3As has a cyclic planar C_{2v} geometry with the C_{3v} cluster residing 0.2 eV higher in energy [151]. Additionally, with the same basis set, Guo and Wu calculated the ground state structures of the neutral and anionic Al_3As cluster with pure and hybrid exchange correlation functionals and found a similar result [152]. Studies on Al_3N show the ground state to maintain a D_{3h} geometry with its stability being attributed to its planar geometry [153 -154]. Using a variety of DFT methods, the ground state of the Al_3P cluster was shown to have C_{3v} symmetry [155 -156]. Archibong and St-Amant find that for the Al_3P cluster the C_{2v} , D_{3h} , and C_{3v} structure are nearly degenerate, with C_{2v} and C_{3v} states being the genuine minima at the CCSD(T) level [157]. With the varying geometries for the clusters with the Al_3M ($\text{M} = \text{N}, \text{P}, \text{As}, \text{Sb}, \text{Bi}$), with only slight differences being the dopant atom, why do we not see the aromatic construct as the guiding stability principle for all of these clusters?

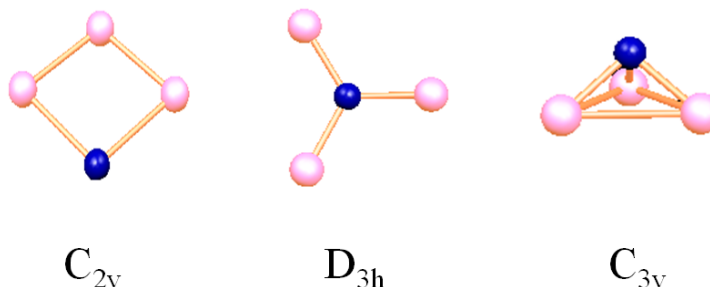


Figure 5.2.1 Schematic of the C_{2v} , D_{3h} , and C_{3v} geometries.

To gain a better insight on this perplexing question calculations on the C_{2v} , D_{3h} and C_{3v} geometries for the Al_3M ($M= N, P, As, Sb, Bi$) clusters were performed within the density functional formalism. Table 5.2.1 shows the relative energies of the clusters with the varying geometries for each of these clusters. We find the ground state for these doped clusters to retain a C_{2v} geometry, with the lone exception being Al_3N which has a D_{3h} ground state. However, we do note that both the D_{3h} and C_{3v} geometries reside very close in energy to the ground state for the Al_3P cluster much like that found in the studies by Archibong and St-Amant [157].

Figure 5.2.2 shows the molecular orbitals of the C_{2v} and D_{3h} geometries of the Al_3P cluster with the subsequent one electron levels. In the D_{3h} cluster, if one were to assign orbitals based on symmetry point groups and character tables, the HOMO, HOMO-1, HOMO-2, and HOMO-3 would be assigned as $1d_{xz}$, $1d_{yz}$, $1p_z$ and $1d_{z^2}$ respectively. This appears to be slightly different from the C_{2v} case, where the HOMO, HOMO-1, HOMO-2 and HOMO-3 can be assigned as $1d_{z^2}$ or $2s$, $1d_{xz}$, $1p_y$, and $1d_{z^2}$. However the similarity is in the assignment of d -orbitals in both the D_{3h} and C_{2v} geometries which led to the question: Could the stability and emergence of aromatic character be understood within a deformation of the three-dimensional jellium to a two-dimensional one?

Table 5.2.1 Relative Energies for the Al₃M (M = N, P, As, Sb, and Bi) clusters in the C_{2v}, D_{3h} and C_{3v} geometries.

	Relative Energy (eV)		
	C _{2v}	D _{3h}	C _{3v}
Al ₃ N	--	0	1.07
Al ₃ P	0	0.17	0.27
Al ₃ As	0	0.42	0.44
Al ₃ Sb	0	0.84	0.82
Al ₃ Bi	0	1.02	0.98

To answer this question, we begin by revisiting the jellium model in three-dimensions. In Chapter 1 we were introduced to the idea of using a jellium like potential to solve the Schrodinger equation, which resulted in electronic levels much like those found in atoms. The spherical jellium model (SJM) ultimately brought forth “magic” numbers. This was followed with the two-dimensional jellium model, which has proven to be successful for many cluster systems (See Chapter 1). The attraction to this model is not only rooted in the concreteness of the quantum physics used in its derivation, but in the fact aromaticity has at times been intertwined as a characteristic as well. If we now attempt to apply the 2-D jellium model to the mixed systems here, it appears to fall short. This lies in the cluster having a total number of valence electrons (14) that does not correspond to a “magic” number within the 2-D model. However, I would like to point out the two-dimensional jellium model may not completely fail, if the Al atom is assumed to behave monovalently.^J The resulting interaction would allow for the electron count to correspond to a magic number in the 2D model, if one were to also assume

^J It has previously been reported that for aluminum clusters smaller than seven, they behave monovalently instead of trivalently.

the Group 15 atoms only had three valence electrons, as pointed out in 2001 by Leskiw and co-workers. This idea is not the case in these clusters as evidenced through symmetries and molecular orbital shapes. So the question remains, can the jellium model truly be used to explain the stability of the planar 14-electron system and the manifestation of the aromatic character?

The lack of success in using both the spherical and 2-D jellium models to understand the stability found in these planar systems was initially somewhat surprising. However, it may be more valid approach to view this problem from a physical description. Let us begin from the structure and ultimately the free electron gas in three-dimensions and continue to a representation in two-dimensions. The levels of a free electron gas in three dimensions (spherical) allows for the molecular orbitals to form along the z-axis or contain a z-component. For example, the p -orbitals in three dimensions contain a p_x , p_y , and p_z component giving rise to three degenerate p -orbitals in a spherical free electron gas. If one were to now confine or disturb the spherical free electron gas to two dimensions, the molecular orbital volume in the z-direction (p_z orbital) would be displaced or confined to two-dimensions appearing oblate or prolate in shape. This type of distortion within the jellium picture, would have three primary effects, 1) the orbitals with z-component would appear smashed or delocalized, with the other orbitals appearing slightly confined; 2) any orbital along the z-axis would rise in energy from its three-dimensional energy; and 3) the number of electrons needed to be a stable cluster would be altered due to the splitting of the levels induced by this distortion. In fact, this is the picture formed from the ellipsoidal jellium shell model.

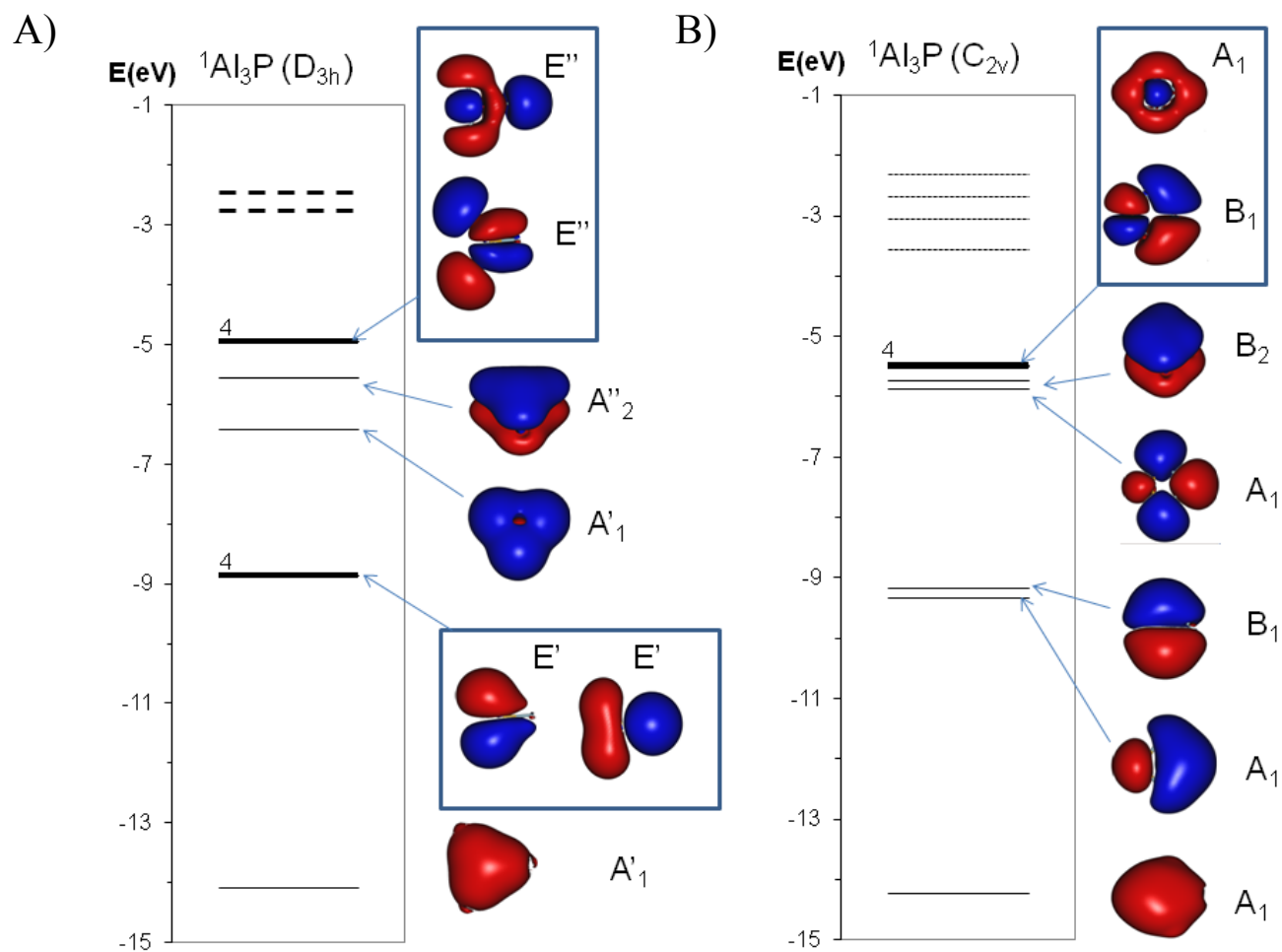


Figure 5.2.2 One-electron levels and molecular orbitals isosurfaces with symmetry assignments for the Al_3P cluster. The molecular orbital isosurfaces (isovalue = 0.01 a.u.) and levels for the D_{3h} geometry (Panel A) and the C_{2v} geometry (Panel B) structures are given. The solid and dashed lines represent the occupied and unoccupied levels, respectively. The superscripts indicate spin multiplicity. The degeneracy is assumed to be 2, unless otherwise noted.

In order to investigate if the ellipsoidal picture can be used to explain the stability and ultimately the aromatic character, we turn to the C_{3v} and D_{3h} geometries for the Al_3N cluster. Figure 5.2.3a shows the molecular orbitals and one electron levels in the C_{3v} geometry of the Al_3N cluster. The C_{3v} geometry is a three-dimensional compact structure, which allows for the one-electron levels to be ordered within the spherical jellium model. The levels proceed to fill as follows, $1s^2 1p^6 2s^2$ and $1d^4$, for a total of 14 electrons in the three-dimensional system. (The switching of the $2s$ and $1d$ levels can occur and is seen when studying doped clusters.) Now, by simply going from the C_{3v} spherical cluster to the two-dimensional D_{3h} cluster (Figure 5.2.3b), the p_z level rises in energy 2.66 eV and the orbital shape becomes “oblate” in nature. Indeed, this seems to agree with the ellipsoidal jellium model and seems to explain the manifestation of the delocalized p -orbital. We find this to be true for each of the D_{3h} structures. However, we wondered would also be the case for the transition to the C_{2v} ground state structures as well.

Figure 5.3.4 shows the one-electron levels with the molecular orbital isosurfaces for the both the C_{3v} and C_{2v} geometries in the Al_3Sb cluster. We find a similar electronic orbital order seen in the previous C_{3v} structure. However, the C_{2v} geometry shows a slight difference. The Al_3Sb cluster with C_{2v} geometry has orbital symmetries with assignments that contain a z -component. Not only do we see these unexpected z -components, but the split between the p_z and p_x, p_y orbitals is missing. Instead, we see the p_y -orbital separate from the $1p_z$ and $1p_x$ orbitals, but the delocalization is still prevalent with the p_y -orbital. These results appear to point towards an eminent failure for the ellipsoidal jellium model; however, these results bring up two questions: 1) Why do we see the expected split in the p -orbitals, but in the y -direction? 2) Why do we see a z -component in the C_{2v} case, but not in the D_{3h} case? In order to gain insight into both of these questions, we must first think about symmetry in a cluster and/or molecule.

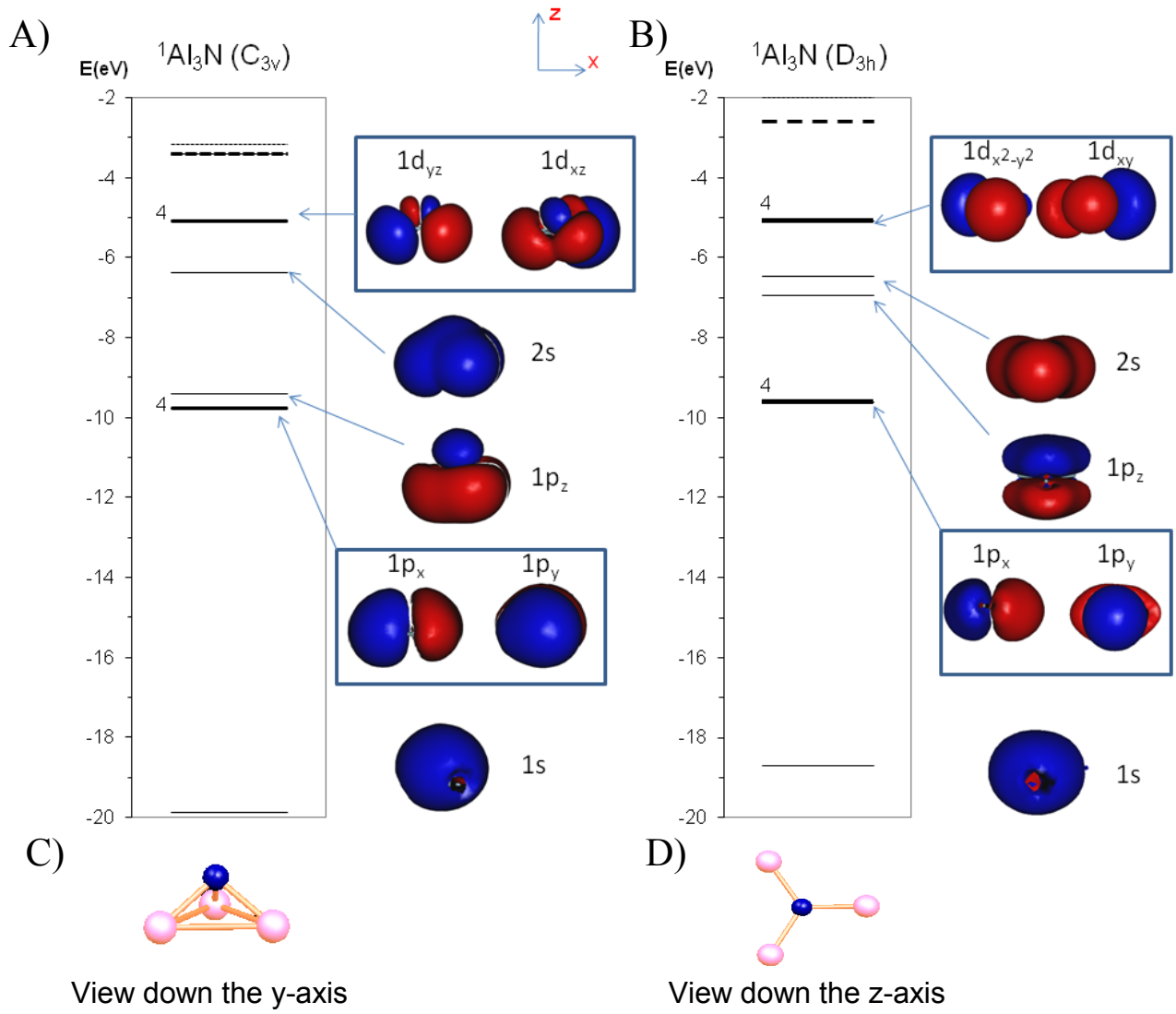


Figure 5.2.3 One-electron levels, molecular orbital isosurfaces (isovalue = 0.01 au) and geometries for the Al_3N cluster with C_{3v} (Panels A and C) and D_{3h} (Panels B and D). Each orbital is labeled with its representation. The Cartesian axis is given as a reference for the molecular orbitals. The pink and blue balls represent the Al and N atoms, respectively. For further information refer to Figure 5.2.2.

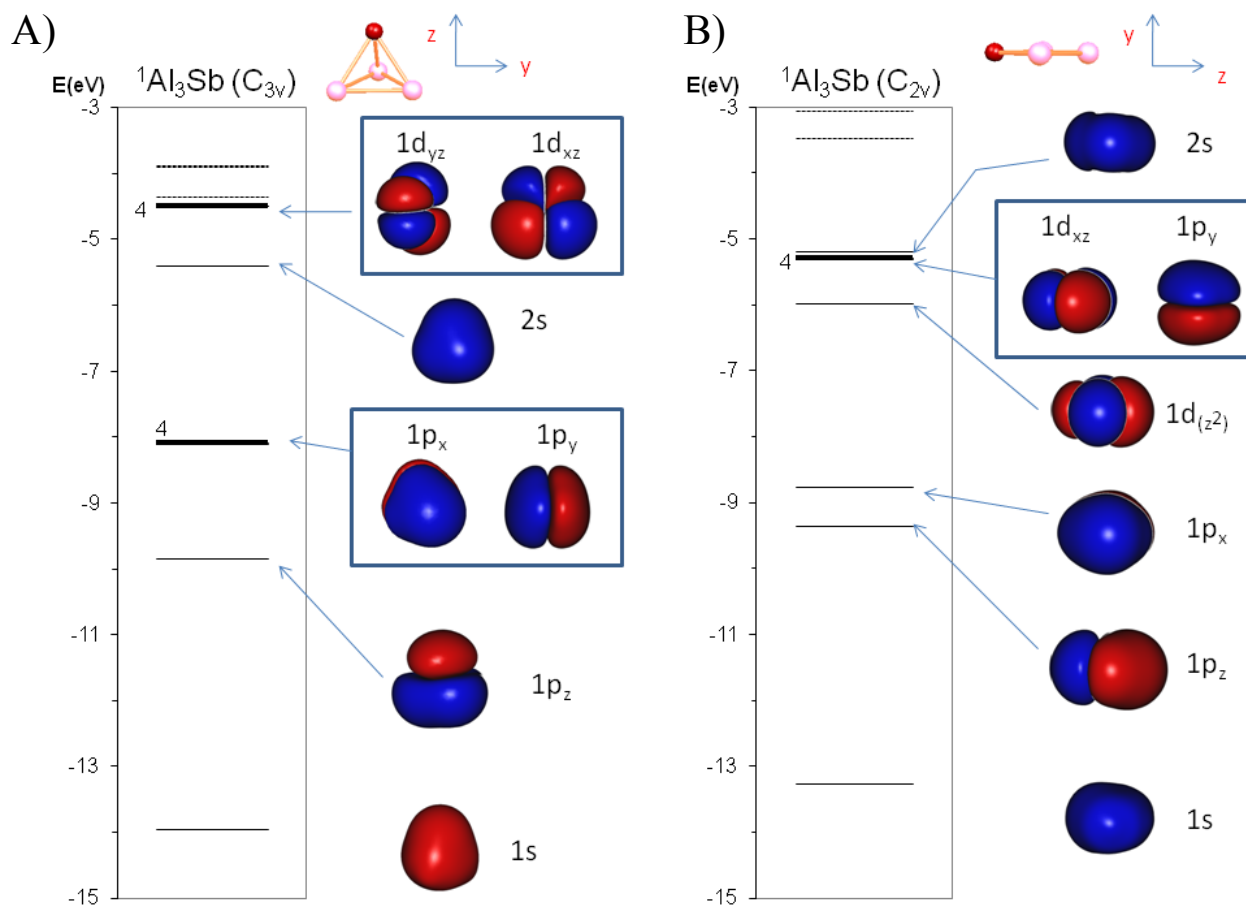


Figure 5.2.4 One-electron levels, molecular orbital isosurfaces (isovalue = 0.01 au) and geometries for the Al_3Sb cluster. The geometries and isosurfaces for the C_{3v} and C_{2v} geometries are given in Panel A and Panel B respectively. The red and pink balls represent the Sb and Al atoms respectively. For further information, please refer to Figure 5.2.3.

Symmetry in a cluster or molecule is based upon the principle axis. In order to determine the principle axis one must first look at the orientation of the cluster and determine the axis of rotation. The principle axis is then designated as the z-axis in the cluster geometry of interest. This implies that the z-axis would change depending upon the cluster geometry. However, this is contrary to the ellipsoidal jellium model. The ellipsoidal jellium model is dependent upon the z-axis remaining the same. If this were the case, clusters with a z-axis aligned in a similar manner would result in similar orbital orientations as one proceeds from an initial geometry to another. For example, in both the D_{3h} and C_{3v} geometries for the Al_3N cluster, the z-axis is through the “center” of both geometries. In fact, the transition from the C_{3v} to the D_{3h} could be viewed as simply pushing the N atom down the z-axis, into the xy-plane with the three Al atoms. Thus, the change in orbital energy and splitting predicted by the ellipsoidal jellium model can be easily observed.

This is very different when comparing a cluster with the C_{2v} geometry to its C_{3v} counterpart. In the C_{2v} geometry, the z-axis is no longer north-south as it was in the C_{3v} geometry but east-west.^K As a result, the C_{2v} cluster resides in the xz-plane, implying three things; 1) any molecular orbital with a y-component in the C_{2v} geometry, would rise in energy (or split) from orbitals with x and z components; 2) the y-orbital would become smeared in appearance (i.e.- delocalized) and 3) orbitals with z-components would remain in the C_{2v} geometry. In fact, this is the case found in not only the C_{2v} geometry of the Al_3Sb cluster, but we find this to be the case for each of the C_{2v} Al_3M clusters in this study. This result poses two manners in which this result can be viewed. In the first manner, one could say the cluster proceeds from its C_{3v} geometry to the C_{2v} geometry in a prolate (compression along the y-axis)

^K The choice of principal axis is governed by the chosen software to run the cluster or molecule. As such, the reader should be made aware of this option in any software program when assigning orbitals based on symmetry in a code.

manner. The implication of which is that the ellipsoidal jellium model would be an unacceptable description, since the result would not correspond to 14 valence electrons. If instead one were to require the principle axis to be established in the center of the C_{2v} geometry, this would allow for the cluster to reside in the xy -plane; thus the jellium would behave oblate in nature. The result would change the orbital assignments between the y and z components. Thereby, giving the exact picture predicted by the ellipsoidal jellium model if compressed along the z -axis.

If the ellipsoidal jellium picture is a true description of these systems, one would expect to see some type of splitting in the d -states (and f -states) similar to what is expected in the p -states, modifying the degenerate character seen in the spherical model. In the Al_3As case (Figure 5.2.6), the occupied states resemble what one would expect, with the p_z -orbital being delocalized to the compression and residing 3.45 eV higher than the nearest $1p$ -state. The first two d -states observed, $1d_{x^2-y^2}$ and $1d_{xy}$, are located at the HOMO-1 and HOMO-3 positions. The next d -state is the LUMO+1 ($1d_{xz}$), with the LUMO+2 being assigned as the $1d_{yz}$ state, both of which are clearly separated from the HOMO states with the expected splitting (the LUMO resembles one of the $1f$ -states). However, there is one d -state remaining which we find residing 3.33 eV higher than the nearest d -state (LUMO+2). It is interesting to note, the separation between the p_x, p_y and p_z states (3.45 eV) is similar to the separation energy between the d -states (3.33 eV) in the Al_3As cluster. The similar values of the energy separation found in the electron levels is not just isolated to the Al_3As case, we find this to hold true for each of the Al_3M ($M = N, P, As, Sb,$ and Bi) ground state clusters (Table 5.2.2). The equivalent energetic separation between states is in agreement with the ellipsoidal jellium model and the idea of a distortion parameter on the potential.

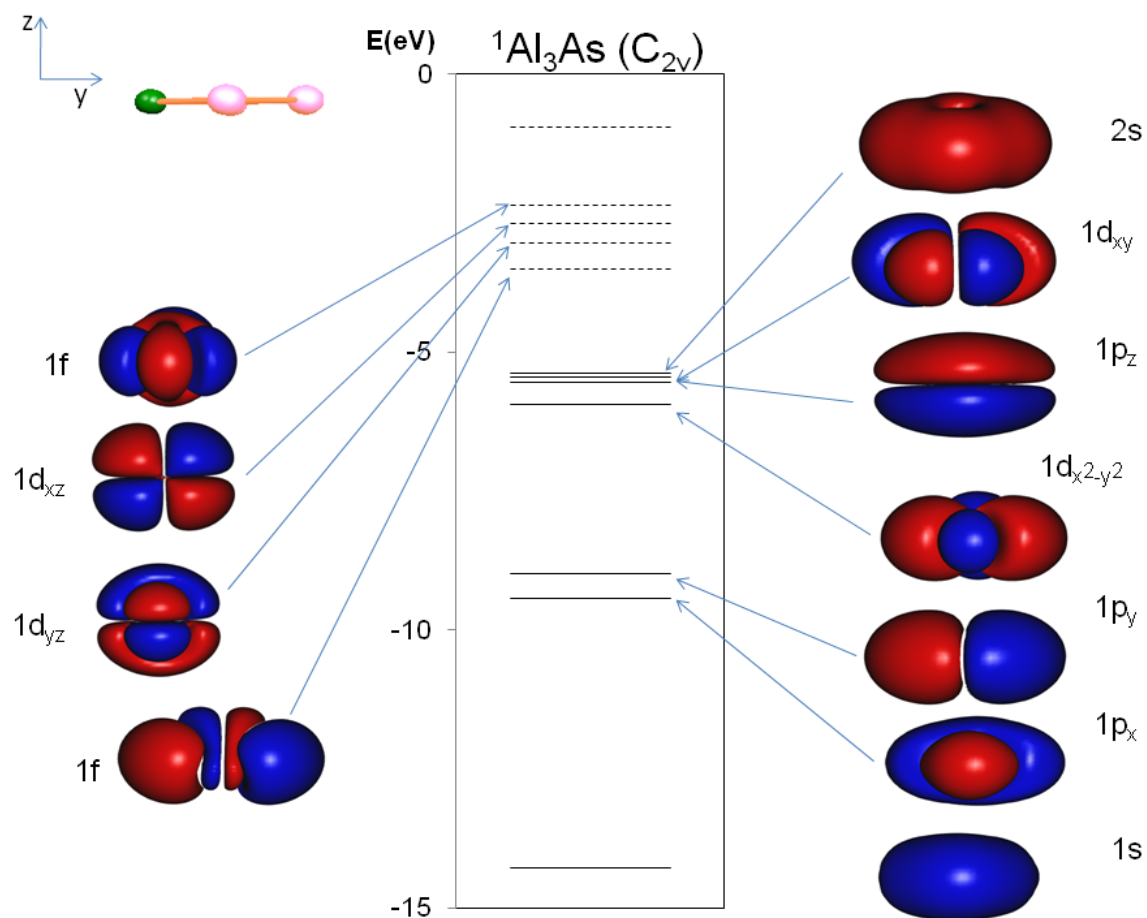


Figure 5.2.5 One-electron levels, molecular orbital isosurfaces (isovalue = 0.01 au) for the lowest energy Al_3As cluster. The green and pink balls represent the Sb and Al atoms respectively. For further information, please refer to Figure 5.2.4.

Table 5.2.2 The symmetry, separation energies of the p-states (ΔE_p), d-states (ΔE_d), and average (Avg.), with the HOMO-LUMO gaps (E_{gap}) for the ground state Al_3M ($\text{M} = \text{N}, \text{P}, \text{As}, \text{Sb}, \text{and Bi}$) clusters (in eV).

M	Symmetry	ΔE_p	ΔE_d	Avg.	E_{gap}
N	D_{3h}	2.66	2.44	2.25	2.50
P	C_{2v}	3.43	3.35	3.39	1.92
As	C_{2v}	3.45	3.33	3.39	1.87
Sb	C_{2v}	3.48	3.33	3.41	1.73
Bi	C_{2v}	3.49	3.29	3.39	1.69

Indeed, the idea of all-metal aromatic as a way to describe stability based on the two criteria established by organic chemist appears at first to be a viable explanation for the stable behavior observed in many planar inorganic systems. However, another classification is found in the ellipsoidal jellium model. The ellipsoidal jellium model (EJM) predicts a stable closed shell when the number of electrons in a cluster system that is oblate in nature is 14, which corresponds to the number of valence electrons found in the clusters studied here (Al_3N , Al_3P , Al_3As , Al_3Sb , Al_3Bi) and even the Al_4^{2-} cluster initially reported by Li and co-workers [43]. Further evidence from the molecular orbital diagrams, character tables and one-electron levels, support the EJM as the preferred model. The similar separation values obtained through the splitting of the *p*- and *d*- states for the D_{3h} and C_{2v} geometries further confirm this picture. We believe these results show that the aromatic character (i.e.- delocalization of orbitals) found in planar metallic systems is a manifestation of the compressed three-dimensional nearly free

electron gas. These results show the importance of the ellipsoidal jellium model in understanding of stability for planar inorganic clusters.

5.3 Chapter 5 Summary

In utilizing density functional techniques, we have identified a group of stable planar bimetallic neutral clusters. The Al_3 cluster when doped with a Group 15 atom, tends to show stability due to its large HOMO-LUMO gap, energy gain and ionization potential calculations. First, we investigated the idea of all-metal aromaticity as the source of the stable behavior. The requirements of all-metal aromaticity were explored and appeared to agree with this stability description for the Al_3As , Al_3Sb and Al_3Bi clusters. As an alternate approach, evidence was given to question the idea of all-metal aromaticity by labeling molecular orbitals through the use of character tables for the commonly found symmetries when extending the study to include the remaining Group 15 elements (N and P). In the exploration of all of the Al_3M clusters ($M = N, P, As, Sb, \text{ and } Bi$), little evidence was given to support the use of the spherical and two-dimensional jellium models as the source of stability in these systems. However, by investigating the physical transformation from a three-dimensional structure in the nearly free electron gas to a planar two-dimensional structure, the framework was given for an explanation of the all-metal aromatic construct. The physical transformation could be interpreted as compressing the jellium from spherical to oblate down the z -axis. This results in the loss of degeneracy within the electronic levels and, as predicted by the ellipsoidal jellium model, clusters with 14 valence electrons would show stable behavior. Furthermore, the appearance of delocalized molecular orbitals can be understood through the distortion of the spherical nearly free electron gas. The Al_3As , Al_3Sb and Al_3Bi clusters are strong candidates for cluster assembly due to their stable nature.

Chapter 6 Stability Analogous to Zintl Polyanions: Zintl Analogue Clusters

From the introduction, it is known that there are groups of polyatomic anions of post-transition metals and semimetals that are readily defined as Zintl Ions. These clusters each have been structurally identified through experiment for hundreds of years. Many of the more well known Zintl Ions include, Pn_7^{3-} , E_5^{2-} , and E_9^q where $Pn = P, As, Sb$, $E = Si, Ge, Sn, Pb$, and $q = 1 - 4$ [158 - 160]. Zintl polyatomic ions are heavily reliant upon their electron count, which in turn assist in determining the geometry due to polyskeletal theory. Now, it is proposed the class of Zintl clusters can be extended to the heteroatomic bismuth-tin system using first principle calculations and gas phase experiments.

6.1 Sn_nBi System ($n = 1 - 9$)

One of the most studied Zintl ions are tin clusters or stannides. The vast class of clusters has grown and provided insight, along with its alloys, on various aspects in nanoscience and technology [161 - 162]. Since the electron count in the Zintl stannide system plays a significant role in the stability of these clusters, a question emerges: Can one maintain similar geometry configurations by simply changing one atom (i.e.-using a dopant) that retains number of electrons needed to fulfill Wade-Mingos rules? In order to assess this intriguing question, theoretical calculations were performed to determine the geometries, electronic structure and energetics of $Sn_nBi^{0/-}$ ($n = 1 - 9$) clusters using the density functional formalism. The method incorporated the exchange and correlation effects within the GGA functional proposed by Becke and Perdew (BP86). The atoms were represented by a quadruple- ζ basis with polarization functions (QZ4P) with an all electron calculation. Relativistic effects were accounted for using

the ZORA method described previously. All calculations, including excited states, were performed using ADF.^L

The theoretical method was verified using previous studies and the collected PES values for the SnBi⁻ dimer. The optimized distance in this study for the SnBi⁻ dimer was 2.65 Å. It is identical to the theoretical value obtained by Sun et. al [163]. Using the optimized dimer values for the ADE and VDE were compared to the values from experiment. The optimized dimer theoretical value is much larger than the experimentally obtained dimer. However, the hot environment of the experiment will allow for some isomers. Therefore we attempted excited states to verify each of the experimental peaks in the collected spectra for the dimer. The excited states for the VDE values (i.e- VDE2 and VDE3) can be seen in Table 6.1 and show relative good agreement with the dimer experimental values, therefore the method is deemed acceptable.

Figure 6.1 shows the global minimum structures for the Sn_nBi⁻ clusters (n = 2 - 9). The structures obtained for BiSn⁻, BiSn₂⁻, BiSn₃⁻, BiSn₄⁻ and BiSn₅⁻ are in agreement with the ones previously reported by Sun and co-workers. Notice that in most cases the structures are highly symmetrical, the exception being BiSn₇⁻. The BiSn₄⁻ cluster has C_{3v} symmetry, while the BiSn₅⁻ has C_{4v} symmetry, which resemble the Zintl clusters Sn₅²⁻ and Sn₆²⁻. In fact upon closer investigation all of the bismuth doped tin clusters show the same geometrical shapes as their Sn_n²⁻ counterparts. It is interesting to note that for the Sn₄Bi⁻ and Sn₅Bi⁻, the bismuth atom has a coordination number of four, however for the larger cluster sizes the coordination number increases to five. In an effort to verify the theoretical structures were the ground state structures, we employed negative photodetachment experiments.

^L Refer to Chapter 3.

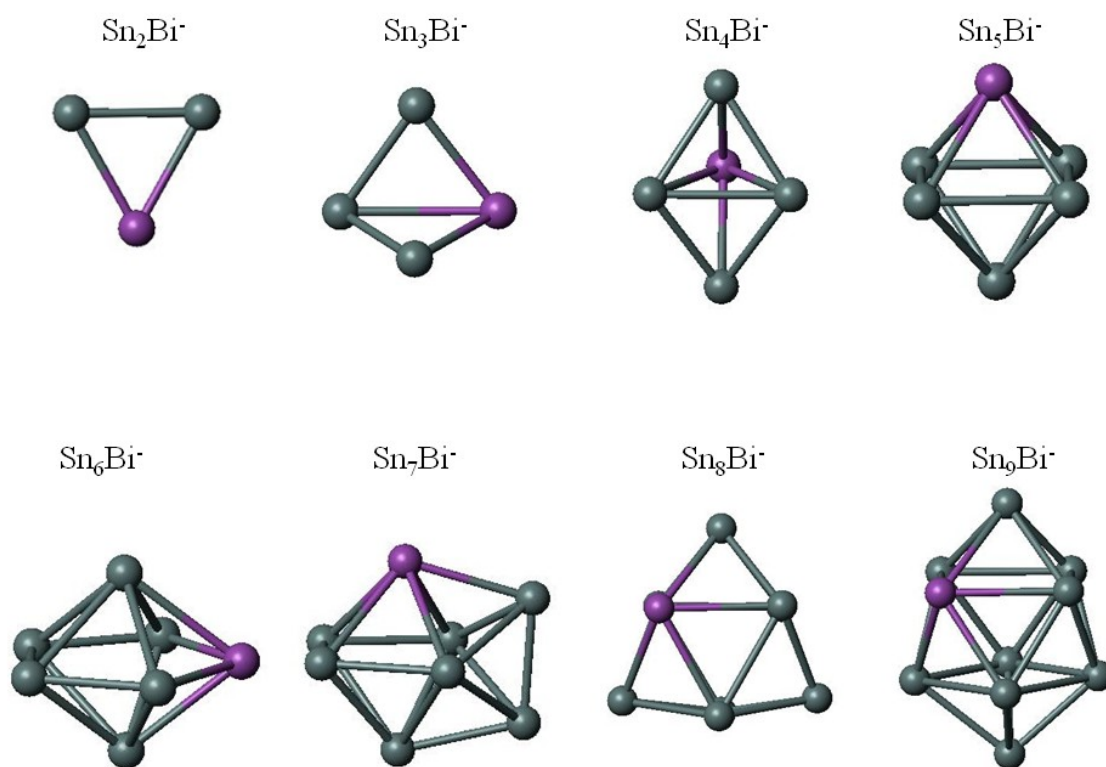


Figure 6.1.1 Lowest energy structures for Sn_nBi^- clusters ($n = 2 - 9$). The gray and purple balls represent the Sn and Bi atoms respectively.

In brief, the Sn_xBi_y^- clusters were formed by using a 1/4" 50:50 molar ratio Sn-Bi molded rod in a laser vaporization source, experimentally. For more information please refer to reference 74.^M The resulting mass spectra can be seen in Figure 6.1.2. The photodetachment electron spectra collected yields information on the electron detachment energies of each species and the values can be seen in Table 6.1 along with the theoretical values for the adiabatic and vertical detachment energies. The difference between the theoretical and experimental values for many of the clusters falls within the margin of error.

^M For further information please refer to Chapter 2.

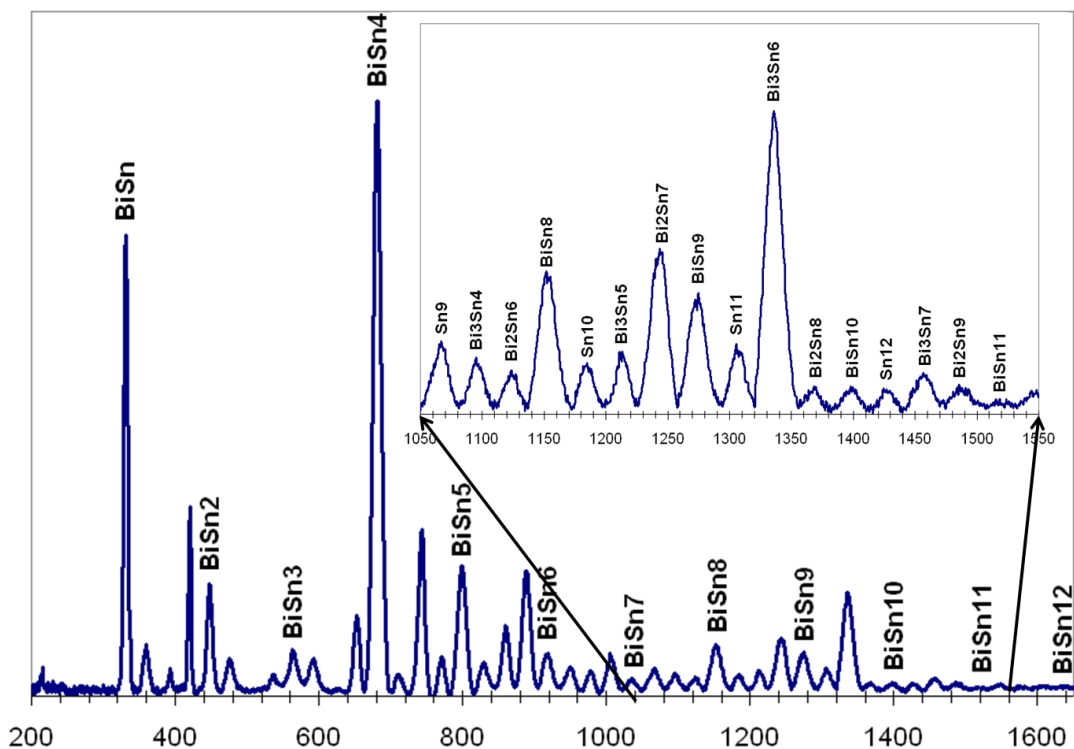


Figure 6.1.2. Collected mass spectra of Sn_nBi^- clusters. The insert is a magnified portion of the tin-bismuth anionic clusters.

The photodetachment electron spectra collected yields information on the electron detachment energies of each species and the values can be seen in Table 6.1 along with the theoretical values for the adiabatic and vertical detachment energies. The difference between the theoretical and experimental values for many of the clusters falls within the margin of error.

We now turn our attention to the energetics of the clusters in this study. First let us look at determining the stability of a cluster. One indicator of stability in clusters is through the energy gain, via,

$$E(\text{Sn}) + E(\text{Sn}_{n-1}\text{Bi}^-) - E(\text{Sn}_n\text{Bi}^-).$$

Table 6.1. Theoretical and experimental adiabatic and vertical electron detachment energies, as well as the calculated HOMO-LUMO gaps for the Sn_nBi^- clusters. The theoretical VDE2 and VDE3 are excited state transitions (for more information please refer to the text). Experimental error is ± 0.1 eV for ADE and VDE; experimental error is ± 0.2 for VDE2 and VDE3. All energies are in eV.

	Experimental				Theoretical				
	ADE	VDE	VDE2	VDE3	ADE	VDE	VDE2	VDE3	Gap
1	2.10	2.36	2.64	3.56	2.44	2.51	2.59	2.93	1.87
2	2.20	2.39	2.87	3.26	2.19	2.22	2.95	3.30	1.01
3	2.55	2.81	3.01	3.31, 3.63	2.44	2.67	3.27	3.65	1.32
4	2.82	3.18	3.70		2.72	2.92	3.47	3.62	1.92
5	2.52	2.83	3.15	3.4	2.54	2.80	3.36	3.55	1.76
6	2.32	2.72	3.45		2.38	2.59	3.46	3.63	1.26
7	2.65	2.93	3.35	3.35	2.72	2.91	3.51	3.57	0.97
8	2.95	3.26	3.47	3.73	2.97	3.11	3.59	3.70	1.17
9	2.98	3.31	3.55	3.56	2.96	3.06	3.38	3.72	1.40

The calculated values for the energy gain of the Sn_nBi^- ($n = 1 - 9$) can be seen in Figure 6.1.3. From the figure, Sn_4Bi^- , Sn_6Bi^- and Sn_8Bi^- each show the largest gain in energy from the previous cluster sizes. The largest value for the energy gain is found when $n = 4$ for all of the clusters. This shows agreement with what was found in the mass spectra. Another measure of stability is verified through the HOMO-LUMO gap. Figure 6.1.3 shows the calculated values for

the HOMO-LUMO gaps in the Sn_nBi^- series. The Sn_4Bi^- cluster clearly has the largest HOMO-LUMO gap (1.9 eV); again illustrating the enhanced stability of the Sn_4Bi^- cluster. We now turn to understanding the stability through electron count and bonding.

First let us look at the effect of electron count by replacing a tin atom with a bismuth atom in the cluster. The tin atom has two s-electrons and two p-electrons in its valence shell ($5s^25p^2$) which is one less valence electron than the bismuth atom ($6s^26p^3$). One can simply view the bismuth atom as a negatively charged tin atom (Sn^-). This would mean by substituting one tin atom with a bismuth atom on pure tin clusters and adding an electron, the resulting tin-bismuth cluster would have the identical electron count Sn_n^{2-} clusters. Previous studies on Sn_n^{2-} clusters have shown these cluster have very interesting characteristics. Interestingly, Sn_n^{2-} clusters adhere to Wade's $2n + 2$ skeletal rule for bonding and show both anti- and pure aromaticity. We have seen through the geometry that these Sn_nBi^- clusters do show the same type of structures and adhere to Wade's rules; however, one wonders if the electronic structure and aromatic characteristics of the Sn_nBi^- clusters mimic those of the Sn_n^{2-} .

To investigate the similarities between Sn_n^{2-} and Sn_nBi^- clusters, we give the isosurfaces of the molecular orbitals in Figure 6.1.4 for the Sn_4Bi^- and Sn_5^{2-} clusters. For the Sn_4Bi^- cluster, the HOMO, HOMO-1, HOMO-2, HOMO-3, HOMO-4 and HOMO-5 are virtually identical to those found in Sn_5^{2-} . Notice that the HOMO-5 in both cases is a sigma orbital, whereas the others can be considered *pi*-orbitals in the two clusters. One can also see, the number of bonding orbitals for both the Sn_5^{2-} and Sn_4Bi^- clusters. The Sn_4Bi^- cluster has five vertices and a *closo* geometry as predicted by the Wade-Mingos rules.

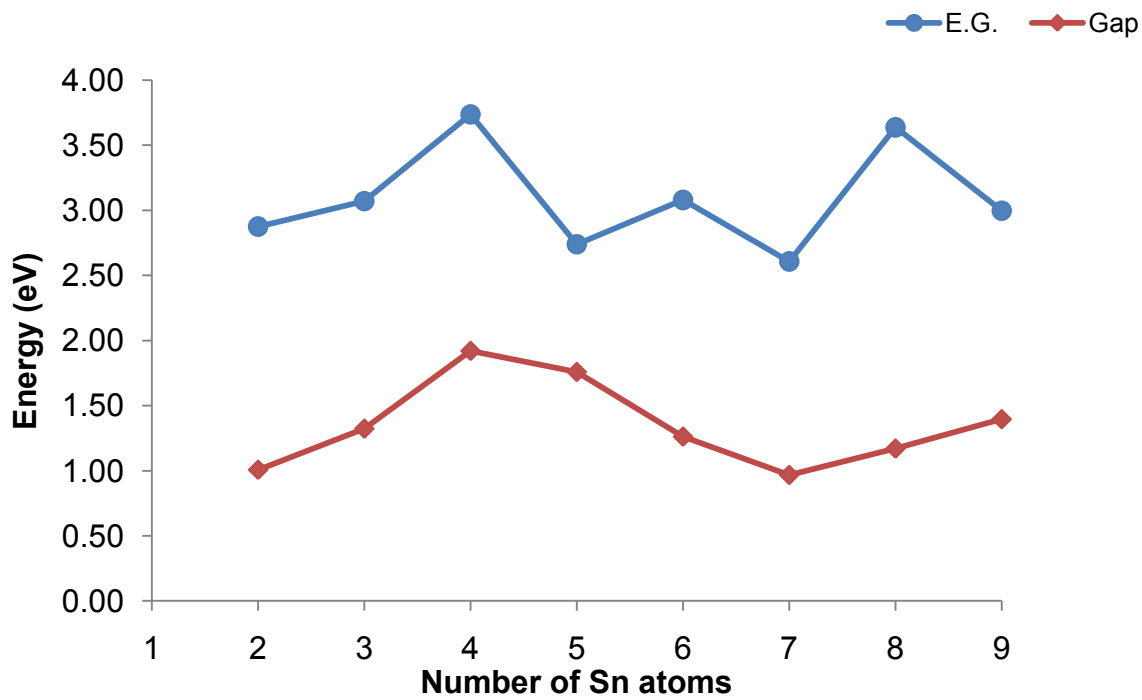


Figure 6.1.3 Plot of the energy gain (E.G.) and HOMO-LUMO gap (Gap) for the Sn_nBi - clusters ($n = 2 - 9$).

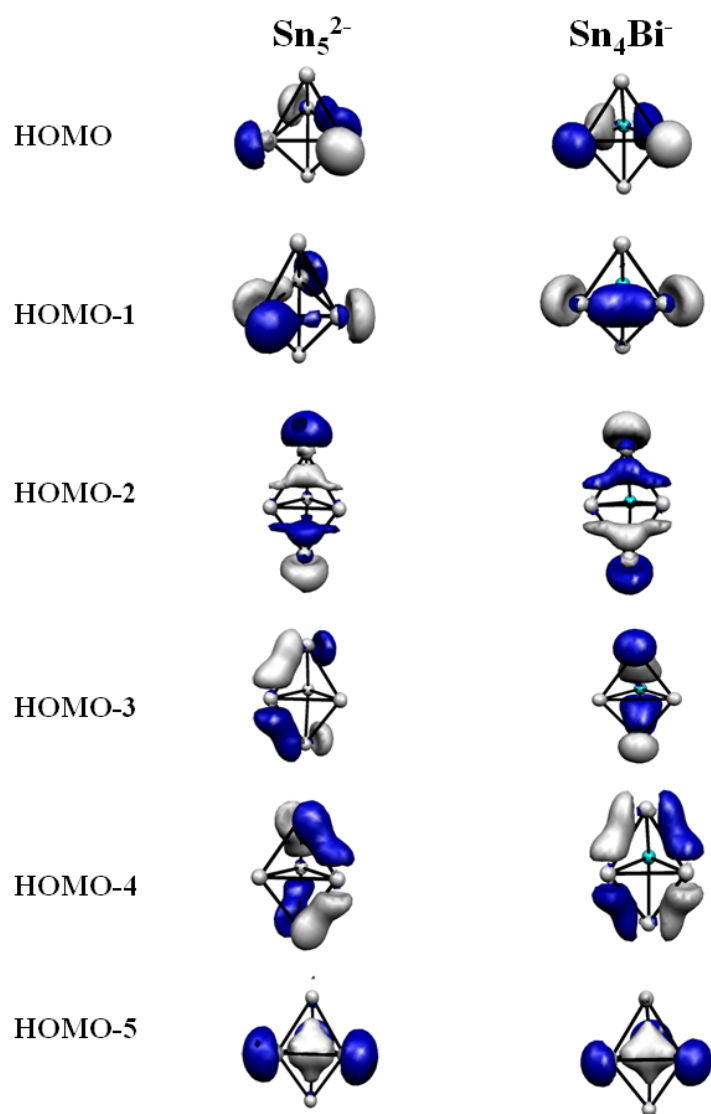


Figure 6.1.4 Isosurfaces of the molecular orbitals for Sn_4Bi^- and Sn_5^{2-} . The white balls represent Sn atoms and the blue ball represents the Bi atom.

Table 6.1.2. NICS (0) values for Sn_nBi^- , Sn_{n+1}^{2-} and Ge_{n+1}^{2-} where $n = 4 - 9$. All NICS values are in ppm.

	Sn_nBi^-	Sn_{n+1}^{2-}	Ge_{n+1}^{2-}
4	-26.9	-26.4	-33.4
5	16.7	14.5	14.3
6	-11.7	-2.5	0.4
7	-6.6	-4.2	-5.3
8	-33.4	-33.4	-39.2
9	-29.3	-39.3	-51.9

Multiple studies have been carried out on the aromatic and antiaromatic character seen in Zintl dianions of Group 14 clusters. Schleyer et al. showed Si_n^{2-} clusters have both aromatic and antiaromatic character. Chen and co-workers furthered this endeavor by showing both the Sn_n^{2-} and Ge_n^{2-} clusters illustrate the same behavior. Since the Sn_nBi^- are isoelectronic to the aforementioned dianions, we investigated the possibility of aromatic and anti-aromatic character of the identified Sn_nBi^- clusters. We carried out a nucleus independent chemical shift (NICS) analysis within the ADF software package. As explained in the previous section, if the cluster is aromatic it will have a diatropic (negative) value and if a cluster is antiaromatic it will have a paratropic (positive) value. Table 6.1.2 contains the determined NICS values for all the Sn_nBi^- clusters as well as those previously reported by Chen and co-workers. The Sn_4Bi^- , BiSn_6^- , BiSn_8^- and BiSn_9^- all have negative NICS values, indicating each of those clusters are aromatic. Remarkably, BiSn_5^- has an overall paratropic NICS(0) value and thus is considered antiaromatic. Immediately one can see the bismuth doped negatively charge tin clusters follow the same trend

as doubly charged Zintl clusters. The aromatic and anti-aromatic character in the Sn_nBi^- cluster shows these clusters can indeed be considered Gas Phase Zintl analogues, however the question remaining is where exactly does the aromatic character originate in the three-dimensional cluster system?

To answer this question, we performed a NICS analysis of the individual molecular orbitals (MO-NICS) using the ADF software package on Sn_4Bi^- and Sn_5Bi^- clusters. The one-electron levels and their NICS values are shown in Figure 6.1.5. The highly aromatic cluster BiSn_4^- has a positive value of 16.88 for its highest occupied molecular orbital (HOMO), indicating that the HOMO is antiaromatic in character (Figure 6.1.5A). However, the HOMO-1, HOMO-2, HOMO-3, etc. all have negative NICS values. The sum of the upper combination of *p*-electrons (-0.65 ppm), thus slightly aromatic. If one now adds in the high negative value of the lower electronic levels (-25.46 ppm), one sees the aromaticity originates from the s-electrons. This trend is similar in the antiaromatic cluster, Sn_5Bi^- . (Figure 6.1.5B) The lower levels still show aromatic character with a NICS value of -29.65 ppm, but the upper electronic levels are different than those from the Sn_4Bi^- cluster. The HOMO, HOMO-1, and HOMO-2 all are antiaromatic with values of 24.42, 24.42, and 24.32 ppm respectively. The total of these three levels alone amount to a dramatically larger paratropic value than the diatropic value obtained from the lower electronic levels. Thus, the antiaromatic value (16.71 ppm) evolves almost exclusively from the HOMO, HOMO-1 and HOMO-2 for this cluster. One can clearly see that the aromatic character seen in bismuth doped tin clusters primarily comes from the combination of the lower level electrons, whereas the antiaromatic character originates from the combination of upper (*p*) electrons.

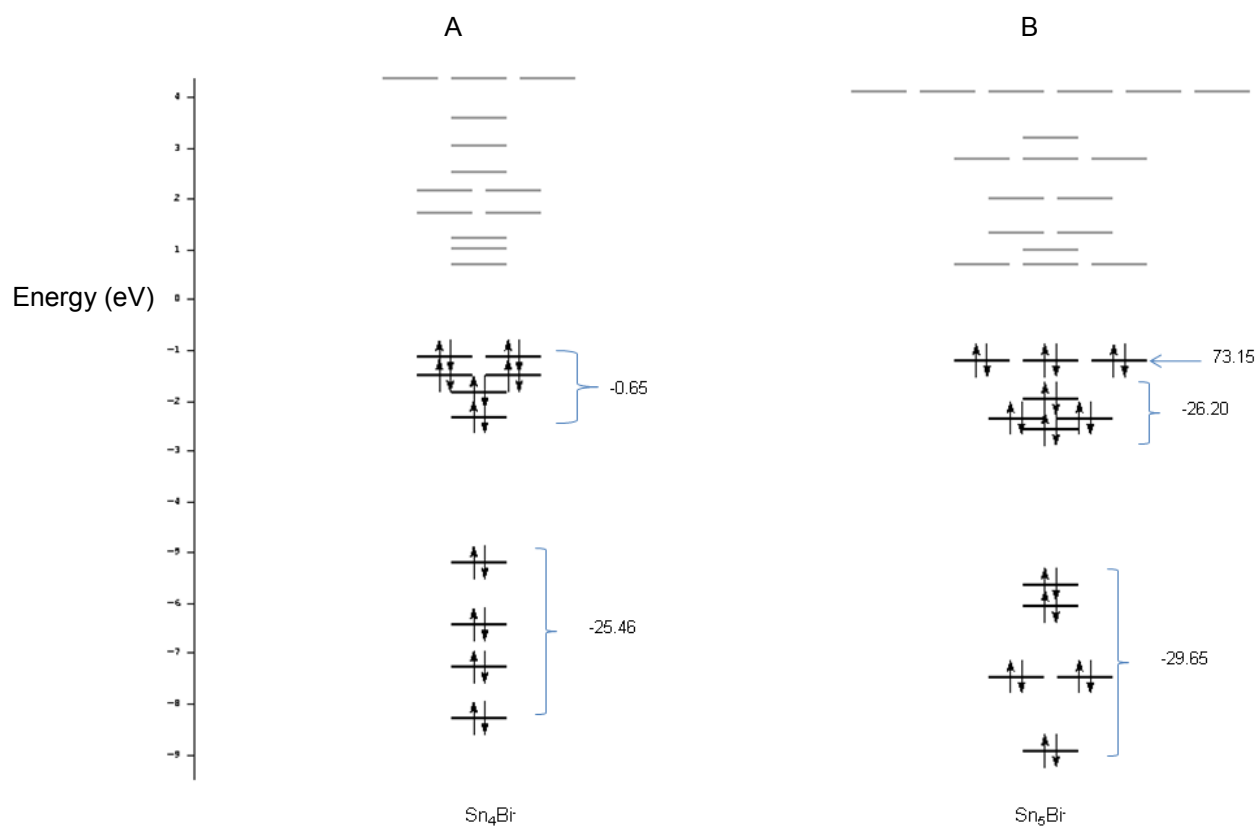


Figure 6.1.5 One-electron levels of Sn_4Bi^- (Column A) and Sn_5Bi^- (Column B). Molecular orbital NICS values are given for the group of molecular orbitals (in ppm).

From both experimental and theoretical calculations, doping pure tin clusters with one bismuth atom and adding one electron is a very effective way of maintaining similar electron counts in the system in designing stable clusters. The Sn_nBi^- clusters presented here are isoelectronic and have similar aromatic (antiaromatic) character as previously studied Sn_n^{2-} clusters. The Sn_4Bi^- has the largest HOMO-LUMO gap and large energy gain indicating the cluster is particularly stable compared to the other clusters in the series. The stable behavior of the Sn_4Bi^- cluster and geometry can be rationalized through Wade-Mingos rules for electron

counting and aromatic character, much like its Sn_5^{2-} Zintl Ion counterpart. Therefore, the Sn_4Bi^- cluster is a stable gas phase Zintl analogue that shows promise for cluster assemblies.

6.2 Sn_xBi_y^- System ($x + y = 9$): Deltahedral Gas Phase Zintl Analogues

As stated previously, using a bismuth atom as a dopant in pure tin clusters, can result in the ability to design stable gas phase Zintl cluster analogs. This discovery has sparked an interest in investigating a unique class of known Zintl clusters commonly seen in Zintl phases, deltahedral Zintl clusters. Deltahedral Zintl clusters are a special sub class of polyatomic clusters with geometries that are made up of triangular faces with nine-atoms. It is well known that Zintl clusters with deltahedral geometry can be found for many of the Group 14 elements. The first structurally characterized compound with a nine-atom deltahedral was Cs_4Ge_9 [112]. This discovery of Ge_9^{4-} in a solid opened the door to search for other deltahedral clusters and have resulted in many Group 14 deltahedral clusters.

The beauty and attraction of the deltahedral clusters is their ability to handle different charges with very small structural distortions. It has been shown that for germanium the lengthening and shortening of the edges involves very little energy, but can greatly affect the electronic structure. This affect can be seen in deltahedral tin clusters as well. Previous theoretical studies have indicated that the Sn_9^{4-} cluster has a square-antiprismatic ground state and represents a nido-type cluster. According to the Wade-Mingos rules, a closo (D_{3h}) cluster with n vertices exhibits enhanced stability for $2n + 2$ electrons while a nido (C_{4v}) cluster with n vertices exhibits enhanced stability for $2n+4$ electrons. From a valence point of view, each Sn atom contributes two p-electrons to the valence pool, thus the stability of Sn_9^{2-} and Sn_9^{4-} can be reconciled within such a simple model. It is also interesting to note that the nido- C_{4v} structure found for the Sn_9^{4-} cluster has a closely lying isomer with a closo- D_{3h} structure. This gives the cluster some structural fluxionality. The fluxional character is also shown by the Zintl anions Ge_9^{4-} and Pb_9^{4-} .

With the observation of the fluxional behavior of the deltahedral Zintl anions, one begins to question if this same behavior will be seen if one substitutes a Bi atom for a Sn atom in the nine-atom cluster. It has already been explained how the electron count can result in an isoelectronic species by using the Bi atom as a dopant in Sn clusters. However, now studies will be undertaken to see the effect of size difference, since the Bi atom is larger than the Sn atom, has on the fluxional behavior and the change on the electronic structure with the studies of the deltahedral Bi_xSn_y^- ($x + y = 9$) clusters.

It is important to understand the effect of charge on the fluxional behavior of the Sn_9^{-q} ($q = 1-4$) clusters with the D_{3h} and C_{4v} isomers. The lowest energy structures were obtained within symmetry constraint with their relative stability are shown in Figure 6.2.1. The D_{3h} structure is more stable in Sn_9^- , Sn_9^{-2} , and Sn_9^{-3} . However, for Sn_9^{-4} the D_{3h} structure differs from the C_{4v} structure by only 0.003 eV. Previous studies have shown that the polyatomic anion Sn_9^{-4} in the condensed phase exhibits D_{3h} and C_{4v} structures that can interconvert. The charge has a major effect on the fluxional behavior of the cluster. As shown in Figure 6.2.1, when the charge is reduced from -4 to -3, the C_{4v} structure is destabilized by about 0.33 eV relative to the D_{3h} structure. Further, as the charge is reduced from -2 to -1, the C_{4v} structure is destabilized by 0.18 eV compared to the D_{3h} structure. As expected, the D_{3h} structure for Sn_9^{-2} is much more stable, 1.02 eV lower in energy. The stability is a direct result of Wade-Mingos rules.

Multiply charged clusters are observed in the condensed phase, however the coulomb repulsion destabilizes the binding of multiple electrons in free clusters. This issue can be solved if one dopes the cluster with an atom resulting in an isoelectronic species. The doped tin clusters, Sn_6Bi_3^- , Sn_7Bi_2^- , and Sn_8Bi^- have the same number of electrons as Sn_9^{-4} , Sn_9^{-3} , and Sn_9^{-2} , respectively. It should be noted that the size of a Bi atom is larger than that of a Sn atom.

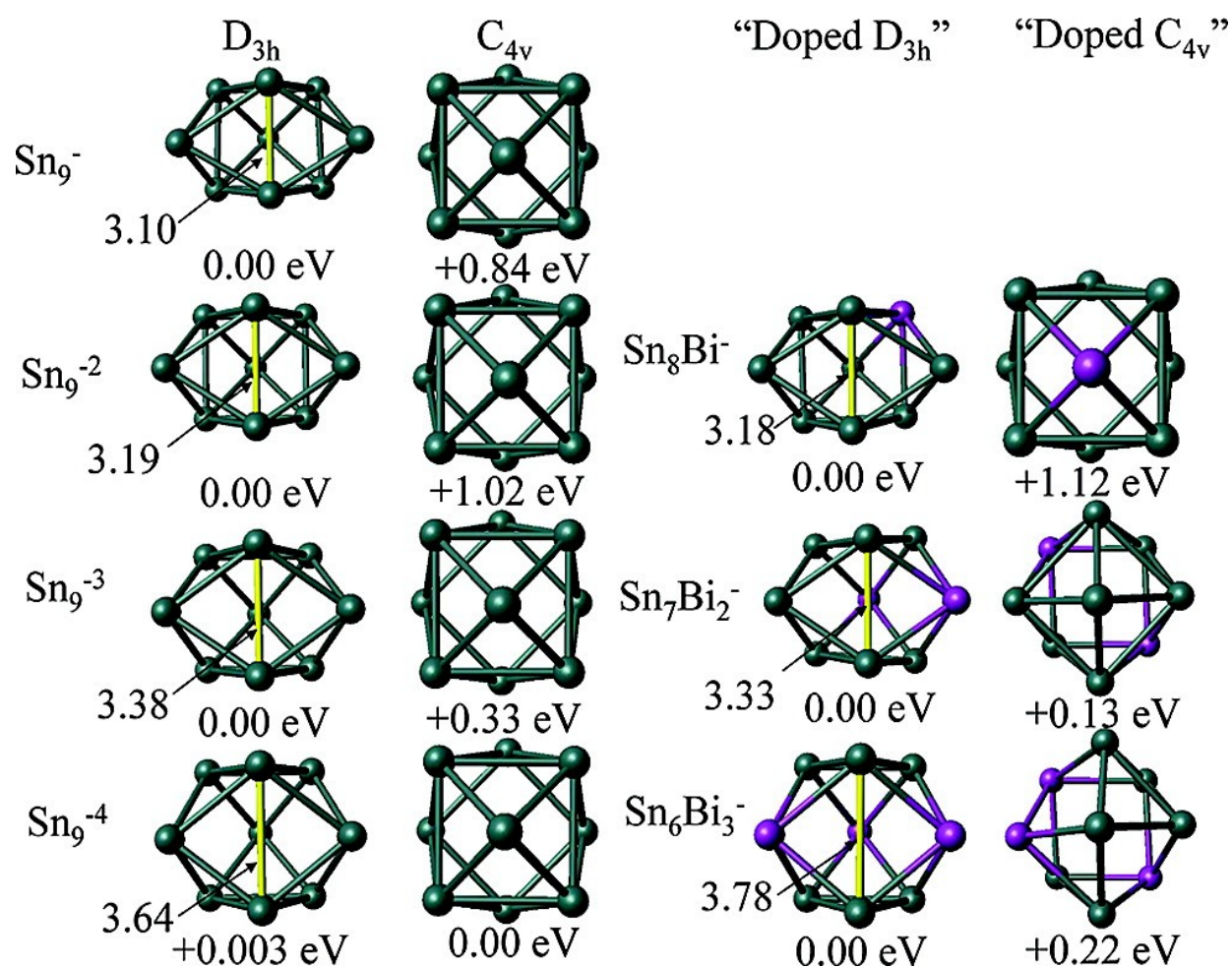


Figure 6.2.1 Comparison of the C_{4v} and D_{3h} structures for Sn_9^{-q} ($q = 1 - 4$) and $Sn_xBi_y^-$ ($x + y = 9$) clusters. The relative energies are given below each structure in electron volts. The gray and purple balls represent the tin and bismuth atoms respectively. Bond lengths are given in Angstroms.

Table 6.2.1. Experimental and theoretical values for the vertical electron detachment energies (VDE and VDE2), adiabatic electron detachment energies (ADE) and calculated HOMO-LUMO gap (Gap) and removal energies (R.E.) for the deltahedral tin-bismuth clusters (in eV). The values in parenthesis represent the experimental error.

	Experimental			Theoretical				
	VDE	VDE2	ADE	VDE	VDE2	ADE	Gap	R.E.
Sn ₈ Bi ⁻	3.26 (0.02)	3.47 (0.05)	2.95 (0.07)	3.11	3.19	2.97	1.18	3.64
Sn ₇ Bi ₂ ⁻	2.93 (0.07)	3.40 (0.07)	2.47 (0.11)	2.72	3.27	2.26	0.21	3.43
Sn ₆ Bi ₃ ⁻	3.25 (0.04)	3.63 (0.05)	2.96 (0.06)	3.04	3.61	2.92	2.25	3.60

the Sn₆Bi₃⁻, Sn₇Bi₂⁻, and Sn₈Bi⁻ clusters. The calculated AEDE and VDE values are in good agreement with the values obtained through experiment. As mentioned before, the vertical transitions provide a fingerprint of the geometrical structure, and the close agreement shows that the calculated structures match with experiment. Notice that the AEDE is higher for the Sn₈Bi⁻ and Sn₆Bi₃⁻ clusters, which should be expected, since they are analogues to the Sn₉⁻² and Sn₉⁻⁴ clusters which are particularly stable.

To examine cluster stability further we also calculated the energy required to remove a Sn or a Bi atom from the cluster, listed as ΔE_{Sn} and ΔE_{Bi} . Also shown in Table 6.2.1 are the Removal Energies (R.E.) calculated using the equation

$$\text{R.E.}(\text{Sn}) = E(\text{Sn}_{x-1}\text{Bi}_y^-) + E(\text{Sn}) - E(\text{Sn}_x\text{Bi}_y^-)$$

Here $E(\text{Sn})$ is the total energy of a Sn atom, $E(\text{Sn}_x\text{Bi}_y^-)$ is the total energy of the Sn_xBi_y⁻ cluster, and $E(\text{Sn}_{x-1}\text{Bi}_y^-)$ is the total energy of the cluster with one fewer Sn atom.

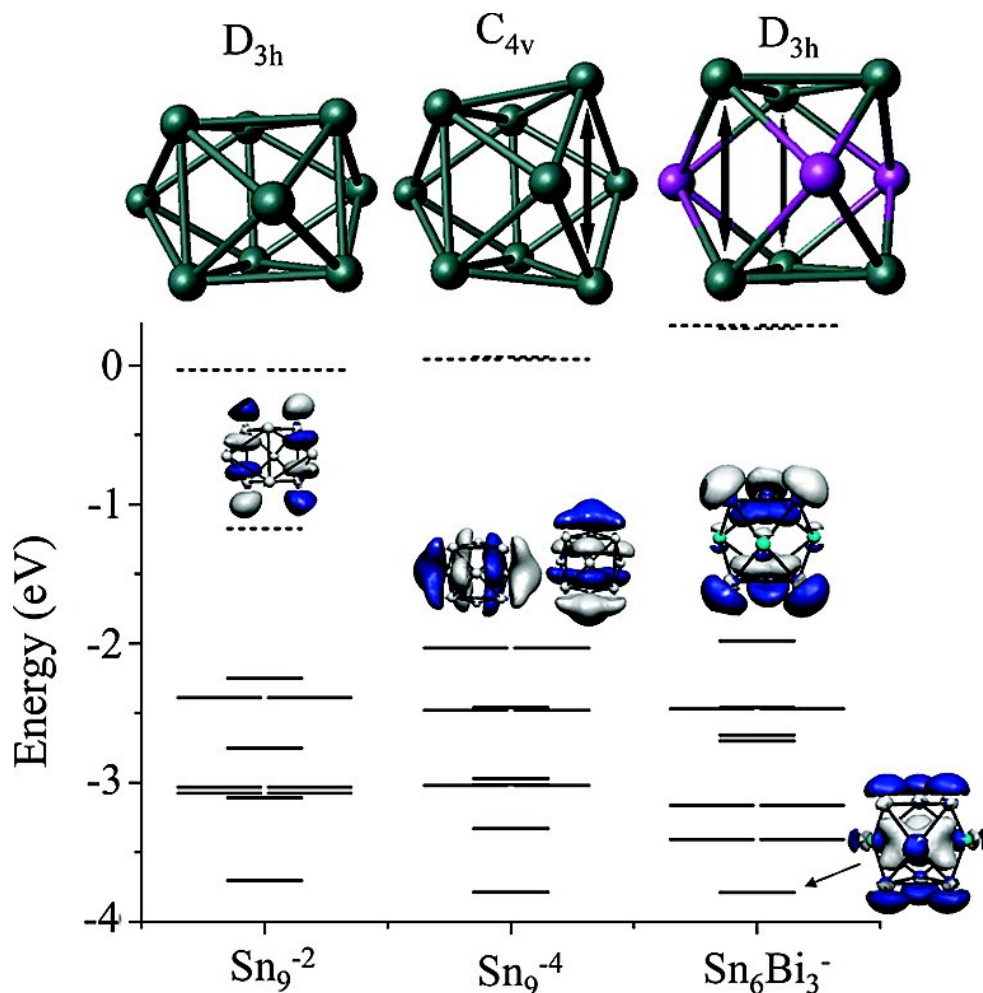


Figure 6.2.2 One-electron levels for the Sn_9^{-2} , Sn_9^{-4} , and Sn_6Bi_3^- .

Since stability of the deltahedral clusters have been successfully verified, we now turn our attention to the features of the some of the electronic structure of these systems. Figure 6.2.2 shows the one electron levels in Sn_9^{-2} , Sn_9^{-4} (C_{4v}), and Sn_6Bi_3^- . The continuous lines represent the occupied states while the dashed lines represent the unfilled p-states. The p-orbitals normal to the cage can form π -orbitals which is different from the expected Wade-Mingos structures. This interaction may lead to spherical aromaticity (which was explained previously) while the other orbitals form skeleton molecular orbitals. To show this more explicitly, the charge density distribution in the most stable electronic orbital, which corresponds to an overall π -bonding

orbital is shown in Figure 6.2.2. The next orbitals are either σ or composed of a mixture of σ -like and π -like. In the case of Sn_9^{-2} , the manifold of the skeleton orbitals is separated by the LUMO that has π -bonding in the top and bottom triangles leaving a node in the middle. Since the LUMO in Sn_9^{-2} is separated substantially from the LUMO+1, another stable species could be formed if the LUMO state could possibly be filled by the addition of two electrons. This in fact is exactly what happens in the pure Sn case with the Sn_9^{-4} cluster. Now, by adding three Bi atoms to form Sn_6Bi_3^- one can accomplish a similar effect. As shown in Figure 6.2.2, the cluster exhibits a large HOMO-LUMO gap.

Here, the deltahedral Sn_6Bi_3^- , Sn_7Bi_2^- , and Sn_8Bi^- clusters behave much like their deltahedral Zintl counterparts. These clusters are isoelectronic and illustrate the fluxional behavior found in the E_9^{q-} ($\text{E} = \text{Ge}, \text{Pb}, \text{and Sn}; q = 1 - 4$) clusters previously studied. The Sn_6Bi_3^- has the largest HOMO-LUMO gap (2.2 eV). Each of the deltahedral clusters were shown to be stable gas phase Zintl analogue clusters through experimental and theoretical verification and are candidates for cluster assemblies.

6.3 Stable Zintl Analogues using Counteranions

Typically, Zintl clusters in known Zintl phases incorporate the use of counteranions such as a crypt, crown, or various Group 1 atoms. Therefore, it is logical to use these well-known counteranions in order to stabilize the neutral counterparts to the aforementioned Zintl analogue clusters for assemblies. However, current advances have been made in functionalizing deltahedral clusters with organic functional groups in the solid state, which may be advantageous to pursue. Hull and Sevov have functionalized the Ge_9^{4-} cluster in experiment using alkynes and alkyl halides [165 – 166]. These studies have extended to the deltahedral Sn_9^{4-} cluster as well. Using alkyl chlorides and alkynes, Chapman and Sevov were able to synthesize the first tin-based deltahedral organo-Zintl ions, such as $[\text{Sn}_9\text{-CH=CH}_2]^{3-}$ in the solid state [167]. Kocak and coworkers reported that both the C_{4v} and D_{3h} structures for the deltahedral cage were found for RSn_9^{3-} anions using NMR. These authors proposed two mechanisms for exchange for the fluxional anions, which they found to be dependent upon the substituent [168].

The excitement produced in the new class of organo-Zintl clusters has prompted this study using the deltahedral gas phase Zintl Sn_xBi_y clusters ($x + y = 9$). Recall, that the heteroatomic Zintl clusters, Sn_6Bi_3^- , Sn_7Bi_2^- , and Sn_8Bi^- are analogous to the Sn_9^{4-} , Sn_9^{3-} and Sn_9^{2-} Zintl clusters and were successfully synthesized through gas phase synthesis. With the similarities between the heteroatomic Sn_xBi_y^- clusters and pure tin Zintl clusters, we now embark upon designing stable organo-Zintl clusters using these gas phase Zintl analogue clusters (GPZC) through a purely theoretical approach using the addition of a R-group, such as ethene or propene, to the heteroatomic deltahedral Sn_xBi_y ($x + y = 9$) clusters and compare those structures to those stabilized through the more conventional Group 1 counteranion.

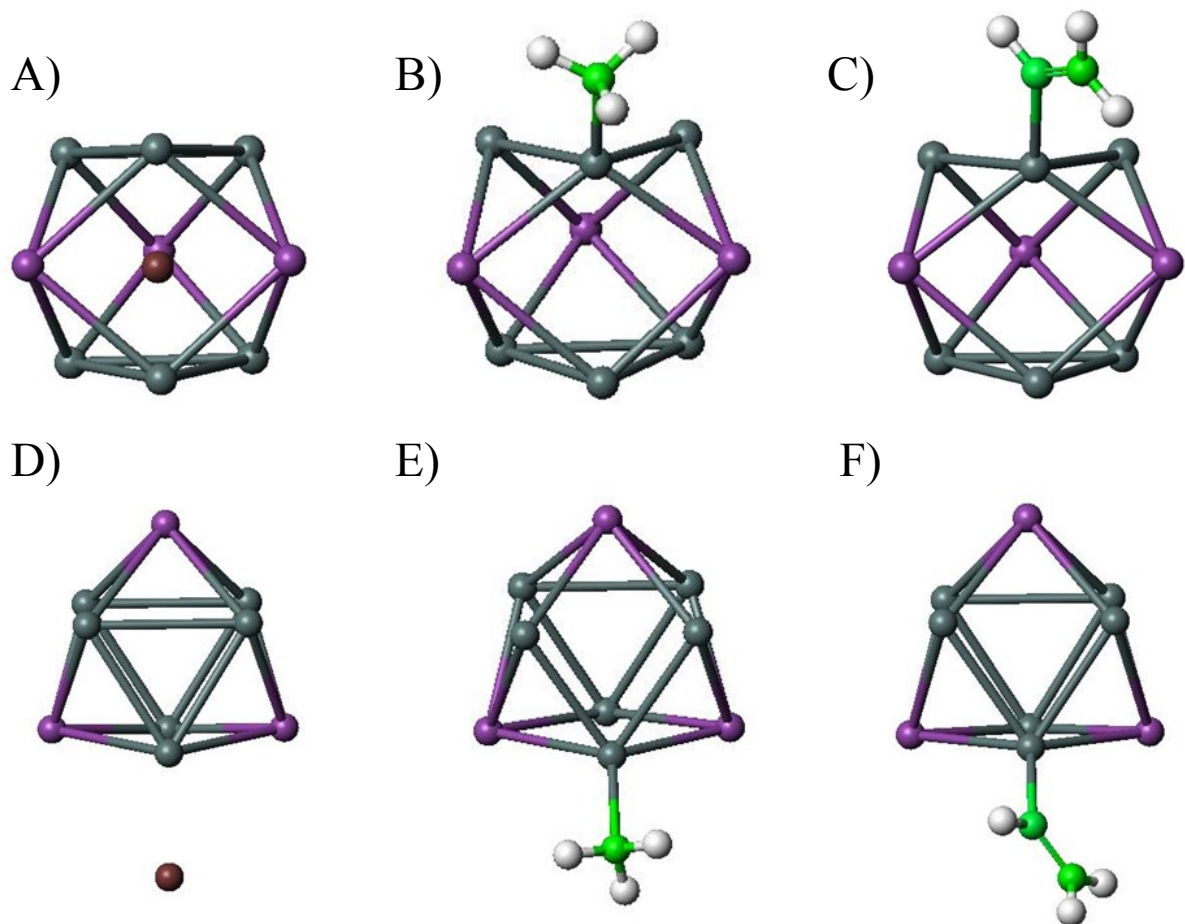


Figure 6.3.1 Optimized geometries of KSn_6Bi_3 (Panels A and D), $\text{Sn}_6\text{Bi}_3\text{-CH}_3$ (Panels B and E) and $\text{Sn}_6\text{Bi}_3\text{-C}_2\text{H}_3$ (Panels C and F) clusters.

First we look at the effects of using the Group 1 countercation to stabilize the Sn_6Bi_3^- cluster. The simplest case is the neutral cluster Sn_6Bi_3 is one electron short of becoming stable with 22 electrons like the Sn_9^{4-} Zintl cluster. The Sn_6Bi_3 anionic cluster was previously reported to have a gap size of 2.2 eV and a ground state geometry of D_{3h} with the three bismuth atoms residing at the each of the three vertices. Figure 6.3.1 shows the ground state geometries for the KSn_6Bi_3 cluster as an example.

Table 6.3.1 The calculated HOMO-LUMO Gap, Binding Energies (B.E.), electron affinities (E.A.) and parent cluster symmetries for Sn_6Bi_3^- , $\text{ASn}_6\text{Bi}_3^-$ (A = Na, K, and Cs), and $\text{Sn}_6\text{Bi}_3\text{-R}$ (R = CH_3 and C_2H_3).

	Gap	B.E.	E.A.	Symmetry
Sn_6Bi_3^-	2.16	n/a	2.98	D_{3h}
NaSn_6Bi_3	1.99	2.08	1.37	D_{3h}
KSn_6Bi_3	2.03	2.16	1.25	D_{3h}
CsSn_6Bi_3	2.06	2.11	1.26	D_{3h}
$(\text{Sn}_6\text{Bi}_3)\text{CH}_3$	1.88	1.90	1.79	pseudo- D_{3h}
$(\text{Sn}_6\text{Bi}_3)\text{C}_2\text{H}_3$	1.88	2.08	1.87	pseudo- D_{3h}

The Group 1 atom resides on the exterior of the cluster for the ASn_6Bi_3 clusters (A = Na, K, and Cs). The parent cluster (Sn_6Bi_3), in the ASn_6Bi_3 cluster has a D_{3h} geometry, which is the same as the Sn_6Bi_3^- cluster. However, the HOMO-LUMO gap for the ASn_6Bi_3 cluster shows a slight drop from the anionic Sn_6Bi_3 cluster to 2.0, 2.0, and 2.1 eV for Na, K, and Cs respectively. Equally as important for the determination of stability, is the binding energy of the counteraction to the cluster. Table 6.3.1 shows the binding energies for the Na, K, and Cs atoms. Notice that the KSn_6Bi_3 cluster has the highest binding energy, but each of the ASn_6Bi_3 cluster have a binding energy of over 2 eV.

Next we turn our attention to the organo-Zintl cluster $\text{R-Sn}_6\text{Bi}_3$, where the R groups are either a methyl ($-\text{CH}_3$) or ethyl ($-\text{C}_2\text{H}_3$) group. The binding energy of the R group to the cluster is approximately 2 eV, which is almost identical to the binding energies for the alkali atom case (Table 6.3.1). The HOMO-LUMO gaps of these R-group ligated clusters are lower than the bare

Sn_6Bi_3 anion and the ASn_6Bi_3 clusters. We hypothesize that the nature of this change is most likely due to the covalent nature of the R-group. The alkali atom easily donates its electron to achieve a closed atomic shell to the deltahedral cluster. However, the R group would not behave in an ionic nature but its covalent behavior with the cluster would result in the possible lowering of the HOMO-LUMO gap.

The geometry of the cluster seems to change slightly depending on the choice of counteraction. The pure Sn_6Bi_3^- cluster has D_{3h} symmetry with the C_{4v} structure residing +0.22 eV higher in energy. Once the alkali counter cation is added to the Sn_6Bi_3 cluster, the cluster retains the D_{3h} symmetry as the lowest energy structure. With the addition of an R group, such as CH_3 or C_2H_3 , the cluster becomes slightly distorted and has a pseudo- D_{3h} symmetry. It is interesting to note the Sn-C bond length for the clusters here are 2.2 Å, which is similar to what is found for the pure tin organo-Zintl clusters found previously [167-168]. This fluxional behavior appears to be dependent upon the counteraction of choice.

Since the alkali counter cations align themselves upon a face of the Sn_6Bi_3 cluster, it is advantageous to look at the sites where the organic counteractions bind. There are two primary sites, a Bi atom on the apex or Sn atom on the cluster, upon which the R groups can attack; we look at the case of $-\text{C}_2\text{H}_3$ for comparison. If the ethyl-group is attached on the Bi apex of the cluster, the HOMO-LUMO gap is 1.40 eV and the binding energy is 1.54 eV. However, when the R group is attached on a Sn site, the structure resides 0.55 eV lower in energy. This is accompanied by an increase in both the gap (1.88 eV) and binding energy of the $-\text{C}_2\text{H}_3$ group (2.08 eV). The cluster geometry also changes as well. The lowest energy structure, has a pseudo- D_{3h} geometry, however if the R-group binds to the Bi site, the parent cluster retains a D_{3h} geometry. This is accompanied by a slight inversion, with the Sn atom extending to the apex.

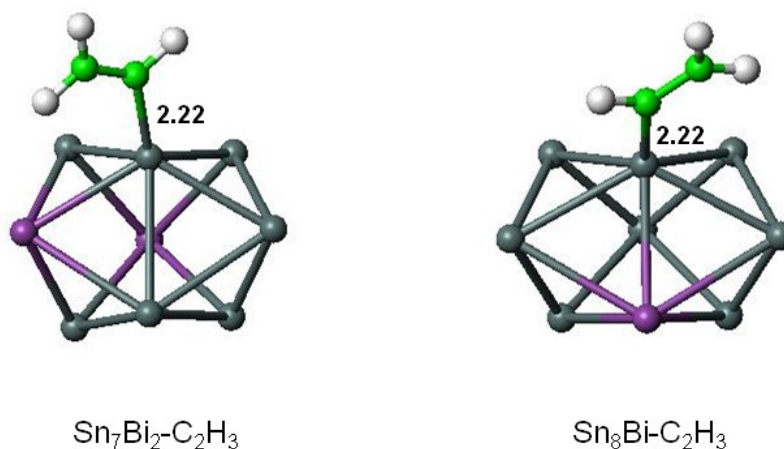


Figure 6.3.2 Lowest energy structures for the $\text{Sn}_7\text{Bi}_2\text{-C}_2\text{H}_3$ and $\text{Sn}_8\text{Bi-C}_2\text{H}_3$ clusters. The bond length between the $\text{-C}_2\text{H}_3$ and the parent clusters are given in Angstroms.

These results show that the R group prefers the Sn site on the cage for the Sn_6Bi_3 cluster but the question remains what if the Bi atom were replaced with a Sn atom, would the R group prefer a Sn site on the apex?

To answer this question, we investigated the addition of $\text{-C}_2\text{H}_3$ to the deltahedral cluster Sn_7Bi_2 . This allows for three possible sites for attachment of the ethene group, a Bi atom, a Sn atom on the apex of the cluster, and the final site for possible attachment resides in the cage. Figure 6.3.2 shows the optimized structure for the $\text{Sn}_7\text{Bi}_2\text{-C}_2\text{H}_3$ cluster. Once the ethylene group is attached to the Sn_7Bi_2 cluster, we find the R-group behaves much like the previous case in the Sn_6Bi_3 cluster and prefers to bind to a tin site versus a bismuth site. The Sn_7Bi_2 cluster with the C_2H_3 group bound to the Bi site exhibits the C_{2v} geometry, with a slight inversion as seen in the previous case but resides 0.67 eV above the ground state structure. The Sn_7Bi_2 cluster with the C_2H_3 group bound to the Sn site at the apex of the cluster has C_{2v} geometry. However, the

lowest energy structure has C_s geometry with an additional Sn-Sn bond forming, but resides only 0.07 eV lower in energy than the Sn-C₂H₃ cluster with C_{2v} geometry. Here, the fluxional behavior is seen more prevalent than in the Sn₆Bi₃-R case.

The energy difference between the D_{3h} and C_{4v} geometries found in the Sn₇Bi₂ and Sn₆Bi₃ clusters with the addition of the C₂H₃ counteranion bring out several points on the possible fluxional behavior of deltahedral clusters. First, it is well known that the E_9^{q-} clusters ($E = \text{Si, Ge, Sn; } q = 2, 3, 4$) display fluxional behavior. For Sn_9^{q-} ($q = 2$ and 3), each of the clusters have a ground state geometry of D_{3h} ; yet, the D_{3h} and C_{4v} geometries for the Sn_9^{4-} geometry are degenerate and have been shown to interconvert in solid state materials [169]. One way to increase the overall stability of the D_{3h} cluster is by using an atom that is larger in size such as Bi. For instance, the energy difference between the D_{3h} and C_{4v} geometries increases by 0.22 eV if one replaces three tin atoms in the Sn_9^{4-} cluster with Bi and adding an electron to form the analogous $Sn_6Bi_3^-$. If now one uses the neutral Sn₆Bi₃ with a counteranion, such as an alkali atom or an organic substituent, the fluxional behavior is still reduced. However, by decreasing the amount of the dopant, the fluxional behavior becomes prevalent once again. It is also interesting to note that the organic ligands prefer to bond to the Sn sites on the cluster. This implies one can protect certain sites on a cluster simply by using a suitable dopant.

The deltahedral Zintl analogue clusters provide a unique opportunity for cluster assemblies. It has been shown that by using different counteranions such as alkali metals or organics the gap size for the stable cluster can vary to the desired size. Also, the fluxional behavior can be seen in the doped clusters when using an organic ligand. This advantage can be used to now build a new class of cluster assemblies based on deltahedral Zintl analogue clusters with different types of counteranions.

6.4 Chapter 6 Summary

Tin clusters have long been identified as Zintl polyatomic anions in various Zintl phases. We have shown through a combination of a first principle theoretical approach and gas phase experiments that by doping tin clusters with one bismuth atom one can design stable Zintl analogues. The tin-bismuth cluster Sn_4Bi^- showed stability through its HOMO-LUMO gap size, electron affinity, large removal energy and larger intensity in the mass spectrum. This cluster with high symmetry and unique bonding governed by Wade-Mingos rules was determined to relate to the polyanionic Zintl clusters like Sn_5^{2-} . The idea of Zintl analogues was then extended to the hetero-deltahedral clusters Sn_8Bi^- , Sn_7Bi_2^- , and Sn_6Bi_3^- . The clusters were reminiscent of the well known Zintl clusters Sn_9^{2-} , Sn_9^{3-} , and Sn_9^{4-} respectively. In order to use these clusters as building blocks, the neutral counterparts of the deltahedral Zintl analogues were combined with both alkali and organic counteranions to achieve stability. The geometries of the parent cluster retained its D_{3h} when using the alkali counteranion, however when using the organic substituents the geometry of the parent cluster changed significantly. We also discovered an organic counteranion, such as an ethyl group ($-\text{C}_2\text{H}_5$) preferred to form a bond on a Sn site on the deltahedral cluster. Further investigation reveal the organic counteranion formed a bond with a Sn atom not residing on the apex of the cluster, while the alkali atom aligned on a face of the deltahedral cluster. Also, the HOMO-LUMO gap was lower when adding a counteranion versus the anionic cluster. We propose the KSn_6Bi_3 cluster, which has a large HOMO-LUMO gap (1.88 eV), making it an ideal candidate for assembly.

Chapter 7 Forming Metallo-carbohedrenes: Triniobium- carbide Clusters

One interesting metal-carbide complex is that of niobium-carbide. It has been shown experimentally that variations in cluster source conditions lead to two dominant cluster structure types: the aforementioned Met-Cars and nanocrystallite species. Experimental studies carried out by Jarrold and coworkers revealed that fullerenes easily incorporate niobium atoms into their structure by replacing carbon atoms [170]. Harris and Dance used density functional calculations and predicted various structural motifs to be present in the Nb_xC_y species [171]. Wang and co-workers have made an extensive study of the electronic and vibrational properties of mono-niobium carbide clusters, NbC_n^- ($n = 2-7$) [172]. Using anion photoelectron spectroscopy, they observed two structure types: NbC_2^- and NbC_3^- were shown to have cyclic structures, NbC_6^- and NbC_7^- to have linear structures, and NbC_4^- and NbC_5^- to display evidence of both cyclic and linear isomers. In a more recent report, we showed that diniobium-carbon clusters also have evidence of linear isomers for odd numbered cluster species, along with planar rings and three-dimensional structures [173]. Metha and co-workers have carried out photoionization experiments and density functional studies on niobium-carbide clusters with the stoichiometries Nb_3C_n ($n = 1-4$), Nb_4C_n ($n = 1-6$), and Nb_5C_n ($n = 0-6$) [174 – 175]. In their studies, they report various structures consistent with the development of a face-centered cubic structure and structures with molecular C_2 units.

In an effort to understand the electronic structure and stability of $Nb_xC_y^-$ clusters and their role in formation of met-cars, we carried out density functional theory and photoelectron spectra to determine the structures and their stable isomers of $Nb_3C_n^-$ ($n = 5-10$) clusters. All calculations were performed using the density functional theory (DFT) code deMon2k explained in Chapter 3. The exchange and correlation effects were incorporated within the generalized gradient approximation (GGA) using the functional proposed by Perdew, Burke, and Ernzerhof (PBE). The niobium atoms were described by the 13-electron scalar quasi-relativistic effective core potential (QECP) proposed by Andrae et al. in combination with the LANL2DZ basis set, while the DZVP all electron basis set for the carbon atoms was used. For the C and Nb atoms the A2 and GEN-A2* auxiliary function were respectively used. All the isomers were fully optimized without any constraints, and a frequency analysis was performed to verify that the structure was a true minimum. The initial geometries for optimization were based on the structural triangular Nb_3 motif with the addition of carbon atoms in a variety of configurations. The carbon atoms were added to the Nb_3 triangular ring on either the “face” and/or edges. In order to describe the resulting structures, in the cases where only one carbon atom is added to the face, it is termed “capping”, while if either a chain of carbons, consisting of at least two carbon atoms, is added on the “face” they are termed “bridging”. In all of the initial geometries, either one carbon atom, C_2 , C_3 , and/or C_4 units were added to the Nb_3 motif. Our group and others have shown the C_2 and C_3 motifs are energetically favorable in various niobium-carbon structures. All the obtained low lying isomers were re-optimized using a larger aug-cc-pVTZ basis set for the carbon atoms that include diffuse functions along with the GEN-A2* auxiliary function set.^N

^N Refer to Chapter 3.

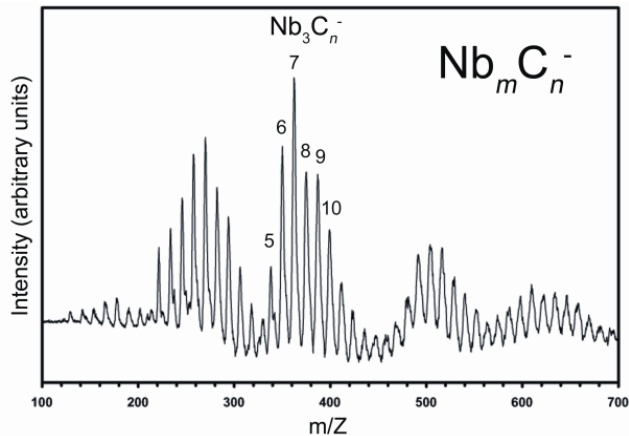


Figure 7.2 Mass spectrum of Nb_mC_n^- clusters formed. The Nb_3C_n^- clusters ($n=5-10$) examined in the present study are labeled.

In each of the geometries presented, the niobium-niobium bonds are drawn where only those with distances less than or equal to twice the covalent radius (2.74 \AA) are shown. However, Niobium-Carbon bonds are drawn at bond lengths of 2.25 \AA , which is longer than the covalent radius of the niobium and carbon atoms combined. This is done to emphasize the importance of the Nb-C bonds for the structures. The carbon-carbon bonds are drawn such that, single bond $> 1.40 \text{ \AA} >$ double bond $> 1.25 >$ triple bond.

The experiments on triniobium carbides Nb_3C_n^- ($n = 5-10$) were carried out using the apparatus explained in chapter 2. In short, Nb_3C_n^- anions are generated with a pulsed laser vaporization supersonic cluster beam source. The Nd:YAG laser (second harmonic) is focused down to a 2 mm spot on a rotating and translating pure niobium rod (0.25-in diameter). A mixture of methane seeded in helium gas is delivered in a short and intense pulse by a pulsed molecular beam valve mounted perpendicularly to the niobium rod. The CH_4 in the helium carrier gas reacts with niobium and cools in the laser-induced plasma to form Nb_mC_n^- clusters.

Table 7.1 Experimental (Exp.) adiabatic electron detachment energies (AEDE) and vertical electron detachment energies (VEDE) for Nb_3C_n^- ($n = 5 - 10$) observed features shown in Figure 2. The experimental uncertainty is about 0.2 eV.

	Exp. AEDE (eV)	Exp. VEDE (eV)
Nb_3C_5^-	1.88	2.30
Nb_3C_6^-	1.14	1.55
	1.74	2.20
	1.81	2.47
	2.48	3.03
Nb_3C_7^-	1.74	2.33
	2.80	3.31
Nb_3C_8^-	1.70	2.19
	2.45	2.99
	2.88	3.36
Nb_3C_9^-	1.43	2.01
	2.30	2.97
$\text{Nb}_3\text{C}_{10}^-$	2.36	2.79
	3.25	3.24
	3.25	3.42

The collected mass spectra for the Nb_mC_n^- clusters can be seen in Figure 7.1. The photoelectron spectra of Nb_3C_n^- ($n = 5-10$) at 308 nm (4.03 eV) are presented in Figure 7.2(A-F) with binding energy (in eV) plotted on the abscissa. These spectra portray electronic transitions from the anions to the ground state, and in some cases low-lying excited states, of the neutral product species. Table 7.1 gives the measured adiabatic electron detachment energy (ADE) and vertical electron detachment energy (VDE) for each experimentally observed anionic cluster isomer. Figure 7.2 shows multiple prominent features in the photodetachment spectra like those found in previous niobium-carbide clusters [173].

The multiple peaks within the spectra for clusters with six or more carbons could indicate the presence of multiple structural isomers present in the molecular beam. Their formation can be

attributed to the laser vaporization cluster source, which is capable of generating isomers that are higher in energy than the ground state structures, and in many cases their individual detachment energies are detectable in the spectra.

Figures 7.3 and 7.4 depict the ground state isomer structures determined using first principles theoretical techniques described in detail in the computational methods section. The vertical electron detachment energies (VDE) are also reported in the figures. The VDEs were determined theoretically by taking the difference between the energy of the ground state geometry of the anion and the energy of the neutral at the geometry of the anionic ground state. In each of the clusters, the determined spin multiplicity was a singlet; therefore the VDEs are the transitions between the singlet ground state of the anion and the doublet neutral cluster at the geometry of the ground state anion cluster.

The first cluster Nb_3C_5^- has C_{2v} symmetry and contains a three-membered niobium triangle, with bond distances of 2.63 Å, and a “capping” carbon. This tetrahedral base has two C_2 units in the “flanking” position, with C-C bond distances of 1.33 Å making double bond between them. This latter type of metal carbon bonding seems important in Met-Car precursors, where the MC_2 unit is thought to be a major building block.

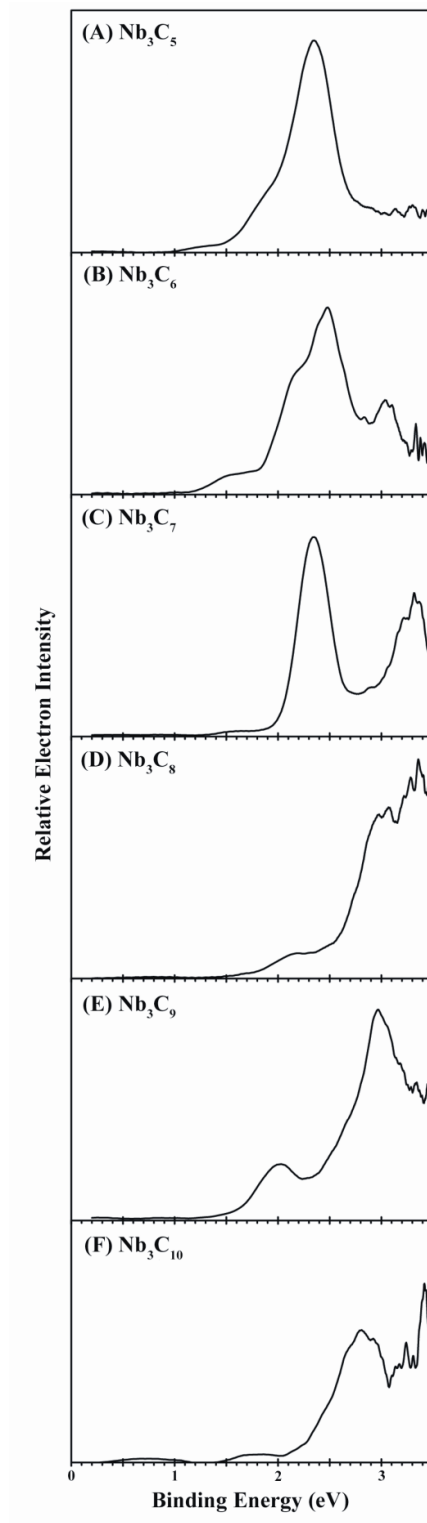


Figure 7.2 Anion photoelectron spectra of Nb_3C_n^- ($n = 5-10$) clusters.

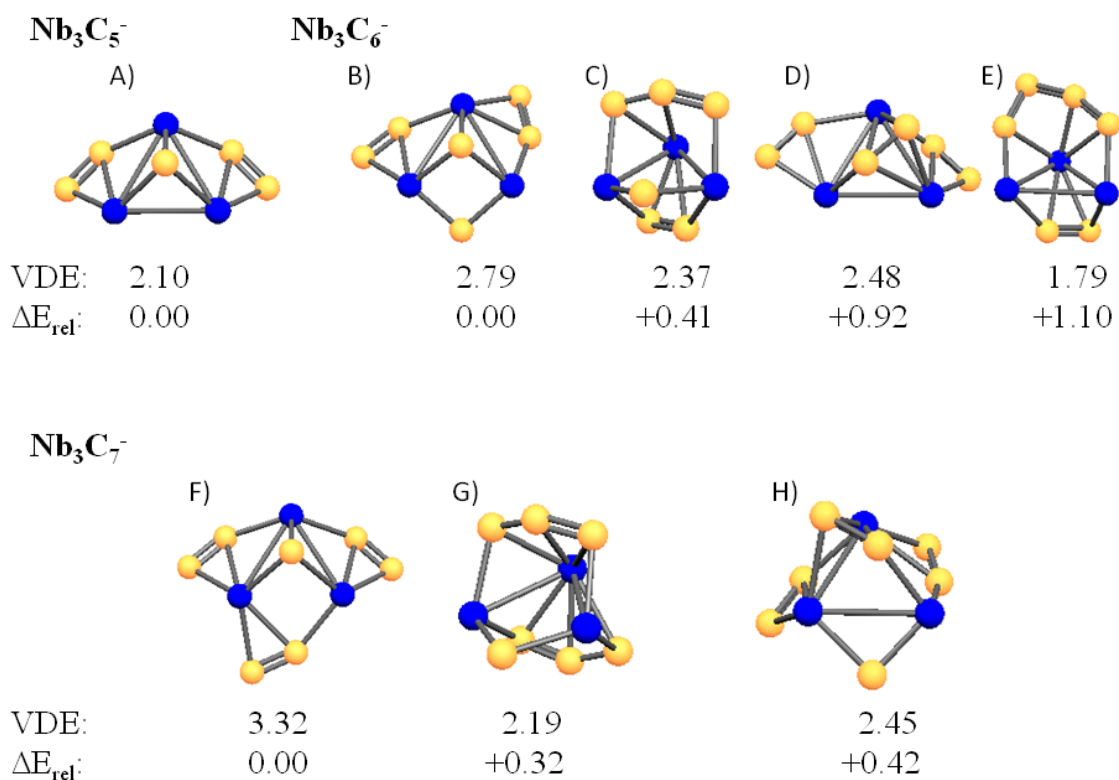


Figure 7.3 The ground state and relevant isomer structures for Nb_3C_5^- (A), Nb_3C_6^- (B-E), and Nb_3C_7^- (F-H) with the theoretical vertical detachment energies (VDE) and relative energies (ΔE_{rel}). Vertical Detachment and Relative energies are in eV and do not include zero-point energies. The blue and yellow balls represent the Nb and C atoms, respectively.

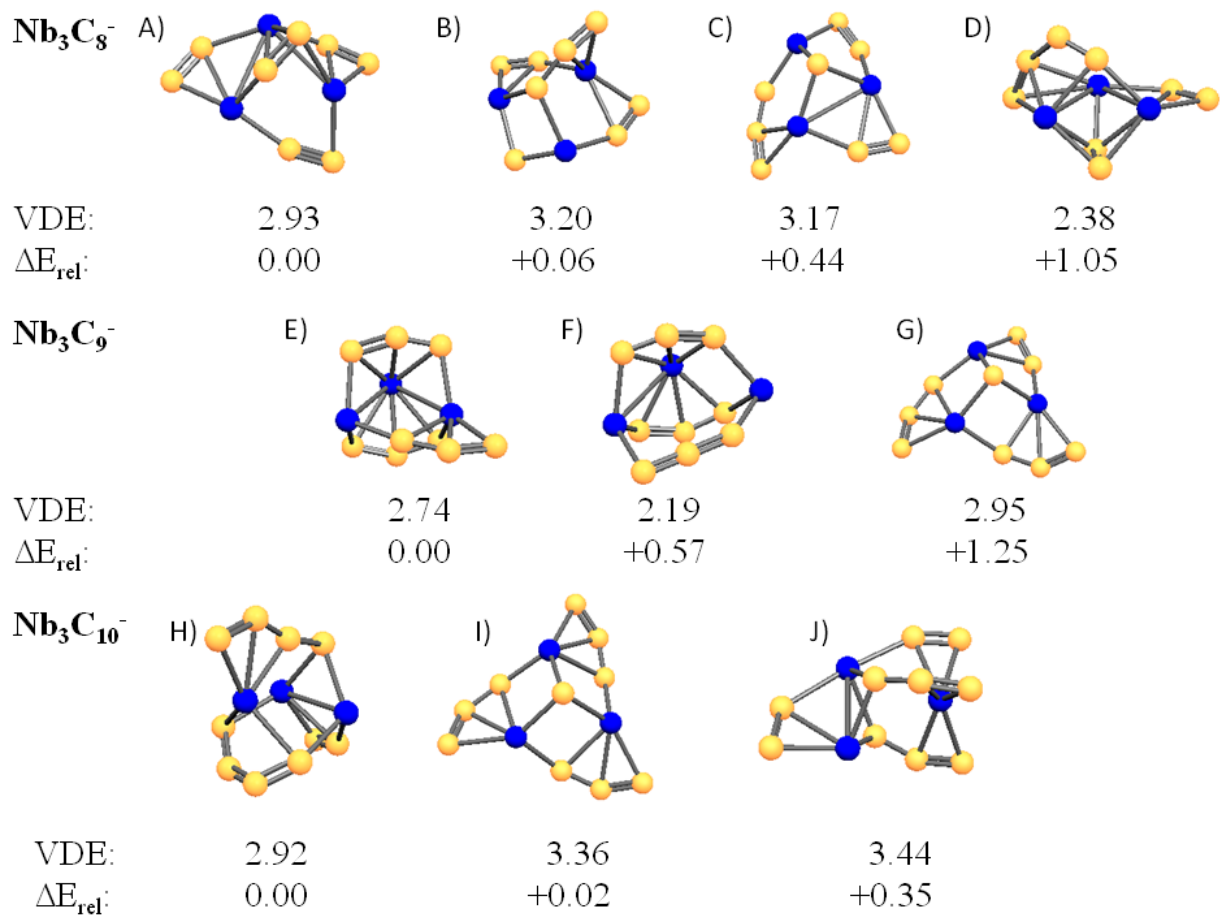


Figure 7.4 The ground state and relevant isomer structures for Nb_3C_8^- (A-D), Nb_3C_9^- (E-G), and $\text{Nb}_3\text{C}_{10}^-$ (H-J) with the theoretical vertical detachment energies (VDE) and relative energies (ΔE_{rel}). The reported VDEs and relative energies do not include the zero-point energies and are in eV. The blue and yellow balls represent the Nb and C atoms, respectively.

The ground state for the Nb_3C_6^- cluster can be seen in Figure 7.3(B). The ground state geometry for this cluster appears to retain the “capping” carbon motif seen in the Nb_3C_5^- cluster, with one lone carbon at the “front-edge” of the Nb_3 triangle. The largest change is in the Nb-Nb bond lengths, which are slightly longer than those seen in Nb_3C_5^- . The two Nb-Nb bonds that remain intact have distances of 2.73 and 2.70 Å. Even though the niobium bond distances increase, the C-C bonds slightly decrease by 0.03 Å, still maintaining double bonds.

However the Nb_3 triangular motif is still present. The theoretically determined isomers for the Nb_3C_6^- cluster has the “bridging” carbon chains across the Nb_3 triangular motif. The first isomer (Figure 7.3C) contains two chains consisting of C_2 and C_3 across the Nb_3C planar motif. This isomer is only 0.4 eV above the ground state of the anion. The C-C bond distances are 1.36 and 1.35 Å for the C_2 and C_3 carbon chains, respectively. This structure has two Nb-Nb bonds that are 2.65 Å, with there being no other Nb-Nb bond. There are two remaining isomers (Figure 7.3(D-E)) for the Nb_3C_6^- cluster which both have a triangular Nb_3 unit with Nb-Nb bond lengths ranging from 2.5 – 2.74 Å. Both of these structures incorporate at least one C_2 bridging carbon chains. However, the isomer seen in Figure 3D has two double bonded C_2 units flanking the sides of the Nb_3 triangle. The final isomer has two bridging carbon chains, the aforementioned C_2 -chain and a C_4 -chain atop the cluster. The C_4 -chain has two double bonds, with only one carbon atom with no carbon-metal bond interaction.

Continuing to Nb_3C_7^- , the ground state structure (Figure 7.3F) has a “capping” carbon with three flanking C_2 -units. The C_2 units have bond lengths of 1.32 Å and the Nb-Nb bonds range from 2.65 – 2.70 Å. The ground state structure is much like the “wheel” structure motif first reported by Harris and Dance, the exception being that one carbon atom resides at a raised center of the structure [171]. The first isomer can be seen in Figure 8.3G and is only higher in

energy by 0.32 eV. This isomer consists of two C_3 -bridging units across a planar Nb_3C motif. This structure is reminiscent of the lowest isomer seen in $Nb_3C_6^-$ with the addition of a carbon atom forming an additional C_3 unit. The C-C double bonds and Nb-Nb bonds in the isomer are nearly identical to those seen in $Nb_3C_6^-$ with values of 1.35 and 2.66 Å respectively. The final isomer (Figure 7.3H) resides 0.42 eV above the ground state energy, and differs from the ground state structure by forming a C_2 bridging unit atop the Nb_3 triangle. This structure seems to be analogous to the isomeric structure seen for the $Nb_3C_6^-$ cluster, having two C_2 units flanking the sides of the Nb_3 motif. The only difference is the additional carbon that resides on the edge of the Nb_3 motif.

The ground state and theoretically obtained isomers for the $Nb_3C_8^-$ cluster can be seen in Figure 7.4A. The ground state cluster is composed of one bridging C_2 unit and three other C_2 units flanking the edges of the Nb_3 motif. (The Nb_3 motif is used loosely here due to the loss of one of the Nb-Nb bonds; the two remaining Nb-Nb bonds range from 2.64 to 2.71 Å.) It is interesting to note that there are three C_2 units containing double bonds, with one having a triple bond with a shorter distance (<1.30 Å). The ground state cluster for $Nb_3C_8^-$ and isomers for Nb_3C_6 and Nb_3C_7 that contain bridging C_2 units are indicative of the “cradle” motif reported previously by Harris and Dance [171]. There are two isomers for the $Nb_3C_8^-$ cluster, each containing a combination of C_2 and C_3 chains, albeit in two different ways. The lowest isomer (Figure 7.4B) forms a C_3 bridging chain with bond distances of 1.4 and 1.3 Å. There are two C_2 chains residing on the edges of the Nb_3 motif, which have C-C distances of 1.3 Å and Nb-C distances ranging from 2.1 to 2.2 Å. In contrast to having a bridging C_3 chain, the isomer in figure 7.4C for $Nb_3C_8^-$ has one C_3 chain flanking one of the edges of the Nb_3 base and as was seen in previous cluster sizes, contains a capping carbon. The C_3 chain on the edge has distances

of 1.4 and 1.3 Å much like the bridging chain seen in the other isomer. There is also a decrease in the number of Nb-Nb bonds from the previous capping structures. The lone Nb-Nb bond is 2.65 Å. The last isomer, shown in Figure 7.4C, resides 1.05 eV above the most stable cluster, and resembles that of Nb_3C_6^- with a C_2 and C_4 bridging unit, but an additional C_2 unit is on the edge of the Nb_3 base. This structure has two Nb-Nb bonds at 2.63 and 2.55 Å, which is the shortest distance of all the clusters studied so far. The C_4 chain has two double bonds, at 1.35 Å. The two C_2 chains along with the two Nb atoms in the cluster closely resemble that of the Nb_2C_4 ground state cluster reported previously. The C-C and Nb-C bond distances range from 1.33 - 1.35 and 2.04 - 2.22 Å, respectively.

Figure 7.4(E-G) shows the ground state and isomeric cluster for Nb_3C_9^- . The ground state structure (Figure 7.4E) has two C_3 bridges, much like that seen in Nb_3C_7^- . The bond lengths on both of the C_3 chains are 1.35 Å. Notice the ground state cluster as well as the lowest isomer contain an additional C_3 chain units perched on the edge of the Nb_3 base motif, however their structures are quite different. The isomer cluster, which resides about 0.5 eV above the ground state, has a straight C_3 chain with two double bonds, much like propadiene, with only a total two Nb-C bonds to the terminal ends of the chain (Figure 7.4F). However, the ground state cluster has two additional Nb-C bonds on the C_3 chain, one to the central carbon of the chain and one to the front carbon. Figure 7.4G shows the final isomer for the Nb_3C_9^- cluster. The cluster has a capping carbon and two C_3 chains along the edges of the Nb_3 motif along with one C_2 motif.

The largest cluster studied, $\text{Nb}_3\text{C}_{10}^-$ has three very distinct isomeric clusters. The ground state (Figure 7.4H) contains two C_4 -bridges with a C_2 unit on the edge of the Nb_3 base. The C-C bond lengths on this structure vary from 1.40 to 1.31 Å. There is only one short Nb-Nb bond at 2.65 Å that incorporates the C_2 edging unit. The shortest Nb-C bond is 2.16 Å, however, notice

from Figure 7.4H, not all carbon atoms are involved in metal-carbide bonding. The lower C_4 chain has two carbon atoms that are not bonded to a Nb atom. Thus, this lower chain appears to be more symmetric than the C_4 chain above the Nb_3 motif. The first isomer is higher in energy by only 0.02 eV and employs the capping motif, surrounded by three C_3 chains. Figure 7.4I shows this isomer has no Nb-Nb bonds, instead preferring the Nb-C bonding in the cluster much like the previous capping motifs seen in other clusters. The final isomer for the $Nb_3C_{10}^-$ cluster can be seen in Figure 7.4J and has two C_3 bridging units and two C_2 units on the edges of the Nb_3 base. Here, there is one Nb-Nb bond (2.65 Å). The C-C bonds vary from 1.4 to 1.33 Å, with no evidence of a triple bond in the cluster.

The collected PES shows multiple peaks in many of the tri-niobium-carbide clusters with the lone exception being that of $Nb_3C_5^-$. The $Nb_3C_5^-$ spectra show one distinct peak at 2.30 eV, which corresponds to the ground state cluster in Figure 7.3. The calculated vertical detachment energy is 2.10 eV for this cluster, which is within the amount of error. The first triniobium cluster with multiple peaks is $Nb_3C_6^-$ (Figure 7.2B). This is indicative of the existence of isomers in the experiment. The largest detachment energy seen in experiment (3.03 eV) corresponds to the ground state structure of the $Nb_3C_6^-$ cluster with a vertical detachment energy (VDE) of 2.79 eV. Figures 7.3C and 7.3D are the isomeric structures that correspond to the middle experimental peak values of 2.20 and 2.47 eV respectively. These two experimental peaks have a great deal of overlap and the lowest isomer could correspond to either of the two middle peak values collected from experiment, since its value (2.37 eV) is within experimental error. The peak with the lowest detachment energy corresponds to the highest isomer seen in figure 7.3E.

Figure 7.2C shows the spectrum of the $Nb_3C_7^-$ at 308 nm, and has two distinct peaks. Additionally, the cluster has the highest abundance in the mass spectra (Figure 7.1). The highest

observed VDE of 3.31 eV is close to the calculated value of 3.32 eV for the most stable cluster based on relative energy for the Nb_3C_7^- cluster. The observed lower binding energy peak of 2.20 eV is in good agreement with the theoretical transition for the two isomers (Figure 7.3(G-H)). Both isomers have values of 2.19 and 2.45 eV respectively. Figure 7.2D gives the photoelectron spectrum of the Nb_3C_8^- cluster and has three peaks at 2.19, 2.99 and 3.36 eV. The electron binding feature seen at 2.99 eV is in good agreement with the cluster with the lowest relative energy in Figure 7.4A and the capped structure (Figure 7.4C). While the isomer seen in Figure 7.4B is in agreement with the highest electron binding energy feature observed in the collected spectra. The final relevant isomer resides ~ 1 eV above the ground state cluster, but has the lowest calculated vertical detachment energy (2.38 eV), which corresponds to the lowest electron detachment energy observed in the spectra.

Unlike the previous cluster, the photoelectron spectrum for Nb_3C_9^- has only two binding energy features (Figure 7.2E), with the most prominent feature at 2.97 eV. There are two theoretical structures that correspond to the higher binding feature. The ground state cluster (Figure 7.4E) has a VDE of 2.74 eV, while the isomer seen in Figure 7.4G has a VDE much closer of 2.93 eV. Figure 8.4F shows the calculated isomer that corresponds to the low binding energy feature observed at 2.01 eV. Comparison of the collected spectra for the $\text{Nb}_3\text{C}_{10}^-$ cluster has three electron binding energy peaks at 2.79, 3.24, and 3.42 eV and is the only cluster that shows no vertical electron binding energy below 2.5 eV (Figure 7.2F). The lowest feature agrees with the ground state structure that has a calculated vertical detachment energy of 2.92 eV (Figure 7.4H). The higher binding energies correspond to the two isomers (Figure 7.4 (I-J)).

Of the tri-niobium clusters studied, clusters that range in size where $n = 6 - 10$ have at least one observed experimental detachment energy around or above 3 eV and multiple peaks in

the collected spectra. The existence of the multiple peaks is indicative of isomers formed in the experiment. It can be seen that many of the clusters have multiple (at least 3) clusters with varying geometries and electron binding energies. The higher binding energies, those greater than 2.7 eV, tend to agree well with at least one geometric motif. Structures that incorporate a “capping” carbon, or a “wheel” –like motif all have theoretical vertical detachment energy values ranging from 2.9 – 3.4 eV. Figure 7.5 shows a comparison of the experimental and theoretical values for the “capping” motif. This motif agrees very well with the higher features, with the largest error being that of Nb_3C_6^- at 7% from the observed experimental peak.

The lower values collected (< 2.4 eV) are only seen where $n = 6 - 9$. The lower values correlate to at least two types of cluster motifs. The first motif contains two “bridging” units. In the case of Nb_3C_6^- , there are at least two of these type structures, one containing a C_3 and C_2 bridge, the other containing the largest bridging unit C_4 and one C_2 bridge. The vertical detachment energies are 1.79 and 2.37 eV respectively and correspond to the experimental values of 1.55 and 2.20 eV.

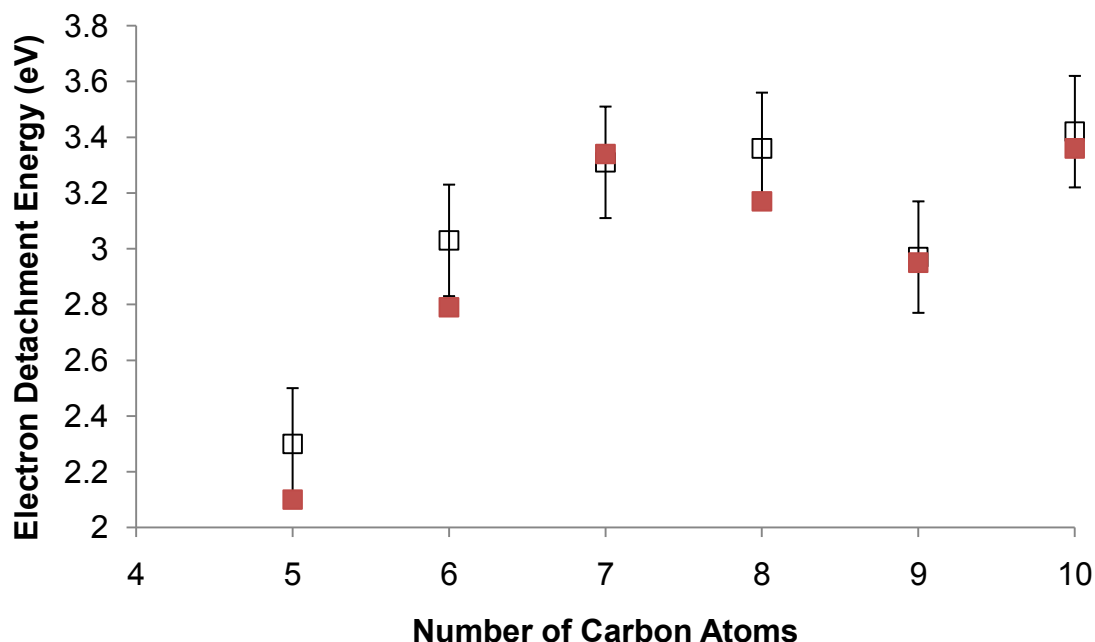


Figure 7.5 Comparison of experimental electron detachment energy with calculated vertical detachment energies for Nb_3C_n^- ($n = 5 - 10$). Red squares represent the “capping” motifs for each of the clusters. Experimental values are open squares with error of ± 0.02 eV.

The latter two clusters with an odd number of carbon atoms, Nb_3C_7^- and Nb_3C_9^- , have structures containing dual bridging motifs with the C_3 chain, much like the first motif in Nb_3C_6^- . However, the Nb_3C_8^- cluster has a dual bridging motif that contains a C_4 and C_2 chain like the second motif found in the Nb_3C_6^- cluster. It is interesting to note even though the $\text{Nb}_3\text{C}_{10}^-$ cluster does not have an experimentally observed binding energy below 2.5 eV, the lowest binding energy (2.79 eV) corresponds to a structure with a dual bridging motif. The second motif takes advantage of the C_2 chain in a bridging manner. These clusters can be seen where $n = 6, 7$ with calculated detachment energies of 2.48 and 2.45 eV respectively. Even though for Nb_3C_6^- and Nb_3C_7^- this type of “cradle” structure accounts for a few of the lower detachment energies, it can also account for the relatively high experimental VDE value of 2.99 eV for Nb_3C_8^- . However, the C_2

motif does not seem to correlate to any calculated detachment energies where $n = 9-10$. A comparison of both motifs with experimental values can be seen in Figure 7.6.

The isomeric findings from this study are in agreement with previous experimental studies of both mononiobium and diniobium carbide clusters. Zhai *et al.* found evidence of two isomers in both NbC_4^- and NbC_5^- [172]. We have previously examined diniobium carbides and the findings suggested a similar trend where both linear and three-dimensional isomers were for Nb_2C_n^- for $n = 4-9$, with the exception of Nb_2C_8^- [173]. Each of the aforementioned examinations suggested that a niobium atom can substitute for a carbon atom in linear structures, mostly due to similarities between the electronic structures of pure carbon clusters of small sizes with mononiobium and diniobium clusters. More recent studies by Dryza and co-workers found the neutral clusters for Nb_3C_n ($n = 1-4$) have structures with the Nb_3 triangle intact [175]. More intriguing they showed for Nb_3C_4 there are two isomers, one with a C_2 unit, seen in carbon rich clusters, and the other much like a Nb-deficient nanocrystal fragment. Here, we find three isomeric structural motifs. One structural motif involves a central Nb_3 unit, in which the three niobium atoms are in a triangular configuration with a lone carbon atop the face of the Nb_3 triangular base, these structures are referred to as “capping” motifs. This first motif is much like those found for the neutral smaller clusters reported by Dryza and co-workers for niobium clusters [174 – 175]. In the second major isomer-type, either a C_2 or C_3 unit resides in a bridging configuration across the Nb_3 triangular base, referred to as S-bridging. The final more dominant motif involves a dual bridging configuration, with a combination of C_2 , C_3 and/or C_4 bridging units across both the top and bottom faces of the base Nb_3 unit, referred to as D-bridging.

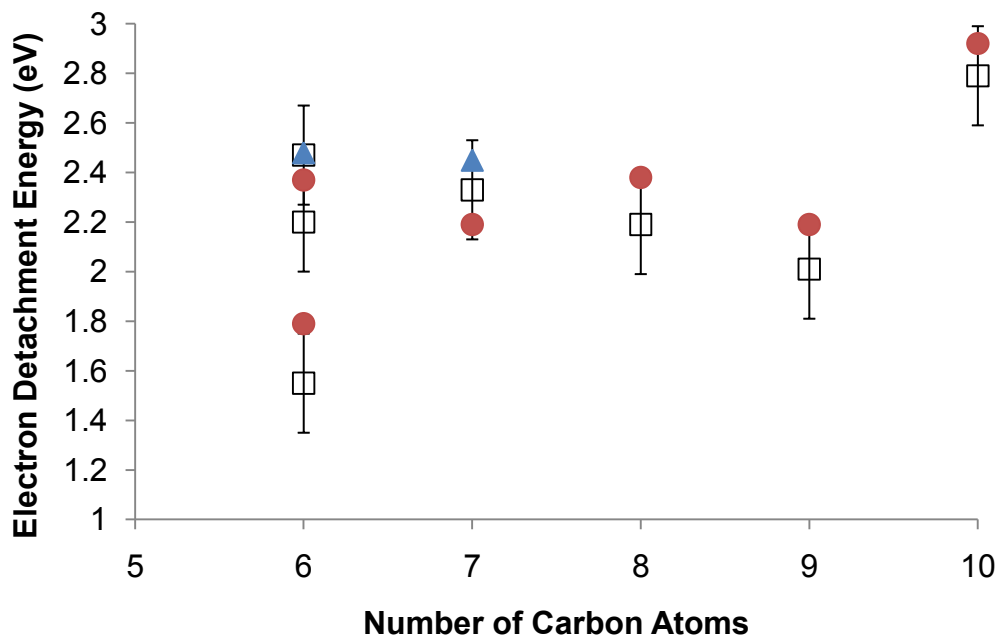


Figure 7.6 Comparison of experimental electron detachment energy with calculated vertical detachment energies for Nb_3C_n^- ($n = 6 - 9$). Red circles represent the D-bridging motifs. Blue triangles represent the single C_2 bridging chain structures. Experimental values are open squares with error of ± 0.02 eV.

In each of the three structural motifs accentuate the importance of the C_2 unit. Harris and Dance reported that the C_2 unit was essential in the formation of Met-Cars [171]. From this study all of the cluster sizes studied have some type of C_2 unit in either the lowest energy state or isomers. For cluster sizes containing 5, 6, 7, and 8 carbon atoms, there are structures with either more than one C_2 unit on the Nb_3 edge or some type of C_2 bridging or “cradle” motif. The Nb_3C_8^- cluster tends to have the largest number of C_2 units with four, with the Nb_3 base having a C_2 bridge and three C_2 units on the edges. These smaller sizes have a ratio closer to that of 1:2 for Nb and C, and seem they may be the building blocks of Met-Cars. It is surprising that the Nb_3C_9^- cluster does not seem to take advantage of the C_2 -unit, however this structure did not

correspond to any experimental detachment energies for the cluster. It is interesting to note, in the previous study by Harris and Dance, they show that Nb_xC_y clusters with C_3 chains were not stable when compared to the energetically lower clusters with C_2 -units [171]. This study shows evidence for the existence of not only C_3 chains, but C_4 carbon chains as well.

Using first principles density functional calculations and photodetachment spectra, we have systematically studied the structures for anionic tri-niobium carbide clusters. We find three structural motifs present, including “capping”, S-bridging, and D-bridging structures. There are not only C_2 units present in the clusters, but a clear indication of longer C_n chains for the anionic clusters studied here. As the ratio of C to Nb atoms increase, the trend is to form larger C_n chains from C_2 to C_4 , thereby also encouraging metal-carbon bonding. This is indicative of competition between C_2 , C_3 and C_4 chains in the $Nb_3C_n^-$ ($n = 5 - 10$). The evolution of the $Nb_3C_n^-$ clusters may be instrumental in gaining insight on the formation of Met-Cars as building blocks for cluster assemblies.

Chapter 8 Cluster Assemblies I: All-metal Aromatic Assemblies

The discovery of stable all-metal aromatic species has prompted many to review organic assemblies in the hopes of finding correlations between the organic and inorganic worlds. For example, the aromatic species benzene (C_6H_6) has been known to form various sandwich complexes with transition metals. Species like naphthalene ($C_{10}H_8$), anthracene ($C_{14}H_{10}$), and even tetracene involve the fusing of benzene rings to form complexes. These complexes exhibit a wide range of properties, which result in a wide range of uses in industry, medicine and scientific disciplines [176 – 180]. With a great deal of success with organic aromatic species, it comes as no surprise that researchers hope to make correlations to all-metal aromatic species and organic ones. We now attempt to assemble the all-metal aromatic species Al_3Sb using complexes formed by benzene as a guide in the hopes of finding similar architectures with varying properties. It should be noted the reason for using Al_3Sb versus the other two species, Al_3As and Al_3Bi , stems from the fact that Al_3Sb has the largest NICS value from all three species, making it the most aromatic.

The first attempt at cluster assemblies involves combing two planar Al_3Sb rings. The starting configurations were with the structures in the same xy -plane, which were allowed to optimize without constraints. Figure 8.1 shows the lowest energy structure, which is fused. Of the configurations attempted only one did not conglomerate (Figure 8.1B); however, this configuration was higher in energy by 3.14 eV.

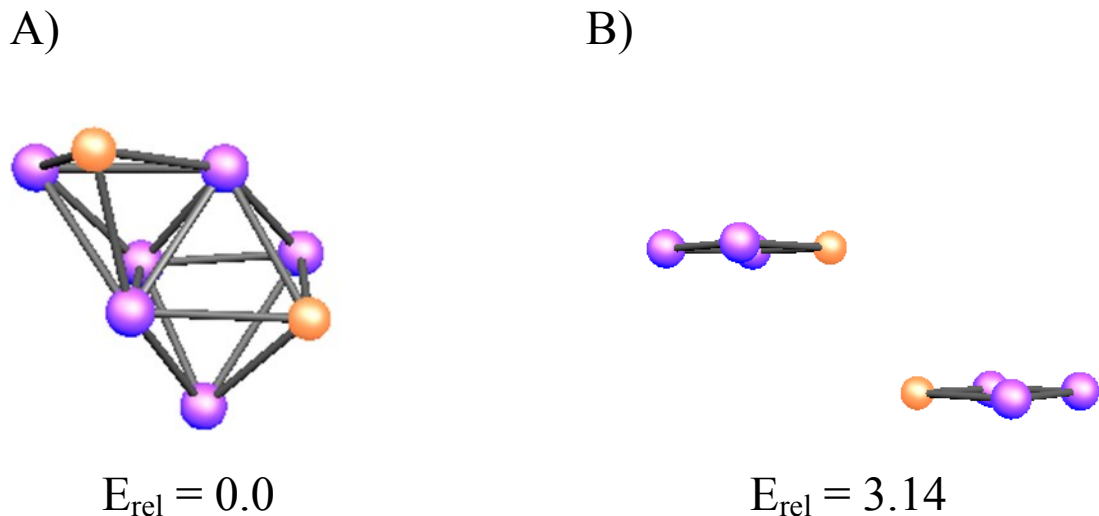


Figure 8.1 Lowest Energy structures for the Al_3Sb dimer. The fused Al_6Sb_2 structure (Panel A) and the unfused structure (Panel B) are given with relative energies in electron volts. The pink and orange balls represent the Al and Sb atoms, respectively.

It appears the idea of assembling all-metal aromatic rings is one that is unrealistic. It should be noted that many III-V compositions attain semiconductor status such as InAs, GaAs, AlN, AlAs and AlSb with either diamond, zincblende and wurtzite structures [181].

We now turn to a common architecture found in metallo-organic chemistry, sandwiches. Since the discovery of ferrocene, there have been a wide variety of metallocenes or sandwich complexes investigated both experimentally and theoretically [182 – 185]. There is a great deal of interest in these compounds because of their magnetic and electronic properties with the possibility of device applications [186]. This area of interest has expanded into the inorganic

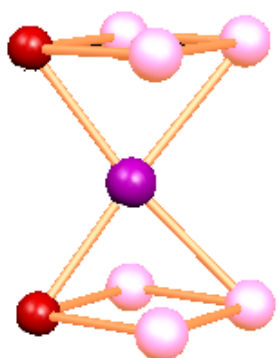
realm with the idea of designing all-metal aromatic sandwiches. Multiple theoretical studies have attempted to solidify assemblies using all-metal aromatic species. Mercero and Ugalde investigated sandwich-like complexes for the Al_4^{2-} ring at the B3LYP level [187]. Yang and co-workers have studied $SiAl_3^-$ and Ga_3^- aromatic sandwiches [188 – 189]. Chattaraj and Giri designed multi-decker sandwich complexes with Be_3^{2-} and Mg_3^{2-} aromatic compounds [190]. These studies employ all-metal aromatic species that require a charge with varying degrees of success. However, no studies have investigated a neutral aromatic in a sandwich-like complex. Thus, we now attempt for the first time sandwich-like assemblies with the neutral all-metal aromatic Al_3Sb .

The initial attempt at sandwich assemblies we wanted to mimic a common aromatic assembly. First we chose to investigate a sandwich system based on the organometallic benzene-vanadium system. The organometallic benzene-vanadium system is a very well known and studied system [191 – 193]. It has been shown to form wires as a multidecker cluster assembly with magnetic properties [194 – 196]. Therefore, our initial attempt at an inorganic assembly utilized this motif with the all-metal aromatic Al_3Sb cluster and the vanadium atom.

An example of the starting homodecked all-metal assembly can be seen in Figure 8.2A. The theoretical approach was performed using the density functional formalism within the generalized gradient approximation (GGA). The PBE functional was chosen for the correlation and exchange within the deMon2k software package.^o The Al and Sb atoms were represented using the parameters set forth in Chapter 4. The initial geometric configuration at various spin multiplicities was allowed to optimize without constraints.

^o Refer to Chapter 3.

A)



B)

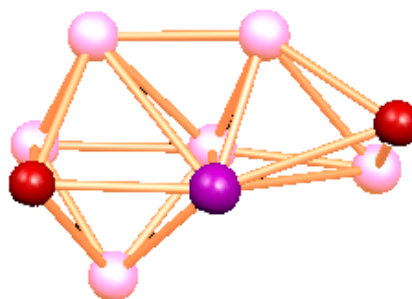


Figure 8.2 Initial and optimized configurations of the homodecked all-metal assemblies. The starting $(Al_3Sb)_2M$ geometry is located in Panel A. The final configurations of the Al_6Sb_2V (Panel B) is given as a representation of the lowest energy structure for the optimized homodecked assemblies. The red, light pink, and dark pink balls represent the Sb, Al and V atoms respectively.

The lowest energy structure can be found in Figure 8.2B. Notice, the structure has completely lost its sandwich motif. The final structure has formed more Al-Al bonds with the V atom lying in the center of the coalesced structure. The magnetic moment of the cluster is higher than that of the vanadium atom at 5 μ_B . The higher magnetic moment is not completely a surprise since the moment of other vanadium systems have been shown to be higher than that of the atom, as well [197]. One possible reason for the fusion of the initial sandwich motif, may be due to the binding energy of the individual atoms. For example, the binding energy of the Al-Al, Al-V, V-Sb, and Al-Sb dimers are 1.6, 2.0, 2.7 and 2.0 eV, respectively. The strength of the Al-

V bond is much stronger than the Al-Al bond and equivalent to that of the Al-Sb bond, this would imply a competition between the Al-Sb and Al-V bonds; however the overwhelming binding energy for the VSb dimer would yield the formation of V-Sb bonds and ultimately destroy the all-metal aromatic cluster.

It may be advantageous to use a metal with a relatively low M-Al and M-Sb binding energy, which may help sterically with the sandwich motif. The Mn atom meets this criterion since the Mn-Al and Mn-Sb binding energy is 1.31 eV and 1.75 eV respectively. Also, by using the Mn atom, it requires no charge due to its stable magnetic configuration. If indeed the all-metal aromatic species were to truly behave much like a benzene ring, which requires no charge as well, the structure is expected to retain a sandwich-like motif and maintain the magnetic moment of the atom. Upon full optimization, we find the sandwich-like geometry is destroyed. In fact, the structure tends to conglomerate by again increasing the number of Al bonds in the cluster. The magnetic moment of the cluster also exhibits some change and is reduced in the lowest energy structure to $3\mu_B$.

The conglomeration of the homo-decked sandwich motifs leaves to a question on the true stability of the all-metal aromatic cluster. It has been proposed by Yang and co-workers that the binding energy within all-metal aromatic clusters is not strong enough to prevent fusion [188]. In order to see if this picture is correct, we compared the binding energy of the Al_3Sb cluster with that of the fused clusters. We find the binding energy is 1.97 eV/atom for the Al_3Sb cluster. This is indeed much lower than the 2.29 eV/atom value for the Al_6Sb_2Mn fused cluster. However, there is one other possible explanation; that is the definition of all-metal aromaticity is not a true definition of the source of stability seen in these clusters. If the source of stability were explained through the ellipsoidal jellium model or Clemenger-Nilsson model, the reason

for this fusion may be understood more readily. Through the Clemenger-Nilsson model, stable clusters that did not correspond to the typical magic numbers within the jellium model were explained as relatively stable. Thus, these clusters would not remain if etched or if they were to interact with other clusters.

One final option in designing sandwich motifs is to employ the use of a sterically stable organic planar motif with the Al_3Sb planar “all-metal aromatic” cluster. This hetero-decked motif may retain its sandwich-like geometry like those seen with other all-metal aromatic compounds. In order to build the hetero-decked sandwich, we chose to examine the compound $[\text{C}_6\text{H}_6]\text{V}[\text{Al}_3\text{Sb}]$. The initial and optimized configuration for the compound can be seen in Figure 8.3. The lowest energy configuration has a magnetic moment of $3\mu_{\text{B}}$, with an isomer with a higher magnetic moment ($5\mu_{\text{B}}$) residing 0.1 eV higher in energy. This is different from what is found for vanadium-benzene sandwiches. The lowest energy structure has a magnetic moment of $1\mu_{\text{B}}$ [149 – 151]. The lowest energy structure does not fuse to form a larger cluster, instead the organic benzene “tilts” to the side of the z-axis. This type of tilt is seen in other charged heterodecked systems with all-metal aromatics and organic counterparts [188-189]. It is interesting to note that the isomer assembly retains complete planarity. The benzene remains intact and planar, which is to be expected due to its proven stable behavior. However, the Al_3Sb cluster is slightly bent out of the plane. The Al-Al bond lengths remain 2.60 Å as was seen in the neutral cluster, however the Al-Sb bond length has elongated from 2.59 to 2.73 Å.

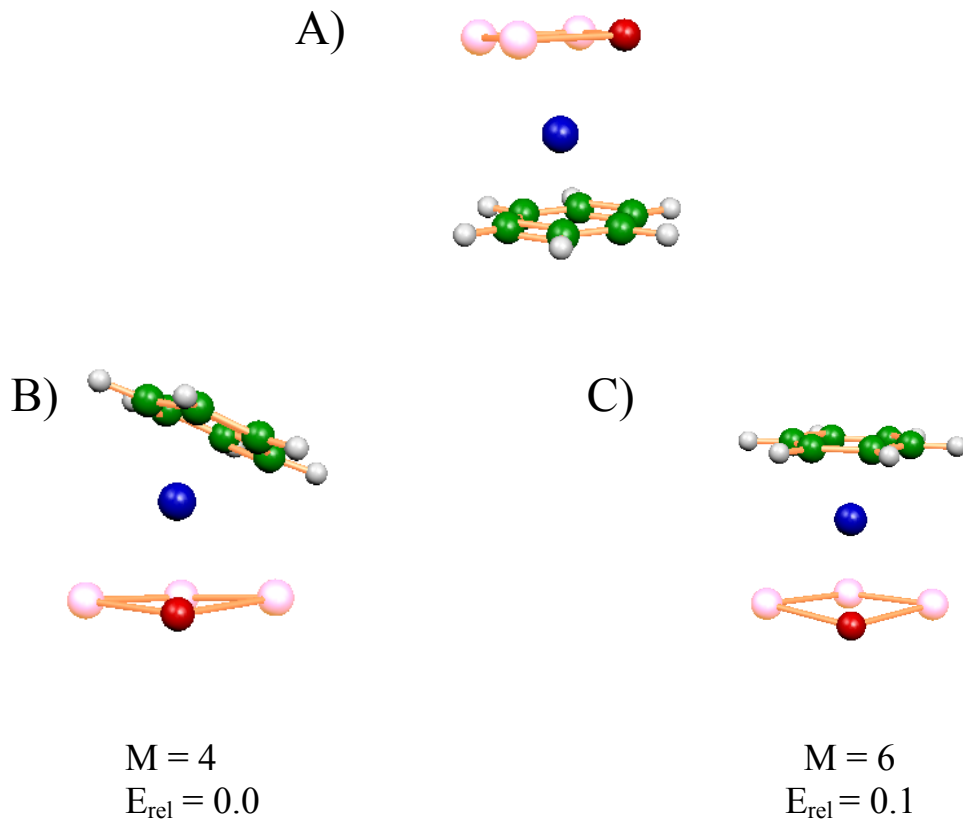


Figure 8.3 Initial and optimized configurations of the heterodecked assemblies. The starting (Al₃Sb)VBz structure is located in Panel A. The lowest energy structure (Panel B) and lowest lying isomer (Panel C) are given with spin multiplicities (M) and relative energies (E_{rel}) in electron volts. The red, light pink, green, white and blue balls represent the Sb, Al, C, H, and V atoms respectively.

The Sb-V bond length is slightly shorter (2.76 Å) than the Al-V bond lengths (2.80- 2.86 Å), which is to be expected since the Sb-V bond is stronger than the Al-V bond. In order to determine the stability of the overall motif, we calculated the binding energy (B.E.) of the assembly via,

$$\text{B.E.} = [E(\text{V}) + E(\text{Bz}) + E(\text{Al}_3\text{Sb}) - E(\text{Al}_3\text{SbVBz})]/3.$$

The assembly's binding energy is 3.09 eV, which is a strong indication the motif is stable. We also investigated the HOMO-LUMO gap. The calculated HOMO-LUMO gap was determined to be 0.6 eV for the magnetic hetero-decked lowest energy assembly. This is a much smaller value than the more prototypical vanadium benzene sandwich clusters, however the triumph here is the ability of the all-metal aromatic and benzene ring to retain their individuality. One should be able to further this research endeavor using other neutral all-metal aromatic cluster in conjunction with other organic molecule to form larger magnetic hetero-decked sandwich motifs.

Chapter 9 Cluster Assemblies II: Assemblies with Magnetic Superatom Candidates

One of the exciting aspects of the research on superatoms is to make macroscopic assemblies using clusters as the building blocks. Using DFT Liu et al explored cluster assembled materials composed of the superhalogen Al_{13} and K [199]. Ashman examined the cluster assembled solid $BAI_{12}Cs$ using first principle calculations [40]. More recent advances have included ligated gold clusters and Al_5O_4 as possible cluster assemblies.^P In our group, we have attempted to assemble the newly discovered magnetic superatom, VCs_8 , with much success [27]. This endeavor is undertaken with the assembly of the bare three-dimensional magnetic superatom candidate, Ag_6Mn .

One key to cluster assemblies is the short range interaction. For example, the assembly of the VCs_8 dimer resulted in the bare cluster maintaining its geometry and the Mn atoms remained separated. The magnetic moment of the superatomic assembly was retained and behaved identical to that found for the Mn atoms. In an effort to gain understanding and see the behavior of the magnetic superatom Ag_6Mn , we attempted to theoretically design the dimer $(Ag_6Mn)_2$. Figure 9.1 shows the lowest energy structure and isomers obtained from the theoretical method previously explained in Chapter 4. The lowest energy structure allows the two Mn atoms to form a bond and become surrounded by the Ag atoms. The new fused $Ag_{12}Mn_2$ cluster has a very high magnetic moment of $11 \mu_B$, this also occurs with the isomers.

^P Refer to Chapter 1.

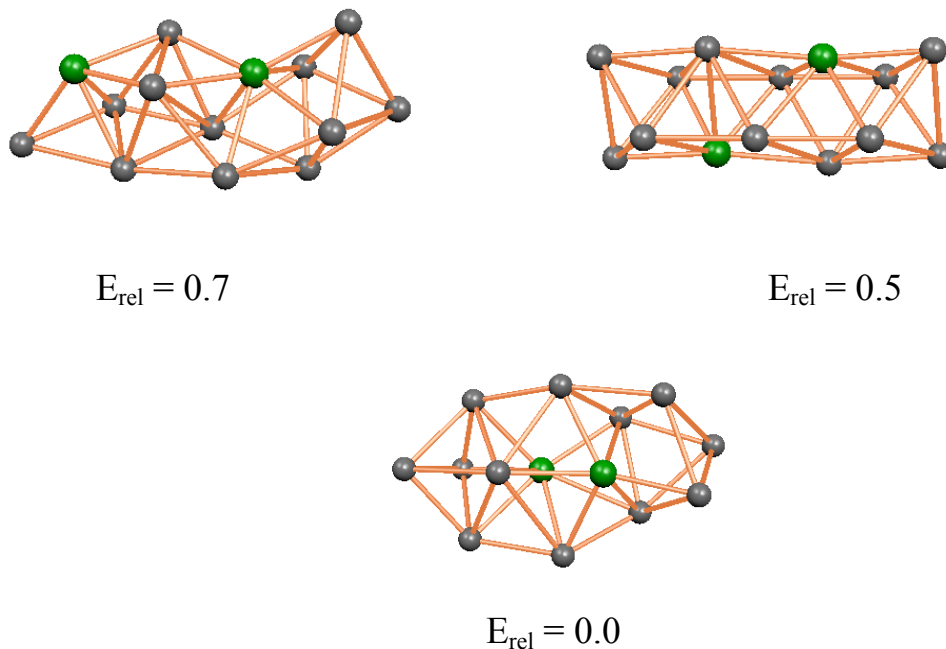


Figure 9.1 Lowest energy structures with relative energies (E_{rel}) in electron volts for the $\text{Ag}_{12}\text{Mn}_2$ cluster. The gray and green balls represent the Ag and Mn atoms respectively.

This leads to the discussion on the importance of cluster geometry for future assemblies with superatomic clusters. For comparison, let us first look at the magnetic superatom, Cs_8V . In the magnetic superatom, Cs_8V , the eight Cs atoms surround a central V atom [27]. One way to view this cluster is as the Cs atoms are “protecting” the V atom and its magnetic moment. If the cluster is allowed to interact with other Cs_8V clusters, these clusters will not fuse to form a Cs_{16}V_2 like structure, maintaining distance between V atoms. This directly results in the superatom analogy for Cs_8V to the Mn atom. Even though we find the similar electronic structure for the magnetic superatom Ag_6Mn as for Cs_8V , their geometries are very different. The Ag_6Mn cluster has an “open” geometry leaving the Mn atom and its localized magnetic moment exposed. Therefore if the cluster is allowed to interact, the Mn atoms form a Mn-Mn

dimer and the original Ag_6Mn cluster becomes distorted leading to the fused $\text{Ag}_{12}\text{Mn}_2$ structure. The interaction of the Ag_6Mn cluster reiterates the large role that geometry can play in a cluster's ability to be useful in cluster assemblies.

Chapter 10 Cluster Assemblies III: Using Zintl Analogues

Zintl phases have been studied by a multitude of theorists and experimentalist. Typical Zintl phases are defined as compounds that are electronically balanced and/or closed-shell compounds where there is complete charge transfer from a highly electropositive element, either an alkali or alkaline-earth, to a more electronegative main group element, generally from groups 13-15. These traditional Zintl phases have shown various optical, magnetic and even superconductive properties exciting scientists to search for other new and unique Zintl phases.^Q

In this effort, our group recently reported on helical and linear chains composed of the Zintl As_{11}^{3-} [77]. From their study, they found the linear chain without solvent is very stable. In another study, Castleman and co-workers showed that a cluster assembled material may contain a larger gap than the cluster building block for Zintl clusters [13]. Denning and Goicoechea have studied mercury-linked cluster chains with the Ge_9 Zintl cluster [200]. With such promise in an ever growing field, it is advantageous to assemble the newly added gas phase Zintl clusters, $Sn_xBi_y^-$ ($x + y = 9$), in the hopes of designing novel assemblies.

10.1 $(KSn_6Bi_3)_n$ ($n = 2 - 6$)

The deltahedral Sn_6Bi_3 cluster has been stabilized using a counteranion in Chapter 8. The stable building block unit, KSn_6Bi_3 , retained a D_{3h} symmetry and large HOMO-LUMO gap (2.03 eV) making it ideal for assemblies. However, two large questions loom over the initial

^Q Refer to Chapter 1.

steps in this investigation; 1) will the $(\text{KSn}_6\text{Bi}_3)_2$ cluster coalesce and 2) If the assembly does not coalesce, how will this affect the geometry and electronic properties?

In an effort to answer both of these questions, calculations were carried out on the KSn_6Bi_3 dimer. The initial geometries were chosen by bringing the KSn_6Bi_3 building block together in a variety of ways. The structure was fully optimized without constraints. The calculations were performed using the ADF package explained previously.

Figure 10.1 shows the final geometries for the $(\text{KSn}_6\text{Bi}_3)_2$ assembly. The optimization of each cluster assembly resulted in two KSn_6Bi_3 units instead of a fused $\text{K}_2\text{Sn}_{12}\text{Bi}_6$ cluster. This is a strong indication that these units are highly favorable for assemblies. The lowest energy structure has two potassium atoms between two Sn_6Bi_3 units (Figure 10.1A). The shortest distance between the two Sn_6Bi_3 clusters is 3.7 Å. The potassium atoms are 3.7 Å away from the Sn_6Bi_3 clusters. The isomer (Figure 10.1B) resides 0.05 eV higher in energy and favors two KSn_6Bi_3 units in a step-like formation. The distance between the two KSn_6Bi_3 units is shorter than the ground state by 0.3 Å. The next isomer is 0.4 eV above the lowest energy state and one K atom separates two Sn_6Bi_3 units with the second K atom opposite the second Sn_6Bi_3 unit (Figure 10.1.2C). A sound determination of stability for these initial assemblies can be gauged by looking at the HOMO-LUMO gap based in the electronic structure. The HOMO-LUMO gap in each assembly is larger than 1 eV, with the exception of the highest isomer. In fact, the lowest energy dimer has the largest gap size of 1.78 eV. Even though the gap size is impressive, it is smaller than the isolated KSn_6Bi_3 cluster (2.03 eV). Interestingly, the smaller gap size relative to the cluster building block was also seen by Reber and co-workers in their ionic $(\text{K}_3\text{OAl}_{13})_2$ superatom assemblies [201].

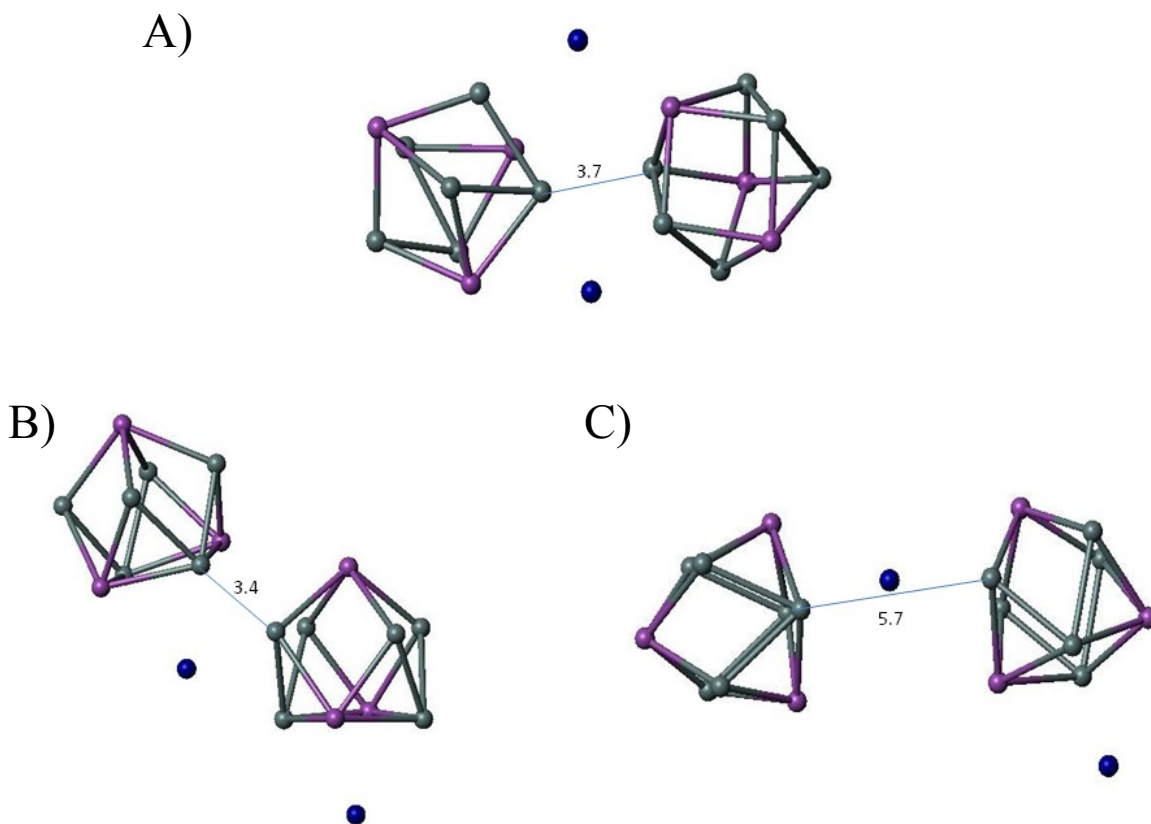


Figure 10.1.1 Lowest energy structures for the $[\text{KSn}_6\text{Bi}_3]_2$ assembly. Lowest energy configuration (Panel A), lowest isomer (Panel B) and second lowest isomer (Panel C) are given for the dimer. The pink, gray and blue balls represent the Bi, Sn and K atoms respectively. The distance between parent clusters are given in Angstroms and are represented with the blue line.

The initial calculations on the $(\text{KSn}_6\text{Bi}_3)_2$ species indicates that further assembly of these building blocks may lead to a stable assembly with a smaller gap size than its cluster building block. Therefore, we successively added KSn_6Bi_3 building blocks to form either ring or chain cluster assemblies to see if this indeed would be the case.

Figure 10.1.2 gives the lowest energy configurations for $(\text{KSn}_6\text{Bi}_3)_n$ ($n = 3 - 5$). The lowest energy structure for the trimer $(\text{KSn}_6\text{Bi}_3)_3$ is a ring formation with one K atom residing

between each Sn_6Bi_3 unit. The distance between the Sn_6Bi_3 units on average is 4.9 Å and is slightly different from the dimer. Upon the addition of more KSn_6Bi_3 units, the structure prefers to form larger rings with an average distance increasing from 5.1 to 6.2 Å between the Sn_6Bi_3 parent clusters. The formation of rings brings several interesting points to the surface. First, it is well known that Zintl polyanions can form a variety of low-lying structures depending upon the type of counteraction used in the system (which may lead to different electronic structures). Such is the case in the dimer. However, as one begins to add more KSn_6Bi_3 units, the favorable geometry is ring like, with chain-like structures residing at least 0.7 eV higher in energy than their ring counterparts. Second, the well known Zintl phases (including deltahedral clusters) typically require more than one counteraction in the system and to this author's knowledge there is no mention of the successful formation of a Zintl phase with a Zintl ion requiring only one charge, making the $(\text{KSn}_6\text{Bi}_3)_n$ assemblies the first of its kind. Third, the ring structures formed by the KSn_6Bi_3 unit could be viewed more simply as ionic rings which behave like the rings formed in alkali-halide molecules [202]. The success of the formation of the $(\text{KSn}_6\text{Bi}_3)_n$ ring architectures now lead us to investigate their stability and electronic properties.

In order to ascertain the stability of the ring structures we calculated the removal energy that represents the amount of energy required to remove a KSn_6Bi_3 unit from the cluster,

$$R.E. = E(\text{KSn}_6\text{Bi}_3)_n - E(\text{KSn}_6\text{Bi}_3) + E(\text{KSn}_6\text{Bi}_3)_{n-1}$$

Figure 10.1.3 shows the calculated removal energies for the clusters. There is a peak for the $(\text{KSn}_6\text{Bi}_3)_3$ assembly, which has the largest removal energy for each of the cluster assemblies. Afterwards there is a continual drop off, with an increase occurring where $n = 6$. The large removal energy for $n = 3$ is most like due in part to the closed ring formation of the structure, much like what was seen in the case of the ionic superatom assemblies[200].

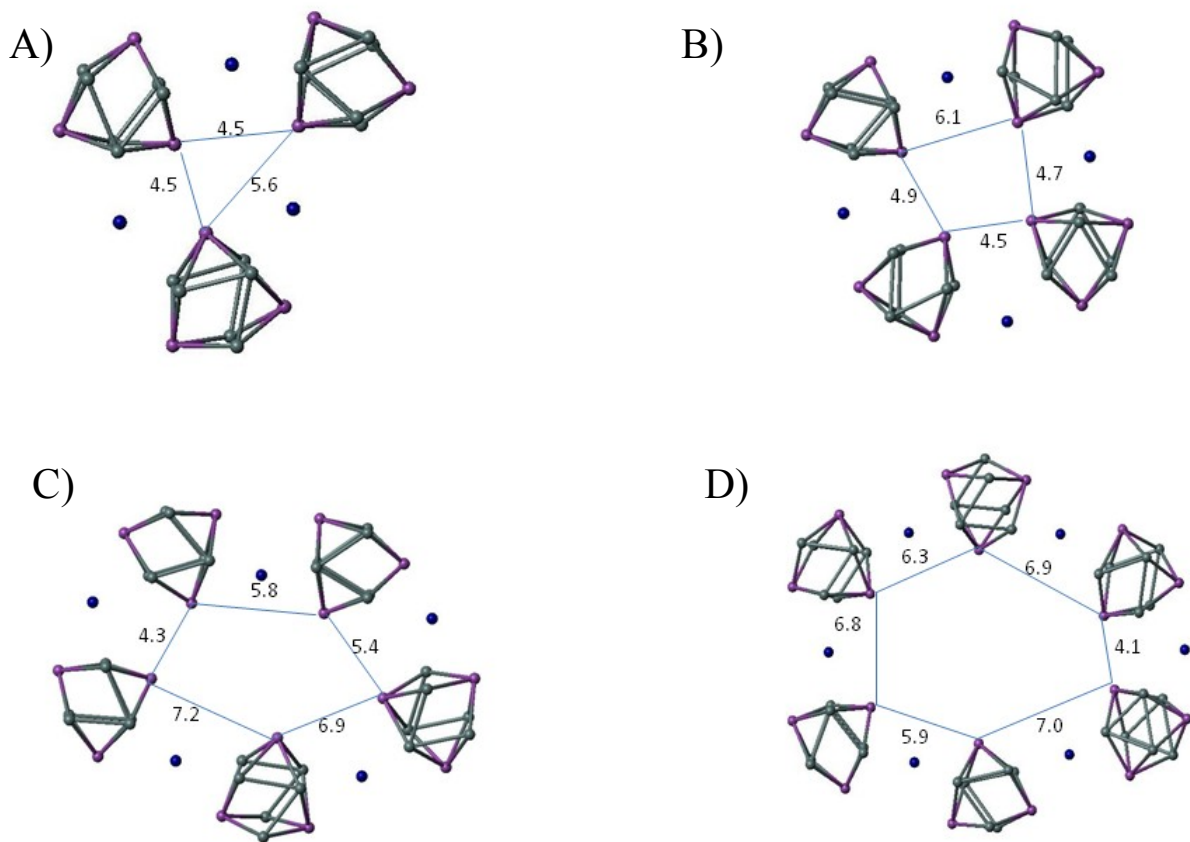


Figure 10.1.2. Lowest energy geometries for [KSn₆Bi₃]₃ (Panel A), [KSn₆Bi₃]₄ (Panel B), [KSn₆Bi₃]₅ (Panel C) and [KSn₆Bi₃]₆ (Panel D) are given with the pink, gray, and blue balls represent the Bi, Sn, and K atoms, respectively. The distance between the parent clusters are given in Angstroms and are marked with the solid blue line.

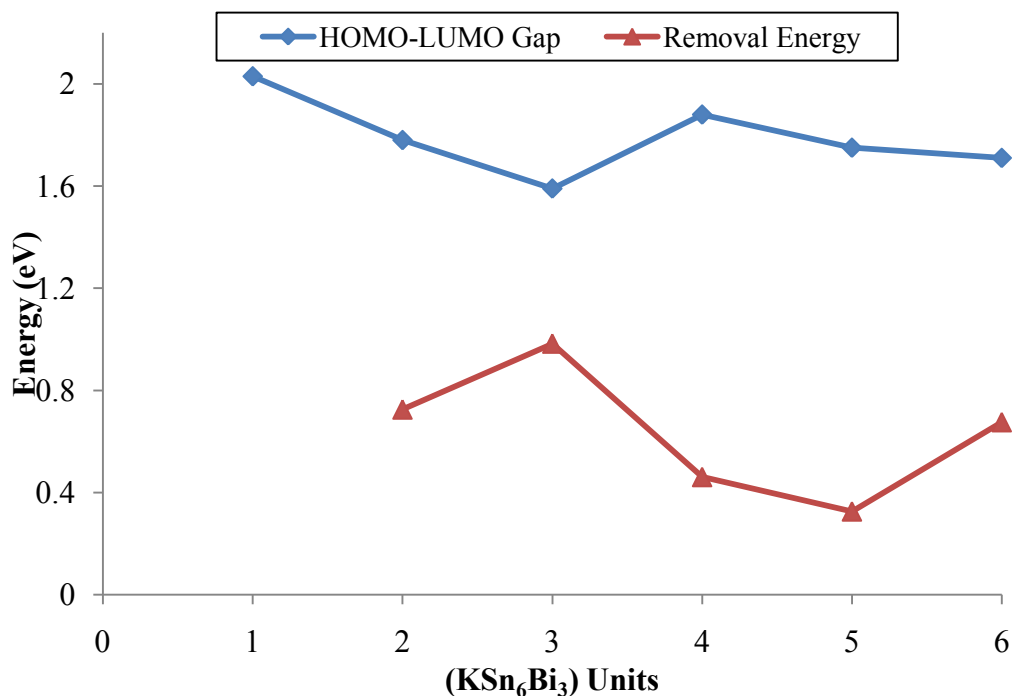


Figure 10.1.3 Removal Energy and HOMO-LUMO gap for (KSn₆Bi₃)_n assemblies.

Reber and co-workers proposed the sudden drop off in removal energy could be a result of larger assemblies preferring to form cage like structures; but cage structures were not attempted in this study. The fragmentation energy (*F.E.*) per fragment, the amount of energy to separate the assembly into the monomer units, was also calculated via,

$$F.E. = \frac{nE(KSn_6Bi_3) - E(KSn_6Bi_3)_n}{n}$$

From the data, the trimer and tetramer have the highest fragmentation energies of 0.57 and 0.54 eV/unit for the assemblies studied here. We also investigated the electronic structure and HOMO-LUMO gap of the assemblies. As mentioned previously, the assemblies HOMO-LUMO gap is very important to determine if the cluster building block is able to maintain its electronic features as well as an indication on the stability of the cluster or cluster assembly. For example,

the HOMO-LUMO gap of the KSn_6Bi_3 unit is 2.03 eV, while the dimer is significantly lower (1.78 eV). Further investigation of the electronic structure larger assemblies reveals that the trimer has the lowest gap size at 1.59 eV, however the tetramer assembly takes a sudden increase to 1.88 eV. This seemingly abrupt change in the gap size led us to wonder if somehow there was a change in the ordering of the electronic structure as the assemblies changed from $(\text{KSn}_6\text{Bi}_3)_3$ to $(\text{KSn}_6\text{Bi}_3)_4$. To answer this question, we investigated the one-electron levels for the lowest energy assemblies.

Figure 10.1.4 shows the one-electron levels for $(\text{KSn}_6\text{Bi}_3)_n$ ($n = 1 - 5$) with the dark lines corresponding to the occupied levels, while the gray lines correspond to the unoccupied levels. The cluster assembly $(\text{KSn}_6\text{Bi}_3)_2$ shows the addition of levels one would expect, but does not resemble the electronic structure seen for the original KSn_6Bi_3 unit. However, for the trimer the levels tend to “bunch” resembling the electronic structure of the KSn_6Bi_3 monomer unit. Once an additional monomer unit is added, the $(\text{KSn}_6\text{Bi}_3)_4$ electronic structure again shows a dramatic change with the LUMO rising in energy and the HOMO lowering in energy from the previous assemblies. This new order found in the electronic structure for the $(\text{KSn}_6\text{Bi}_3)_4$ assembly tends to continue as one adds the monomer to form the $(\text{KSn}_6\text{Bi}_3)_5$ assembly. These results show there is a sudden change in the order of the electronic levels as the growth of the assembly continues, which does attribute to the change in HOMO-LUMO gap, but one question remains: What causes the change in the order of the electronic structure? To answer this question, we must turn back to the geometry of the assemblies to see the interaction of our initial building blocks. First, the distance between the Sn_6Bi_3 units in the lowest energy dimer is extremely small (3.7 Å), whereas for larger assemblies the distance between the monomer units is much larger.

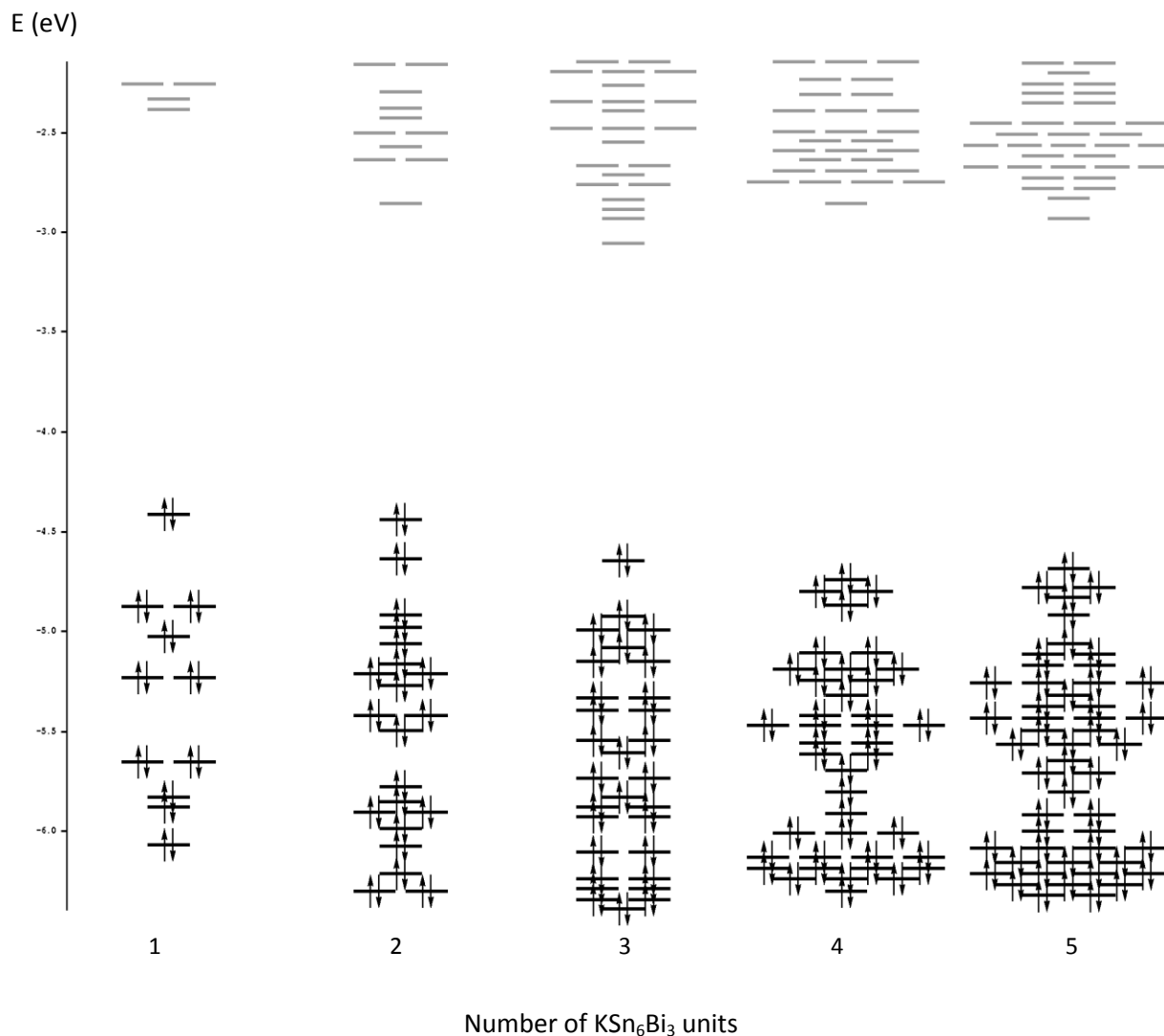


Figure 10.1.4 One-electron levels for $(\text{KSn}_6\text{Bi}_3)_n$ assemblies.

Therefore, the change in electronic structure, we suspect, is due to the differing interaction mechanisms in the assemblies. For the $(\text{KSn}_6\text{Bi}_3)_n$ where $n \geq 3$, the interaction is facilitated through the alternating K atoms. However, for the dimer, the cluster-cluster interaction is facilitated in a more direct route with the neighboring Sn_6Bi_3 unit. The change in distance does explain the difference between the dimer and trimer assemblies, however it is not acceptable for the change as one moves from the trimer to the tetramer.

In both the trimer and tetramer assemblies, the distance between the monomer units remains large, but there is a dramatic change in the electronic structure. The explanation begins with the LUMO in the cluster assemblies, with similar geometries. The LUMO in the $(\text{KSn}_6\text{Bi}_3)_3$ assembly is separated from the LUMO+1 state, if the LUMO were to become filled with two electrons, this would allow for another stable species to form and a large HOMO-LUMO gap would evolve. Indeed this is the case, with the $(\text{KSn}_6\text{Bi}_3)_4$ tetramer having a larger HOMO-LUMO gap (1.78 eV) than its predecessor.

The composition of the $(\text{KSn}_6\text{Bi}_3)_n$ cluster assemblies, were designed from the previously identified gas phase Zintl analogue cluster Sn_6Bi_3^- using a potassium atom as the counteraction to the analogues neutral counterpart. We observed assemblies with smaller HOMO-LUMO gaps than its initial building block. The cluster-cluster interaction for the dimer is a direct interaction, whereas for assemblies composed of three or more monomers showed an indirect mechanism due to the intra-cluster distance. We have shown it is possible to build a stable Zintl analogue cluster assembly requiring only one counteraction.

10.2 Organo-Zintl Analogue Cluster Assemblies

As seen in Chapter 8, Zintl clusters can be stabilized using either traditional alkali atoms or organic ligands as counterions with varying results on geometry and electronic properties of the cluster. However, no one has attempted to assemble clusters utilizing the organo-Zintl clusters, so one must ask the question, how would an organic substituent effect the electronic structure of a cluster assembled material? In an effort to try and answer this question, we carried out theoretical studies on organo-Zintl analogue cluster assemblies.

The Sn_7Bi_2^- cluster was previously shown to be a stable deltahedral cluster using experimental and theoretical techniques. The cluster's stable behavior was attributed to having a deltahedral geometry and an electron count similar to the Sn_9^{3-} Zintl cluster. This analogous behavior would imply that even though the cluster is stable, if one were to add one electron the structure may become more stable due the clusters having 22 electrons and a closed shell configuration, like the Sn_9^{4-} cluster. This stability would also be seen in an increase in its HOMO-LUMO gap. In fact, upon investigation, the $\text{Sn}_7\text{Bi}_2^{2-}$ cluster (Figure 10.2.1) has a HOMO-LUMO gap of 1.99 eV, which is much larger than the gap seen in the Sn_7Bi_2^- cluster (0.21 eV). The increase in HOMO-LUMO gap by simply adding an electron leads us to believe that the neutral Sn_7Bi_2 cluster can accept up to two more units of charge to form a stable cluster building block. This is a clear advantage over the Sn_6Bi_3 cluster, in that one may be able to utilize multiple organic substituents as linkers to form an array of organo-Zintl analogue assemblies, instead of being limited to an ionic like motif.

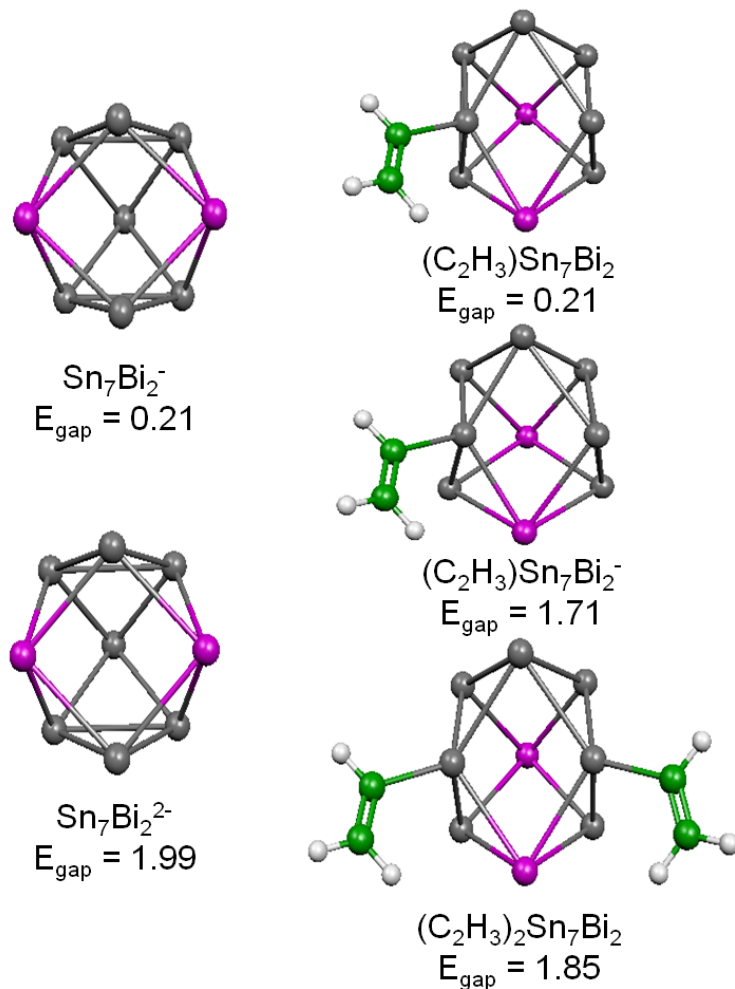


Figure 10.2.1 Lowest Energy structures for the $\text{Sn}_7\text{Bi}_2^{x-}$, $(\text{C}_2\text{H}_3)\text{Sn}_7\text{Bi}_2^{y-}$, and $(\text{C}_2\text{H}_3)_2\text{Sn}_7\text{Bi}_2$ clusters ($x = 1-2$; $y = 0-1$). The HOMO-LUMO gap (E_{gap}) values are given below the structures in electron volts. The gray, pink, green, and white balls represent the Sn, Bi, C, and H atoms respectively.

Previously, I have showed how organic groups, such as methyl- and/or ethyl-, can be utilized as a counteraction to stabilize the electron deficient Sn_6Bi_3 cluster. It was shown that the organic ligand preferred to bond to a Sn site on the cluster and would not only alter the geometry of the cluster, but alter the HOMO-LUMO gap as well for the Sn_6Bi_3 cluster. In the Sn_7Bi_2 case, once an organic ligand is attached, such as $-\text{C}_2\text{H}_3$, we find a similar effect. The $\text{Sn}_7\text{Bi}_2-\text{C}_2\text{H}_3$

cluster (Figure 10.2.1) is distorted but has a gap of 0.22 eV, which is identical to the gap found in the Sn_7Bi_2^- anion. Thus one would expect by adding one electron the HOMO-LUMO gap would show a significant increase, like in the case of $\text{Sn}_7\text{Bi}_2^{2-}$. Indeed, we find the gap size has increased from 0.22 eV to 1.71 eV for the $\text{Sn}_7\text{Bi}_2\text{-C}_2\text{H}_3^-$ cluster. The increase in HOMO-LUMO gap and high electron affinity (2.88 eV) indicate the $\text{Sn}_7\text{Bi}_2\text{-C}_2\text{H}_3$ anion cluster is more stable than its neutral counterpart. This revelation encouraged us to attach a second $\text{-C}_2\text{H}_3$ substituent to the $\text{Sn}_7\text{Bi}_2\text{-C}_2\text{H}_3$ cluster in the hopes of further stabilizing the cluster. The resulting $\text{Sn}_7\text{Bi}_2\text{R}_2$ ($\text{R} = \text{C}_2\text{H}_3$) organo-Zintl cluster has a low electron affinity (1.18 eV) and large HOMO-LUMO gap of 1.85 eV. This along with a calculated fragmentation energy (the amount of energy needed to break the cluster into Sn_7Bi_2 and two C_2H_3 units, i.e. $-2\text{E}(\text{C}_2\text{H}_3)+\text{E}(\text{Sn}_7\text{Bi}_2) - \text{E}(\text{Sn}_7\text{Bi}_2\text{R}_2)$) of 3.9 eV are indicative of a highly stable cluster that can be used as a building block for cluster assemblies.

The initial cluster assembly, involves two $\text{Sn}_7\text{Bi}_2\text{-R}$ units connected by one double bonded $\text{-C}_2\text{H}_2$ ligand. The reason for this motif is two-fold. First, both the organo-Zintl analogues and the organic ligand require at least one addition unit of charge for stability. The second is the $\text{CH}=\text{CH}$ cluster can act as a rigid linker with its double bond to maintain spacing between the organo-Zintl analogue clusters. The lowest energy structure for the $(\text{Sn}_7\text{Bi}_2\text{R})_2\text{C}_2\text{H}_2$ cluster can be seen in Figure 10.2.2. Immediately, one can see the Sn_7Bi_2 parent clusters remain intact, separated by the C_2H_2 in a *trans*-manner. The bond distance between the tin and carbon atoms range from 2.22 – 2.25 Å, similar to that found in other organo-Zintl clusters [165 - 168]. The HOMO-LUMO gap for the $(\text{Sn}_7\text{Bi}_2\text{C}_2\text{H}_3)_2\text{C}_2\text{H}_2$ assembly is 1.68 eV. This is 0.17 eV lower than the gap found for the $\text{Sn}_7\text{Bi}_2(\text{C}_2\text{H}_3)_2$ cluster, but the assembly is only lower by 0.03 eV than the gap found for the $\text{Sn}_7\text{Bi}_2\text{C}_2\text{H}_3^-$ cluster. This result breeds confidence in the ability to build

Table 10.2.1 The HOMO-LUMO gap (E_{gap}), fragmentation energy (F.E.) and removal energy (R.E.) for the organo- $(\text{Sn}_7\text{Bi}_2)_n$ assemblies (in eV).

n	E_{gap}	F.E.	R.E.
1	1.87		
2	1.68	6.94	1.03
3	1.60	9.90	1.00
4	1.59	12.91	1.05
5	1.55	15.80	0.93

larger assemblies, based on the organo-Zintl analogue cluster that will not coalesce. Therefore we attempted to expand the organo-linked motif by adding $\text{Sn}_7\text{Bi}_2\text{-C}_2\text{H}_2$ monomer units.

The optimized trans-chain assemblies can be seen in Figure 10.2.2. All of the assemblies retain the Sn_7Bi_2 parent clusters and spacing due to the rigid ligand. The Sn-C bond distances also remain similar to the original Sn-C bond lengths with very minimal change. The fact that the motifs do not conglomerate now leads us to investigate the stability and electronic structure of these assemblies.

Table 10.2 gives the HOMO-LUMO gap as well as the fragmentation and removal energies for the cluster assemblies. The fragmentation energy (F.E.) and removal energy (R.E.) were determined via,

$$F.E. = jE(\text{Sn}_7\text{Bi}_2) + kE(\text{C}_2\text{H}_2) + 2E(\text{C}_2\text{H}_3) - E[(\text{Sn}_7\text{Bi}_2)_j(\text{C}_2\text{H}_3)_2(\text{C}_2\text{H}_2)_k]$$

and

$$R.E. = E(\text{Sn}_7\text{Bi}_2\text{C}_2\text{H}_2) + E[(\text{Sn}_7\text{Bi}_2)_k(\text{C}_2\text{H}_2)_m(\text{C}_2\text{H}_3)_2] - E[(\text{Sn}_7\text{Bi}_2)_j(\text{C}_2\text{H}_3)_2(\text{C}_2\text{H}_2)_k]$$

where j is the total number of Sn_7Bi_2 units, $k = j - 1$, and $m = k - 1$. The fragmentation energy increases as the motif increases in size and ranges from 1.39 to 1.44 eV per fragment. The removal energy reveals an even-odd oscillation, with motifs that contain an even number of Sn_7Bi_2 clusters having higher values. The largest removal energy is found for the organo-Zintl analogue with four Sn_7Bi_2 cluster units.

The HOMO-LUMO gap provides greater insight as a measure of stability. The initial $(\text{Sn}_7\text{Bi}_2\text{R})_2\text{C}_2\text{H}_2$ assembly has a gap of 1.85 eV. Then by adding a $\text{Sn}_7\text{Bi}_2\text{C}_2\text{H}_2$ unit, the gap is smaller by 0.08 eV. Once the chain assembly has four Sn_7Bi_2 units, the gap appears to begin to level off at 1.6 eV. The observation of the minimal change in HOMO-LUMO gap size, led us to investigate the electronic structure more closely. As the organo-motif increases in size, more levels are added (Figure 10.2.3), as expected. However, the levels “bunch” with minimal change in the overall electronic structure, which is contrary to the electronic structure in the ionic assemblies in the previous section.

The organo-Zintl assemblies shown here have similarities and differences from the ionic $(\text{KSn}_6\text{Bi}_3)_n$ assemblies in the previous section. Both assemblies are designed from taking advantage of the electron count in the identified stable clusters. For example, the initial building blocks were born out of the analogous Zintl behavior of the Sn_7Bi_2^- and Sn_6Bi_3^- clusters. The assemblies, both organo-Zintl and ionic, have relatively large gap sizes, but the similarities end there. The organo-Zintl assembly is built from neutral organo-Zintl building blocks, $\text{Sn}_7\text{Bi}_2\text{-C}_2\text{H}_3$ and $\text{Sn}_7\text{Bi}_2\text{-C}_2\text{H}_2$, which have smaller gap sizes than the resulting assemblies, while the ionic assembly has a smaller gap size than its building block, KSn_6Bi_3 . The changes in the electronic structure in the organo-Zintl and ionic assemblies show two different results as well.

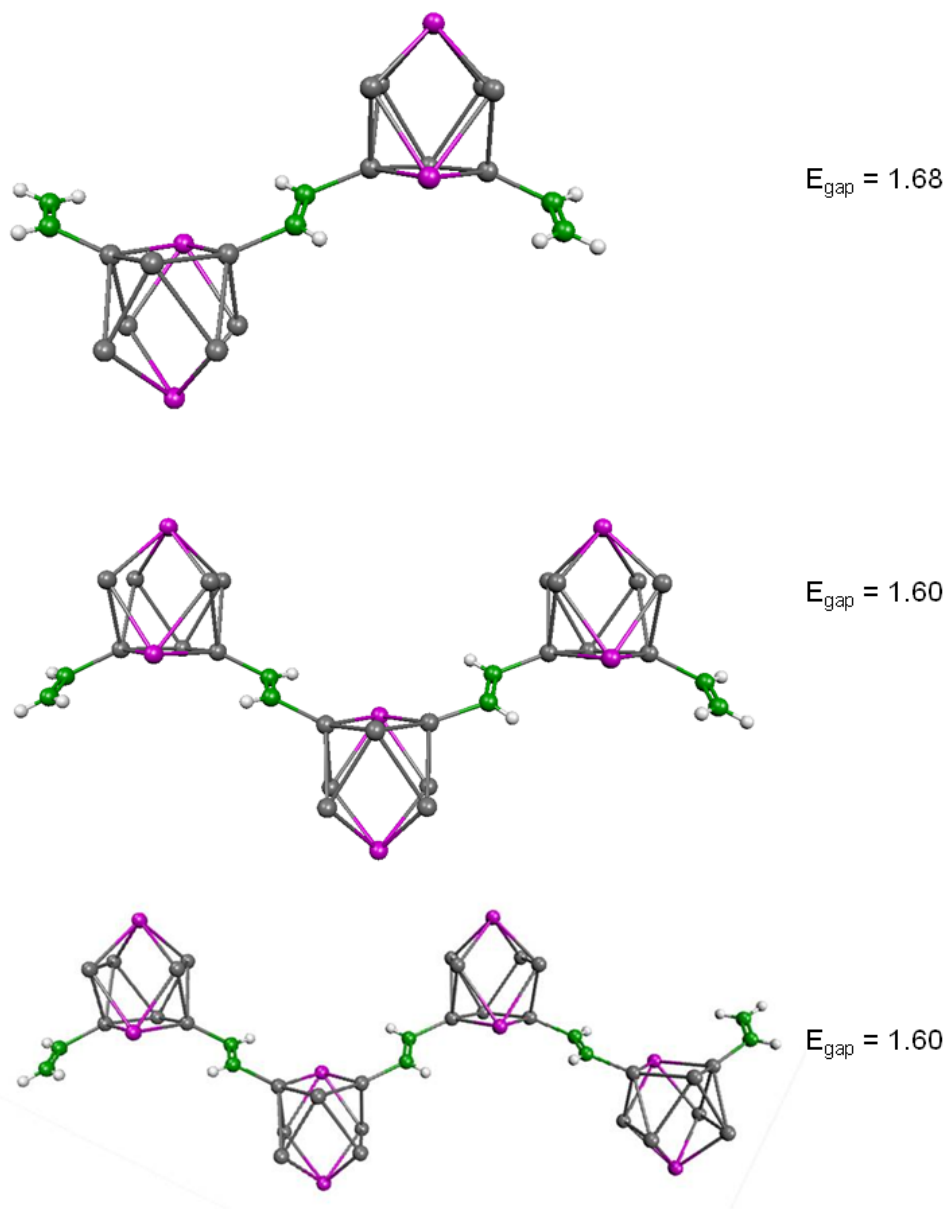


Figure 10.2.2 Lowest Energy structures for the $(\text{C}_2\text{H}_2)_k(\text{C}_2\text{H}_3)_2(\text{Sn}_7\text{Bi}_2)_j$ cluster assemblies ($j = 2 - 4$; $k = j - 1$). The HOMO-LUMO gap (E_{gap}) values are given in electron volts. The gray, pink, green, and white balls represent the Sn, Bi, C, and H atoms respectively.

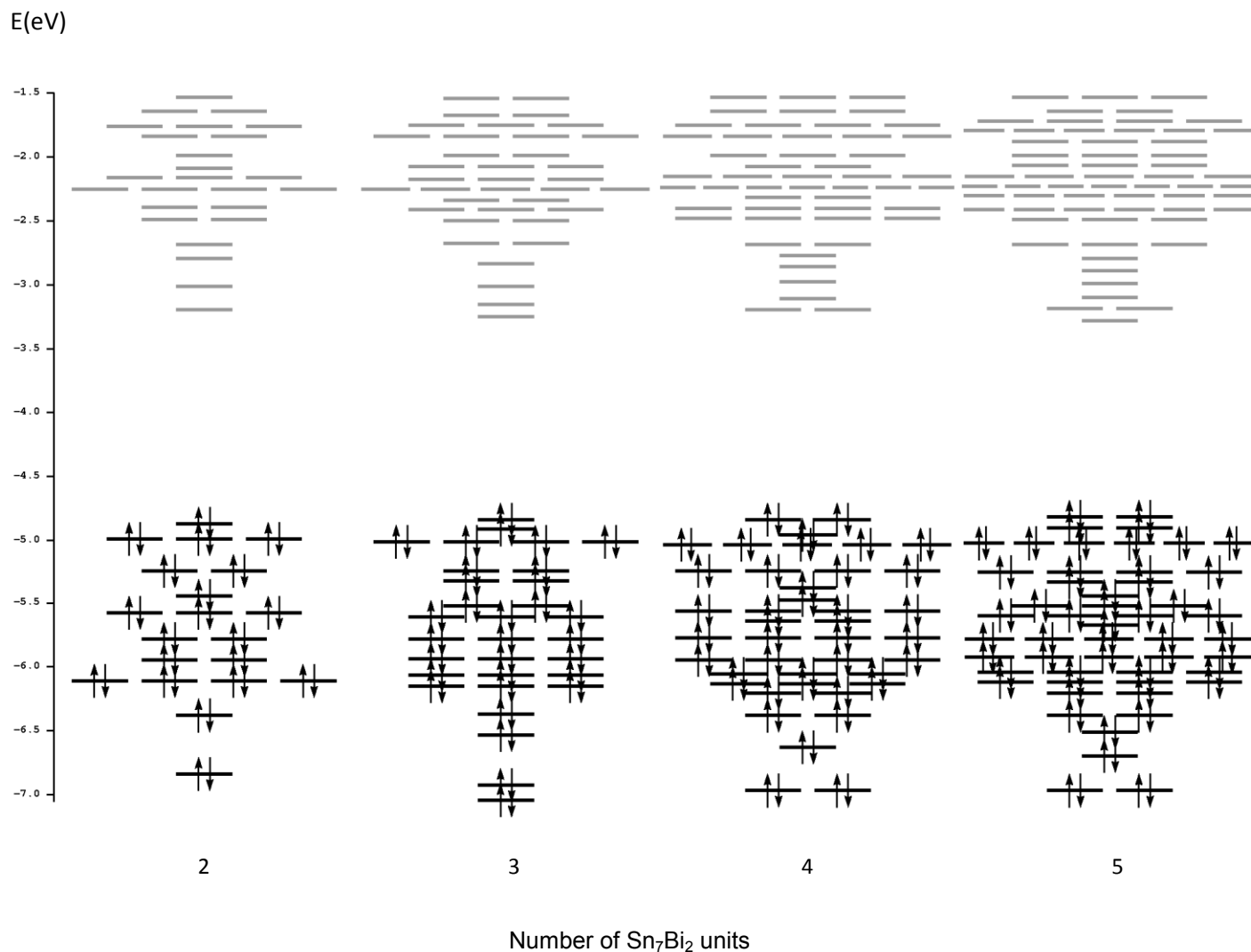


Figure 10.2.3 Electron levels for the organo-Zintl cluster assemblies.

In the ionic assemblies, $(\text{KSn}_6\text{Bi}_3)_n$, the change in the electronic levels seemed dramatic when increasing the number of monomers. These changes were attributed to 1) distance between building blocks and 2) the behavior of the monomer electronic level filling, which in both cases coerced a change in the nature of the electronic levels. However, the organo-Zintl cluster assemblies illustrated equivalent spacing, facilitated through the use of the organic substituent,

which allowed the electronic structure to “stack” or “bunch” maintaining similar HOMO and LUMO energy levels as the assemblies continue to grow.

The main reason for the major difference seen between the organo- and alkali-based Zintl cluster assemblies is due to the nature of counteraction itself. In the case where a more typical counteraction is used, such as an alkali like potassium, the atom readily donates its electron to the cluster with the donated electron residing in the upper occupied states. This is different for an organic ligand in that the organic substituent behaves in a covalent manner resulting in its electron residing in deeper occupied states than its ionic counterpart. The similarities and differences between the $(\text{KSn}_6\text{Bi}_3)_n$ and organo-Zintl assemblies show that by utilizing clusters with the same stability mechanism as building blocks one can design intriguing materials with varying properties.

10.3 Chapter 10 Summary

From the identification of gas phase Zintl analogues two we have discovered two possible avenues for designing cluster assemblies. The first involves using a typical Group 1 counteraction to stabilize the Zintl analogue. Using the KSn_6Bi_3 motif as a building block, $[\text{KSn}_6\text{Bi}_3]_n$ ring assemblies were designed with variation in the HOMO-LUMO gap values. The variation was found to evolve from the difference in electronic structure from the building block KSn_6Bi_3 to the dimer, trimer and tetramer. Once the assembly incorporates more than four KSn_6Bi_3 clusters, the electronic structure appears to be similar to that found in the tetramer. The largest HOMO-LUMO gap, 1.8 eV is found for the $[\text{KSn}_6\text{Bi}_3]_4$ ring assembly. The second assembly involves the use of an organic molecule as a ligand and counteraction. The Sn_7Bi_2^- cluster was found to be analogous to the Sn_9^{3-} and by using two organic molecules, $-\text{C}_2\text{H}_3$, the Sn_7Bi_2 cluster became analogous to the Sn_9^4- . The cluster assembly was composed of $\text{Sn}_7\text{Bi}_2(\text{C}_2\text{H}_2)_2$ building blocks surrounded by two $\text{Sn}_7\text{Bi}_2\text{C}_2\text{H}_3$ clusters. As more organo-Zintl clusters were combined, the resulting $(\text{C}_2\text{H}_2)_k(\text{C}_2\text{H}_3)_2(\text{Sn}_7\text{Bi}_2)_j$ ($j = 1 - 4$; $k = j - 1$) cluster assembled chains were composed of equidistant neutral Sn_7Bi_2 clusters with $-\text{C}_2\text{H}_2$ organic substituents behaving as spacers and counteractions. From the electronic structure, the trans-assembled dimer HOMO-LUMO gap was approximately 1.7 eV, with the trimer and tetramer slightly smaller at 1.6 eV. The electronic structure for each of the organo-Zintl assemblies remained similar in appearance which is attributed to the equidistant nature of the organo-Zintl assembly. The differences in the evolution in the electronic structure using Zintl analogues as building blocks show that the properties can be tuned in cluster assemblies.

Chapter 11 Conclusions

We have discussed a process in which by first identifying and secondly classifying stable clusters, one can design nanomaterials with control over the architecture and electronic properties. Using theoretical computations based on the Kohn-Sham density functional formalism, we have identified and classified a variety of stable clusters through their respective electronic structures. The categorized clusters in this study include those based on the confined nearly free electron gas or jellium, “all-metal” aromatic, Zintl analogues and metal-carbides. By understanding the stability mechanism in a given cluster, we were able to design cluster assemblies with tailored properties. The organo-metallic sandwich motif, $[C_6H_6]V[Al_3Sb]$, showed the possibility of designing a series of magnetic materials based on stable “all-metal” aromatic clusters. The most promising cluster building blocks were the deltahedral Zintl analogues. The insight gained with the use of an alkali and/or organic substituents as counterions illustrated how one could tune the electronic and structural properties of a cluster assembled material. This step-wise methodology beginning from identification to classification and ultimately the assembly construction is proposed as a viable procedure in designing property precise nanomaterials using stable clusters as building blocks.

Chapter 12 Future Prospects

Though some of the questions on cluster assemblies have been answered, there is further room for scientific investigation. For example, even though many of the clusters studied have been synthesized in the gas phase, some have not been attempted as of this date. The organo-Zintl clusters previously identified theoretically have not been synthesized though these clusters have large gap sizes and electron affinities. Included in this experimental endeavor is the possibility of synthesizing magnetic superatoms such as $\text{Ag}_{24}\text{Mn}(\text{SH})_{18}$. These cluster show extreme promise in the ability to be synthesized through either the gas phase or liquid synthesis.

Once synthesized, these clusters can be assembled and deposited on a surface. The future of this possibility leads to the question, how will the cluster-surface and assembly-surface interactions affect the properties of the cluster assembly? Or, if synthesized as a crystal, what effect will the solvent have on the clusters and cluster assembly? If one were to use a larger counteranion such as a superatomic alkali or a crypt-counteranion, how would this change the assembly? Even in the case of the organo-Zintl assembly, how would the electronic structure change if one were to use a larger organic substituent? Can one design a porous three-dimensional organo-Zintl cluster assembly with the ability to be used for hydrogen storage? This opens the door to investigations on the nanocatalytic effects of these new assemblies.

Of course and even larger implication resides in the magnetic effects of cluster assemblies. For example, by extending the sandwich motif to triple-decker or even longer wires the investigation on the magnetic anisotropy of the assembly. Can these be used in the future of spintronics or have superconductive properties? Furthermore what happens to the optical

properties as the magnetic assemblies, including those composed of the magnetic superatoms, continue to assemble?

Thus there is a larger range of possibilities that can grow from the research found in this document. The clusters and assemblies can be utilized in the ever growing fields of technology and cluster science. The unique construction of the assemblies based on the cluster's electronic structure will lead to new possibilities and applications in nanoscience. One can see the future of cluster assembled materials is a strong and viable endeavor from the research presented here.

References

- [1] M. Arenz; U. Landman; U. Heiz; “Co Combustion on Supported Gold Clusters” *ChemPhysChem* **7**, 1871 (2006).
- [2] B.V. Reddy; S.N. Khanna; B.I. Dunlap; “Giant Magnetic-moments in 4D clusters” *Physical Rev. Lett.* **70**, 3323 (1993).
- [3] J. McMurry; R.C. Fay; Chemistry 3rd Edition; (Prentice Hall, New Jersey, 2001).
- [4] P.A. Clayborne; T.C. Nelson; T.C. DeVore; “Temperature programmed desorption-FTIR investigation of C₁-C₅ primary Alcohols adsorbed on gamma-alumina” *Applied Catalysis A* **257**, 2, 225, (2004).
- [5] A.R. McInroy; D.T. Lundie; J.M. Winfield; C.C. Dudman; P. Jones; D. Lennon; “The application of diffuse reflectance infrared spectroscopy and temperature programmed desorption to investigate the interaction of methanol on eta-alumina” *Langmuir* **21**, 11092, (2005).
- [6] R.E. Leuchtner; A.C. Harms; A.W. Castleman Jr.; “Thermal Metal Cluster Anion Reactions: Behavior of Aluminum Clusters with oxygen” *J. Chem. Phys.* **91**, 2753, 1989.
- [7] J.A. Alonso; Structure and Properties of Atomic Nanoclusters (Imperial College Press 2005).
- [8] P.A. Clayborne; N.O. Jones; A.C. Reber; J.U. Reveles; M.C. Qian; S.N. Khanna; “Superatoms and their assemblies based on alkali and super-alkali motifs” *Journal of Computational Methods in Sciences and Engineering* **7**, 417 (2007).
- [9] H. W. Kroto; J. R. Heath; S. C. O'Brien; R. F. Curl; R. E. Smalley; “C₆₀: Buckminsterfullerene” *Nature* **318**, 162 (1985).

- [10] M.C. Qian; S.V. Ong; S.N. Khanna; M.B. Knickelbein; "Magnetic endohedral metallofullerenes with floppy interiors" *Phys. Rev. B* **75**, 10 (2007).
- [11] R.D. Bolskar; "Gadofullerene MRI Contrast Agents" *Nanomedicine* **3**, 2 (2008)
- [12] Z. Zhang; C. C. Chen; S. P. Kelty; H. J. Dai; C. M. Lieber; ""The Superconducting Energy-Gap of Rb₃C₆₀" *Nature* **353**, 333 (1991).
- [13] L.C. Chong; J. Sloan; G. Wagner; S.R.P. Silva; R.J. Curry; ""Controlled Growth of True Nanoscale Single Crystal Fullerites for Device Applications" *J. Mater. Chem.* **18** (2008).
- [14] D.E. Bergeron; A.W. Castleman, Jr.; T. Morisato; S.N. Khanna; "Formation of Al₁₃F: Evidence for the Superhalogen Character of Al₁₃" *Science* **304**, 84 (2004).
- [15] A. Ugrinov, A. Sen, A.C. Reber, M. Qian and S.N. Khanna *Journal of the American Chemical Society* **130**, 782 (2008).
- [16] S.N. Khanna; P. Jena; "Assembling Crystals from Clusters" *Phys. Rev. Lett.* **69**, 1664 (1992).
- [17] W. D. Knight; K. Clemenger; W.A. de Heer; W.A. Saunders; M.Y. Chou; M.L. Cohen; "Electronic Shell Structure and Abundances of Sodium Clusters" *Phys. Rev. Lett.* **52**, 2141 (1984)
- [18] W. Ekardt; "Work Function of Small Metal Particles- Self-Consistent Spherical Jellium-Background Model" *Phys. Rev. B* **29**, 11558, (1984).
- [19] W. Ekardt; "Dynamical Polarizability of Small Metal Particles- Self-Consistent Spherical Jellium Background Model" *Phys Rev Lett* **52**, 21 (1984).
- [20] W. D. Knight; K. Clemenger; W. A. de Heer; W. A. Saunders; ""Electronic Shell Structure in Potassium Clusters" *Solid State Commun.* **35**, 445 (1985).

- [21] Roy L. Johnston Atomic and Molecular clusters (Taylor and Francis, London 2002).
- [22] W.A. de Heer; “The physics of simple metal clusters: experimental aspects and simple models” *Reviews of Modern Physics* **65**, 3 (1993).
- [23] A.W. Castleman, Jr.; S. N. Khanna; “Clusters, Superatoms, and Building Blocks of New Materials” *J. Phys. Chem. C* **113**, 2664 (2009).
- [24] D.E. Bergeron; P. J. Roach; A.W. Castleman Jr.; N.O. Jones; S. N. Khanna; “Al Cluster Superatoms as halogens in polyhalides and as alkaline earths in iodide salts” *Science* **307**, 231 (2005).
- [25] N.O. Jones, “A Prelude to a Third dimension of the Periodic Table: Superatoms of Aluminum Iodide clusters” (Ph.D. dissertation, Virginia Commonwealth University, 2006)
- [26] J.U Reveles; S.N. Khanna; P.J. Roach; A.W. Castleman; “Multiple valence superatoms” *Proceeding of the National Academy of Sciences of the United States of America* **103**, 18405 (2006).
- [27] J.U. Reveles; P.A. Clayborne; A.C. Reber; S.N. Khanna; K. Pradhan; P. Sen; M.R. Pederson. “Designer magnetic superatoms” *Nature Chemistry* **1**, 310 (2009).
- [28] M. Walter; J. Akola; O. Lopez-Acevedo; P.D. Jadzinsky; G. Calero; C.J. Ackerson; R.L. Whetten; H. Gronbeck; H. Hakkinen; “A unified view of ligand-protected gold clusters as superatom complexes” *Proceedings of the National Academy of Sciences of the United States of America* **105**, 9157 (2008).
- [29] K. Clemenger; “Ellipsoidal Shell Structure in free-electron metal clusters” *Phys. Rev. B* **32**, 2 (1985).
- [30] J. Zheng; P.R. Nicovich; R.M. Dickson; “Highly Fluorescent noble-metal quantum dots” *Annual Review of Physical Chemistry* **58**, 409 (2007).

- [31] Palpant B; Negishi Y; Sanekata M; Miyajima K; Nagao S; Judai K; Rayner DM; Simard B; Hackett PA; Nakajima A; Kaya K; "Electronic and geometric properties of exohedral sodium- and gold-fullerenes." *J. Chem. Phys.* **114**, 8459 (2001).
- [32] Kohn A; Weigend F; Ahlrichs R; "Theoretical study on clusters of magnesium" *PhysChem ChemPhys* **3**, 711 (2001).
- [33] Ingolfsson O; Busolt U; Sugawara K; "Energy-resolved collision-induced dissociation of Cu_n^+ ($n = 2-9$): Stability and fragmentation pathways" *J. Chem Phys* **112**, 4613 (2000).
- [34] W. Bouwen; Vanhoutte F; Despa F; Bouckaert S; Neukermans S; Kuhn LT; Weidele H; Lievens P; Silverans RE; "Stability effects of Au_nX_m^+ ($X = \text{Cu}, \text{Al}, \text{Y}, \text{In}$) clusters" *Chem Phys Lett* **314**, 227 (1999).
- [35] H. Hakkinen; "Atomic and Electronic Structure of gold clusters: understanding flakes, cages, and superatoms from simple concepts" *Chem Soc Rev* **37**, 1847 (2008).
- [36] E. Janssens; H. Tanaka; S. Neukermans; R. E. Silverans; P. Lievens; "Two-dimensional magic number in mass abundances of photofragmented bimetallic clusters" *New Journal of Physics* **5**, (2003).
- [37] T. Holtz; E. Janssens; N. Veldeman; T. Veszpermi; P. Lievens; M.T. Nguyen; "The Cu_7Sc cluster is a stable sigma-aromatic seven-membered ring." *ChemPhysChem* **9**, 833 (2008).
- [38] C. Rajesh; C. Majumder; "Oxidation of Al doped Au clusters: A first principles study" *J Chem Phys* **130**, 234309 (2009).
- [39] Y.P. Chiu; L.W. Huang; C.M. Wei; C.S. Chang; T.T. Tsong; "Magic Numbers of Atoms in Surface-Supported Planar Clusters" *Phys Rev Lett* **97**, 165504 (2006).
- [40] C. R. Ashman; "Geometries, electronic Structure and Magnetic Properties of Pure and Mixed Clusters" Ph.D. Dissertation, 2002.

- [41] S.A. Rutta; P.A. Hintz; S.L. Anderson; "Boron cluster ion oxidation – Reaction with CO₂, Dissociation of boron cluster oxide (BNO⁺) ions and sequential oxidation" *J. Chem. Phys.* **94**, 2833 (1991).
- [42] P. Y. Bruice; Organic Chemistry (Prentice Hall, New Jersey 1995)
- [43] X. Li; A. Kuznetsov; H. Zhang; A. Boldyrev; L.S. Wang; "Observation of all-metal aromatic molecules" *Science* **291**, 5505 (2001).
- [44] W.G. Xu; B. Jin; "Aromaticity of the planar pentagonal As₅⁻ anion in the MAs₅ (M = Li, Na, K, Rb, and Cs) and MAs₅⁺ (M = Be, Mg Ca, Sr and Ba) clusters" *Journal of Molecular Structure-Theochem* **759**, 101 (2006).
- [45] D.Y. Zubarev; B.B. Averkiev; H.J. Zhai; L.S. Wang; A.I. Boldyrev; "Aromaticity and antiaromaticity in transition-metal systems" *Phys Chem Chem Phys* **10**, 257 (2008).
- [46] A.N. Alexandrova; A.I. Bodyrev; "Sigma-aromaticity and sigma-antiaromaticity in alkali metal and alkaline earth metal small clusters" *J Phys Chem A* **107**, 554 (2003).
- [47] P. Prakash; A. Kundu; S.K. Pati; "The Electronic and Magnetic Properties of a few transition-metal Clusters" *J. Comp. Chem.* **20**, 355 (2009).
- [48] A. Hirsch; Z. Chen; H. Jiao; *Angew. Chem., Int. Ed.* **40**, 2834 (2001).
- [49] Z.F. Chen; C.S. Wannere; C. Corminboeuf; R. Puchta; P.V. Schleyer; *Chem Rev* **105**, 3842 (2005).
- [50] P.v.R. Schleyer; C. Maerker; A. Dransfeld; H. Jiao; N.J.R.v E. Hommes; "Nucleus-Independent Chemical Shifts: A Simple and Efficient Aromaticity Probe" *J Amer Chem Soc* **118**, 6317 (1996).
- [51] C.A. Tsipis; "DFT study of "all-metal" aromatic compounds" *Coordination Chemistry Reviews* **249**, 2740 (2005).

- [52] J.A.N.F. Gomes; R.B. Mallion; “Aromaticity and ring currents” *Chemical Reviews* **101**, 1349 (2001).
- [53] A.I. Boldyrev; A.E. Kuznetsov; “On the Resonance Energy in New All-Metal Aromatic Molecules” *Inorganic Chemistry* **41**, 3 (2002).
- [54] D.K. Seo; J.D. Corbett; “Perspectives: Chemistry – Aromatic metal clusters”; *Science* **291**, 841 (2001).
- [55] J.D. Corbett; “Polyatomic Zintl Anions of the Post-Transition Elements” *Chemical Reviews* **85**, 383 (1985).
- [56] Zintl E. *Phys. Chem. Abt. A* (1931)
- [57] Corbett, JD *Chem. Rev.* (1985)
- [58] Corbett J.D. *J. Chem. Soc., Chem. Commun.* (1975)
- [59] M. Somer, W Carrillo-Cabrera, EM Peters, K Peters, M Kaupp, HG Schnering; “The Sn_5^{2-} compound $[\text{K}-2,2,2\text{-crypt}]_2\text{Sn}_5$ – Synthesis, crystal structure, Raman spectrum and hierarchical relationship to CaIn_2 ” *Zeitschrift Fur Anorganische und allgemeine Chemie* **635**, 37 (1999).
- [60] A. Ugrinov; S. C. Sevov; “Synthesis and structure of $[\text{K}-(12\text{-crown-4})(2)]_2[\text{K}-(12\text{-crown-4})]_2[\text{Sn}_9]$ center dot 4en” *Appl Organometallic Chem* **17**, 373 (2003).
- [61] S. J. Kim; S. D. Hoffman; T. F. Fasser; “ $\text{Na}_{29}\text{Zn}_{24}\text{Sn}_{32}$: A Zintl phase containing a novel type of Sn_{14} enneahedra and heteroatomic Zn_8Sn_4 icosahedral” *Angewandte Chemie-International Edition* **46**, 3144 (2007).
- [62] S. C. Sevov; J. M. Goicoechea; “Chemistry of deltahedral Zintl ions” *Organometallics* **25**, 5678 (2006).

- [63] S Bobev; S. C. Sevov; "Synthesis and characterization of the largest isolated clusters of tin, Sn_{12}^{2-} , in $(\text{AE})\text{Na}_{10}\text{Sn}_{12}$ (AE = Ca or Sr)" *Inorg Chem* **40**, 5361 (2001).
- [64] S Bobev; S. C. Sevov; "Arachono- Sn_8^{6-} or closo- $[\text{Li}_2\text{Sn}_8]^{4-}$? Synthesis and Characterization of $\text{A}_4\text{Li}_2\text{Sn}_8$ (A = Rb, K)" *Angewandte Chemie International Ed* **39**, 4108 (2000).
- [65] J.D. Corbett; "Polyanionic clusters and networks of early p-element metals in the solid state: Beyond the Zintl boundary" *Angewandte Chemie-Internation Edition* **39**, 4 (2000).
- [66] L.F. Cui; X. Huang; L.M. Wang; D.Y. Zubarev; A.I. Boldyrev; J. Li; L.S. Wang; " Sn_{12}^{2-} : Stannaspherene" *J Amer Chem Soc* **128**, 8390 (2006).
- [67] R.E. Williams; "Carboranes and Boranes: Polyhedra and Polyheral Fragments" *Inorg Chem* **10**, 210 (1971).
- [68] K. Wade; "The Structural Significance of the Number of Skeletal Bonding electron-pairs in Carboranes, the Higher Boranes and Borane Anions, and Various Transition-metal Carbonyl Cluster Compounds" *Chemical Society Chemical Communication* **15**, 792 (1971).
- [69] K. Wade; "Skeletal Bond orders in Borane anions $\text{B}_n\text{H}_n^{2-}$ and related Closo-cluster species" *Inorganic & Nuclear Chemistry Letters* **8**, 823 (1972).
- [70] D.M.P. Mingos; "General theory for cluster and Ring compounds of Main Group and Transition-Elements" *Nature-Physical Science* **239**, 16 (1972).
- [71] M. Driess; N. Heinrich; *Molecular Clusters of the Main Group Elements* (Wiley-VCH, Germany, 2004).
- [72] J.D. Corbett; "Homopolyatomic ions of heavy post-transition elements. The Preparation, Properties, and Bonding of $\text{Bi}_5(\text{AlCl}_4)_3$ and $\text{Bi}_4(\text{AlCl}_4)$ " *Inorg Chem* **7**, 198 (1968).

- [73] Intermetallic Compounds: Vol. 3, Principles and Practice. Ed. JH Westbrook and R.L. Fleischer John Wiley & Sons, Ltd. 2002.
- [74] U. Gupta; A.C. Reber; P.A. Clayborne; J.J. Melko; S.N. Khanna; A.W. Castleman; “Effect of charge and Composition on the structural fluxionality and stability of nine atom tin-bismuth Zintl Analogues” *Inorg Chem* **47**, 23 (2008).
- [75] U. Gupta; J.U. Reveles; J.J. Melko; S.N. Khanna; A.W. Castleman; “Electronic structure of Bi_3Ga_y^- semiconductor clusters and the special stability of Bi_3Ga_2^- : A gas phase Zintl analogue” *Chem Phys Lett* **467**, 223 (2009).
- [76] Z. Sun; Q.H. Zhu; Z. Gao; Z.C. Tang; “Experimental and theoretical investigation on binary anionic clusters of Al_mBi_n^- ” *Rapid Communication in Mass Spectrometry* **23**, 2663 (2009).
- [77] A.C. Reber; A. Ugrinov; A. Sen; M. Qian; S.N. Khanna; “Helical and linear $[\text{K}(\text{As}_{11})]^{2-}$ chains: Role of solvent on the conformation of chains formed by Zintl anions” *Chem Phys Lett* **473**, 305 (2009).
- [78] L.S. Wang; H. Cheng; “Growth Pathways of Metallo-carbohedrenes: Cagelike or Cubic” *Phys. Rev. Lett.* **78**, 2983 (1997).
- [79] N. Akman; E. Durgun; T. Yildirim; S. Ciraci; “Hydrogen storage capacity of titanium met-cars” *J. Phys.: Condens. Matter* **18**, 9509 (2006).
- [80] H. S. Domingos; “Stability and properties of the cluster assembled solid phases of X_8C_{12} and YX_7C_{12} ” *J. Phys. Condens. Matter* **17**, 2571 (2005).
- [81] Y. Wang; J. Szczepanski; M. Vala; “Silver-Carbon Cluster AgC_3 : Structure and Infrared Frequencies” *J. Phys. Chem. A* **112**, 11088 (2008).

- [82] H.T. Deng; K.P. Kerns; R.C. Bell; A.W. Castleman, Jr; "Oxidation induced ionization and reactions of metal carbide clusters (Nb, Zr, V, Ta)" *International Journal of Mass Spectrometry* **167**, 615 (1997).
- [83] B.V. Reddy; "Electronic Structure and Magnetic Properties of Mixed clusters" Ph.D. dissertation, 1994.
- [84] B.C. Guo; K.P. Kerns; A.W. Castleman Jr.; "Ti₈C₁₂⁺-Metallo-Carbohedrenes: A New Class of Molecular Clusters?" *Science* **255**, 1411 (1992).
- [85] B.V. Reddy; S.N. Khanna; "Formation and stability of dodecahedral and fcc structures in metal--carbon clusters.:" *Chem. Phys. Lett.* **290**, 104 (1993).
- [86] H. Sakurai; A.W. Castleman, Jr.; "Ionization Potentials for the Titanium, Zirconium, and the Mixed Metal Met-Cars." *J. Phys. Chem. A* **102**, 10486 (1998).
- [87] S.E. Kooi; A.W. Castleman Jr.; "Delayed ionization in transition metal--carbon clusters: Further evidence for the role of thermionic emission." *J. Chem. Phys.* **108**, 8864 (1998).
- [88] P. Liu; J. A. Rodriguez; J. T. Muckerman; "The chemical activity of metal compound nanoparticles: Importance of electronic and steric effects in M₈C₁₂ (M=Ti, V, Mo) metcars" *J. Chem. Phys.* **121**, 10321 (2004).
- [89] D.E. Clemmer; J.M. Hunter; K.B. Shelimov; M.F. Jarrold; "Physical and chemical evidence for metallofullerenes with metal atoms as part of the cage." *Nature* **372**, 248 (1994).
- [90] J.S. Pilgrim; L.R. Brock; M.A. Duncan; "Photodissociation of Niobium-Carbon Clusters and Nanocrystals" *J. Phys. Chem.* **99**, 544 (1995).
- [91] K.L. Knappenberger; C.E. Jones; M.A. Sobhy; A.W. Castleman, Jr.; "Versatile Cluster Based Photoelectron Spectrometer" *Rev. Sci. Instrum.* **77**, 123901 (2006).

- [92] Electronic Structure Basic Theory and Practical Methods Richard M. Martin Cambridge University Press 2004
- [93] *Quantum Chemistry* Donald A. McQuarrie (University Science Books 1983)
- [94] Hohenberg, P. and Kohn, W., Phys. Rev. 136:B864-871, 1964.
- [95] W. Kohn and L.J. Sham, Phys. Rev. **140**, A1133 (1965).
- [96] Density Functional Theory of Atoms and Molecules Robert G. Parr Oxford University Press 1994.
- [97] T. Henderson, B.G. Janesko, and G.E. Scuseria, *J. Phys. Chem. A* **112**(49), 2008.
- [98] *A Chemist's Guide to Density Functional Theory 2nd ed.* Wolfram Koch and Max. C. Holthausen (Wiley-VCH, Weinheim 2007)
- [99] J.C. Slater; *Phys Rev.* **36**, 51 (1930).
- [100] Roothaan, C.C.J. and Bagus, P.S. Methods in Computational Physics (Academi Press, New York, 1963) Vol.II
- [101] Lenthe, van E.; E.J. Baerends; J.G. Snijders; "Relativistic total energy using regular approximations" *J. Chem. Phys.* **101**, 9783 (1994).
- [102] Electronic Structure Modeling: Connections Between Theory and Software. Carl Trindle and Donald Shillady CRC Press FL 2008.
- [103] S.F. Boys; F. Benrardi; "Calculation of small molecular interactions by differences of separate total energies- Some procedures with reduced errors." *Molecular Physics* **19**(4) 1970.
- [104] S. Simon; M. Duran; J.J. Dannenberg; "How does basis set superposition error change the potential surfaces for hydrogen bonded dimers?" *Journal of Chemical Physics* **106**(24) 1996.

[105] Köster, A. M.; Calamininci, P.; Flores, R.; Geudtner, G.; Goursot, A.; heine, T.; Janetzko, F.; Patchkovskii, S.; Reveles, J. U.; Vela, A.; Salahub, Dr. deMon, NRC, Canada, 2004. Available from: <http://www.deMon-software.com>.

[106] a) M.R. Pederson and K.A. Jackson, *Phys. Rev. B* **41**, 7453 (1990); b) K.A. Jackson and M.R. Pederson, *Phys. Rev. B* **42**, 3276 (1990); c) D.V. Porezag, M.R. Pederson, *Phys. Rev. A* **60**, 2840 (1999).

[107] ADF2006.01d, SCM, Theoretical Chemistry; Vrije Universiteit: Amsterdam, The Netherlands; <http://www.scm.com>

[108] Frisch, M. J.; Trucks, G. W.; Schlegel, H. B.; Scuseria, G. E.; Robb, M. A.; Cheeseman, J. R.; Montgomery, J. A., Jr.; Vreven, T.; Kudin, K. N.; Burant, J. C.; Millam, J. M.; Iyengar, S. S.; Tomasi, J.; Barone, V.; Mennucci, B.; Cossi, M.; Scalmani, G.; Rega, N.; Petersson, G.A.; Nakatsuji, H.; Hada, M.; Ehara, M.; Toyota, K.; Fukuda, R.; Hasegawa, J.; Ishida, M.; Nakajima, T.; Honda, Y.; Kitao, O.; Nakai, H.; Klene, M.; Li, X.; Knox, J. E.; Hratchian, H. P.; Cross, J. B.; Bakken, V.; Adamo, C.; Jaramillo, J.; Gomperts, R.; Stratmann, R.E.; Yazyev, O.; Austin, A. J.; Cammi, R.; Pomelli, C.; Ochterski, J.W.; Ayala, P. Y.; Morokuma, K.; Voth, G. A.; Salvador, P.; Dannenberg, J. J.; Zakrzewski, V. G.; Dapprich, S.; Daniels, A. D.; Strain, M. C.; Farkas, O.; Malick, D. K.; Rabuck, A. D.; Raghavachari, K.; Foresman, J. B.; Ortiz, J. V.; Cui, Q.; Baboul, A. G.; Clifford, S.; Cioslowski, J.; Stefanov, B. B.; Liu, G.; Liashenko, A.; Piskorz, P.; Komaromi, I.; Martin, R. L.; Fox, D. J.; Keith, T.; Al-Laham, M. A.; Peng, C. Y.; Nanayakkara, A.; Challacombe, M.; Gill, P. M. W.; Johnson, B.; Chen, W.; Wong, M. W.; Gonzalez, C.; Pople, J. A. *Gaussian 03*; Gaussian, Inc.: Wallingford, CT, 2004.

[109] R. Flores-Moreno; J. Alvarez-Mendes; A. Vela; A.M. Koster; “Half-numerical evaluation of pseudopotential integrals” *J. Comput. Chem.* **27**, 1009 (2006).

- [110] J.U. Reveles; A.M. Koster; "Geometry optimization in density functional methods" *J. Comput Chem* **25**, 1109 (2004).
- [111] <http://www.scm.com>.
- [112] Velde, G.; Bickelhaupt, F.M.; Baerends, E.J.; Fonseca Guerra, C.; van Gisbergen, S.J.A.; Snijders, J.G.; Ziegler, T.; "Chemistry with ADF" *Journal of Computational Chemistry* **22**, (2001).
- [113] C.G. Broyden; "Convergence of single rank quasi-newton methods" *Math. Comp.* **25**, 365 (1970).
- [114] E. van Lenthe; E.J. Baerends; J. G. Snijders; "Relativistic regular two-component Hamiltonians" *J. Chem Phys.* **99**, 4597 (1993).
- [115] E. van Lenthe; J.G. Snijders; E.J. Baerends; "The zero-order regular approximation for relativistic effects: The effect of spin-orbit couplings in closed shell molecules" *J. Chem. Phys.* **105**, 6505 (1996).
- [116] E. van Lenthe; R. van Leeuwen; E.J. Baerends; J. G. Snijders.; *Int. J. Quant. Chem.* **57**, 281 (1996).
- [117] G. Schreckenbach; T.J. Ziegler; "Calculation of NMR shielding tensors using gauge-including atomic orbitals and modern density-functional theory" *J. Phys. Chem.* **99**, 606 (1995).
- [118] R. Ditchfield; "Self-consistent perturbation theory of diamagnetism. 1. Gauge-invariant LCAO method for NMR Chemical-Shifts" *Molecular Phys.* **27**, 789 (1974).
- [119] T.A. Keith; R.F.W. Bader; "Calculation of magnetic response properties using atoms in molecules" *Chem. Phys. Lett.* **194**, 1 (1992).
- [120] T.A. Keith; R.F.W. Bader; "Calculation of magnetic response properties using a continuous set of gauge transformations" *Chem. Phys. Lett.* **210**, 223 (1993).

- [121] J.R. Cheeseman; G.W. Trucks; T.A. Keith; M.J. Frisch; “A Comparison of Models for Calculating Nuclear magnetic Resonance Shielding Tensors” *J. Chem. Phys.* **104**, 5497 (1996).
- [122] J.P. Perdew; K. Burke; M. Ernzerhof; “Generalized Gradient Approximation Made Simple” *Phys. Rev. Lett.* **77**, 3865 (1996).
- [123] a) B.I. Dunlap; J.W.D. Connolly; J.R. Sabin; “On first-row diatomic molecules and local density models” *J. Chem. Phys.* **71**, 4993 (1979). b) N. Godbout; D. Salahub; J. Andzelm; E. Wimmer; “Optimization of Gaussian-type basis sets for local spin density functional calculations. Part I. Boron through neon, optimization technique and validation.” *Can. J. Chem.* **70**, (1992).
- [124] a) A.D. Becke; “Density functional Exchange-Energy approximation with correct asymptotic-behavior” *Phys. Rev. A* **38**, 3098 (1988); b) J.P. Perdew; “Density-functional approximation for the correlation-energy of the inhomogeneous electron-gas” *Phys Rev. B* **33**, 8822 (1986).
- [125] K.A. Peterson; “Systematically convergent basis sets with relativistic pseudopotentials. I. correlation consistent basis sets for the post-d group 13-15 elements” *J. Chem. Phys.* **119**, 11113 (2003).
- [126] B. Metz; H. Stoll; M. Dolg; “Small-core multiconfiguration-Dirac-Hartree-Fock-adjusted pseudopotentials for post-d main group elements: Application to PbH and PbO” *J. Chem. Phys.* **113**, 2563 (2000).
- [127] a) D. Feller; “The role of databases in support of computation chemistry calculations” *J. Comp. Chem.* **17**, 1571 (1996). b) K.L. Schuchardt; B.T. Dieder; T. Elsethagen; L. Sun; V. Gurumoorthi; Chase, J.; Li, J.; Windus, T.L.; *J. Chem. Inf. Model.*, **47**, 3, 1045-1052,2007, doi: 10.1021/ci600510j.

- [128] P.J. Hay; W.R. Wadt; “Ab initio effective core potentials for molecular calculations. Potentials for the transition metal atoms Sc to Hg” *J. Chem. Phys.* **82**, 270 (1985).
- [129] D. Andrae; U. Häußermann; M. Dolg; H. Stoll; H. Preuß: “Energy-adjusted ab initio pseudopotentials for the second and third row transition elements.” *Theor. Chim. Acta* **77**, 123 (1990).
- [130] E. Janssens; S. Neukermans; P. Lievens; “Shells of electrons in metal doped simple metal clusters” *Current Opinion in Solid State & Materials Science* **8**, 185 (2004).
- [131] D.E. Jiang; R.L. Whetten; “Magnetic doping of a thiolated-gold superatom: First-principles density functional theory calculations” *Phys. Rev. B* **80**, 115402 (2009).
- [132] M. Pereiro; D. Baldomir; J. Botana; J.E. Arias; K. Warda; L. Wojtczak; “Biomedical applications of small silver clusters” *J. Appl. Phys.* **103**, 07A315 (2008).
- [133] L. Shang; S.J. Dong; “Sensitive detection of cysteine based on fluorescent silver clusters” *Biosensors & Bioelectronics* **24**, 1569 (2009).
- [134] E. Borsella; E. Cattaruzza; G. De Marchi; f. Gonella; G. Mattei; P. Mazzoldi; A. Quaranta; G. Battaglin; R. Polloni; “Synthesis of silver clusters in silica-based glasses for optoelectronics applications” *J. Non-Crystalline Solids* **245**, 122 (1999).
- [135] R. Fournier; “Theoretical study of the structure of silver clusters” *J. Chem. Phys.* **115**, 2165 (2001).
- [136] E.M. Fernandez; J.M. Soler; I.L. Garzon; L.C. Balbas; “Trends in the structure and bonding of noble metal clusters” *Phys. Rev. B* **70**, 165403 (2004).
- [137] E. Janssens; S. Neukermans; X. Wang; N. Veldeman; R.E. Silverans; P. Lievens; “Stability patterns of transition metal doped silver clusters: Dopant- and size-dependent electron delocalization” *Eur. Phys. Journ. D* **34**, 23 (2005).

- [138] E. Janssens; S. Neukermans; H.M.T. Nguyen; M.T. Nguyen; P. Lievens; “Quenching of the Magnetic Moment of a Transition metal Dopant in silver Clusters” *Phys. Rev. Lett.* **94**, 113401 (2005).
- [139] X.J. Hou; E. Janssens; P. Lievens; M.T. Nguyen; “Theoretical study of the geometric and electronic structure of neutral and anionic doped silver clusters, $Ag_5X^{0,-}$ with X = Sc, Ti, V, Cr, Mn, Fe, Co and Ni” *Chem. Phys.* **330**, 365 (2006).
- [140] M. Harb; F. Rabilloud; D. Simon; “Density functional study of structural and electronic properties of small bimetallic silver-nickel clusters” *J. Phys. Chem. A* **111**, 7726 (2007).
- [141] H.G. Kramer; V. Beutel; K. Weyers; W. Demtroder; “Sub-doppler laser spectroscopy of silver dimers Ag_2 in a supersonic beam” *Chem Phys. Lett.* **193**, 331 (1992).
- [142] M.D. Morse; “Clusters of Transition-metal atoms” *Chem. Rev.* **86**, 1049 (1986).
- [143] D. Tian; H. Zhang; J. Zhao; “Structure and structural evolution of Ag_n ($n = 3-22$) clusters using a genetic algorithm and density functional theory method” *Solid State Communications* **144**, 174 (2007).
- [144] V.E. Matulis; O.A. Ivashkevich; V.S. Gurin; “*J. Molecular Structure (Theochem)* **664**, 291 (2003).
- [145] C.M. Aikens; “Origin of Discrete Optical Absorption Spectra of $M_{25}(SH)_{18}^-$ Nanoparticles (M = Au, Ag)” *J. Phys. Chem. C* **112**, 19797 (2008).
- [146] O.M. Bakr; V. Amendola; C.M. Aikens; W. Wenseleers; L. Rui; L.D. Negro; G.C. Schatz; F. Stellacci; “Silver Nanoparticles with Broad Multiband Linear Optical Absorption” *Angew. Chem. Internation Ed.* **48**, 5921 (2009).
- [147] Raymond Chang; Chemistry 8ed. (McGraw-Hill, New York 2005).

- [148] Q. Bai; B. Song; J. Hou; P. He; “First Principles study of structural and electronic properties of Al_nN ($n = 1-19$) clusters” *Phys. Lett. A* **372**, 4545 (2008).
- [149] C.E. Jones; P.A. Clayborne; J.U. Reveles; J.J. Melko; U. Gupta; S.N. Khanna; A.W. Castleman, Jr.; “ Al_nBi Clusters: Transitions Between Aromatic and Jellium Stability” *J. Phys. Chem. A* **112**, 13316 (2008).
- [150] J.J. Melko; P.A. Clayborne; C.E. Jones; J.U. Reveles; U. Gupta; S.N. Khanna; A.W. Castleman; “A Combined Experimental and Theoretical Study of Al_nX ($n = 1-6$, $X = As, Sb$) Clusters: Evidence of Aromaticity and the Jellium Model” *J. Phys. Chem.* (Submitted).
- [151] E.F. Archibong; A. St-Amant; “An Ab Initio and Density Functional Study of Al_3As , Al_3As^- , $AlAs_3$, and $AlAs_3^-$ ” *J. Phys. Chem. A* **106**, 7390 (2002).
- [152] L. Guo; H.S. Wu; “The Aluminum Arsenides Al_mAs_n ($m+n= 2-5$) and their Anions: Structures, Electron Affinities and Vibrational Frequencies.” *Eur. Phys. J. D* **42**, 259 (2007).
- [153] L. Guo; H.S. Wu; “Density Functional study of structural and electronic properties of Al_nN ($1 < n < 12$) clusters.” *Inter. J. Quant. Chem.* **106**, 1250 (2005).
- [154] Bai, Q, Song B, Hou J, He P; First Principles study of structural and electronic properties of Al_nN ($n=1-19$) clusters. *Physics Letters A* **372**, 4545-4552, 2008.
- [155] L. Guo; H.S. Wu; Z.H. Jin; “The aluminum phosphides Al_mP_n ($m + n = 2-5$) and their anions: structures, electron affinities and vibrational frequencies.” *Intern. J. Mass Spectrometry* **240**, 149 (2005).
- [156] P. Feng; K. Balasubramanian; “Electronic states of Al_3P and AlP_3 and their positive ions.” *Chem. Phys. Lett.* **301**, 458 (1999).
- [157] E. Archibong; A. St-Amant; “Structure and Electron Detachment Energies of Al_3P^- and $Al_3P_3^-$ ” *J. Phys. Chem. A.* **106**, 5932 (2002).

- [158] T.F. Fassler; "The renaissance of homoatomic nine-atom polyhedral of the heavier carbon-group elements Si-Pb" *Coord. Chem. Rev.* **215**, 347 (2001).
- [159] N Korber; "The Shape of germanium Cluster To Come" *Angew. Chem. Inter. Ed.* **48**, 3216 (2009).
- [160] J.M. Goicoechea; S.C. Sevov; "Naked deltahedral silicon clusters in solution: synthesis and characterization of Si_9^{3-} and Si_5^{2-} " *J. Amer. Chem. Soc.* **126**, 6860 (2004).
- [161] X.Q. Cheng; P.F. Shi; "Electroless Cu-plated Ni_3Sn_4 alloy used as anode material for lithium ion battery" *J. Alloys and Compounds* **391**, 241 (2005).
- [162] N.T.S. Lee; V.B.C. Tan; K.M. Lim; "Structural and mechanical properties of Sn-based intermetallics from ab initio calculations" *Appl. Phys. Lett.* **89**, 141908 (2006).
- [163] S.T. Sun; H.T. Liu; Z.C. Tang; "Experimental and theoretical investigation on binary semiconductor clusters of Bi/Si, Bi/Ge and Bi/Sn" *J. Phys. Chem. A* **110**, 5004 (2006).
- [164] U.U Gupta; P.A. Clayborne; A.C. Reber; J.J. Melko; S.N. Khanna; A.W. Castleman Jr.; "Effect of Charge and Composition on the Structural Fluxionality and Stability of Nine Atom Tin-Bismuth Zintl Analogs" *Inorg. Chem.* **47**, 23 (2008).
- [165] M.W. Hull; S.C. Sevov; "Organo-Zintl clusters Soluble in Conventional Organic Solvents: Setting the Stage for Organo-Zintl Cluster Chemistry" *Inorg. Chem.* **46**, 10953 (2007).
- [166] M.W. Hull; S.C. Sevov; "Functionalization of Nine-Atom Deltahedral Zintl Ions with Organic Substituents: Detailed Studies of the Reactions" *J. Amer. Chem. Soc.* **131**, 9026 (2009).
- [167] D.J Chapman; S.C. Sevov; "Tin Based Organo-Zintl Ions: Alkylation and Alkenylation of Sn_9^{4-} " *Inorg. Chem.* **47**, 6009 (2008).
- [168] F.S. Kocak; P.Y. Zavalij, Y.F. Lam; B.W. Eichhorn; "Substituent-dependent exchange mechanisms in highly fluxional RSn_9^{3-} anions" *Chem. Comm.* **28**, 4197 (2009).

- [169] J. Rosdahl; T.F. Fassler; L. Kloo; "On the structure of nonastannide clusters in liquid and solid state" *Eur. J. Inorg. Chem.* **14**, 2888 (2005).
- [170] K.B. Shelimov; D.E. Clemmer; M.F. Jarrold; "Metal-Containing Carbon Clusters." *J. Chem. Soc., Dalton Trans.*, **5**, 567 (1996).
- [171] H. Harris; I. Dance; "The Geometric and Electronic Structures of Niobium Carbon Clusters" *J. Phys. Chem. A* **105**, 3340 (2001).
- [172] H.-J. Zhai; S.R. Liu; X. Li.; L.-S. Wang; "Photoelectron spectroscopy of mono-niobium carbide clusters NbC_n^- ($n = 2-7$): Evidence for a cyclic to linear structural transition." *J. Chem. Phys.* **115**, 5170 (2001).
- [173] K.L. Knappenberger; P.A. Clayborne; J.U. Reveles; M.A. Sobhy; C.E. Jones Jr.; U. Gupta; S.N. Khanna; I. Iordanov; J. Sofo; A.W. Castleman, Jr.; "Anion Photoelectron Spectroscopy and Density Functional Investigation of Diniobium-Carbon Clusters." *ACS Nano* **1**, 319 (2007).
- [174] V. Dryza; J.R. Gascooke; M.A. Buntine; G.G. Metha; "Onset of carbon-carbon bonding in the Nb_5C_y ($y = 0-6$) clusters: a threshold photo-ionisation and density functional theory study." *Phys Chem Chem Phys* **11**, 1060 (2009).
- [175] V. Dryza; J.R. Gascooke; M.A. Buntine; G.G. Metha; "Threshold Photionization and Density Functional Theory Studies of the Niobium Carbide Clusters Nb_3C_n ($n = 1-4$) and Nb_4C_n ($n = 1-6$)." *J. Phys. Chem A* **112**, 5582 (2008).
- [176] X.M. Khang; S. Jin; Q.Y. Zhang; "Antitumor and Antiangiogenic Activity of Soy Phytoestrogen on 7,12-Dimethylbenz[alpha]anthracene-Induce Mammary Tumors following Ovariectomy in sprague-Dawley Rats" *Journal of Food Science* **74**, H237 (2009).

- [177] K. Ghosh; G. Masanta; “Anthracene-based open and macrocyclic receptors in the fluometric detection of urea” *New Journal of Chemistry* **33**, 1965 (2009).
- [178] M.A. Baldo; M.E. Thompson; S.R. Forrest; “High-efficiency fluorescent organic light-emitting devices using a phosphorescent sensitizer” *Nature* **403**, 750 (2000).
- [179] P. Puengjinda; N Sano; W Tanthapanichakoon; T. Charinpanitkul; “Selective synthesis of carbon nanotubes and nanocapsules using naphthalene pyrolysis assisted with ferrocene” *Journal of Industrial and Engineering Chemistry* **15**, 375 (2009).
- [180] S. Salman; MCR Delgado; V Coropceanu; JL Bredas; “Electronic Structure and Charge-Transport Parameters of Functionalized Tetracene Crystals: Impact of Partial Fluorination and Alkyl or Alkoxy Derivatization” *Chemistry of Materials* **21**, 15 (2009).
- [181] Peter Y. Yu and Manuel Cardona; “Fundamentals of Semiconductors: Physics and Materials Properties” 3rd ed. (Springer New York, 2005)
- [182] S. Nagaoka; K. Ikemoto; K. Fujio; K. Hiehata; A. Sasahara; M. Mitsui; H. Onishi; A. Nakajima; “An atomic force microscope study of vanadium-benzene sandwich clusters soft-landed on self-assembled monolayers” *Eur. Phys. Journ. D* **52**, 103 (2009).
- [183] I. Valencia; A. Guevara-Carcia; M. Castro; “Bonding and Magnetism of $Fe_6-(C_6H_6)_m$, $m = 1-2$ ” *J. Phys Chem A* **113**, 6222 (2009).
- [184] A. Goto; S. Yabushita; “Theoretical study on the spin states and intra-cluster spin relaxation of the one-dimensional metal-benzene sandwich clusters: $M_2(C_6H_6)_3$ ($M = Sc, Ti, V$)” *Chem Phys Lett* **454**, 382 (2008).
- [185] J. Zhou; W.N. Wang; K.N. Fan; “Novel Compounds with cobalt, copper, and nickel dimers sandwiched between benzene molecules: A DFT study” *Chem Phys Lett* **424**, 247 (2006).

- [186] H. Xiang; J. Yang; J.G. Hou; Q. Zhu; “One-dimensional Transition Metal-Benzene Sandwich Polymers: Possible Ideal Conductors for Spin Transport” *J. Amer. Chem. Soc.* **128**, 2310 (2006).
- [187] J. Mercero; J.M. Ugalde; “Sandwich-Like Complexes Based on “All-Metal” (Al_4^{2-}) Aromatic compounds” *J. Amer. Chem. Soc.* **126**, 3380 (2004).
- [188] L. Yang; X. Li; Y. Ding; C. Sun; “Theoretical Study on a class of organometallic complexes based on all-metal aromatic Ga_3^- through sandwiching stabilization” *Eur. Journ. Inorg. Chem.* **12**, 2099 (2008).
- [189] L. Yang; J. Wang; Y. Ding; C. Sun; “Theoretical Study on the assembly and stabilization of a silicon-doped all-metal aromatic unit $SiAl_3^-$ ” *Organometallics* **26**, 4449 (2007).
- [190] P.K. Chattaraj; S. Giri; “Multi-decker Sandwich Complexes using Be_3^{2-} and Mg_3^{2-} dianions” *International Journal of Quantum Chemistry* **109**, 2373 (2009).
- [191] J.L. Wang; P.H. Acioli; J. Jellinek; “Structure and Magnetism of $V_nBz_{(n+1)}$ sandwich clusters” *J. Amer. Chem. Soc.* **127**, 2812 (2005).
- [192] K. Miyajima; S. Yabushita; M.B. Knickelbein; A. Nakajima; “Stern-Gerlach experiments of one-dimensional metal-benzene sandwich cluster: $M_n(C_6H_6)_m$ ($M = Al, Sc, Ti, \text{ and } V$)” *J. Amer. Chem. Soc.* **129**, 8473 (2007).
- [193] Y. Mokrousov; N. Atodiresei; G. Bihlmayer; S. Heinze; S. Blugel; “The interplay of structure and spin-orbit strength in the magnetism of metal-benzene sandwiches: from single molecules to infinite wires” *Nanotechnology* **18**, 495401 (2007).
- [194] V.V. Maslyuk; A. Bagrets; V. Veded; A. Arnold; F. Evers; M. Brandbyge; T. Bredow and I. Mertig; “Organometallic benzene-vanadium wire: A one-dimensional half-metallic ferromagnet” *Phys. Rev. Lett.* **97**, 097201 (2006).

- [195] S.M. Mattar; R. Sammynaiken; “Electronic structure, ground state and electron paramagnetic resonance spectroscopy of the matrix-isolated (eta(6)-C₆H₆)V and (eta(6)-C₆D₆)V half-sandwich transients” *J. Chem. Phys.* **106**, 1080 (1997).
- [196] A.K. Kandalam; B.K. Rao; P. Jena; R. Pandey; “Geometry and electronic structure of V_n(Bz)_m complexes” *J. Chem. Phys.* **120**, 10414 (2004).
- [197] K Pradhan; P Sen; JU Reveles; SN Khanna; “First principles study of Sc, Ti, and V doped Na_n (n = 4, 5, 6) clusters: Enhanced magnetic moments” *Phys Rev B* **77**, 045408 (2008).
- [198] A.W. Castleman, Jr.; S.N. Khanna; A. Sen; A.C. Reber; M. Qian; K.M. Davis; S.J. Peppernick; A. Ugrinov; M.D. Merritt; “From designer clusters to synthetic crystalline nanoassemblies” *NanoLetters* **7**, 2734 (2007).
- [199] F. Lui; M. Mostoller; T. Kaplan; S.N. Khanna; P. Jena; “Evidence for a new class of solids. First-principles study of K(Al₁₃)” *Chem Phys Lett* **248**, 213, 1996.
- [200] M.S. Denning; J.M. Goicoechea; “[Hg₃(Ge₉)₄]¹⁰⁻: a nanometric molecular rod precursor to polymeric mercury-linked cluster chains” *Dalton Transactions* **43**, 5882 (2008).
- [201] A.C. Reber; S.N. Khanna; A.W. Castleman, Jr.; “Superatom Compounds, Clusters, and Assemblies: Ultra Alkali Motifs and Architectures” *J. Amer. Chem. Soc.* **129**, 10189 (2007).
- [202] C. Ashman; S.N. Khanna; M.R. Pederson; D.V. Porezag; “Thermal ionmerization in Cs₄Cl₃” *Phys. Rev. A* **58**(1), 1998.

Appendix A

Publications related to this Thesis

A.1 Publications in print

- Structural Evolution of Triniobium Carbide Clusters: Evidence of Large C_n Chains ($n = 3-4$) in $Nb_3C_n^-$ ($n = 5 - 10$) Clusters
P.A. Clayborne, C.E. Jones, U. Gupta, J.J. Melko, A.W. Castleman, Jr. and S.N. Khanna
J. Phys. Chem. A, Article **DOI:** 10.1021/jp905022p (2009)
- Designer Magnetic Superatoms
J.U. Reveles, P.A. Clayborne, A.C. Reber, S.N. Khanna, M.R. Pederson, K. Pradhan, and P. Sen
Nature Chemistry **1**, 310 (2009)
- Al_nBi Clusters: Transitions Between Aromatic and Jellium Stability”
C.E. Jones, P.A. Clayborne, J.U. Reveles, U.U. Gupta, J.J. Melko, A.W. Castleman, Jr. and S.N. Khanna
J. Phys. Chem. A **112**, 51 (2008)
- Effect of Charge and Composition on the Structural Fluxionality and Stability of Nine Atom Tin-Bismuth Zintl Analogs
U. Gupta, P.A. Clayborne, A.C. Reber, J.J. Melko, S.N. Khanna, and A.W. Castleman Jr.
Inorganic Chemistry **47**, 23 (2008)
- Anion Photoelectron Spectroscopy and Density Functional Investigation of Diniobium Carbon Clusters

K.L. Knappenberger, Jr., P.A. Clayborne, J.U. Reveles, M.A. Sobhy, C.E. Jones, Jr., U. Gupta, S.N. Khanna, I. Iordanov, J. Sofo, and A.W. Castleman, Jr.
ACS Nano **1**, 4 (2007)

- Superatoms and their assemblies based on Alkali and Super-alkali Motifs
P.A. Clayborne, N.O. Jones, A.C. Reber, J.U. Reveles, M.C. Qian, and S.N. Khanna.
Journal of Computational Methods in Sciences and Engineering **7**, p.417 (2007)

A.2 Publications in preparation

- A Combined Experimental and Theoretical Study of Al_nX ($n = 1-6$, $X = As, Sb$) Clusters: Evidence of the Jellium Model and Aromaticity
J.J. Melko, P.A. Clayborne, C.E. Jones, Jr., J.U. Reveles, U. Gupta, S.N. Khanna, A.W. Castleman, Jr. (Submitted)
- Building Magnetic Superatoms in within the framework of the unified jellium model
P.A. Clayborne, J.U. Reveles, and S.N. Khanna
- The effects of counteractions on Gas Phase Zintl Analogue Clusters: Stepping stones towards new cluster assembled materials
P.A. Clayborne, A.C. Reber and S.N. Khanna
- Organo-Zintl Cluster Assemblies based on the Gas Phase Zintl Analogue Cluster $Sn_7Bi_2^-$
P.A. Clayborne, A.C. Reber and S.N. Khanna
- Aromatic and Antiaromatic Character in Sn_nBi^- Clusters
P.A. Clayborne, U. Gupta, A.C. Reber, J.J Melko, S.N. Khanna, A.W. Castleman, Jr.
- Aromaticity within the ellipsoidal jellium model
P.A. Clayborne and S.N. Khanna

Appendix B

Point Group Character Tables

B.1 Selected C_{nv} Groups

C_{2v}	E	C_2	$\sigma_v(xz)$	$\sigma'_v(yz)$		
A_1	1	1	1	1	z	x^2, y^2, z^2
A_2	1	1	-1	-1	R_z	xy
B_1	1	-1	1	-1	x, R_y	xz
B_2	1	-1	-1	1	y, R_x	yz

C_{3v}	E	$2C_3$	$3\sigma_v(xz)$		
A_1	1	1	1	z	$x^2 + y^2, z^2$
A_2	1	1	-1	R_z	
E	2	-1	0	(x, y), (R_x, R_y)	$(x^2 - y^2, xy), (xz, yz)$

B.2 D_{3h} Group

D_{3h}	E	$2C_3$	$3C_2$	σ_h	$2S_3$	$3\sigma_v$	
A_1'	1	1	1	1	1	1	$x^2 + y^2, z^2$
A_2'	1	1	-1	1	1	-1	R_z
E'	2	-1	0	2	-1	0	(x, y) $(x^2 - y^2, xy)$
A_1''	1	1	1	-1	-1	-1	
A_2''	1	1	-1	-1	-1	1	z
E''	2	-1	0	-2	1	0	(R_x, R_y) (xz, yz)

Tables taken from the book *Molecular Symmetry and Group Theory* (John Wiley & Sons Inc., New York 1998) Robert L. Carter, author.

VITA

Peneé A. Clayborne was born in Rocky Mount, Virginia, USA on January 26, 1978 and attended Franklin County High School. In the quest of education, Clayborne attended Radford University and received a Bachelor of Science in Physical Science with a concentration in Physics in 2002. After receiving the B.S. degree, P. Clayborne was employed in industry for two years and returned to pursue a graduate education in Physics at Virginia Commonwealth University. In December 2006, Clayborne was awarded a Master of Science in Applied Physics and began doctoral work in 2007.